12-2014

Materials Science of Electrochemical Formation of Tungsten Nanosharp Probes

Maryana I. Nave
Clemson University

MATERIALS SCIENCE OF ELECTROCHEMICAL FORMATION OF TUNGSTEN NANOSHARP PROBES

A Dissertation
Presented to
the Graduate School of
Clemson University

In Partial Fulfillment
of the Requirements for the Degree
Doctor of Philosophy
Materials Science and Engineering

---

by
Maryana I. Nave
December 2014

Accepted by:
Dr. Konstantin G. Kornev, Committee Chair
Dr. Alexey Vertegel
Dr. Stephen H. Foulger
Dr. Igor Luzinov

ABSTRACT

This dissertation is centered on the development of a methodology that aims to engineer millimeter long and ten microns thin nanosharp tungsten probes. The current state of the art of electropolishing techniques is reviewed. We discuss the probes produced by electrochemical etching of a wire until it breaks into two pieces. This process is difficult to control because of the complexity of the associated hydrodynamic flows. These techniques were called convection-limited electropolishing (CLE) because the kinetics of wire etching is controlled by the convective diffusion of ions. We introduced a newly developed technique, precipitation-limited electropolishing (PLE), which enables production of the long probes with nanosharp tips. In the PLE regime, the electrochemical reaction leads to formation of the porous surface layer that hinders the flow of the electrolyte. The probe's sharpness and length are controlled by choosing an appropriate thermodynamic pathway of metal to metal oxide/hydrates transformations. As an example of the treatable metals, we use tungsten wires. However, the developed methodology might be applicable for other metals.

DEDICATION

This dissertation is dedicated to my family. Their constant support, love and encouragement have helped me during this PhD journey.

ACKNOWLEDGMENTS

I would like to express my appreciation to my research advisor Dr. Konstantin G. Kornev for his support, patience, and guidance. His ideas, aspiration for perfection and enthusiasm helped me reach new heights, motivated me to learn new concepts and shaped me as an independent research scientist. I am thankful to my committee members, Dr. Igor Luzinov, Dr. Stephen H. Foulger, and Dr. Alexey Vertegel for their guidance, comments and valuable suggestions in my research.

I wish to thank my colleagues, group members and everyone that worked with me for their help and encouragement. I would like to thank Dr. Yu Gu for his help with the nodoid model and Dr. Daria Monaenkova for her help with MATLAB® and Mathematica®. Also, I wish to thank Dr. Binyamin Rubin, Dr. Alexander Tokarev, Dr. Taras Andrukh, Mahmut O. Kesimci, Dr. Vijoya Sa, Dr. Chen-Chin Tsai, Dr. Vladislav Vekselman, Dr. Mykola Kulakov, Dr. Marius Chyasnavichyus and Dr. Ruslan Burtovyy.

I would like to acknowledge my collaborators on a variety of projects. At Brookhaven National Laboratory, I would like to thank Dr. Jun Wang, Dr. Yu-chen Karen Chen-Wiegart, Dr. Jiajun Wang and Dr. Wah-Keat Lee for their help with X-ray phase contrast imaging experiments. At Clemson University, Department of Entomology, I wish to thank Dr. Peter Adler and Dr. Charles E. Beard for the exciting collaboration on the butterfly's research that inspired the design of the probe for single cell piercing, and Department of Bioengineering, Dr. Victor Maximov for providing vascular smooth muscle cells and helping with the cell staining methods. Additionally, I want to thank

Prof. L. L. Pesterfield and Prof. J. B. Maddox for providing me with the original Wolfram Mathematica® code for the construction of the Pourbaix diagrams that I modified for the tungsten case.

I am extending my gratitude to Dr. Stephen Creager, Dr. Olt Geiculescu and Jamie Shetzline for their help in the electrochemical aspects of this dissertation. I wish to thank Dr. Colin McMillen and Dr. Don VanDerveer for their help with the XRD experiments and analysis; Dr. Taghi Darroudi, Dayton Cash and George Wetzel for their assistance with the SEM and EDS techniques. I would like to thank Kim Ivey for her help with the IR and thermal analysis techniques and MSE staff, particularly David White, James Lowe, Stanley Justice, Shelby Sheriff and Kathy Bolton.

I would like to acknowledge the National Science Foundation for funding the following projects: EFRI-BSBA "Lepidoptera proboscises as prototypes of multifunctional fluidic devices with distributed actuation and sensing", grant number 0937985 and CMMI "Design and Surface Engineering of Nanofiber-based Probes", grant number: 0826067.

I wish to express my deepest gratitude to my parents, Svetlana and Ivan for their constant support, love and encouragement. Thank you for everything you have done for me and for all sacrifices that you have made in order to make this all happen. I wish to thank my sister Natasha for her endless optimism and enthusiasm that kept me positive through the tough times and my sister Svetlana for her support and encouragement. I wish to thank my husband Scott for being so caring and understanding. Without his constant support and love this would not have been possible.

TABLE OF CONTENTS

Page

Table of Contents (Continued)

Page

LIST OF TABLES

Table Page

LIST OF FIGURES

Figure Page

List of Figures (Continued)

Figure Page

List of Figures (Continued)

Figure Page

List of Figures (Continued)

Figure Page

List of Figures (Continued)

Figure Page

List of Figures (Continued)

Figure Page

List of Figures (Continued)

Figure Page

List of Figures (Continued)

Figure Page

List of Figures (Continued)

Figure Page

1. FABRICATION OF THE NANOSHARP NEEDLES BY ELECTROPOLISHING

1.1. Introduction to convection-limited electropolishing (CLE)

In different applications such as scanning tunneling microscopy [1-22], atomic force microscopy [11-16, 22], field ion microscopy[10], nanolithography [23, 24], micro/nano welding [25, 26], microelectrodes[27-30] and many biomedical applications [29, 31-41], one needs to have a nanosharp probe. Electropolishing is the most reliable and inexpensive method of wire sharpening used to provide the wire tips with the radius of curvature varying from a few nanometers to submicrons [21, 42-47]. Currently, the available electropolishing techniques take advantage of convection-limited electropolishing (CLE) when the ions of interest are removed/delivered to the metal surface by the flowing electrolyte [22, 31, 32, 42, 44, 48]. For instance, in the electropolishing of tungsten wire, the applied voltage initiates an electrochemical reaction that is described by the following equations (1.1)-(1.3) [48, 49]:

Cathode: $$6H_2O + 6e^- \rightarrow 3H_2(g) + 6OH^- \quad (1.1)$$

Anode: $$W(s) + 8OH^- \rightarrow WO_4^{2-} + 4H_2O + 6e^- \quad (1.2)$$

Overall: $$W(s) + 2OH^- + 2H_2O \rightarrow WO_4^{2-} + 3H_2(g) \quad (1.3)$$

The anodic oxidation of the vertically placed tungsten wire results in the formation of tungstate ions on its surface in the form of a thin highly viscous film immiscible with the surrounding electrolyte [3, 48]. This film is heavier than the surrounding electrolyte and flows down a wire (Figure 1.1 (a), (b)) [48]. Electropolishing proceeds until the film reaches a critical thickness at which the Plateau-Rayleigh instability causes it to thin down and eventually dewet the surface [48]. Depending on the geometry, this Plateau-Rayleigh instability can result in either the formation of cavities and grains as in the case of thick rods with almost flat films [50], or the formation of a neck as in the case of thin wires [48]. The neck thickness decreases with time and finally the wire breaks into two pieces. In Figure 1.1 (c), (d) as a model of dewetting, the flow of a 3 wt% polyethylene oxide (PEO) aqueous film in hexadecane is shown [48]. PEO film represented reaction products and hexadecane modeled a potassium hydroxide solution. Once the wire with the PEO film is dipped into hexadecane, the film thins down and breaks into droplets indicating instability of the PEO film/hexadecane interface. This supports a possible scenario for the flow instability that takes place during electropolishing.

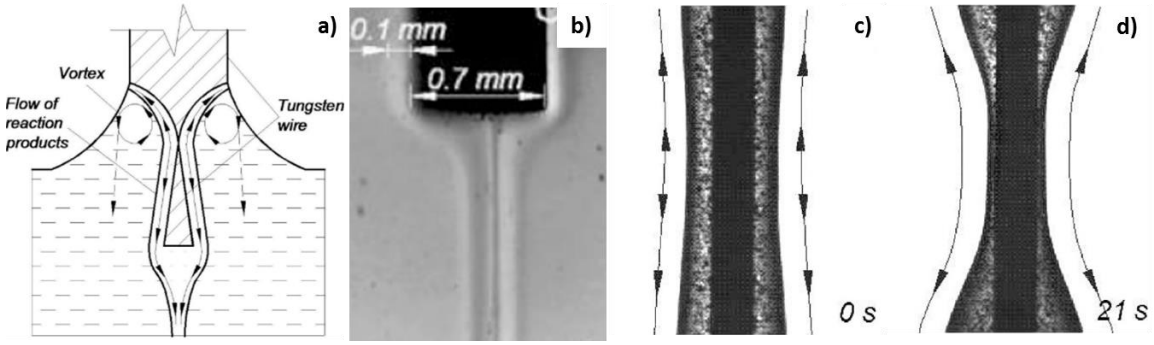

Figure 1.1. Electropolishing of tungsten wire: (a) schematic of the pathway of the reactant products flow during electropolishing with the CLE method, (b) image of flow recorded using high speed camera (applied voltage is 4V), (c),(d) simulation of the Plateau-Rayleigh instability of a 3 wt% PEO aqueous on the tungsten wire immersed into hexadecane [48].

The electrochemical reaction written in the form (1.2) hides the multistep electrochemical reactions discovered by Kelsey[51]. He showed that tungsten electropolishing occurs through a more complex scenario that consists of six steps of electrochemical and non-electrochemical reactions (1.4)-(1.9) [51, 52]:

$$W(s)+2OH^- \rightarrow WO^+(s)+3e^- +4H_2O \tag{1.4}$$

$$WO^+(s)+2OH^- \rightarrow WO_2(s)+e^- +H_2O \tag{1.5}$$

$$WO_2(s)+OH^- \rightarrow WO_3H(s)+e^- \tag{1.6}$$

$$WO_3H(s)+OH^- \rightarrow WO_3(s)+e^- +H_2O \tag{1.7}$$

$$WO_3(s)+OH^- \rightarrow HWO_4^-(aq) \tag{1.8}$$

$$HWO_4^-(aq)+OH^- \leftrightarrow WO_4^{2-}(aq)+H_2O \tag{1.9}$$

From eq.(1.4), one can see that the first step of the tungsten dissolution is the formation of the WO^+ ions. These ions are positive and are pushed away from the

positively charged electrode. However, these ions are not the end products of the electrochemical reaction, but they react with the OH^- groups to produce insoluble tungsten oxides (reactions(1.5)-(1.7)). In turn, these oxides are prone to interact with the OH^- groups to form heavy tungstate ions, WO_4^{2-}, which are negative and are attracted back to the positively charged electrode (tungsten). This mechanism explains the formation and flow of the heavy tungstate ions along the tungsten surface. Their diffusion toward the cathode is hindered by electrostatic attraction to the anode and by the spontaneous film flow as shown in Figure 1.1 (b).

The electropolishing setup usually consists of two electrodes with a tungsten wire as an anode immersed into a potassium hydroxide (KOH) solution. Different environmental parameters and geometry of the electrodes, depth of immersion, applied voltage and electrolyte concentration influence the shape of the electropolished wires. Most often, the rod-like [6, 40, 48, 53] and loop/ring/hollow cylinder/capillary [3, 9-12, 15, 16, 19, 47, 53-56] cathodes are employed.

There are two main modes of electropolishing: alternating current (AC) [23, 54, 57] and direct current (DC) [1, 3, 5-7, 11, 12, 22, 40, 48, 58] electropolishing. Depending on the electropolishing mode, the resulting products differ by shapes and the radius of curvature of the wire tips. The AC tips are conical with a large cone angle. The DC tips have a slender paraboloidal shape. Different modifications of these techniques employed static and dynamic menisci [1, 3, 48, 49, 53, 56, 59], attached masses [58], lamellae [2, 7, 8, 13, 22], or reverse etching of the wires [57, 60]. Examples of these techniques are shown in Figure 1.2.

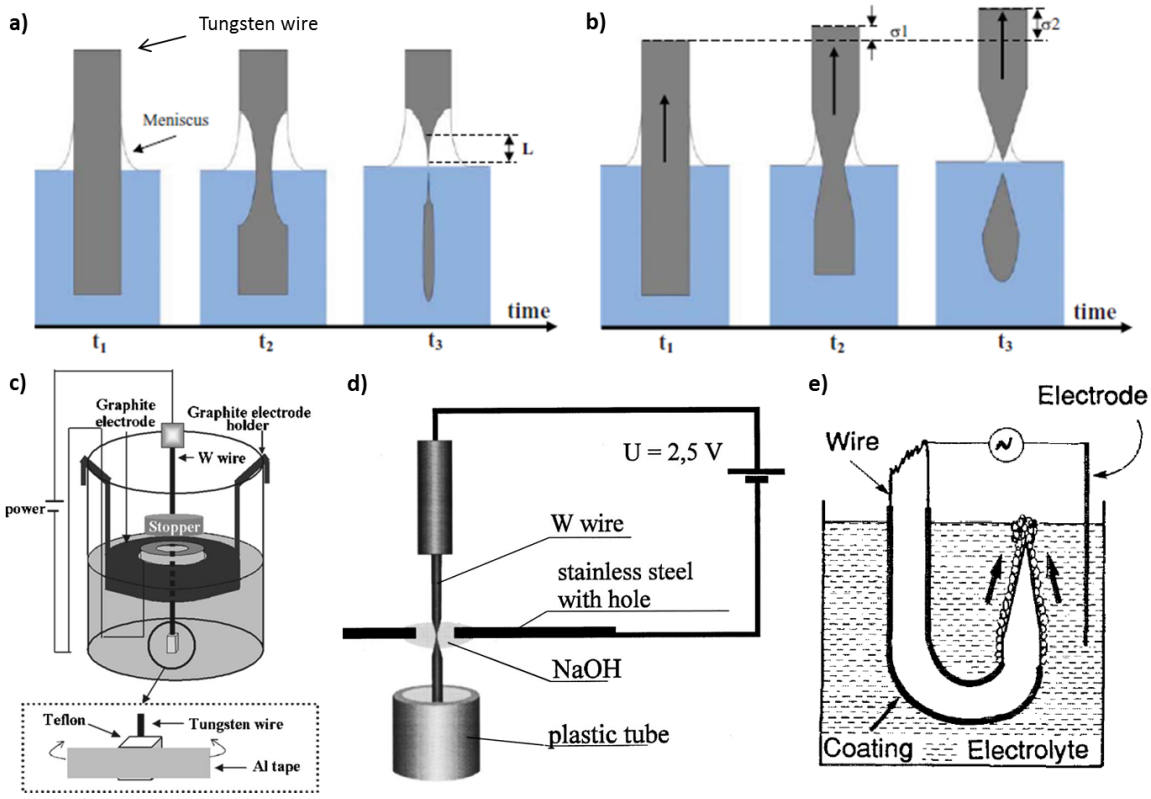

Figure 1.2. Different electropolishing techniques: (a) Static electropolishing [56], (b) dynamic electropolishing [56], (c) with an attached mass [58], (d) lamellae [2] and (e) reverse etching [57].

Static [56] electrochemical etching technique (Figure 1.2 (a)) represents the etching of tungsten wire, that is fixed in the vertical position perpendicularly to the electrolyte surface, until the wire brakes into two pieces under the meniscus region. Dynamic [56] etching technique employs a lifting up procedure of tungsten at a certain speed (σ1, σ2) during the polishing (Figure 1.2 (b)). Using this technique one can vary the shape of the needle by changing the lifting speed of the wire. The static meniscus method provides a parabolic type shaped needle while the dynamic provides a more elongated and conical shape or multidiameters long needle. Electropolishing technique

with an attached mass shown in Figure 1.2 (c) employs the effect of tensile stress on the etching process. Authors in ref. [58] tapped Teflon mass to the end of the tungsten wire that was passed through the cylindrical graphite electrode. Using different mass one can control the sharpness of the needle. To perform lamellae electropolishing a cathode in a form of loop with a liquid membrane of electrolyte suspended on its edges is used with tungsten wire passing through the center of the membrane and perpendicular to it. An example of this type of setup is shown in Figure 1.2 (d). Another popular technique is a reverse etching when tungsten in immersed into electrolyte pointing upwards (Figure 1.2 (e)).

The current CLE electropolishing technique can be used to produce nanosharp tips from variety of materials such as platinum [21, 61], gold [44, 61-73], silver [45, 74-76], nickel [14, 43], stainless steel [77], nichrome [42], optical fibers [78, 79], silicon [80], Pt-Ir [14, 81], Re [46] and others. However, all described techniques rely on the idea of the wire breakup: tungsten is etched up to the point when it breaks into two pieces. Typically, the length of the conical part of the broken piece is limited to 500 μm; this length is difficult to control because it significantly depends on the development of the Plateau-Rayleigh instability and on the rate of neck formation prior to the wire breakup. The flow of the film surrounding the wire adds to the process complexity. Hence, electropolishing of the wires is often called the art of making nanosharp tips [53, 59].

In order to avoid dealing with the Plateau-Rayleigh instability and natural convection, and overcome the main drawbacks of the conventional CLE regime, we

introduce the precipitation-limited electropolishing (PLE) regime. In this regime, a porous protective film separates a metal surface from the electrolyte. Even though the PLE regime has been actively studied within corrosion science [82, 83], a porous film around a tungsten wire has never been used to protect the wire against breakup. We show that this porous film decreases the rate of the downward and upward flows of the reaction products. With this reduction of the convection transfer of ions along the wire surface, one decreases the gradients of the ion concentrations along the wire axis. This PLE regime enables the wires to be etched almost uniformly with a small taper; the necking instability can be eliminated and the submersed part of the wire can be protected from the breakup. Thus, the wire can be etched only from the submersed end. As a result, very long electropolished needles with the nanosharp paraboloidal tips can be formed.

1.2. Scope of research

We aim to develop a scientifically sound methodology of making millimeter long and ten microns thin nano-sharp needles. Our objective is to explore and extend the existing limits of electropolishing technique [48]. As an example of the treatable metals, we use tungsten wires. Currently, convection-limited electropolishing (CLE) has been extensively used. Nanosharp probes were produced by electrochemically etching a wire until it breaks into two pieces. This process is difficult to control because of the complexity of the associated hydrodynamic flows. We show that electrochemical formation of long probes with nanosharp tips can be controlled by choosing an appropriate thermodynamic pathway of metal to metal oxides and hydroxides

transformations. We introduce precipitation-limited electropolishing (PLE) when the electrochemical reaction results in the formation of metal oxides and hydroxides which form a porous surface layer hindering the flow of electrolyte. The developed PLE regime enables one to make long tapered needles. The taper can spread over more than 6 mm while the radius of tip curvature can be decreased down to 30 nm.

An important application of long nanosharp needles is the cell probe [32, 37, 38, 84-86]. The main problem with real-time cell analysis is that all existing procedures of cell piercing lead to irreversible damage of the cell membranes. A single cell suspended in a buffer or spread over a surface has the diameter varying from 5 to 70 micrometers. Therefore, in order to make in vivo analysis of the cell biofluids, the probe has to be equipped with a thin nano-sharp tip [38]. The sharpness of the probe will assure that after piercing, the cell will recover and survive for further analysis[32].

It is expected that the results of this study will offer numerous applications that are not limited to the probe design. Ultimately, the proposed study will broaden the traditional limits of existing electropolishing techniques to allow controllable fabrication of thin and long nano-sharp needles out of many metals.

1.3. Precipitation-limited electropolishing (PLE)

1.3.1. Experimental procedure

In our experiments, the cathode was made of a stainless steel rod with 1.5 cm diameter and 5 cm length. Tungsten wires (99.95%, Advent Research Materials Ltd) with 0.125 mm diameter were used as anodes. Electrodes were immersed in a beaker with

aqueous solution of potassium hydroxide (KOH). Three different concentrations of KOH were used in experiments: 3M, 2M, and 1M. These solutions provided us with three different pH levels: 14.5, 14.3, and 14, respectively. The electrodes were connected to a programmable power supply (Gwinstek PSS-2005). The tungsten wire was attached vertically to a micromanipulator stage to allow its precise manipulation. The depth of the wire immersion into the electrolyte was varied from 1 to 10 mm. The LabVIEW® software program was interfaced with and controlled the Dalsa Falcon 1.4M100 camera with the Navitar® lens and power system with USB-1208LS data acquisition device from Measurement Computing™. This allowed us to record the time, voltage, and current in the system. The DC electropolishing mode with voltages ranging between 1-10V was employed in this study. After electropolishing, all probes were rinsed with the DI water for 1-2 minutes. All experiments were carried out at the room temperature (68±1 °F).

The three-electrode setup with the CHI1140B potentiostat (CH Instruments, Inc.) was used for the measurements of overpotential. As a reference electrode, we employed the Ag/AgCl electrode (+0.197V vs. SHE), as a counter electrode we used the platinum wire, and as a working electrode we used the tungsten wire.

1.3.2. Effect of applied voltages on tip morphology

In these experiments, we used the 2M KOH electrolyte solution. When the voltage difference (ΔE) between the cathode and anode was set greater than 4V (4-10V), we only observed the wire breakup with all features described in Ref. [48]. When the voltage was decreased to 4V, the reaction products increased the viscosity of the flowing

film even more. We noticed that some porous flakes started growing from the wire surface. Finally, when the voltage was decreased even further below 2.5V, we observed that the viscous film was transformed into a solid porous shell completely wrapping the immersed part of the tungsten wire. A solid porous shell first appeared at the wire end and grew to a visible microscopic shell in about 90 seconds (Figure 1.3 (b)). The shell propagated upward and wrapped the whole wire in the next 190 seconds. When the current reached 2.65±0.2 mA, the wire attained its smallest visible diameter and electropolishing was stopped, Figure 1.3 (a). The analysis of the tip morphology using SEM revealed that, at this current, the tip acquired a minimum radius of curvature. Therefore, the wire was removed from the solution as soon as the current dropped to 2.65±0.2 mA. Assuming that the porous shell is formed from tungsten oxides and hydrates which are non-conductive [87], one can explain a direct correlation between the thickness of the solid porous film and the current (Figure 1.3): the protective solid porous shells of tungsten oxides and hydrates shield the metal surface from the hydroxide ions. As the shell grows the current decreases and drops to a minimum.

The nanosharp tips were formed only within the 1.7-2.5V voltage range. Using this voltage range, the formation of porous shells was reliably reproduced. This led to the consistent creation of nanosharp tips. Neither wire necking nor any flow instability were detected within this voltage range.

We also studied the range of voltages situated closer to the standard electrode potential ΔE_c = 1.43V needed for initiation of the electrochemical reactions [49]. At the voltages just above ΔE_c but below ΔE = 1.7V, the surface of electropolished wires

appeared rough with many grooves, bumps, and spikes, Figure 1.4. The surface remained rough even after cleaning it with the DI water. These observations suggest that the roughness was created on the physical surfaces of the wires; the shells, most likely, were thrown off the surface during its rinsing. Then, the depth of immersion (H_0) of the tungsten wires was varied from 1 to 10 mm and the same electropolishing features were observed.

The SEM pictures in Figure 1.3 (c), (d) show different spots of the shell that was collected from the 1 mm diameter wire. All attempts to collect shells from smaller wires of 0.127 – 0.5 mm diameters failed because the shells were loosely bonded to the needle surfaces and upon withdrawal of the needles from the container, the shells immediately detached and dispersed in the electrolyte. However, it is expected that the shell structure from the smaller wires should remain similar to that shown in Figure 1.3.

In order to specify the standard hydrogen electrode (SHE) potential, Eh, corresponding to the PLE, we conducted experiments on a three-electrode system. The insert in Figure 1.3 (a) shows a correlation between the Eh-potential of tungsten versus the potential difference ΔE in a two-electrode system ($Eh = \Delta E - 1.13V$). The window 0.57V < Eh < 1.37V corresponds to the conditions 1.7V < ΔE < 2.5V where we observed the shells and obtained the probes with the minimum radius of curvature.

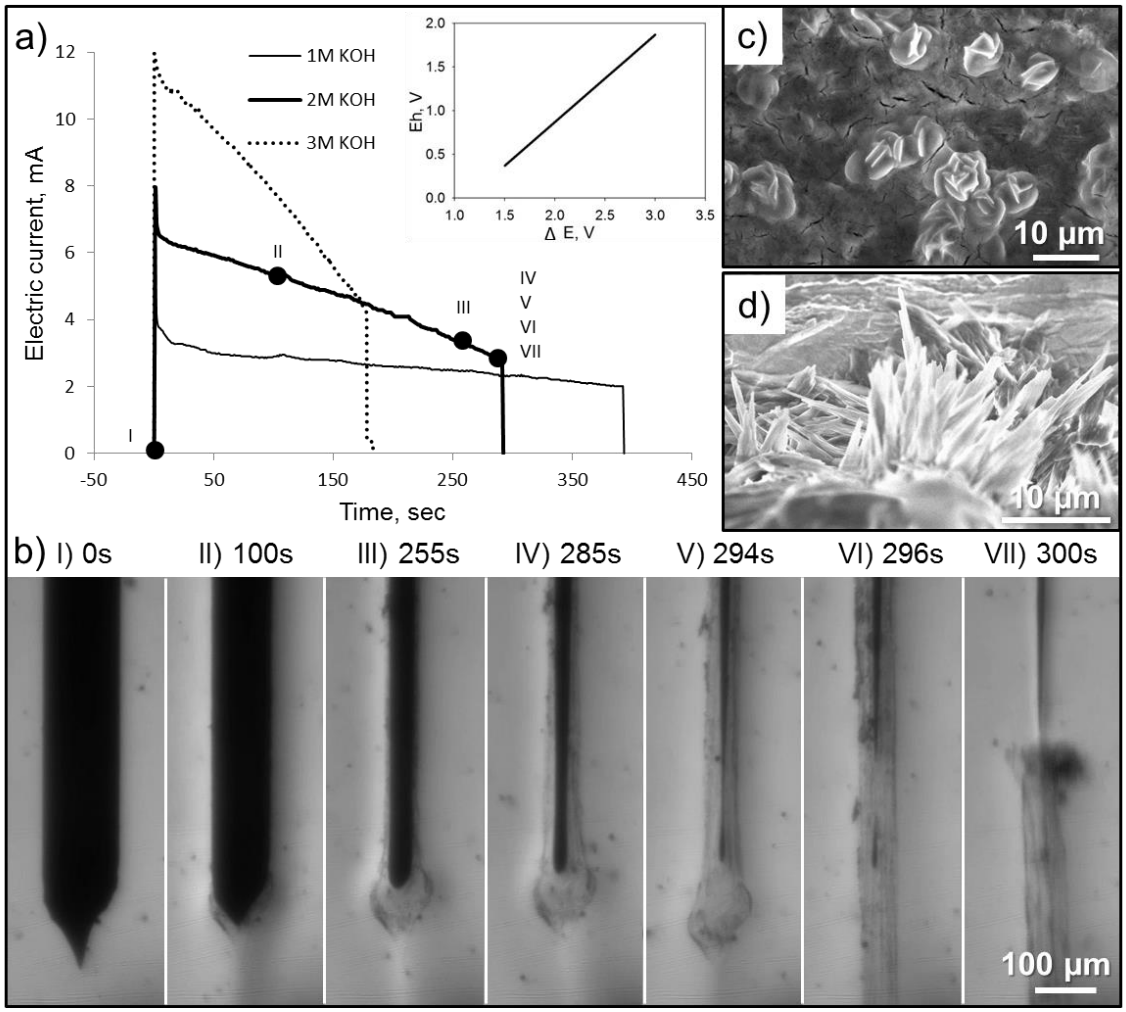

Figure 1.3 (a) The change of the current as a function of time during electropolishing of the 0.125 mm diameter tungsten wires at the applied potential of ΔE=2V. The wires were submersed to a depth of H_0=2mm below the free surface of the 2M KOH solution. (b) The dynamics of formation of a solid porous shell during electropolishing. See Figure (a) for the current corresponding to these snapshots. (c) and (d) The SEM pictures taken from different spots of a solid porous shell collected from the tungsten wire (diameter of 1 mm). The wire was electropolished at ΔE=2V for 1h in the 2M KOH solution and was not rinsed in the DI water after electropolishing.

1.3.3. Effect of KOH concentration on the tip morphology and radius

The 1M - 3M range of KOH concentrations was chosen to see how the concentration of the electrolyte affects the tip morphology and its radius of curvature. The depth of wire immersion was constant, H_0 =2mm, in this set of experiments. The 1.5V - 3V range of voltages was applied to these solutions. Figure 1.3 (a) shows the dependence of the current on time for different electrolytes. The larger the KOH concentration, the shorter the electropolishing time. In the 3M KOH solutions, the wires always broke in the neck region. The 2M KOH solutions revealed different regimes of electropolishing as discussed above. When the same voltages were applied to the 1M KOH solutions, we obtained long needles. Wires were removed from the solution as soon as the current dropped to 2.0±0.2 mA. Neither necking nor breakup of these needles was noticed. Examination of the needle surfaces revealed that these surfaces are rough (Figure 1.4). Table 1.1 gives the summary of data for the different concentrations of potassium hydroxide and applied voltages ΔE.

Table 1.1. Dependence of the probe parameters on concentration of the KOH solutions and applied voltage ΔE; *r* is the radius of tip curvature, *d* is the wire diameter measured at h_m = 400 μm below the base, h is the length of the electropolished portion of the wire. These wires were elecropolished at the constant depth of immersion into the electrolyte, H_0 =2 mm.

KOH (M)	ΔE (V)	r (nm)	d (μm)	h (mm)
3	2		Wire breakup	
	1.5	—	30.4 ± 7.6	1.80 ± 0.16
	1.7	—	26.1 ± 5.0	1.94 ± 0.15
2	2	50 ± 15	28.6 ± 1.3	1.96 ± 0.15
	2.5	105 ± 39	43.3 ± 7.3	2.01 ± 0.12
	3	146 ± 22	31.5 ± 4.9	1.90 ± 0.05
1	1.5	301 ± 259	47.5 ± 6.6	2.03 ± 0.06
	1.7	187 ± 54	57.9 ± 4.4	2.06 ± 0.12
	2	470 ± 81	58.9 ± 1.6	2.06 ± 0.08
	2.5	615 ± 275	42.0 ± 9.0	2.05 ± 0.08

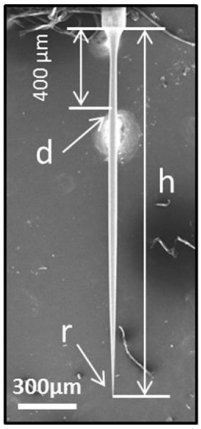

1.3.4. Effect of the immersion depth on the tip morphology

Since the best results were observed with the 2M KOH solution and the ΔE=2V applied voltage, we have chosen these conditions to study the effect of the submersion depth on the radius of curvature of the tip. For this study, the following depths of wire immersion were selected: H_0 = 2mm, 3m, 4mm, 5mm, and 6mm. We collected the produced wires and analyzed their morphology using SEM micrographs. It was found that the radii of curvature of the produced tips did not change significantly from one wire to another resulting in an average radius of curvature r = 50±17nm.

In Figure 1.4, we constructed phase diagram characterizing the tip morphology. Regime I represent the conventional CLE technique leading to the wire breakup and drop-off of the products. In Regime II, the obtained needles have rough surfaces and the

radii of curvature of the tips cannot be estimated. In Regime III, the needles are smooth and the radius of curvature of each tip varied from a few to hundreds of nanometers.

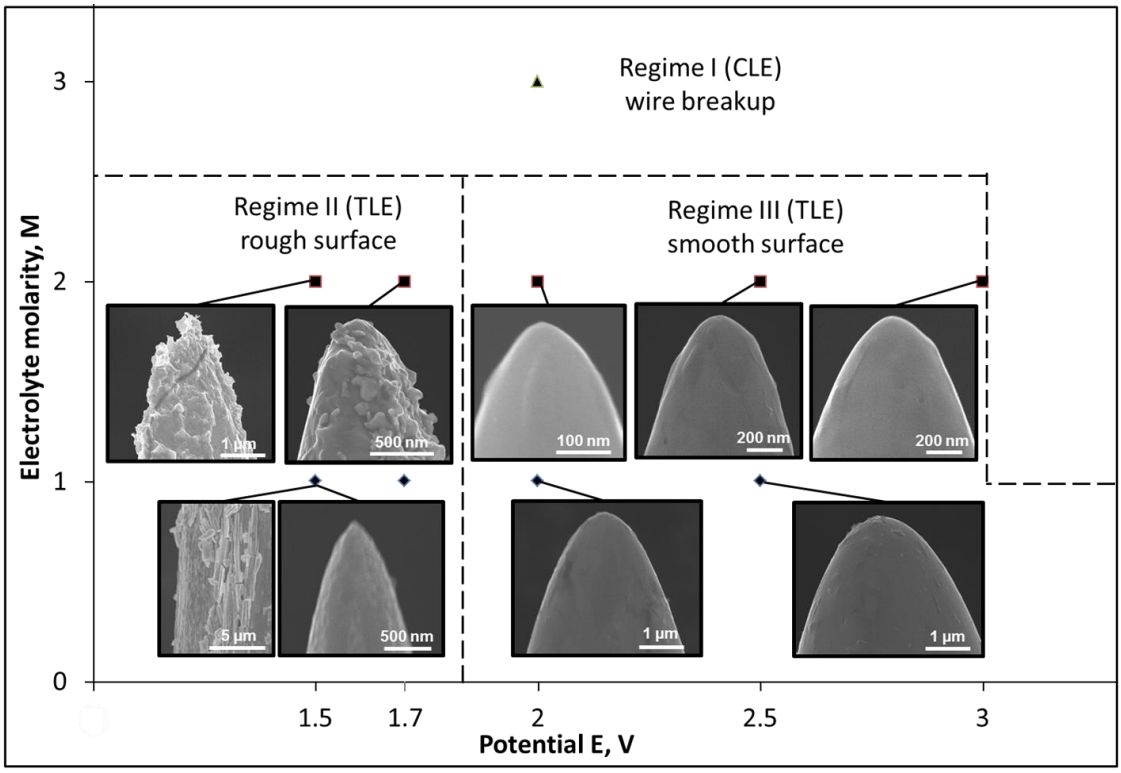

Figure 1.4 Phase diagram characterizing the surface morphology of electropolished tips.

1.3.5. Kinetics of tip formation

Because of the small pores, the shells provided significant resistance to flow, making a drastic change in the flow pattern. The flow of ions through the porous shell was slowed down; hence the contribution of convection to the ion transfer was significantly reduced. Moreover, the development of the Plateau-Rayleigh instability of this interface was delayed because the flow of the thickened electrolyte through porous

material requires much longer time compared to that of a free film [48, 88]. Therefore, the porous shell stabilized the interface between the thickened liquid in the pores and the external immiscible electrolyte. This explains why setting up the voltage range closer to the ΔE_c level resulted in a drastic change in the tip morphology and the tungsten behavior during electropolishing.

In order to study the kinetics of tip formation, several experiments were conducted. The wires of $R = 62.5\,\mu m$ radius were submersed at different depths below the free surface of the 2M KOH electrolyte. Electropolishing was filmed and the images were analyzed with Matlab®.

Figure 1.5 (a), (b), (d), (e), (f) displays the SEM pictures of the tungsten tips at low and high magnification produced by two different regimes of electropolishing. In the analysis, we approximated the wire as a truncated cone (Figure 1.5 (c)) of variable height $h(t)$, radius of the cone base, $R_0(t)$, and variable radius of the cone tip, $r(t)$.

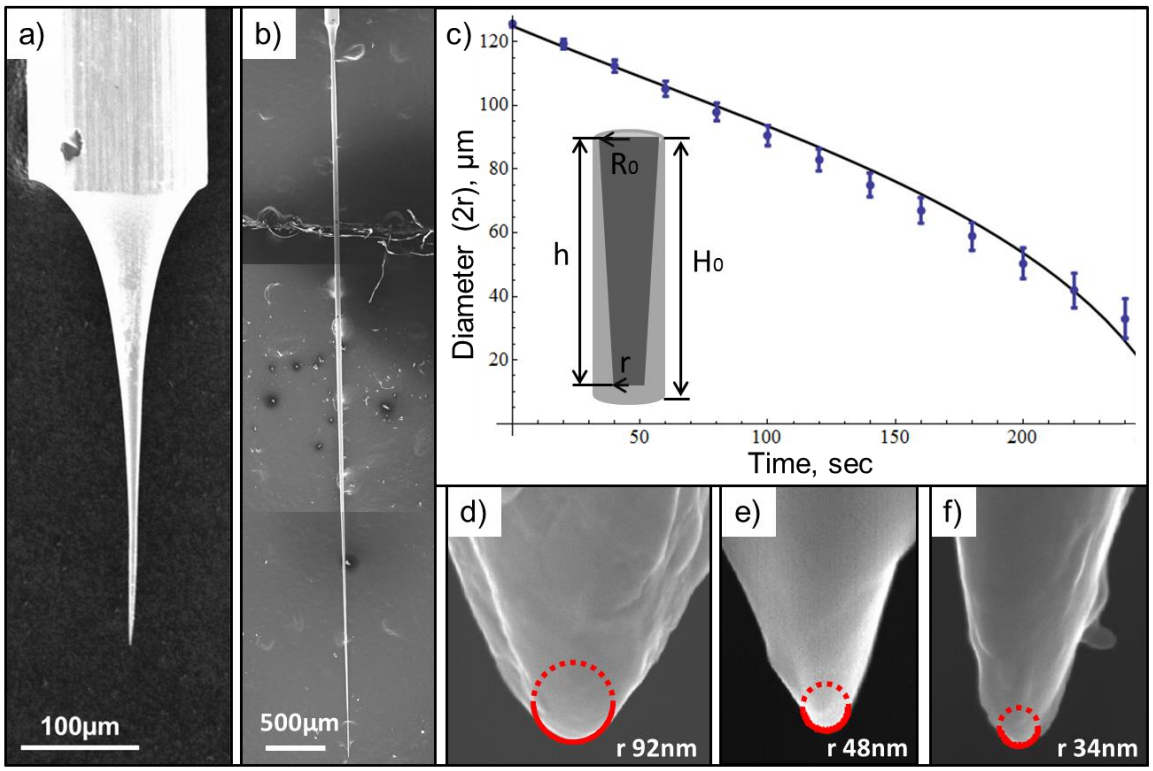

Figure 1.5. The SEM pictures of electropolished probes. (a), (d) The probes were obtained at the CLE regime with the applied voltage of $\Delta E = 10V$ and H_0=2mm. (b), (e) The probes were obtained at the PLE regime with the applied voltage of $\Delta E = 2V$ and H_0=6mm; (f) The probes were obtained at the PLE regime with the applied voltage of $\Delta E = 2V$ and H_0=2mm. (c) Truncated cone model of electropolished wire. The theoretical solid line and experimental data points show the time dependence of the tip radius. ($2R_0 = d$, see (Table 1.1)

The rate of change of the wire mass when electric current passes through the electrolytic cell was estimated using Faraday's law as $G = IM/zF$, where I is an electric current (A), $M = 183\,\text{g/mol}$ (tungsten molar mass), z = 6 (tungsten valence number), and $F = 96485\,\text{C/mol}$ is Faraday's constant. Integrating the Faraday law over time t, and expressing the change of wire mass Δm through the change of wire volume ΔV as

$\Delta m = \rho \Delta V = G\Delta t = {QM}/{zF}$, where $\rho = 19.25 \times 10^{-12}$ g/μm^3 is the tungsten density and Q is the total charge at time t, $Q = \int I(t)dt$, we obtain:

$$r^2 h + rR_0 h + R_0{}^2 h - 3R^2 H_0 + \frac{Q}{F}\frac{M}{z}\frac{3}{\pi\rho} = 0 \qquad (1.10)$$

In our calculations, we used the following approximation of the experimental data, $h(t) = -0.0016t^2 - 0.07t + H_0$, where t (sec), h (μm). Using this approximation, eq. (1.10) has been solved for $r(t)$. Figure 1.5 (c) shows the calculated and experimental diameters confirming that the truncated cone model describes the wire shape fairly well.

The literature data on the radius of curvature of the CLE tips is controversial [1, 6, 22, 49, 53, 59]. Most references neither specify the standard deviation nor the number of samples analyzed. Our experiments with the CLE techniques resulted in a broad size distribution of the tip radii measured from 65 nm to 500nm. The Omicron NanoTechnology [89] does not state the standard deviation either proving that the drop-off-technique is not a technology, but an art. The length of the CLE tips measured from its apex to the base varied from 100 to 500 μm. By changing the immersion length of the wire from 1 mm to 8 mm, one can alter the length of the PLE tips from 500 μm to 7000 μm (Figure 1.5). A long probe is shown in Figure 1.5 (b), where the tip length is 6.1 mm. When the submersion depth was increased greater than 8 mm, the tips tend to curl slightly. This type of morphological instability when the tips spontaneously coil during electropolishing has never been reported in the literature and its analysis will be discussed elsewhere.

1.4. Conclusion

In summary, while the CLE technique was implemented and studied for more than half a century, the formation of the solid porous film and its effect on tip formation has never been mentioned. We discovered a new electropolishing PLE regime which resulted in the formation of centimeter long probes with nanometer sharp tips. It is believed that the solid porous shells formed by the products of electrochemical reaction play a crucial role in this process by controlling the uniformity of the wire taper and the tip sharpness. The CLE regime is governed by the increased dissolution rate in the meniscus region due to the Plateau-Rayleigh instability while in the PLE regime the etching is uniformly distributed due to the porous solid shell formed around the wire that help to avoid the formation of Plateau-Rayleigh instability.

This new regime of electropolishing of tungsten wires is expected to broaden the applications of tungsten needles. As an example, we show that these long probes can successfully pierce single smooth muscle cells (Chapter 7). Therefore, these probes can be used as medical instruments for the single cell surgery or as nanoelectrodes for probing the electrochemical state within areas of a single cell or microorganisms.

1.5. Appendix

Measurement of the tip curvature using Matlab® program

The curvature of the electropolished tungsten tip was measured using Matlab® realized algorithm. An SEM image of the needle, at the maximum magnification, is needed for the most accurate measurement. The algorithm detects the transition from the tip to the background and draws a half circle at the tip of a needle on the SEM image and provides a value of the circle radius. Figure 1.6 shows an example of the SEM image of the tungsten needle.

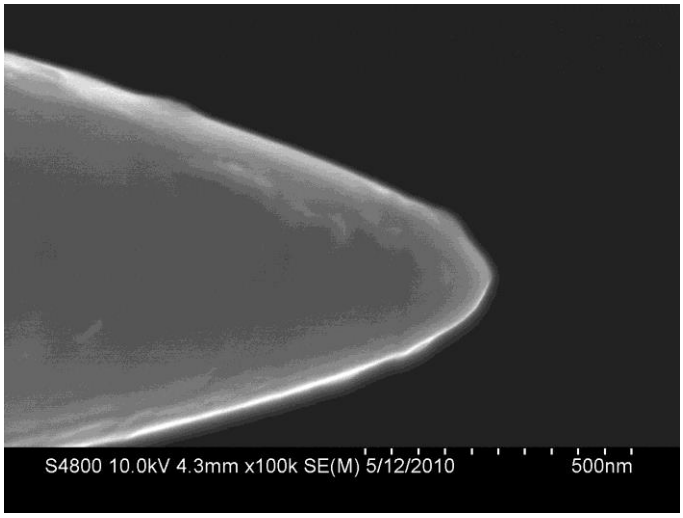

Figure 1.6. SEM image of the electropolished tungsten wire tip at maximum magnification.

The algorithm of the program can be described with the following steps:

1) First, an SEM image was opened in Matlab® program
2) Then, in order to determine the scale of the image, the scale on the SEM image was picked by selecting the first and last points of the scale. The length of the scale, as shown in the SEM image, was then entered in the program.

3) Sobel method (Matlab® function 'edge') was used to define the edges of the wire tip. The Sobel method finds edges in the image using the Sobel approximation of the derivative. It returns edges at those points where the gradient of image brightness is maximum. On the resulting black and white image the pixels corresponding to the edge of the tip are white (brightness=1), the rest of the pixels are black (brightness=0). Figure 1.7 show the image produced using this method.

4) The endpoint of the tip was determined either using an assumption that the wire is oriented horizontally and pointing from left to right or was asked by the program to be pointed at. Figure 1.7 show the blue cross representing the very end of the needle.

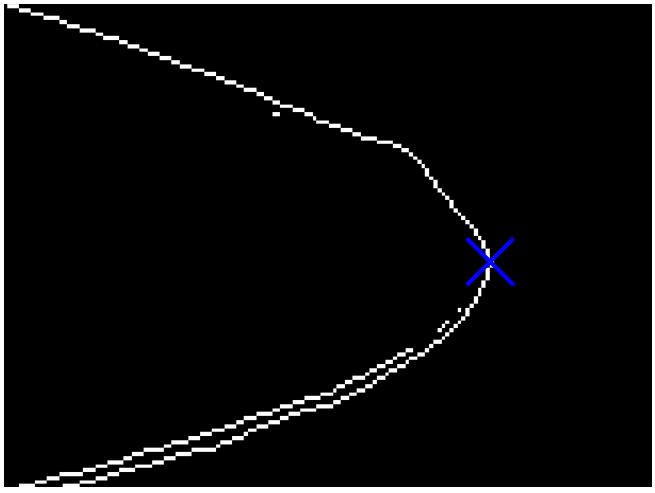

Figure 1.7. Black and white image of the tip edges with the wire tip endpoint marked.

5) Then, using the least square method (Matlab® function lsqnonlin) the circle was fitted to the cross in Figure 1.7 at the end section of the tip. Initially the end section within 20 pixels of the endpoint is fitted, and then this length is

incrementally increased until the distance between the circle rightmost point and the tip endpoint increases to 2 pixels. This value was selected in order to reduce the perturbation from the sharp features sometimes present on the tip. In Figure 1.8 the final product with the half circle fitted at the end of the tungsten needle is shown. The radius of the tip curvature was then defined as the radius of this circle. Thickness of the half circle line was adjusted afterwards.

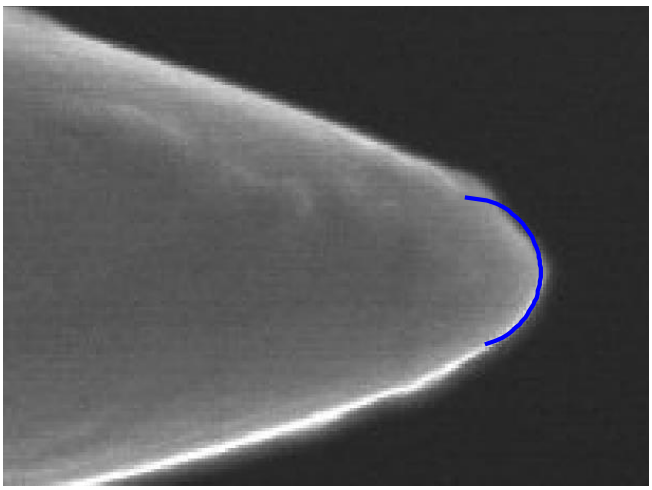

Figure 1.8. Image of the wire tip with the circle fitted to the tip edge.

1.6. References

[1] Zhang R and Ivey D G 1996 Preparation of sharp polycrystalline tungsten tips for scanning tunneling microscopy imaging *J Vac Sci Technol B* **14** 1-10

[2] Muller A D, Muller F, Hietschold M, Demming F, Jersch J and Dickmann K 1999 Characterization of electrochemically etched tungsten tips for scanning tunneling microscopy *Rev Sci Instrum* **70** 3970-2

[3] Ibe J P, Bey P P, Brandow S L, Brizzolara R A, Burnham N A, Dilella D P, Lee K P, Marrian C R K and Colton R J 1990 On the electrochemical etching of tips for scanning tunneling microscopy *J Vac Sci Technol A* **8** 3570-5

[4] Albrektsen O, Salemink H W M, Morch K A and Tholen A R 1994 Reliable Tip Preparation for High-Resolution Scanning-Tunneling-Microscopy *J Vac Sci Technol B* **12** 3187-90

[5] Oliva A I, Romero A, Pena J L, Anguiano E and Aguilar M 1996 Electrochemical preparation of tungsten tips for a scanning tunneling microscope *Rev Sci Instrum* **67** 1917-21

[6] Ekvall I, Wahlstrom E, Claesson D, Olin H and Olsson E 1999 Preparation and characterization of electrochemically etched W tips for STM *Meas Sci Technol* **10** 11-8

[7] Basnet G, Schoelz J K, Xu P, Barber S D, Ackerman M L and Thibado P M 2013 Etch-stop method for reliably fabricating sharp yet mechanically stable scanning tunneling microscope tips *J Vac Sci Technol B* **31**

[8] Schoelz J K, Xu P, Barber S D, Qi D J, Ackerman M L, Basnet G, Cook C T and Thibado P M 2012 High-percentage success method for preparing and pre-evaluating tungsten tips for atomic-resolution scanning tunneling microscopy *J Vac Sci Technol B* **30**

[9] McKendry J E, Allen C S, Critchley K, Gorzny M L, Walton A S and Evans S D 2008 Magnetic field enhanced nano-tip fabrication for four-probe STM studies *Nanotechnology* **19**

[10] Tahmasebipour G, Hojjat Y, Ahmadi V and Abdullah A 2009 Optimization of STM/FIM nanotip aspect ratio based on the Taguchi method *Int. J. Adv. Manuf. Technol.* **44** 80-90

[11] Ge Y Z, Zhang W, Chen Y L, Jin C and Ju B F 2013 A reproducible electropolishing technique to customize tungsten SPM probe: From mathematical modeling to realization *J. Mater. Process. Technol.* **213** 11-9

[12] Kar A K, Gangopadhyay S and Mathur B K 2000 A reverse electrochemical floating-layer technique of SPM tip preparation *Meas Sci Technol* **11** 1426-31

[13] Lemke H, Goddenhenrich T, Bochem H P, Hartmann U and Heiden C 1990 Improved microtips for scanning probe microscopy *Rev Sci Instrum* **61** 2538-41

[14] Jobbins M M, Raigoza A F and Kandel S A 2012 Note: Circuit design for direct current and alternating current electrochemical etching of scanning probe microscopy tips *Rev Sci Instrum* **83**

[15] Sun W X, Shen Z X, Cheong F C, Yu G Y, Lim K Y and Lin J Y 2002 Preparation of cantilevered W tips for atomic force microscopy and apertureless near-field scanning optical microscopy *Rev Sci Instrum* **73** 2942-7

[16] Hagedorn T, El Ouali M, Paul W, Oliver D, Miyahara Y and Grutter P 2011 Refined tip preparation by electrochemical etching and ultrahigh vacuum treatment to obtain atomically sharp tips for scanning tunneling microscope and atomic force microscope *Rev Sci Instrum* **82**

[17] Ottaviano L, Lozzi L and Santucci S 2003 Scanning Auger microscopy study of W tips for scanning tunneling microscopy *Rev Sci Instrum* **74** 3368-78

[18] Huang C A, Chang J H and Lin Y H 2011 Sharpening behaviour of W-wire electrodes in 10-25 wt.% NaOH solutions *Corros Sci* **53** 2566-74

[19] Ju B F, Chen Y L, Fu M M, Chen Y and Yang Y H 2009 Systematic study of electropolishing technique for improving the quality and production reproducibility of tungsten STM probe *Sensor Actuat a-Phys* **155** 136-44

[20] Bryant P J, Kim H S, Zheng Y C and Yang R 1987 Technique for shaping scanning tunneling microscope tips *Rev Sci Instrum* **58** 1115-

[21] Libioulle L, Houbion Y and Gilles J M 1995 Very sharp platinum tips for scanning-tunneling-microscopy *Rev Sci Instrum* **66** 97-100

[22] Kulawik M, Nowicki M, Thielsch G, Cramer L, Rust H P, Freund H J, Pearl T P and Weiss P S 2003 A double lamellae dropoff etching procedure for tungsten tips attached to tuning fork atomic force microscopy/scanning tunneling microscopy sensors *Rev Sci Instrum* **74** 1027-30

[23] Grunlan J C, Xia X Y, Rowenhorst D and Gerberich W W 2001 Preparation and evaluation of tungsten tips relative to diamond for nanoindentation of soft materials *Rev Sci Instrum* **72** 2804-10

[24] Lyuksyutov S F, Vaia R A, Paramonov P B, Juhl S, Waterhouse L, Ralich R M, Sigalov G and Sancaktar E 2003 Electrostatic nanolithography in polymers using atomic force microscopy *Nature Materials* **2** 468-72

[25] Peng Y, Cullis T and Inkson B 2009 Bottom-up nanoconstruction by the welding of individual metallic nanoobjects using nanoscale solder *Nano Letters* **9** 91-6

[26] Hironori Tohmyoh T T, Masato Fujimori and Masumi Saka 2013 Joule heat welding of thin platinum and tungsten wires and the thermoelectric effects around Bi-metal junctions *J. Micro Nano-Manuf.* **1**

[27] Bard A J 1992 New challenges in electrochemistry and electroanalysis *Pure Appl. Chem.* **64** 185-92

[28] Luneburg S, Muller M, Paarmann A and Ernstorfer R 2013 Microelectrode for energy and current control of nanotip field electron emitters *Appl. Phys. Lett.* **103**

[29] Hermans A and Wightman R M 2006 Conical tungsten tips as substrates for the preparation of ultramicroelectrodes *Langmuir* **22** 10348-53

[30] Wang Y X, Noel J M, Velmurugan J, Nogala W, Mirkin M V, Lu C, Collignon M G, Lemaitre F and Amatore C 2012 Nanoelectrodes for determination of reactive oxygen and nitrogen species inside murine macrophages *Proceedings of the National Academy of Sciences of the United States of America* **109** 11534-9

[31] Yapici M K and Zou J 2008 Permalloy-coated tungsten probe for magnetic manipulation of micro droplets *Microsyst Technol* **14** 881-91

[32] Yum K, Wang N and Yu M F 2010 Nanoneedle: A multifunctional tool for biological studies in living cells *Nanoscale* **2** 363-72

[33] Going J J and Lamb R F 1996 Practical histological microdissection for PCR analysis *Journal of Pathology* **179** 121-4

[34] Hirvonen J, Ronkanen P, Ylikomi T, Blauer M, Suuronen R, Skottman H and Kallio P 2008 Microcutting of living tissue slices and stem cell colonies by using mechanical tool and liquid jet *2008 2nd Ieee Ras & Embs International Conference on Biomedical Robotics and Biomechatronics (Biorob 2008), Vols 1 and 2* 700-5

[35] Wallingford R A and Ewing A G 1988 Amperometric detection of catechols in capillary zone electrophoresis with normal and micellar solutions *Analytical Chemistry* **60** 258-63

[36] Sloss S and Ewing A G 1993 Improved method for end-column amperometric detection for capillary electrophoresis *Analytical Chemistry* **65** 577-81

[37] Schrlau M G and Bau H H 2010 Carbon nanopipettes for cell surgery *Jala-J Assoc Lab Aut* **15** 145-51

[38] Singhal R, Orynbayeva Z, Sundaram R V K, Niu J J, Bhattacharyya S, Vitol E A, Schrlau M G, Papazoglou E S, Friedman G and Gogotsi Y 2011 Multifunctional carbon-nanotube cellular endoscopes *Nat Nanotechnol* **6** 57-64

[39] Ewing A G, Wallingford R A and Curry P D 1988 Chemical-analysis of single cells with capillary zone electrophoresis *Abstracts of Papers of the American Chemical Society* **196** 177-ANYL

[40] Nave M, Rubin B, Maximov V, Creager S and Kornev K G 2013 Transport-limited electrochemical formation of long nanosharp probes from tungsten *Nanotechnology* **24**

[41] Kita J M and Wightman R M 2008 Microelectrodes for studying neurobiology *Current Opinion in Chemical Biology* **12** 491-6

[42] Peng Y, Cullis T, Mobus G, Xu X J and Inkson B 2009 Conductive nichrome probe tips: fabrication, characterization and application as nanotools *Nanotechnology* **20**

[43] Cavallini M and Biscarini F 2000 Electrochemically etched nickel tips for spin polarized scanning tunneling microscopy *Rev Sci Instrum* **71** 4457-60

[44] Williams C and Roy D 2008 Fabrication of gold tips suitable for tip-enhanced Raman spectroscopy *J Vac Sci Technol B* **26** 1761-4

[45] Zhang C, Gao B, Chen L G, Meng Q S, Yang H, Zhang R, Tao X, Gao H Y, Liao Y and Dong Z C 2011 Fabrication of silver tips for scanning tunneling microscope induced luminescence *Rev Sci Instrum* **82**

[46] Watanabe M O and Kinno T 1994 Preparation and characterization of electrochemically etched Re tips for STM *Appl Surf Sci* **76** 353-8

[47] Chang W T, Hwang I S, Chang M T, Lin C Y, Hsu W H and Hou J L 2012 Method of electrochemical etching of tungsten tips with controllable profiles *Rev Sci Instrum* **83**

[48] Kulakov M, Luzinov I and Kornev K G 2009 Capillary and Surface Effects in the Formation of Nanosharp Tungsten Tips by Electropolishing *Langmuir* **25** 4462-8

[49] Xu D W, Liechti K M and Ravi-Chandar K 2007 Mesoscale scanning probe tips with subnanometer rms roughness *Rev Sci Instrum* **78**

[50] Chen X, Noh K W, Wen J G and Dillon S J 2012 In situ electrochemical wet cell transmission electron microscopy characterization of solid-liquid interactions between Ni and aqueous NiCl(2) *Acta Mater* **60** 192-8

[51] Kelsey G S 1977 Anodic-oxidation of tungsten in aqueous base *J Electrochem Soc* **124** 814-9

[52] Lassner E and Schubert W-D 1999 *Tungsten : properties, chemistry, technology of the element, alloys, and chemical compounds* (New York: Kluwer Academic/Plenum Publishers)

[53] Melmed A J 1991 The art and science and other aspects of making sharp tips *J Vac Sci Technol B* **9** 601-8

[54] Toh S L, Tan H, Lam J C, Hsia L C and Mai Z H 2010 Optimization of AC electrochemical etching for fabricating tungsten nanotips with controlled tip profile *J Electrochem Soc* **157** E6-E11

[55] Gao X Q, Hu W C and Gao Y S 2013 Preparation of ultrafine tungsten wire via electrochemical method in an ionic liquid *Fusion Engineering and Design* **88** 23-7

[56] Ju B F, Chen Y L and Ge Y Z 2011 The art of electrochemical etching for preparing tungsten probes with controllable tip profile and characteristic parameters *Rev Sci Instrum* **82**

[57] Fotino M 1993 Tip sharpening by normal and reverse electrochemical etching *Rev Sci Instrum* **64** 159-67

[58] Kim P, Jeong S, Jeong M S, Ko D K and Lee J 2007 Effects of process parameters on the electrochemical etching of sharp metallic tips with an attached mass *Rev Sci Instrum* **78**

[59] Bhushan B and Jung Y C 2011 Natural and biomimetic artificial surfaces for superhydrophobicity, self-cleaning, low adhesion, and drag reduction *Prog. Mater. Sci.* **56** 1-108

[60] Stone R, Rosamond M, Coleman K, Petty M, Kosolov O, Zeze D G and Ieee 2012 *Controlled electrosharpening of tungsten probes* (New York: Ieee)

[61] Libioulle L H, Y.; Gilles, J. M. 1995 Very sharp gold and platinum tips to modify gold surfaces in scanning-tunneling-microscopy *J Vac Sci Technol B* **13** 1325-31

[62] Xu G Z, Liu Z H, Xu K, Zhang Y, Zhong H J, Fan Y M and Huang Z L 2012 Constant current etching of gold tips suitable for tip-enhanced Raman spectroscopy *Rev Sci Instrum* **83**

[63] Eligal L, Culfaz F, McCaughan V, Cade N I and Richards D 2009 Etching gold tips suitable for tip-enhanced near-field optical microscopy *Rev Sci Instrum* **80**

[64] Bonaccorso F, Calogero G, Di Marco G, Marago O M, Gucciardi P G, Giorgianni U, Channon K and Sabatino G 2007 Fabrication of gold tips by chemical etching in aqua regia *Rev Sci Instrum* **78**

[65] Lopes M, Toury T, de La Chapelle M L, Bonaccorso F and Gucciardi P G 2013 Fast and reliable fabrication of gold tips with sub-50 nm radius of curvature for tip-enhanced Raman spectroscopy *Rev Sci Instrum* **84**

[66] Kharintsev S S, Rogov A M and Kazarian S G 2013 Nanopatterning and tuning of optical taper antenna apex for tip-enhanced Raman scattering performance *Rev Sci Instrum* **84**

[67] Kharintsev S S, Noskov A I, Hoffmann G G and Loos J 2011 Near-field optical taper antennas fabricated with a highly replicable ac electrochemical etching method *Nanotechnology* **22**

[68] Eisele M, Kruger M, Schenk M, Ziegler A and Hommelhoff P 2011 Note: Production of sharp gold tips with high surface quality *Rev Sci Instrum* **82**

[69] Kharintsev S S, Hoffmann G G, Fishman A I and Salakhov M K 2013 Plasmonic optical antenna design for performing tip-enhanced Raman spectroscopy and microscopy *J. Phys. D-Appl. Phys.* **46**

[70] Ren B, Picardi G and Pettinger B 2004 Preparation of gold tips suitable for tip-enhanced Raman spectroscopy and light emission by electrochemical etching *Rev Sci Instrum* **75** 837-41

[71] Baykul M C 2000 Preparation of sharp gold tips for STM by using electrochemical etching method *Mater. Sci. Eng. B-Solid State Mater. Adv. Technol.* **74** 229-33

[72] Billot L, Berguiga L, de la Chapelle M L, Gilbert Y and Bachelot R 2005 Production of gold tips for tip-enhanced near-field optical microscopy and spectroscopy: analysis of the etching parameters *Eur. Phys. J.-Appl. Phys* **31** 139-45

[73] Boyle M G, Feng L and Dawson P 2008 Safe fabrication of sharp gold tips for light emission in scanning tunnelling microscopy *Ultramicroscopy* **108** 558-66

[74] Hodgson P A, Wang Y, Mohammad A A and Kruse P 2013 Note: Electrochemical etching of silver tips in concentrated sulfuric acid *Rev Sci Instrum* **84**

[75] Lloyd J S, Williams A, Rickman R H, McCowen A and Dunstan P R 2011 Reproducible electrochemical etching of silver probes with a radius of curvature of 20 nm for tip-enhanced Raman applications *Appl. Phys. Lett.* **99**

[76] Gorbunov A A, Wolf B and Edelmann J 1993 The use of silver tips in scanning-tunneling-microscopy *Rev Sci Instrum* **64** 2393-4

[77] Lin C C and Hu C C 2008 Electropolishing of 304 stainless steel: Surface roughness control using experimental design strategies and a summarized electropolishing model *Electrochim. Acta* **53** 3356-63

[78] Zhu W, Shi T L, Tang Z R, Gong B, Liao G L and Tully J 2013 Dynamic selective etching: a facile route to parabolic optical fiber nano-probe *Opt. Express* **21** 6919-27

[79] Takahashi K M 1990 Meniscus shapes on small diameter fibers *J Colloid Interf Sci* **134** 181-7

[80] Allongue P, Costakieling V and Gerischer H 1993 Etching of silicon in NaOH solutions. 1. Insitu scanning tunneling microscopic investigation of N-Si (111) *J Electrochem Soc* **140** 1009-18

[81] Rogers B L, Shapter J G, Skinner W M and Gascoigne K 2000 A method for production of cheap, reliable Pt-Ir tips *Rev Sci Instrum* **71** 1702-5

[82] Anik M 2006 Effect of concentration gradient on the anodic behavior of tungsten *Corros Sci* **48** 4158-73

[83] Anik M 2010 Anodic reaction characteristics of tungsten in basic phosphate solutions *Corros Sci* **52** 3109-17

[84] Singhal R, Bhattacharyya S, Orynbayeva Z, Vitol E, Friedman G and Gogotsi Y 2010 Small diameter carbon nanopipettes *Nanotechnology* **21**

[85] Yum K, Yu M F, Wang N and Xiang Y K 2011 Biofunctionalized nanoneedles for the direct and site-selective delivery of probes into living cells *Bba-Gen Subjects* **1810** 330-8

[86] Zhang Y and Yu L C 2008 Single-cell microinjection technology in cell biology *Bioessays* **30** 606-10

[87] Lassner E and Schubert W-D 1999 *Tungsten: properties, chemistry, technology of the element, alloys, and chemical compounds* (New York: Kluwer Academic/Plenum Publishers)

[88] Drazin P G and Reid W H 2004 *Hydrodynamic Stability* (Cambridge, UK ; New York: Cambridge University Press)

[89] Omicron NanoTechnology GmbH http://www.omicron.de/en/products/w-tek-tip-etching-tool-/instrument-concept.

2. THERMODYNAMICS OF CHEMICAL REACTIONS

2.1. Introduction

A chemical reaction is a process during which one set of chemical compounds transform into another. The compounds that initially involved in the reaction are called reactants and the compounds generated at the end of the reaction are called products. Chemical reactions are represented by the chemical equations that show reactants on the left-hand side and products on the right-hand side separated by the arrow representing the direction of the reaction. When the chemical reaction reaches the state when the concentration of reactants and products does not change anymore, the system is said to be in equilibrium. This state is reached when the forward and reverse reactions proceed at the same rate, representing no net change in concentrations on both sides. If the system is perturbed, it returns to the equilibrium state after some time [1-7].

2.1.1. Chemical equilibrium in dilute solutions

In order to describe and predict the behavior of the solution, we employ thermodynamics restricting ourselves to dilute solutions.

The solution is considered dilute when the amount of solvent is much greater than that of the solute, so that the solute ions do not interact with each other. Consider a following chemical reaction that involves solvent and solutes[7]:

$$n_0 A_0 + n_1 A_1 + ... + n_r A_r \rightleftarrows m_1 B_1 + ... + m_s B_s, \tag{2.1}$$

where N_0 moles of A_0 solvent molecules is mixed with, $N_1,\ldots, N_i$ moles of $A_1, \ldots A_r$ solutes molecules that react on the left side, producing $N'_1,\ldots, N'_j$ moles of $B_1, \ldots B_s$ solutes molecules that react on the right side, $n_0, n_1,\ldots n_r$ and $m_1,\ldots m_s$ are stoichiometric coefficients of the reacting molecules from left and right sides. If $n_0 = 0$ then the solvent is not involved in the chemical reaction and if $n_0 \neq 0$ then the solvent is involved in the reaction. In dilute solutions the following equality holds true $N_i << N_0$.

To describe the chemical equilibrium in a solution undergoing chemical reaction(2.1), we use the Gibbs free energy G fixing temperature T and pressure P; or we will use the Helmholtz free energy A, fixing volume V and entropy S. The Gibbs free energy G of the system is defined as:

$$G = U + pV - TS, \tag{2.2}$$

where V is the system volume, U is the internal energy and S is the entropy.

The Helmholtz free energy A is defined as:

$$A = U - TS \tag{2.3}$$

We introduce the internal energy u of a solution per one mole of the solvent when solution has N_i/ N_0 moles of solute A_r and N'_j/ N_0 moles of solute B_s then the internal energy U of the total solution will depend on the following values:

$$U = N_0 u\left(T, p, \frac{N_i}{N_0}, ..., \frac{N'_j}{N_0}\right) \tag{2.4}$$

If we assume that the solution is very dilute then the mole ratios are very small and u can be represented by the first term of its Taylor series with respect to the mole ratios. Then we can rewrite eq. (2.4) as:

$$U = N_0 u_0(T, p) + \sum_{i=1}^{r} N_i u_i(T, p) + \sum_{j=1}^{s} N_j' u_j'(T, p), \tag{2.5}$$

where, $u_i = \partial U / \partial N_i$ and $u_j' = \partial U / \partial N_j'$ are the internal energies of solute A_r and B_s, respectively. The volume V can be written in the following form using the same logic:

$$V = N_0 v_0(T, p) + \sum_{i=1}^{r} N_i v_i(T, p) + \sum_{j=1}^{s} N_j' v_j'(T, p), \tag{2.6}$$

where, $v_i = \partial V / \partial N_i$ and $v_j' = \partial V / \partial N_j'$ are the volumes per mole of solutes A_r and B_s, respectively.

The entropy of the system S consists of the entropies of the solvent s_0 and individual solute entities s_i of the A_r and B_s (s'_j) species and entropy of mixing:

$$S = N_0 s_0(T, p) + \sum_{i=1}^{r} N_i s_i(T, p) - R\sum_{i=1}^{r} N_i \ln \frac{N_i}{N_0} + \sum_{j=1}^{s} N_j' s_j'(T, p) - R\sum_{j=1}^{s} N_j' \ln \frac{N_j'}{N_0}, \tag{2.7}$$

where R is the gas constant (R=8.314J/K·mol).

Generally speaking, u, v, and s are functions of temperature T and pressure p, but their changes due to variation of the pressure are insignificant and can be deemed as functions of the temperature only. Therefore, the Helmholtz free energy becomes:

$$A = N_0 u_0(T) + \sum_{i=1}^{r} N_i u_i(T) + \sum_{j=1}^{s} N_j' u_j'(T) - TN_0 s_0(T) - T\sum_{i=1}^{r} N_i s_i(T)$$
$$+RT\sum_{i=1}^{r} N_i \ln\frac{N_i}{N_0} - T\sum_{j=1}^{s} N_j' s_j'(T) + RT\sum_{j=1}^{s} N_j' \ln\frac{N_j'}{N_0}, \quad (2.8)$$

or

$$A = N_0\left(u_0(T) - Ts_0(T)\right) + \sum_{i=1}^{r} N_i\left(u_i(T) - Ts_i(T)\right) + \sum_{j=1}^{s} N_j'\left(u_j'(T) - Ts_j'(T)\right)$$
$$+RT\left[\sum_{i=1}^{r} N_i \ln\frac{N_i}{N_0} + \sum_{j=1}^{s} N_j' \ln\frac{N_j'}{N_0}\right] \quad (2.9)$$

Then the Helmholtz free energy is written as:

$$A = N_0 a_0(T) + \sum_{i=1}^{r} N_i a_i(T) + \sum_{j=1}^{s} N_j' a_j'(T) + RT\left[\sum_{i=1}^{r} N_i \ln\frac{N_i}{N_0} + \sum_{j=1}^{s} N_j' \ln\frac{N_j'}{N_0}\right], \quad (2.10)$$

where, $a(T) = u(T) - Ts(T)$.

Following the same logic the Gibbs free energy takes on the form:

$$G = N_0[a_0(T) + pv_0(T)] + \sum_{i=1}^{r} N_i[a_i(T) + pv_i(T)] + \sum_{j=1}^{s} N_j'[a_j'(T) + pv_j'(T)]$$
$$+RT\left[\sum_{i=1}^{r} N_i \ln\frac{N_i}{N_0} + \sum_{j=1}^{s} N_j' \ln\frac{N_j'}{N_0}\right] \quad (2.11)$$

Introducing $\mu(T) = a(T) + pv(T)$, the Gibbs free energy is rewritten as:

$$G = N_0\mu_0(T) + \sum_{i=1}^{r} N_i\mu_i(T) + \sum_{j=1}^{s} N_j'\mu_j'(T) + RT\left[\sum_{i=1}^{r} N_i \ln\frac{N_i}{N_0} + \sum_{j=1}^{s} N_j' \ln\frac{N_j'}{N_0}\right] \quad (2.12)$$

To determine the condition of chemical equilibrium, we will use the Gibbs free energy and conduct a detailed derivation of the basic equation.

Consider slight isothermal changes in the system during reaction (2.1) assuming that the moles of reactants and products change by some amount ε:

$$N_0, N_1, ..., N_r \rightarrow -\varepsilon n_0, -\varepsilon n_1, ..., -\varepsilon n_r, \tag{2.13}$$

and

$$N'_1, ..., N'_r \rightarrow +\varepsilon m_1, ..., +\varepsilon m_s \tag{2.14}$$

If the system is in a stable equilibrium, the Gibbs free energy tends to reach its minimum. Therefore the following equation must hold as $\varepsilon \rightarrow 0$:

$$\delta G = -\varepsilon n_0 \frac{\partial G}{\partial N_0} - \varepsilon \sum_{i=1}^{r} n_i \frac{\partial G}{\partial N_i} + \varepsilon \sum_{j=1}^{s} m_j \frac{\partial G}{\partial N'_j} = 0 \tag{2.15}$$

Now dividing this equation by ε and calculating the derivatives, we have from eq. (2.12):

$$\begin{aligned} \delta G = 0 = &-n_0 \mu_0(T) - \sum_{i=1}^{r} n_i \mu_i(T) - RT \sum_{i=1}^{r} n_i - RT \sum_{i=1}^{r} n_i \ln \frac{N_i}{N_0} + \sum_{j=1}^{s} m_j \mu'_j(T) \\ &+ RT \sum_{j=1}^{s} m_j + RT \sum_{j=1}^{s} m_j \ln \frac{N'_j}{N_0}, \Rightarrow \end{aligned} \tag{2.16}$$

$$\begin{aligned} &-n_0 \mu_0(T) - \sum_{i=1}^{r} n_i \left(\mu_i(T) + RT \right) + \sum_{j=1}^{s} m_j \left(\mu'_j(T) + RT \right) = \\ &-RT \left(\sum_{j=1}^{s} \ln \left(\frac{N'_j}{N_0} \right)^{m_j} - \sum_{i=1}^{r} \ln \left(\frac{N_i}{N_0} \right)^{n_i} \right), \Rightarrow \end{aligned} \tag{2.17}$$

$$\begin{aligned} &\sum_{j=1}^{s} m_j \left(\mu'_j(T) + RT \right) - \sum_{i=1}^{r} n_i \left(\mu_i(T) + RT \right) - n_0 \mu_0(T) = \\ &-RT \ln \left[\frac{\left(\frac{N'_1}{N_0} \right)^{m_1} \left(\frac{N'_2}{N_0} \right)^{m_2} \cdots \left(\frac{N'_s}{N_0} \right)^{m_s}}{\left(\frac{N_1}{N_0} \right)^{n_1} \left(\frac{N_2}{N_0} \right)^{n_2} \cdots \left(\frac{N_r}{N_0} \right)^{n_r}} \right], \end{aligned} \tag{2.18}$$

where the ratio under the logarithm represents the law of mass action for the equilibrium in the solutions. This ratio is called the equilibrium constant K.

$$K(T) = \frac{\left(\frac{N_1'}{N_0}\right)^{m_1}\left(\frac{N_2'}{N_0}\right)^{m_2}\cdots\left(\frac{N_s'}{N_0}\right)^{m_s}}{\left(\frac{N_1}{N_0}\right)^{n_1}\left(\frac{N_2}{N_0}\right)^{n_2}\cdots\left(\frac{N_r}{N_0}\right)^{n_r}} \tag{2.19}$$

The value of the equilibrium constant is fixed for a particular temperature and involves concentrations of the reactants and products at their equilibrium state under constant conditions (such as T and p), but independent of time.

The Gibbs free energy can also be described in terms of chemical potential. If one adds one particle to a system, holding temperature and pressure fixed, the Gibbs free energy changes by [8]:

$$\mu_i = \left(\frac{\partial G}{\partial N_i}\right)_{T,p} = \bar{G}_i, \tag{2.20}$$

where μ_i is the chemical potential of the species i and $\bar{G}_i$ is a partial molar Gibbs free energy.

The Gibbs free energy can be rewritten in the following form:

$$dG = Vdp - SdT + \sum_j \mu_j dN_j - \sum_i \mu_i dN_i \tag{2.21}$$

Following the step(2.13), we have:

$$dG = Vdp - SdT + \sum_j m_j \mu_j d\varepsilon - \sum_i n_i \mu_i d\varepsilon, \tag{2.22}$$

or

$$dG = Vdp - SdT + \sum_j m_j \bar{G}_j d\varepsilon - \sum_i n_i \bar{G}_i d\varepsilon \tag{2.23}$$

At equilibrium, the Gibbs free energy under constant temperature and pressure takes on the following form:

$$\Delta G = \left[\frac{dG}{d\varepsilon}\right] = \sum_j \mu_j m_j - \sum_i \mu_i n_i = \sum_j \bar{G}_j m_j - \sum_i \bar{G}_i n_i = 0 \tag{2.24}$$

Similarly, the standard Gibbs free energy is defined as:

$$\Delta G^0 = \sum_j \bar{G}_j^0 m_j - \sum_i \bar{G}_i^0 n_i \tag{2.25}$$

According to eq. (2.12), the chemical potential of the species i can be described as:

$$\mu_i = \mu_i^0 + RT \ln \frac{N_i}{N_0} \tag{2.26}$$

The chemical potential can also be described in terms of activity a_i:

$$\mu_i = \mu_i^0 + RT \ln a_i \tag{2.27}$$

Activity, a_i, is an effective concentration that accounts for the solute ions interaction with each other and with solvent molecules in the solution. In this way, ions behave chemically like they are less concentrated than they really are. In a very dilute solution when the amount of the solute is much smaller than that of the solvent these interactions are insignificant and this type of solution also called ideal solution where activity coefficient is equal to 1 and activity is equal to the concentration. Activity can be defined in the following form:

$$a_i = \{a_i\} = \gamma_i \frac{C_i}{C_i^0}, \tag{2.28}$$

where, a_i is activity, γ_i is activity coefficient and C_i is a molar concentration of the species i and; C_i^0 is a molar concentration of the i species in the standard state. Activity and activity coefficient are dimensionless quantities. In the standard state there are no interactions between species and the behavior can be assumed as ideal. In the chemical physics of solutions, the standard state is choosen at C_i^0=1M. Also, in dilute solutions the activity coeffitient γ_i=1 and activity can be rewritten as:

$$a_i = \gamma_i \frac{C_i}{C_i^0} = \frac{C_i}{1M} = [C_i] \tag{2.29}$$

Using eq.(2.29) we can rewrite equation for chemical potential (eq. (2.27)) in ideal solution as:

$$\mu_i = \mu_i^0 + RT \ln[C_i] \tag{2.30}$$

The activity of the pure liquid or solid at one bar is taken as unity [9] ($\gamma_i \rightarrow 1$, $C_i/C_i^0 \rightarrow 1$, $a_i = 1$).

The molarity, C_i, is defined as the amount of mole of the solute, N_i, divided by the volume of the solution, V:

$$Molarity = C_i = \frac{N_i}{V} = \frac{mol}{L} \tag{2.31}$$

Also, an equilibrium constant using activity of the species is presented as:

$$K = \frac{a_{B_1}^{m_1} \ldots a_{B_s}^{m_s}}{a_{A_0}^{n_0} a_{A_1}^{n_1} \ldots a_{A_r}^{n_r}} = \frac{[B_1]^{m_1} \ldots [B_s]^{m_s}}{[A_0]^{n_0} [A_1]^{n_1} \ldots [A_r]^{n_r}} \tag{2.32}$$

Then, the Gibbs free energy of the reaction (2.1) can be rewritten as:

$$\Delta G = \Delta G^0 + RT \ln Q, \tag{2.33}$$

where the term under the natural logarithm is the reaction quotient Q that measures the amount of reactants and products that are present in the system in a particular timeframe and conditions other than the standard. The reaction quotient has the form of the equilibrium constant.

At equilibrium, $\Delta G = 0$ and the standard Gibbs free energy is then:

$$\Delta G^0 = -RT \ln K \tag{2.34}$$

Combining (2.33) and (2.34) we get:

$$\Delta G = RT \ln \frac{Q}{K} \tag{2.35}$$

The reference state of aqueous solutions or "standard state" is conventionally defined as that of pure water H_2O and a concentration of one mole per liter of solvent for the ions. The concentration of ions is measured in molarities.

Since $\ln X = \frac{\log X}{\log(e)} = \frac{1}{0.4343} \log_{10} X = 2.303 \log_{10} X$ we can rewrite eq. (2.34)as:

$$\log K = \frac{\Delta G^0}{-2.303RT} \tag{2.36}$$

All experiments in this work are performed at the room temperature (T=298°K). Thus, it is convenient to rewrite the equation (2.36) in a simpler form:

$$\log K = \frac{\Delta G^0}{-5.71 kJ / mol} \tag{2.37}$$

2.1.2. Dissociation of water

Worked example: we consider dissociation of water:

$$H_2O = OH^- + H^+ \tag{2.38}$$

$$\mu_{H_2O} = \mu_{H^+} + \mu_{OH^-} \tag{2.39}$$

The equilibrium condition is therefore:

$$N_A\mu^0_{H_2O} = N_A\mu^0_{H^+} + RT\ln\frac{[H^+]}{[H_2O]} + N_A\mu^0_{OH^-} + RT\ln\frac{[OH^-]}{[H_2O]}, \tag{2.40}$$

where μ^0 represents the chemical potential of the substance in its standard state, and N_A is the Avogadro's number $N_A=6.02\cdot10^{23}\,mol^{-1}$. Eg. (2.40)leads to:

$$-RT\ln\frac{[H^+][OH^-]}{[H_2O]^2} = N_A\left(\mu^0_{H^+} + \mu^0_{OH^-} - \mu^0_{H_2O}\right) = \Delta G^0, \tag{2.41}$$

where ΔG^0 is the standard Gibbs free energy change of the reaction. This value can be looked up in tables [10, 11]. Following (2.34) we introduce:

$$K = \frac{[H^+][OH^-]}{[H_2O]^2} = e^{-\Delta G^0/RT}, \tag{2.42}$$

as the equilibrium constant for ion molarities.

Then dissociation constant of water will be given as K_w:

$$K_w = [H^+][OH^-] = K\cdot[H_2O]^2 \tag{2.43}$$

The value of ΔG^0 for the dissociation of one mole of water at room temperature and atmospheric pressure is calculated as follows:

$$\begin{aligned}&\Delta G^0 = \bar{G}^0_{H^+} + \bar{G}^0_{OH^-} - \bar{G}^0_{H_2O} = \\ &(0kJ/mol - 157.3kJ/mol) - (-237.2kJ/mol) = 79.9kJ/mol,\end{aligned} \tag{2.44}$$

where the values of the standard partial molar Gibbs free energies can be looked up in tables and are listed in the Table 2.1for convenience.

Hence the equilibrium constant of this reaction is:

$$K_w = \exp\left(-\frac{79,900 J/mol}{(8.314 J/K\cdot mol)(298.15K)}\right)\cdot\left[H_2O\right]^2 = 1\cdot 10^{-14}\cdot\left[H_2O\right]^2 \qquad (2.45)$$

According to the chemical reaction (2.38) in pure water the concentrations of the ions are equal, hence:

$$\frac{\left[H^+\right]}{\left[H_2O\right]} = \frac{\left[OH^-\right]}{\left[H_2O\right]} = 10^{-7} \qquad (2.46)$$

In terms of activity coefficients we have:

$$K_w = \frac{a_{H^+}\cdot a_{OH^-}}{a^2_{H_2O}} \qquad (2.47)$$

In a dilute solution, the activity of water solvent is equal to 1 and eq. (2.47) can be rewritten as:

$$K_w = a_{H^+}\cdot a_{OH^-} = 1\cdot 10^{-14} \qquad (2.48)$$

Now, consider 1L of water with molecular weight of 18.02 g/mol that weighs 1000g. Then the concentration of pure water is found as follows:

$$\left[H_2O\right] = \frac{1000g \,/\, 18.015 g/mol}{1L} = 55.5\frac{mol}{L} = 55.5M \qquad (2.49)$$

In aqueous solutions, the measure of the hydrogen ion H^+ concentration in presented by pH. The pH parameter serves as a measure of the acidity (less than pH7) or

alkalinity (higher than pH7) of the solution. The abbreviation pH stands for "power of hydrogen" and represents negative base 10 logarithm:

$$pH = -\log[H^+] \tag{2.50}$$

If eq. (2.43) is expressed using logarithmic functions, then:

$$\log K_w = \log[H^+] + \log[OH^-] \tag{2.51}$$

From eq. (2.50)we can define parameter pOH that represents the measure of the OH^- ion concentration:

$$pOH = -\log[OH^-] = 14 - pH \tag{2.52}$$

The minus log concentration C of ions versus pH graph is plotted in Figure 2.1 for OH^- and H^+ and show their correlation between each other.

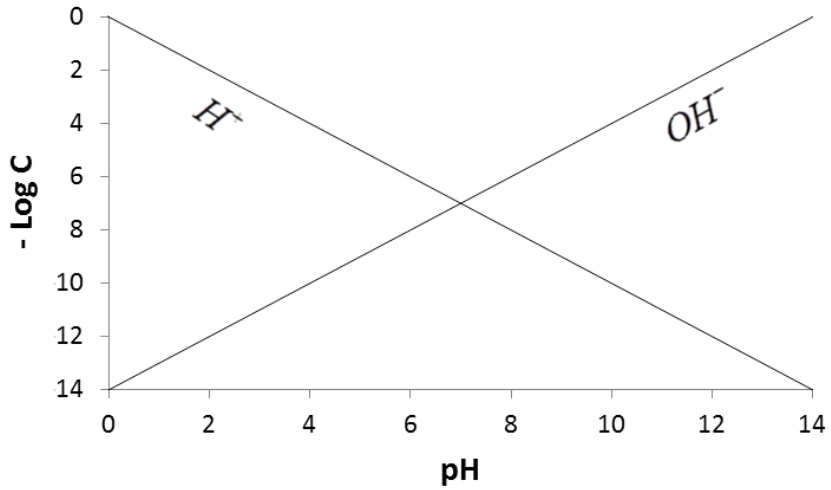

Figure 2.1 The diagram of –LogC of ions dependence on pH for water dissociation.

If the acid is added to the water, the hydrogen ion concentration will increase, and since the equilibrium constant cannot change meaning that the concentration of the

hydroxyl ions should decrease by the equal amount. If the base is added to the water then the concentration of hydroxyl ions increases and hydrogen concentration decreases correspondingly.

2.2. Stability of the chemical compounds in aqueous solution

The stability of different compounds in an aqueous solution can be determined using the same logic of calculations as that for the water. First, the chemical reactions are written down and equilibrium condition is found using the Gibbs free energy data from Table 2.1 and eq. (2.37). The results are plotted on a minus log concentration C of the ions versus pH graph. These graphs can show at what conditions the compounds in the system will precipitate or dissolve in an aqueous solution.

Consider dissolution of potassium hydroxide and solid tungsten compounds in an aqueous solution. These solid compounds and their aqueous products are listed in Table 2.1. Using the equilibrium conditions for the reactions of tungsten with water, the stability of the compounds can be studied.

Table 2.1 List of considered compounds and their standard partial molar Gibbs energies. ((s) - solid, (l) - liquid, (aq) - aqueous).

Name	Species (state)	$\Delta\bar{G}_i^0, (kJ/mol)$	References
Tungsten (VI) trioxide	$WO_3(s)$	-763.9	[10, 12]
Tungsten (VI) trioxide monohydrate	$WO_3 \cdot H_2O(s)$	-1020.9	[13]
Tungsten (VI) trioxide dihydrate	$WO_3 \cdot 2H_2O(s)$	-1220.0	[12]
Tungstate (VI) ion	$WO_4^{2-}(aq)$	-916.7	[12]
Polytungstate ion	$HW_6O_{21}^{5-}(aq)$	-5175.6	[12]
Water	$H_2O(l)$	-237.2	[12]
Hydrogen ion	$H^+(aq)$	0.0	[12]
Hydroxide	$OH^-(aq)$	-157.3	[12]
Potassium hydroxide	$KOH(s)$	-378.7	[11]
Potassium ion	$K^+(aq)$	-283.26	[11]

2.2.1. Dissociation of potassium hydroxide (KOH) in aqueous solution

When KOH is added to water it dissolves producing the K^+ and OH^- ions. Water in this reaction cancels out from both sides. The chemical reaction reads:

$$KOH_{(s)} \leftrightarrow K^+_{(aq)} + OH^-_{(aq)} \tag{2.53}$$

The equilibrium constant for this reaction can be found using eq. (2.32) as follows:

$$K = \frac{\{K^+\}\{OH^-\}}{\{KOH\}}, \tag{2.54}$$

where, the activity of the pure solid KOH is equal to 1 [9] and in a dilute solutions the activities of the ions will be equal to their concentrations:

$$K = [K^+][OH^-] \tag{2.55}$$

Since the graph will be plotted in terms of log concentration versus pH it is convenient to represent the above equation (2.55) in terms of logarithmic functions of concentration:

$$\log K = \log[K^+] + \log[OH^-] \tag{2.56}$$

Also, the $\log K$ value can be found using eq.(2.54) and definition of eq. (2.37) and Table 2.1as follows:

$$\log K = \frac{\Delta\bar{G}^0_{K^+} + \Delta\bar{G}^0_{OH^-} - \Delta\bar{G}^0_{KOH}}{-5.71 kJ/mol} = \\ = \frac{\left[(-283.26 - 157.3) - (-378.7)\right] kJ/mol}{-5.71 kJ/mol} = \frac{-61.86}{-5.71} = 10.8 \tag{2.57}$$

Using the value of $\log K$ from eq. (2.57) and defining log[OH^-] in terms of pOH (2.52), equation (2.56) for equilibrium can be rewritten as follows:

$$\log[K^+] = 10.8 - \log[OH^-] = 10.8 - (pH - 14) = 24.8 - pH \tag{2.58}$$

The minus log C-pH plot is presented in Figure 2.2 and shows the stability of the ion K^+ in water. The line that represents the equilibrium between the solid KOH compound and K^+ ion lies a way above the concentrations considered for dilute solution, meaning that in dilute solutions the solid compound KOH will always dissociate completely into K^+ and OH^- ions.

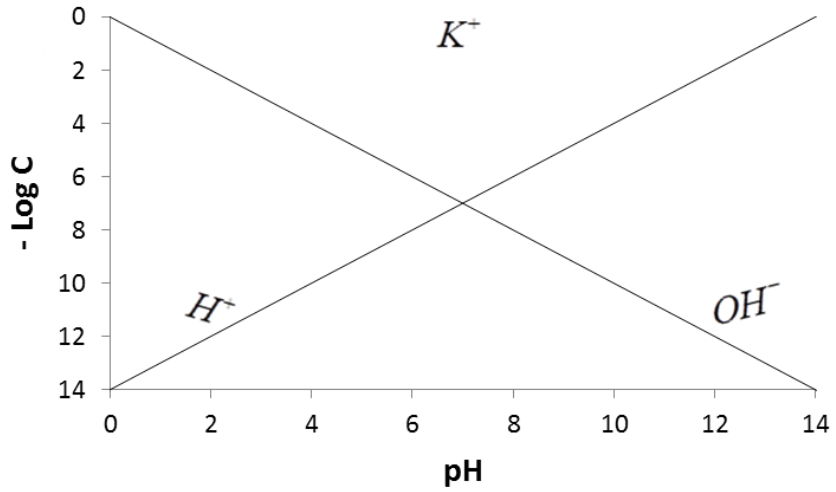

Figure 2.2 –LogC vs pH graph for potassium hydroxide dissociation in water. The concentration C in the plot is the concentration of the ions K^+, OH^- and H^+.

2.2.2. Dissolution of tungsten trioxide WO_3 in aqueous solutions

Consider chemical reactions that take place when WO_3 oxide is immersed in water. This reaction progresses with tungsten thrioxide reacting with water producing tungstate ions or polytungstate ions:

1) The chemical reaction for the transition pair $WO_3(s)/WO_4^{2-}(aq)$ is written in the following form:

$$WO_3 + H_2O = WO_4^{2-} + 2H^+ \tag{2.59}$$

The equilibrium constant for the reaction (2.59) can be found using eq. (2.32) as follows:

$$K = \frac{\{WO_4^{2-}\}\{H^+\}^2}{\{WO_3\}\{H_2O\}} \tag{2.60}$$

where, the activities of the pure solid WO_3 and water H_2O are equal to 1 [9] and in a dilute solutions the activities of the ions are equal to their concentrations. Then eq. (2.60) can be rewritten as:

$$K = [WO_4^{2-}][H^+]^2 \tag{2.61}$$

Introducing logarithmic functions in eq. (2.61), it can be written in the following form:

$$\log K = \log[WO_4^{2-}] + 2\log[H^+] \tag{2.62}$$

Using eq. (2.60) and definition of the reaction constant through the energy eq.(2.37), and the values of corresponding Gibbs free energies from Table 2.1, the logK value is found as:

$$\log K = \frac{\left[(-916.7 + 2\cdot 0) - (-763.9 - 237.2)\right] kJ / mol}{-5.71 kJ / mol} = \frac{84.4}{-5.71} = -14.8 \tag{2.63}$$

Substituting the logK value into eq. (2.62) and introducing pH through eq. (2.50) we get the final equilibrium condition for reaction (2.59) relating pH and the concentration of the tungstate ions:

$$2\,pH = \log[WO_4^{2-}] + 14.8 \tag{2.64}$$

2) The chemical reaction for the transition pair $WO_3(s) / HW_6O_{21}^{5-}(aq)$ is written in the following form:

$$6WO_3 + 3H_2O = HW_6O_{21}^{5-} + 5H^+ \tag{2.65}$$

The equilibrium constant for the reaction (2.65) can be found using eq. (2.32) as follows:

$$K = \frac{\{HW_6O_{21}^{5-}\}\{H^+\}^5}{\{WO_3\}^6\{H_2O\}^3} = [HW_6O_{21}^{5-}][H^+]^5 \tag{2.66}$$

where, the activities of the pure solid WO_3 and water H_2O are equal to 1 [9] and in a dilute solutions the activities of the ions are equal to their concentrations. Introducing logarithmic functions in eq.(2.66), it can be written in the following form:

$$\log K = \log[HW_6O_{21}^{5-}] + 5\log[H^+] \tag{2.67}$$

Using eq. (2.37) and the values of corresponding Gibbs free energies from Table 2.1, logK is found as:

$$\log K = \frac{\left[(-5175.6) - (6\cdot(-763.9) + 3\cdot(-237.2))\right] kJ/mol}{-5.71 kJ/mol} = \frac{119.4}{-5.71} = -20.9 \tag{2.68}$$

Substituting logK value into eq. (2.67) and introducing pH through eq. (2.50) we get the final equilibrium condition for reaction (2.65) relating pH and the concentration of the polytungstate ions:

$$5\,pH = \log[HW_6O_{21}^{5-}] + 20.9 \tag{2.69}$$

3) The chemical reaction representing the transition from polytungstate ion to tungstate ion $HW_6O_{21}^{5-}(aq)/WO_4^{2-}(aq)$ can be written as follows:

$$HW_6O_{21}^{5-} + 3H_2O = 6WO_4^{2-} + 7H^+ \tag{2.70}$$

The equilibrium constant for the reaction (2.70) can be found using eq. (2.32) as:

$$K = \frac{\{WO_4^{2-}\}^6\{H^+\}^7}{\{HW_6O_{21}^{5-}\}\{H_2O\}^3} = \frac{[WO_4^{2-}]^6[H^+]^7}{[HW_6O_{21}^{5-}]} \tag{2.71}$$

where, the activity of the water H_2O is equal to 1 [9] and in a dilute solutions the activities of the ions are equal to their concentrations. Introducing logarithmic functions in eq. (2.71), it can be written in the form bellow:

$$\log K = 6\log[WO_4^{2-}] + 7\log[H^+] - \log[HW_6O_{21}^{5-}] \tag{2.72}$$

Using eq. (2.37) and the values of corresponding Gibbs free energies from Table 2.1, logK is found as:

$$\log K = \frac{\left[(6\cdot(-916.7)+7\cdot 0)-(-5175.6+3\cdot(-237.2))\right] kJ/mol}{-5.71 kJ/mol} = \\ = \frac{387}{-5.71} = -67.8 \tag{2.73}$$

The final equilibrium condition for reaction (2.70) relating pH, the concentration of the polytungstate ions and tungstate ions can be written as:

$$7\,pH = 6\log[WO_4^{2-}] - \log[HW_6O_{21}^{5-}] + 67.8 \tag{2.74}$$

Now, equilibrium equations(2.64), (2.69) and (2.74) are plotted together in Figure 2.3 where $-\log C = -\log[WO_4^{2-}] = -\log[HW_6O_{21}^{5-}]$. The region marked with WO_3 shows the conditions when this compound can be stable with respect to water. The region marked with the polytungstates shows the conditions when WO_3 will react with water producing the polyions. And the region marked with the tungstate ions shows the conditions when the polyions will react with water producing the tungstate ions. The lines represent equilibrium lines along which both species from each side of the line can coexist stably. It can be concluded that by changing the concentration of the ions involved in the reaction one can influence the composition of the solution.

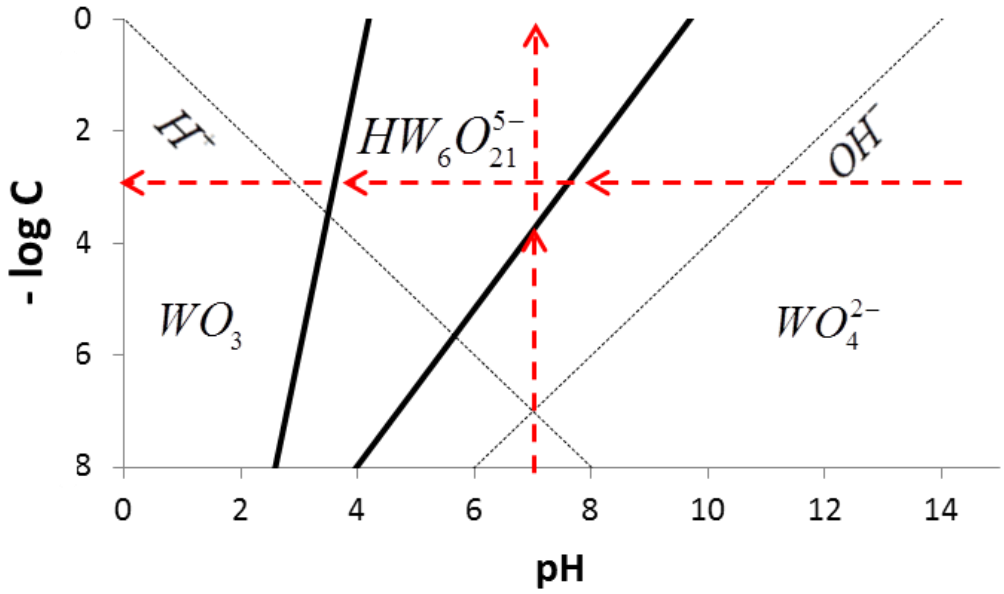

Figure 2.3 Dependence of –LogC on pH, considering thermodynamic stability of WO_3 compound. The concentration C represents the concentration of the ions in the system.

As an example, following the horizontal red arrow from right to left in Figure 2.3 it can be seen that if we add WO_3 to the solution with pH14, it will react with water molecules completely to produce the tungstate ions. Thus, the only stable species at the end of this reaction will be the tungstate ions. If some acid is added to this solution and pH is lowered to pH7.6, the tungstate ion will react with hydrogen ion producing polytungstate ion and both tungsten ions will be in the equilibrium between each other at this point on the line. However, if pH is lowered even more to pH6, then the tungstate ions will react to produce polytungstate ions and only polytungstate ions will be present in the system when it reaches equilibrium. Adding more acid to this solution and lowering it to pH2 will induce the reaction of the polytungstate ions with the hydrogen ions to produce the tungsten trioxide in the form of precipitates. At this pH all the

polytungstate ions will precipitate and the only stable species in the solution will be the tungsten trioxide.

Now, let's follow the vertical red arrow. If the tungsten trioxide solid compound is added to the beaker with the pure water (pH7), the chemical reaction will proceed with formation of the tungstate ions and the hydrogen ions. The concentrations of the ions will increase until the concentration of the tungstate ion will reach $-\log C = -\log[WO_4^{2-}] = 3.8$ or $[WO_4^{2-}] = 10^{-3.8} M$ when the tungstate ion will start reacting with hydrogen ion producing the polytungstate ions. At this point the tungsten trioxide will continue react with water, forming polytungstate ions instead.

2.2.3. Dissolution of tungsten trioxide hydrate $WO_3 \cdot H_2O$ in aqueous solution

Now, consider chemical reactions that take place when $WO_3 \cdot H_2O$ oxide is immersed in water. This reaction progresses with tungsten trioxide monohydrate dissociating into hydrogen ion and tungstate ions or polytungstate ions:

1) The chemical reaction for the transition pair $WO_3 \cdot H_2O(s) / WO_4^{2-}(aq)$ is written in the following form:

$$WO_3 \cdot H_2O = WO_4^{2-} + 2H^+ \tag{2.75}$$

Following steps presented in section 2.2.2 of this chapter the equilibrium condition for reaction (2.75) relating pH and the concentration of the tungstate ions can be written as:

$$2\,pH = \log[WO_4^{2-}] + 18.3 \tag{2.76}$$

2) The chemical equation for the transition for compounds $WO_3 \cdot H_2O(s) / HW_6O_{21}^{5-}(aq)$ is written as follows:

$$6(WO_3 \cdot H_2O) = HW_6O_{21}^{5-} + 3H_2O + 5H^+ \tag{2.77}$$

The equilibrium condition for reaction (2.77) is written as:

$$5pH = \log[HW_6O_{21}^{5-}] + 41.7 \tag{2.78}$$

In Figure 2.4 we plot the derived equations (2.74), (2.76) and (2.78). Using the same logic as that for the previous example it can be concluded that if the tungsten trioxide monohydrate is present in the system, it will precipitate out in water at pH level up to pH8.

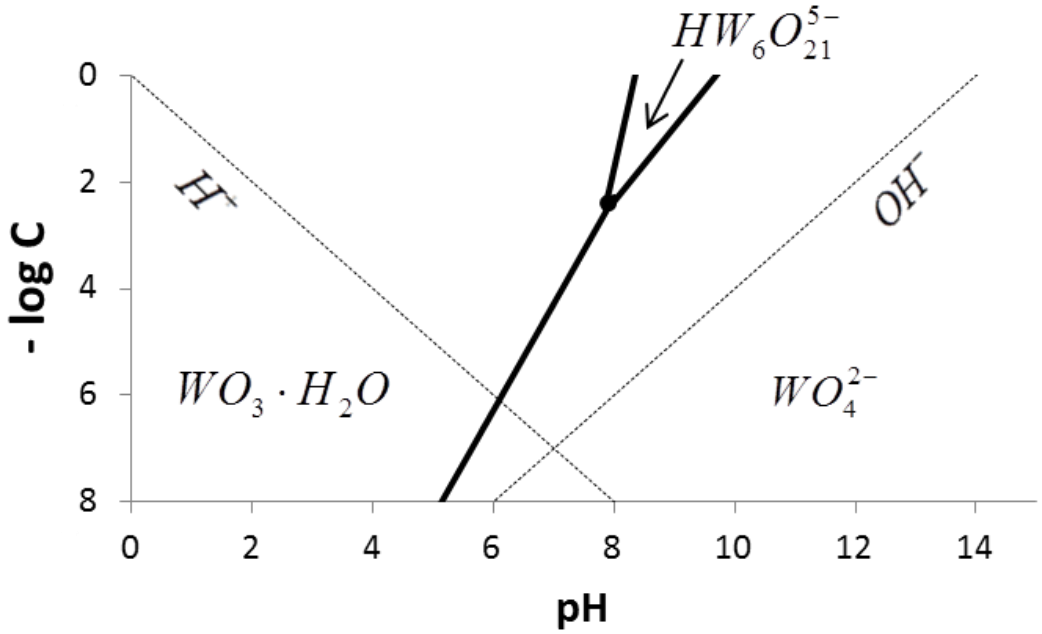

Figure 2.4 Dependence of -LogC on pH, considering thermodynamic stability of the $WO_3 \cdot H_2O$ compound. The concentration C represents the concentration of particular ions in the system.

2.2.4. Dissolution of tungsten trioxide dehydrate $WO_3 \cdot 2H_2O$ in aqueous solution

Lastly, consider chemical reactions when $WO_3 \cdot 2H_2O$ oxide is immersed in water. This reaction progresses with tungsten trioxide dihydrate dissociating into hydrogen ion, water and tungstate ions or polytungstate ions:

1) The chemical reaction for the transition pair $WO_3 \cdot 2H_2O(s) / WO_4^{2-}(aq)$ is written in the following form:

$$WO_3 \cdot 2H_2O = WO_4^{2-} + 2H^+ + H_2O \tag{2.79}$$

The equilibrium condition for reaction (2.79) relating pH and the concentration of the tungstate ions can be written as:

$$2\,pH = \log[WO_4^{2-}] + 11.6 \tag{2.80}$$

2) The chemical equation for the pair $WO_3 \cdot 2H_2O(s) / HW_6O_{21}^{5-}(aq)$ is written as:

$$6(WO_3 \cdot 2H_2O) = HW_6O_{21}^{5-} + 9H_2O + 5H^+ \tag{2.81}$$

The equilibrium condition for reaction (2.81) relating pH and the concentration of the polytungstate ions can be written as:

$$5\,pH = \log[HW_6O_{21}^{5-}] + 1.7 \tag{2.82}$$

Figure 2.5 shows the stability of the compounds we plot the derived equations (2.74), (2.80) and (2.82). If tungsten trioxide dihydrate is present in the system as a solid compound, it will precipitate in water at pH less than pH1.

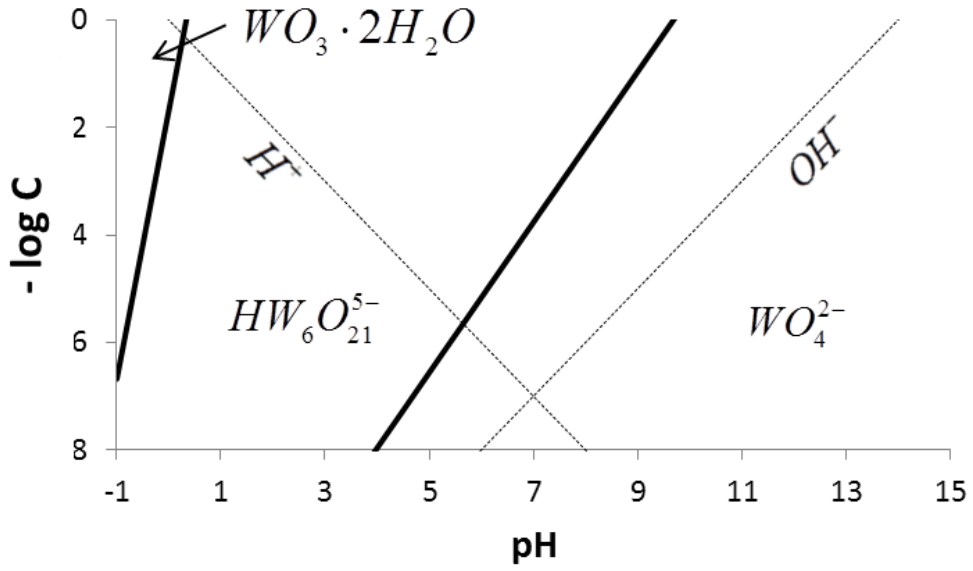

Figure 2.5 Dependence of -LogC on pH, considering the $WO_3 \cdot 2H_2O$ compound as thermodynamically stable. The concentration C represents the concentration of parituclar ions in the system.

It can be noticed that the equilibrium boundaries separating different aqueous solutions are represented in the form:

$$\alpha\, pH = \beta \log[WO_4^{2-}] + \delta \log[HW_6O_{21}^{5-}] + \gamma \tag{2.83}$$

In Table 2.2 we list all coefficients for the particular compounds.

Table 2.2 The list of coefficients for eq.(2.83).

Pair of compounds	α	β	δ	γ
$WO_3(s) / WO_4^{2-}(aq)$	2	1	0	14.8
$WO_3(s) / HW_6O_{21}^{5-}(aq)$	5	1	0	20.9
$HW_6O_{21}^{5-}(aq) / WO_4^{2-}(aq)$	7	6	-1	67.8
$WO_3 \cdot H_2O(s) / WO_4^{2-}(aq)$	2	1	0	18.3
$WO_3 \cdot H_2O(s) / HW_6O_{21}^{5-}(aq)$	5	1	0	41.7
$WO_3 \cdot 2H_2O(s) / WO_4^{2-}(aq)$	2	1	0	11.6
$WO_3 \cdot 2H_2O(s) / HW_6O_{21}^{5-}(aq)$	5	1	0	1.7

2.2.5. Stability of the tungsten ions in the aqueous solutions

Equation (2.74) is plotted using a 3 dimensional plot in Figure 2.6 where the plane represents the equilibrium between the polytungstate ions and tungstate ions and is shown in blue color. Bellow the plane the tungstate ion will convert into the polytungstate ion to reach equilibrium and vice versa.

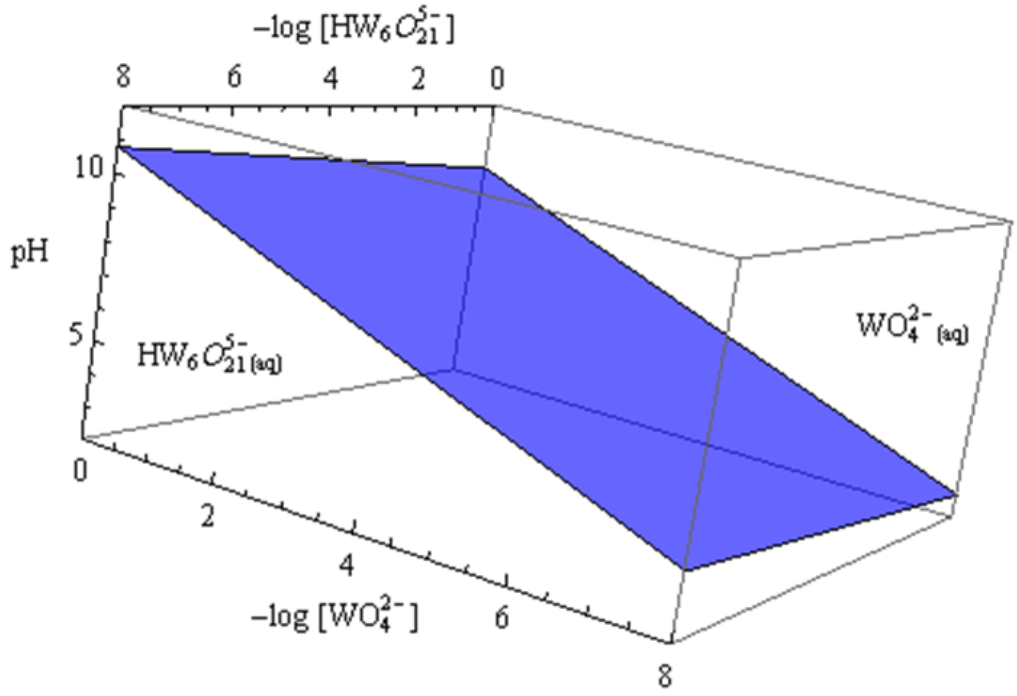

Figure 2.6 Three dimensional graph showing dependence of $-\log[WO_4^{2-}]$ and $-\log[HW_6O_{21}^{5-}]$ on pH for the tungstate and polytungstate ions.

In Figure 2.7 the equilibrium lines for transition between the tungstate and polytungstate ions transitions are plotted for different pH values. It shows that, for instance, if the solution has pH7, then the line marked with pH7 represents the conditions for the solutions of tungstate ions and polytungstate ions to coexist in equilibrium.

Following the red line in Figure 2.7 it can be seen that in the solution with pH7 if the concentration of the polytungstate ions is $-\log[HW_6O_{21}^{5-}]=4$ or $[HW_6O_{21}^{5-}]=10^{-4}M$ then at the concentration of the tungstate ions of $-\log[WO_4^{2-}]=3.8$ or $[WO_4^{2-}]=10^{-3.8}M$ these solutions will be in the equilibrium with each other. If the concentration of the tungstate ions is lower than this value, then polytungstate ions will react producing more tungstate ions until the equilibrium is reached. If the concentration of the tungstate ions is higher than $[WO_4^{2-}]=10^{-3.8}M$, therefore tungstate ions will react to produce more of polytungstate ions until the equilibrium is reached.

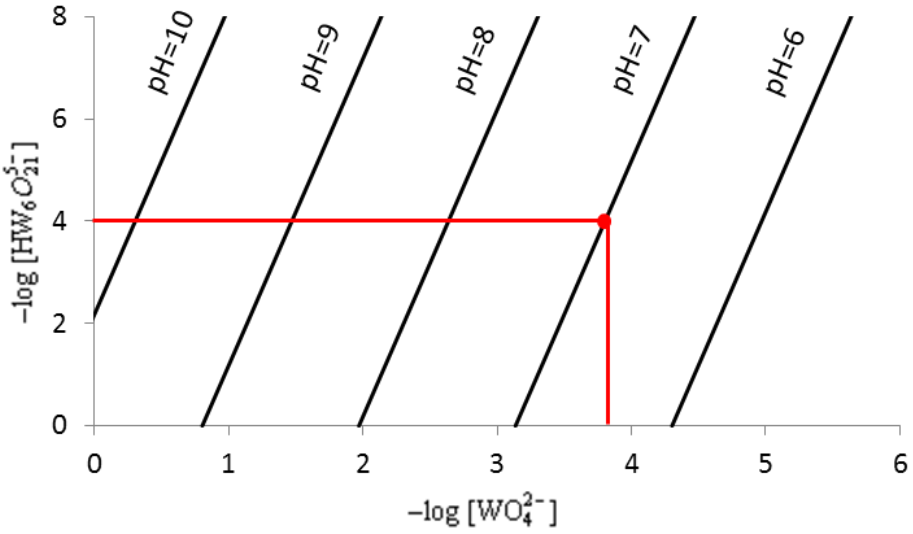

Figure 2.7 The graph relating the concentrations of the tungstate and polytungstate ions in aqueous solutions of different pH.

2.3. Conclusions

Three tungsten solid compounds were studied using theoretical predictions based on the Gibbs free energy and chemical equilibrium to find conditions at which they can be stable in water. It was learned that if one has a basic solution with pH level around pH14, no precipitates can form. When pH is lowered to pH8 the tungsten trioxide monohydrate $WO_3 \cdot H_2O$ will start to precipitate in the solution. If pH is lowered further to pH4, the tungsten trioxide WO_3 will precipitate. And if pH drops below pH1 the tungsten trioxide dehydrate $WO_3 \cdot 2H_2O$ will precipitate.

2.4. References

[1] Nordstrom D K, Munoz J L 1994 *Geochemical Thermodynamics* (Boston: Blackwell Scientific Publications)

[2] Walther J V 2005 *Essentials of Geochemistry* (Sudbury, Massachusetts: Jones and Bartlett Publishers)

[3] Blackburn T R 1969 *Equilibrium A Chemistry of Solutions* (Holt, Rinehart and Winston, Inc.)

[4] Anderson G M, Grerar D A 1993 *Thermodynamics in Geochemistry* (New York: Oxford University Press, Inc.)

[5] Smith J M, Van Ness H C, Abbott M M 2001 *Introduction to Chemical Engineering Thermodynamics* (New York: McGraw-Hill)

[6] Langmuir D 1997 *Aqueous Environmental Geochemistry* (Prentice-Hall, Inc.)

[7] Fermi E 1937 *Thermodynamics* (New York: Prentice-Hall, Inc.)

[8] Jensen J N 2003 *A Problem-Solving Approach to Aquatic Chemistry* (John Wiley & Sons, Inc.)

[9] Atkins P W 1978 *Physical Chemistry* (San Francisco: W.H. Freeman and Company)

[10] Pradyot P 2002 *Handbook of Inorganic Chemicals* (McGraw-Hill Professional)

[11] Dean J A 1972 *Lange's Handbook of Chemistry* (McGRAW-HILL, INC.)

[12] Schweitzer G K and Pesterfield L L 2010 *The Aqueous Chemistry of the Elements* (Oxford; New York: Oxford University Press)

[13] Osseo-Asare K 1982 Solution chemistry of tungsten leaching systems *Metallurgical Transactions B* **13B** 555-64

3. PROPERTIES OF REACTION PRODUCTS RELEASED INTO ELECTROLYTE DURING CLE REGIME

3.1. Introduction

In Chapter 2 it was found that the composition of the solution plays an important role in control of the precipitation kinetics. It is natural to assume that precipitation of tungsten compounds can be traced through the change of the surface tension. During the electrochemical etching the tungsten oxidizes with continuous release of reaction products (tungstate ions WO_4^{2-}) into electrolyte that changes its chemical composition and, therefore, the surface tension of the electrolyte. Adsorption of ionic products on electrolyte surface is poorly understood and rarely studied. However, it is a useful approach that helps investigate the change in chemical composition of the solution.

There are different methods that allows one to determine surface tension of a solution, such as pendant drop [1, 2], Wilhelmy plate [3, 4], capillary rise [5] and other methods[6]. Knowing the surface tension change [7-16] of the electrolytes with different concentrations one can calculate and plot adsorption isotherms [6, 12, 17, 18].

The adsorption isotherm gives information about the adsorption of the ions on the electrolyte surface and can explain the change in surface tension. The water-air interface can either repel or attract the ions to its surface [11, 17, 19]. If the ions are repelled, the

adsorption of ions on the surface is called negative, leading to the increase of surface tension of the solution. If the ions are attracted to the surface of the electrolyte, then the adsorption is called positive and the surface tension of the solution decreases. Acids tend to adsorb positively at the air-liquid interface decreasing the surface tension. For instance, in Figure 3.1 one can see that for HCl acid both chloride anions (yellow) and hydronium cations (red) are situated at the air-liquid interface pointing outwards. It should be noted that the hydronium cation oriented at the surface with the oxygen atom pointing outwards (towards the air phase) and hydrogen atoms pointing inwards (towards the liquid phase). Furthermore, the surface tension of acid aqueous solutions decreases with increase of their concentration that can be seen in Figure 3.2 (a) in the case of HNO_3 and $HClO_4$ acids. Correspondingly, the Gibbs adsorption isotherms show a positive adsorption at the surface (Figure 3.2 (b)). In contrast, bases and salts tend to adsorb negatively on the surface increasing the surface tension.

In Figure 3.2, sodium ions of base NaOH and salt NaCl along with the hydroxide inions are shown to be repelled from the air-liquid interface, but the chloride anions are weakly attracted to it. This behavior results in the increase of the surface tension (Figure 3.2 (a)) producing negative Gibbs adsorption isotherm Figure 3.2 (b).

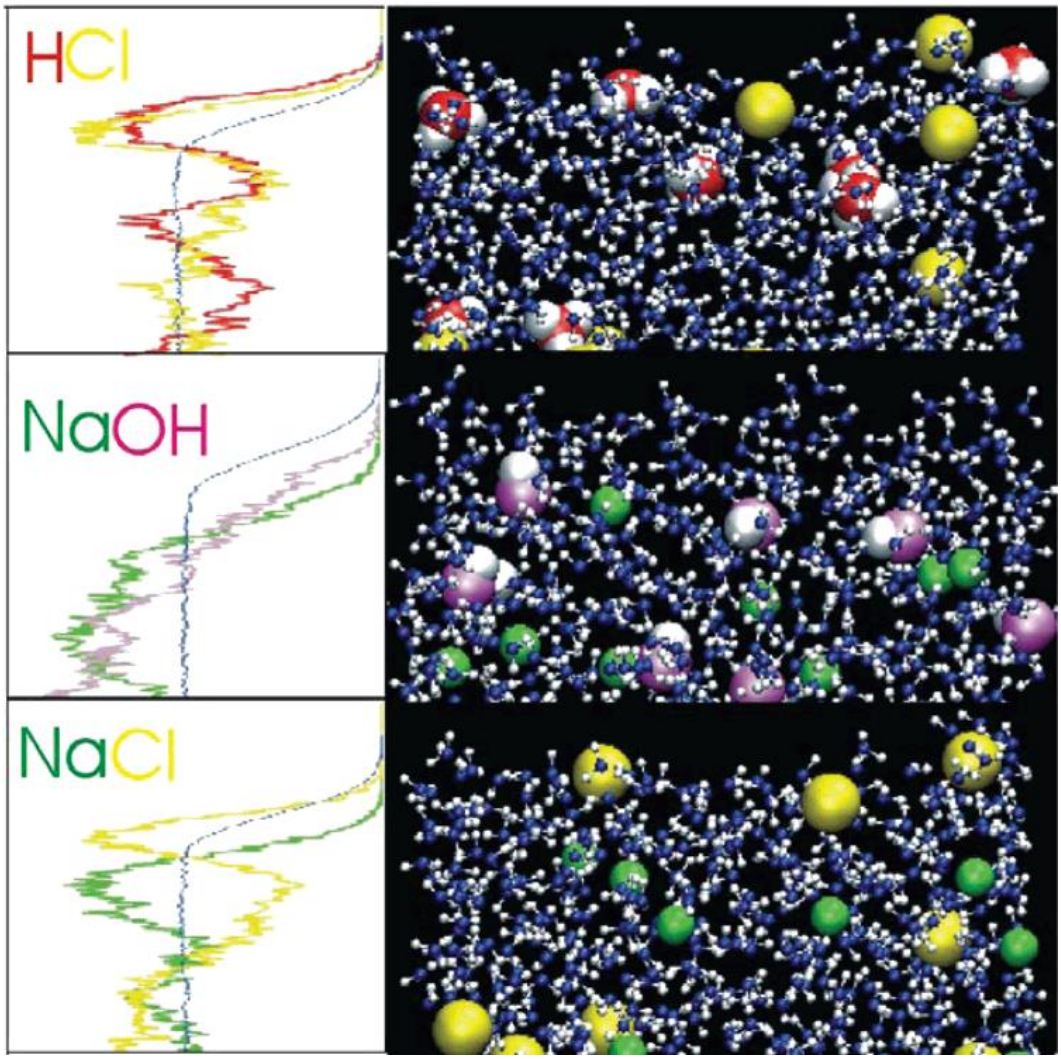

Figure 3.1. Density profiles (i.e., histogrammed densities of the electrolyte ions and water molecules in layers parallel to the surface, from the center of the slab across the interface into the gas phase) and snapshots from molecular dynamics simulations of 1.2 M HCl, NaOH, and NaCl. Coloring scheme: water oxygen, blue; hydronium oxygen, red; hydroxide oxygen, pink; hydrogen, gray; sodium ions, green; chloride ions, yellow. [20, 21]

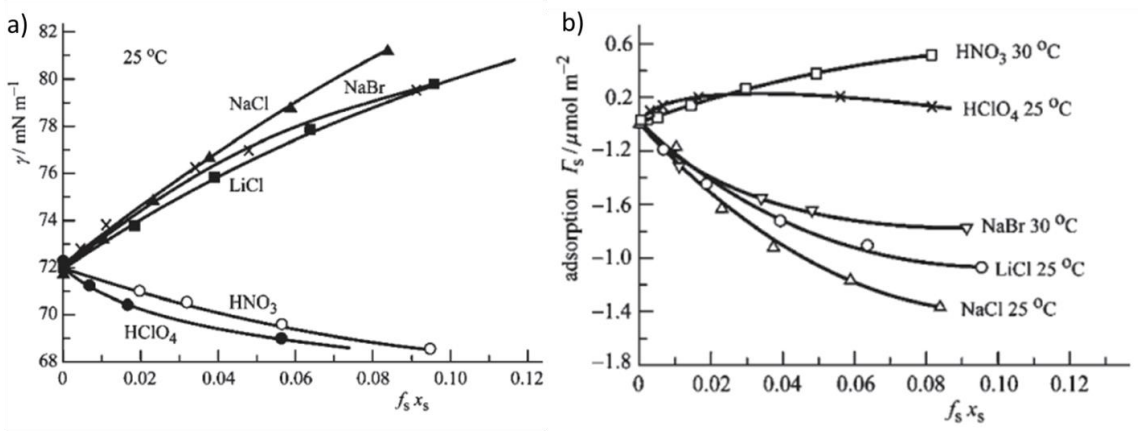

Figure 3.2. (a) Surface tension and (b) adsorption isotherm dependence on activity [17], where f_s is an activity coefficient of the electroneutral electrolyte and x_s is a mole fraction or concentration.

The structure of the water at the air-liquid interface is strongly debated. Some scientists suggest that hydrogen ions are surface active making the air-liquid interface positively charged, while others believe that hydroxyl ions are surface active leading to the negatively charged surface [21-30]. Also, it was confirmed that the size of the ion can be related to its ability to be adsorbed on the surface [12, 21, 31, 32]. The bigger ions tend to dehydrate easier than the smaller ions and are more prone to enrich the surface of the solution [17]. Yet, the mechanism of this behavior is not well understood. Most of the theories are based on some assumptions and it is critical to perform experimental studies in this field in order to understand the nature of the process.

However, the surface tension does not always increase or decrease with concentration, sometimes it can go through a minimum. For instance, in the late 1930s Jones and Ray published a series of articles that received a wide interest in the scientific community showing contradicting results on the surface tension measurements of dilute

inorganic salts solutions, where they observed a minimum in surface tension versus concentration graph (Figure 3.3), the Jones-Ray effect [33-42]. This effect continues to be an unsolved controversy [35].

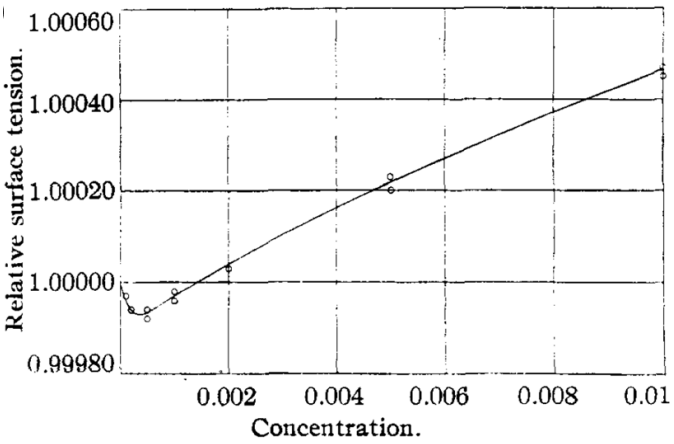

Figure 3.3. Relative surface tension dependence on concentration of $MgSO_4$ [41] solutions. Dots are an experimental data and solid the line fit is a theoretical prediction.

One group of researchers studied the interactions of the polytungstate solutions with cationic surfactants through the surface tension changes [43]. They discovered that when one of the substances was present in excess, the solutions would go in a colloidal state accompanied by the surface tension change (Figure 3.4). When the metatungstate ions were in excess, the surface tension decreased slightly to the point D on the graph with formation of the white colloidal solution. Then, as the concentration of the surfactants was increased beyond the concentration of the metatungstate ion, and the surfactant was in excess, the surface tension dropped drastically to the point E. At this point all metatungstate ions reacted with surfactant and a small amount of the free surfactant is present in the solution. Further addition of the surfactant results in the

adsorption of surfactant cations and their removal from the solution that results in the increase of the surface tension.

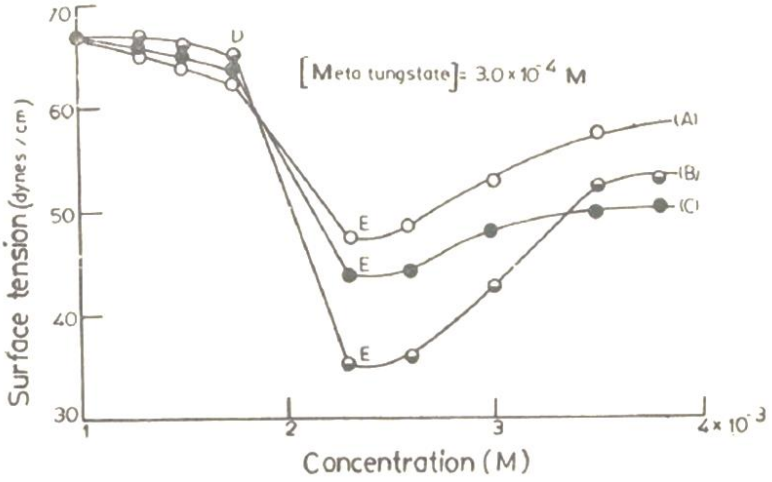

Figure 3.4. Surface tension as a function of the surfactants concentrations (A-CPB, B-DPB, C-CTMAB). Concentration of the metatungstate=$3 \cdot 10^{-4}$M [43].

In this section, surface tension of potassium hydroxide electrolyte with addition of tungstate ions is studied in order to probe the chemical reactions presented in Chapter 2 and to understand how properties of the electrolyte changes during electropolishing described in Chapter 1.

3.2. Gibbs adsorption isotherm

The tungstate ion adsorption at the air-liquid interface can be presented by the Gibbs adsorption isotherm [6, 18, 44-46]. The adsorption process is a dynamic equilibrium between adsorption and desorption of the species, or their attachment and detachment from the surface. The Gibbs adsorption isotherm relates the change of the

electrolyte surface tension to the concentration of components at the air-liquid interface. At constant temperature and pressure, the Gibbs adsorption equation is given as:

$$d\sigma = -\sum_i \Gamma_i d\mu_i, \tag{3.1}$$

where Γ_i is the Gibbs adsorption, or the surface excess of compound i at the interface with respect to the bulk of the liquid, μ_i is its chemical potential and σ is the surface tension of an electrolyte.

There are several models exist that deal with nonionic and ionic mixtures of multicomponent monovalent or multivalent compounds with common ion and with no common ions [45-61]. Using the approach proposed in these articles enables one to calculate the Gibbs adsorption isotherm at the air-liquid interface as well as the mole fraction of the component adsorbed in the bulk and at the surface.

In this Chapter, a multicomponent multivalent ionic mixture is studied and a modified model developed by Motomura and his colleagues [45, 47] is used to find the Gibbs adsorption isotherm of the ions at the air-liquid interface. In the Motomura's model, the concentrations of all the components were varied in order to be able to find the Gibbs adsorption at the constant mole fraction of one of the components and the mole fraction of the compound at the surface at the constant total concentration. However, in this work, one of the compounds precipitates with surface tension decreasing first and then stabilizing after the precipitation occurs. This puts a limitation on the ability to vary the concentrations of both compounds to be able to fix one parameter to find the Gibbs adsorption and mole fraction at the surface. For that reason, the model proposed by the

Motomura was modified to find the Gibbs adsorption when the mole fraction of the compound of interest is very small.

3.2.1. Gibbs adsorption isotherm of KOH base in water

Since the release of tungstate ions during electropolishing proceeds in the electrolyte that is prepared by dissolving potassium hydroxide KOH in water, the Gibbs adsorption of the KOH in water needs to be determined first. The Gibbs adsorption for KOH in water was calculated using surface tension data from ref. [11, 12] and the method described by Ralston in ref. [46].

Consider potassium hydroxide KOH dissolved in water H_2O, both dissociating to ions in the following form:

$$H_2O = H^+ + OH^- \tag{3.2}$$

And

$$KOH = K^+ + OH^- \tag{3.3}$$

At the constant temperature, pressure and pH the surface tension differential $d\sigma$ can be written using eq. (3.1) as:

$$d\sigma = -\Gamma_{H_2O} d\mu_{H_2O} - \Gamma_{OH^-} d\mu_{OH^-} - \Gamma_{H^+} d\mu_{H^+} - \Gamma_{K^+} d\mu_{K^+} - \Gamma_{OH^-} d\mu_{OH^-}, \tag{3.4}$$

where $\Gamma_{H_2O}, \Gamma_{H^+}, \Gamma_{OH^-}, \Gamma_{K^+}$ are Gibbs adsorption isotherms representing an adsorbed quantity of H_2O, H^+, OH^-, K^+ species.

From the law of electroneutrality at the interface and bulk and knowing that the Gibbs adsorption of water at the air-liquid interface is equal to zero by convention we can rewrite eq.(3.4) for the air-water interface plane in the following form:

$$d\sigma = -2\Gamma_{KOH}^{H} d\mu_{KOH}, \tag{3.5}$$

where Γ_{KOH}^{H} is the Gibbs adsorption isotherm for the KOH compound at the air-liquid interface.

From Chapter 2 we know that the chemical potential at constant temperature T and pressure p can be written as:

$$\mu_i = \mu_i^0 + RT \ln a_i \tag{3.6}$$

If we assume that the solution is an ideal solution, then eq. (3.6) will take the following form:

$$\mu_i = \mu_i^0 + RT \ln[C_i] \tag{3.7}$$

where $[C_i] = \frac{C_i}{1M}$.

Now, using eq. (3.7), to determine the chemical potential, eq.(3.5) can be rewritten as:

$$d\sigma = -2\Gamma_{KOH}^{H} RTd \ln[C_{KOH}] \tag{3.8}$$

The Gibbs adsorption isotherm then can be found as:

$$\Gamma_{KOH}^{H} = -\frac{1}{2RT} \frac{d\sigma}{d \ln[C_{KOH}]} \tag{3.9}$$

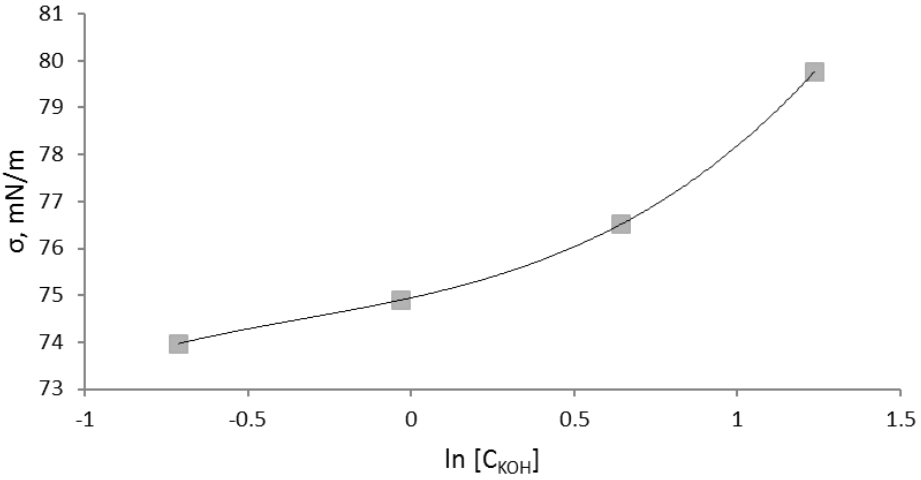

Figure 3.5. Surface tension as a function of the ln[C_{KOH}].

Using Figure 3.5 and eq.(3.9) we can estimate the Gibbs adsorption isotherm for KOH. Figure 3.6 shows that the Gibbs adsorption of the KOH is negative and it becomes more negative with increase of concentration. This means that the ions are repelled from the air-liquid surface towards the bulk increasing with this the surface tension of the solution.

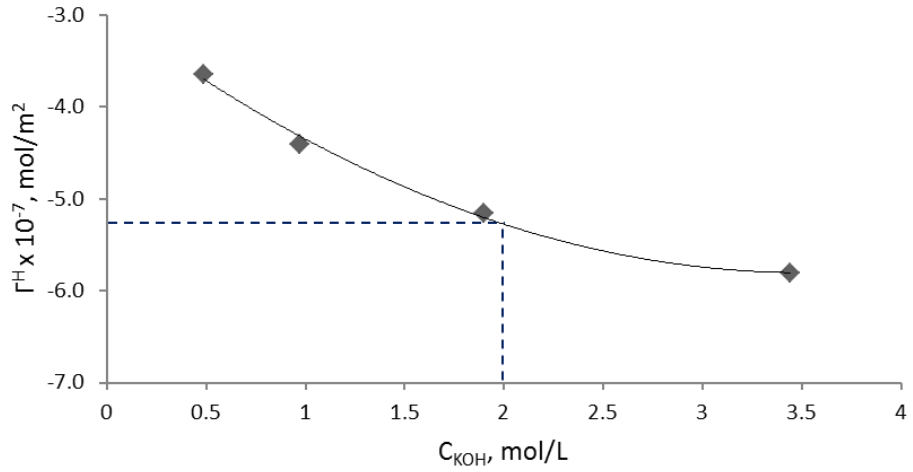

Figure 3.6. The Gibbs adsorption isotherm as a function of the KOH concentration.

From Figure 3.6 it can be estimated that at the 2M concentration of the KOH the Gibbs adsorption is equal to $\Gamma^{H}_{KOH} = -5.3 \cdot 10^{-7}\, mol/m^2$ which is close to the values calculated in ref. [11, 12]. This reveals that at the beginning, when the KOH was added to the water, the Gibbs adsorption was negative and ions were repelled from the surface.

3.2.2. Gibbs adsorption isotherm of the multicomponent, multivalent ionic mixture in water

First, consider dissociation of the KOH in water presented in section 3.2.1 in eq. (3.2) and eq. (3.3).

Then, the tungstate ions are released into the solution through the electrochemical reaction of tungsten in the aqueous potassium hydroxide electrolyte by applying an external potential.

The overall electrochemical reaction proceeds with the consumption of the hydroxyl groups OH^- that react with the tungsten W producing tungstate ions WO_4^{2-}:

$$W + 2OH^- + 2H_2O = WO_4^{2-} + 3H_2 \tag{3.10}$$

It is natural to assume that to establish electroneutrality in the electrolyte; the tungstate ions can form another compound with the K^+ ions in the solution:

$$K_2WO_4 = 2K^+ + WO_4^{2-} \tag{3.11}$$

This compound K_2WO_4 is highly soluble in water [62, 63] and dissociates into ions following eq. (3.11).

Therefore, the law of electroneutrality of the total solution states that:

$$H_2O + H^+ + 2OH^- + 3K^+ + WO_4^{2-} = 0 \tag{3.12}$$

At the constant temperature, pressure and if we assume that the pH is constant, the surface tension for the mixture in eq. (3.12) can be expressed as follows:

$$d\sigma = -\Gamma^H_{H_2O} d\mu_{H_2O} - \Gamma^H_{OH^-} d\mu_{OH^-} - \Gamma^H_{WO_4^{2-}} d\mu_{WO_4^{2-}} - \Gamma^H_{K^+} d\mu_{K^+}, \tag{3.13}$$

where superscript H represents an adsorbed quantity at the air-liquid interface, and $\Gamma^H_{OH^-}, \Gamma^H_{WO_4^{2-}}, \Gamma^H_{K^+}$ represent the number of moles of the adsorbed ions OH^-, WO_4^{2-}, K^+ per unit area at the air-liquid interface, or the Gibbs adsorptions.

The adsorption of the water at the air-liquid interface is equal to zero by convention, thus eq.(3.13) can be rewritten as:

$$d\sigma = -\Gamma^H_{OH^-} d\mu_{OH^-} - \Gamma^H_{WO_4^{2-}} d\mu_{WO_4^{2-}} - \Gamma^H_{K^+} d\mu_{K^+} \tag{3.14}$$

The total concentration C of dissolved species is:

$$C = C_1 + C_2, \tag{3.15}$$

where $C_1 = C_{KOH}$, $C_2 = C_{K_2WO_4}$ are the concentrations of the compounds in mol/L.

Now, following the stoichiometry of the reactions, the total concentration can be expressed as follows:

$$\hat{C} = C_{K^+} + C_{OH^-} + C_{WO_4^{2-}} = n_1 C_1 + n_2 C_2, \tag{3.16}$$

where n_1, n_2 represent the total number of ions in KOH, K_2WO_4 compounds respectively and $n_{1_{K^+}}, n_{1OH^-}, n_{2K^+}, n_{2WO_4^{2-}}$ represent the number of ions involved in the dissociation process of KOH, K_2WO_4 compounds respectively.

$$n_1 = n_{1_{K^+}} + n_{1OH^-} = 1 + 1 = 2, \tag{3.17}$$

$$n_2 = n_{2K^+} + n_{2WO_4^{2-}} = 2+1=3 \tag{3.18}$$

Now, equation (3.16) can be rewritten in the following form:

$$\hat{C} = n_1 C_1 + n_2 C_2 = 2C_1 + 3C_2 \tag{3.19}$$

The mole fraction of the KOH compound in the mixture can be defined with the help of eq. (3.15) as:

$$X_1 = \frac{C_1}{C} = \frac{C_1}{C_1 + C_2} \tag{3.20}$$

Similarly, the mole fraction of the K_2WO_4 compound is defined as:

$$X_2 = \frac{C_2}{C} = \frac{C_2}{C_1 + C_2} \tag{3.21}$$

Introducing the stoichiometry in the mole fraction parameter we get:

$$\hat{X}_1 = \frac{n_1 C_1}{\hat{C}} = \frac{2C_1}{2C_1 + 3C_2} \tag{3.22}$$

and

$$\hat{X}_2 = \frac{n_2 C_2}{\hat{C}} = \frac{3C_2}{2C_1 + 3C_2} \tag{3.23}$$

Also, the relation between mole fractions is as follows:

$$\hat{X}_1 + \hat{X}_2 = 1 \tag{3.24}$$

The total Gibbs adsorption of all ions at the air-liquid interface is represented as:

$$\hat{\Gamma}^H = \Gamma^H_{OH^-} + \Gamma^H_{WO_4^{2-}} + \Gamma^H_{K^+}, \tag{3.25}$$

where, $\Gamma^H_{K^+}$ can be found as follows:

$$\Gamma^H_{K^+} = n_{1K^+}\Gamma^H_1 + n_{2K^+}\Gamma^H_2, \tag{3.26}$$

where, $\Gamma^H_{OH^-}$ and $\Gamma^H_{WO_4^{2-}}$ are defined as:

$$\Gamma^H_{OH^-} = n_{1OH^-}\Gamma^H_1, \tag{3.27}$$

and

$$\Gamma^H_{WO_4^{2-}} = n_{2WO_4^{2-}}\Gamma^H_2 \tag{3.28}$$

The total adsorption of compound 1 and 2 Γ^H is written as:

$$\Gamma^H = \Gamma^H_1 + \Gamma^H_2 \tag{3.29}$$

The mole fraction of the K_2WO_4 compound at the air-liquid interface is then:

$$X^H_2 = \frac{\Gamma^H_2}{\Gamma^H} \tag{3.30}$$

Taking in regard the stoichiometry, the mole fraction of the K_2WO_4 compound at the air-liquid interface can be found as:

$$\hat{X}^H_2 = \frac{\Gamma^H_{WO_4^{2-}} + n_{2c}\Gamma^H_2}{\hat{\Gamma}^H}, \tag{3.31}$$

First, let's find the chemical potential of the OH^- ion. If we assume that the solution is an ideal solution, using eq. (3.7) the chemical potential of the OH^- ion can be expresses as:

$$d\mu_{OH^-} = RTd\ln\left[\hat{C}_1\right] \tag{3.32}$$

Rearranging eq. (3.22) in order to get $\hat{C}_1$ and plugging it in eq. (3.32) we obtain the following expression:

$$d\mu_{OH^-} = RTd\ln\left[\frac{\hat{C}\hat{X}_1}{n_2}\right] \Rightarrow \tag{3.33}$$

$$d\mu_{OH^-} = \frac{RT}{\hat{C}}d\hat{C} + \frac{RT}{\hat{X}_1}d\hat{X}_1 \tag{3.34}$$

or if we introduce eq. (3.24) we can rewrite eq. (3.34) as follows:

$$d\mu_{OH^-} = \frac{RT}{\hat{C}}d\hat{C} - \frac{RT}{\hat{X}_1}d\hat{X}_2 \tag{3.35}$$

Now following the same logic, using eq. (3.7) and eq. (3.23), the chemical potential of the WO_4^{2-} ion is written as:

$$d\mu_{WO_4^{2-}} = \frac{RT}{\hat{C}}d\hat{C} + \frac{RT}{\hat{X}_2}d\hat{X}_2 \tag{3.36}$$

The chemical potential of the K^+ ion is then:

$$d\mu_{K^+} = \frac{RT}{\hat{C}}d\hat{C} - RT\frac{\frac{n_{1K^+}}{n_1} - \frac{n_{2K^+}}{n_2}}{\frac{n_{1K^+}}{n_1}\hat{X}_1 + \frac{n_{2K^+}}{n_2}\hat{X}_2}d\hat{X}_2 \tag{3.37}$$

At the constant temperature and pressure, substituting $d\mu_{OH^-}, d\mu_{WO_4^{2-}}, d\mu_{K^+}$ (eq.(3.35), (3.36), (3.37)) into the surface tension equation (3.14) we can write:

$$d\sigma = -\Gamma^H_{OH^-}\left[\frac{RT}{\hat{C}}d\hat{C} - \frac{RT}{\hat{X}_1}d\hat{X}_2\right] - \Gamma^H_{WO_4^{2-}}\left[\frac{RT}{\hat{C}}d\hat{C} + \frac{RT}{\hat{X}_2}d\hat{X}_2\right] - \Gamma^H_{K^+}\left[\frac{RT}{\hat{C}}d\hat{C} - RT\frac{\frac{n_{1K^+}}{n_1} - \frac{n_{2K^+}}{n_2}}{\frac{n_{1K^+}}{n_1}\hat{X}_1 + \frac{n_{2K^+}}{n_2}\hat{X}_2}d\hat{X}_2\right] \tag{3.38}$$

Now, rearranging eq.(3.38) and using eq.(3.25) and eq.(3.31) we can obtain the following:

$$d\sigma = -\frac{RT}{\hat{C}} d\hat{C}\left(\Gamma^H_{OH^-} + \Gamma^H_{WO_4^{2-}} + \Gamma^H_{K^+}\right) + \Gamma^H_{OH^-} \frac{RT}{\hat{X}_1} d\hat{X}_2 - \Gamma^H_{WO_4^{2-}} \frac{RT}{\hat{X}_2} d\hat{X}_2 + \Gamma^H_{K^+} RT \frac{\frac{n_{1K^+}}{n_1} - \frac{n_{2K^+}}{n_2}}{\frac{n_{1K^+}}{n_1}\hat{X}_1 + \frac{n_{2K^+}}{n_2}\hat{X}_2} d\hat{X}_2 \Rightarrow \tag{3.39}$$

$$d\sigma = -\hat{\Gamma}^H \frac{RT}{\hat{C}} d\hat{C} + \Gamma^H_{OH^-} \frac{RT}{\hat{X}_1} d\hat{X}_2 - \Gamma^H_{WO_4^{2-}} \frac{RT}{\hat{X}_2} d\hat{X}_2 + \Gamma^H_{K^+} RT \frac{n_{1K^+} n_2 - n_{2K^+} n_1}{n_{1K^+}\hat{X}_1 n_2 + n_{2K^+}\hat{X}_2 n_1} d\hat{X}_2 \tag{3.40}$$

The final equation for the surface tension is:

$$d\sigma = -\frac{\hat{\Gamma}^H RT}{\hat{C}} d\hat{C} + \hat{\Gamma}^H RT \frac{\hat{X}_2 - \hat{X}_2^H}{\hat{X}_1 \hat{X}_2}\left[1 - \frac{n_{1K^+} n_{2K^+}}{n_{1K^+} n_2 \hat{X}_1 + n_{2K^+} n_1 \hat{X}_2}\right] d\hat{X}_2, \tag{3.41}$$

3.2.3. Gibbs adsorption at the constant concentration of one component in the mixture

Now, if we consider concentration of the KOH, C_1, constant, eq.(3.23) can be expressed as:

$$d\left(\hat{X}_2 \hat{C}\right) = n_2 dC_2 \tag{3.42}$$

And eq.(3.16) can be rewritten as:

$$d\hat{C} = n_2 dC_2 \tag{3.43}$$

Taking a derivative of the left hand side of eq.(3.42) it can be expressed as:

$$\hat{X}_2 n_2 dC_2 + \hat{C} d\hat{X}_2 = n_2 dC_2 \tag{3.44}$$

Rearrangement of eq.(3.44) leads to:

$$dC_2 = -\frac{n_1 C_1 + n_2 C_2}{n_2 \hat{X}_2 - n_2} d\hat{X}_2 = -\frac{\hat{C}}{n_2 \hat{X}_2 - n_2} d\hat{X}_2 \tag{3.45}$$

Using eq.(3.43) and eq.(3.45) we can rewrite eq.(3.41) in the following form:

$$\begin{aligned} d\sigma = & \frac{\hat{\Gamma}^H RT}{\hat{C}} \frac{n_2 \hat{C}}{n_2 (\hat{X}_2 - 1)} d\hat{X}_2 + \\ & \hat{\Gamma}^H RT \frac{\hat{X}_2 - \hat{X}_2^H}{\hat{X}_1 \hat{X}_2} \left[1 - \frac{n_{1K^+} n_{2K^+}}{n_{1K^+} n_2 \hat{X}_1 + n_{2K^+} n_1 \hat{X}_2} \right] d\hat{X}_2 \Rightarrow \end{aligned} \tag{3.46}$$

$$\frac{d\sigma}{d\hat{X}_2} = \frac{\hat{\Gamma}^H RT}{(\hat{X}_2 - 1)} + \hat{\Gamma}^H RT \frac{\hat{X}_2 - \hat{X}_2^H}{\hat{X}_1 \hat{X}_2} \left[1 - \frac{n_{1K^+} n_{2K^+}}{n_{1K^+} n_2 \hat{X}_1 + n_{2K^+} n_1 \hat{X}_2} \right] \tag{3.47}$$

When $\hat{X}_2 = 0$ eq.(3.47) takes the following form:

$$\left. \frac{d\sigma}{d\hat{X}_2} \right|_{\hat{X}_2 = 0} = -\hat{\Gamma}^H RT + \frac{\hat{\Gamma}^H RT}{\hat{X}_1} \left[1 - \frac{n_{1K^+} n_{2K^+}}{n_{1K^+} n_2 \hat{X}_1} \right] \tag{3.48}$$

Rearranging eq. (3.48) we can express $\hat{\Gamma}^H$ as:

$$\hat{\Gamma}^H = \frac{d\sigma}{d\hat{X}_2} \frac{1}{RT \left(-1 + \frac{1}{\hat{X}_1} - \frac{n_{1K^+} n_{2K^+}}{n_{1K^+} n_2 \hat{X}_1^2} \right)} \tag{3.49}$$

Taking into account eq. (3.24), the final relation takes on the following form:

$$\hat{\Gamma}^H = -\frac{d\sigma}{d\hat{X}_2} \frac{n_{1K^+} n_2}{RT \cdot n_{1K^+} n_{2K^+}} \tag{3.50}$$

Plugging in the values for n from eq.(3.17) and (3.18) into eq.(3.50) we can calculate the total Gibbs adsorption $\hat{\Gamma}^H$ at the air-liquid interface at the point when $\hat{X}_2 = 0$ as:

$$\hat{\Gamma}^H = -\frac{d\sigma}{d\hat{X}_2} \cdot \frac{3}{2RT} \tag{3.51}$$

where $\hat{X}_1 = 1$, $R = 8.314 J / K \cdot mol$, $T = 298 K$.

3.3. Characterization of the CLE reaction products

3.3.1. Surface tension and the Gibbs adsorption of the tungstate ions

The solutions were prepared by electropolishing tungsten with the CLE technique described in Chapter 1. The tungsten square plate (15x15 mm) with thickness of 1.5mm served as an anode. The stainless steel rod with 15mm diameter and 50mm length was used as a cathode. Both electrodes were placed into a glass beaker with diameter of 20 mm and 25 mm tall and connected to a potentiostat CHI 660D (CH Instruments, Inc.). Then, a 1 ml of the freshly prepared 2M KOH electrolyte solution was added to the beaker using a 1ml syringe. In order to prepare solutions with different concentration of the reaction products, tungsten was electropolished with 10V DC potential for different periods of time. Each experiment was repeated three times to obtain a standard deviation. The current versus time dependence was saved for each experiment for further calculations of the tungsten mass loss. After electopolishing, solutions were collected

using the 1ml syringe and transferred into the glass vial. Each experiment was performed with a freshly prepared KOH solution every time in a new beaker.

When electric current passes through the electrolytic cell, the number of moles liberated during the reaction can be estimated using Faraday's law as:

$$m = \frac{Q}{zF} \tag{3.52}$$

where Q is the total charge at time t, z = 6 is tungsten valence number, and $F = 96485\,\mathrm{C/mol}$ is Faraday's constant. The total charge Q is found by integrating the current:

$$Q = \int I(t)dt \tag{3.53}$$

The concentration is determined as follows:

$$C_i = \frac{N_i}{V}, \tag{3.54}$$

where C_i, is defined as the amount of moles of the solute, N_i, divided by the volume of the solution, V. The number of moles was estimated from the overall electrochemical reaction (3.10) that shows that the reaction proceeds with oxidation of one mole of tungsten to one mole of tungstate ions.

Density and surface tension measurements

The density measurements were performed using a microbalance and a micropipette. For each solution, a drop of V=30µL was placed on the pan of the microbalance to measure the weight in mg. For each solution five drops were measured

to obtain the standard deviation of the measurements. The densities were calculated using equation: ρ=m/V. The measured density of the 2M KOH solution was equal to $\rho_{2MKOH} = 1.0990 \pm 0.0024 g/cm^3$ and of the 1M KOH solution $\rho_{1MKOH} = 1.0554 \pm 0.0028 g/cm^3$ and was in a good agreement with the density found in the literature [64]. Figure 3.7 (a) show the density dependence on the concentration of the tungstate ions released in the electrolyte solution during electropolishing in our experiments. The literature values of aqueous KOH solution densities and viscosity at T=20˚C as a function of mass fraction are presented in Figure 3.7 (b).

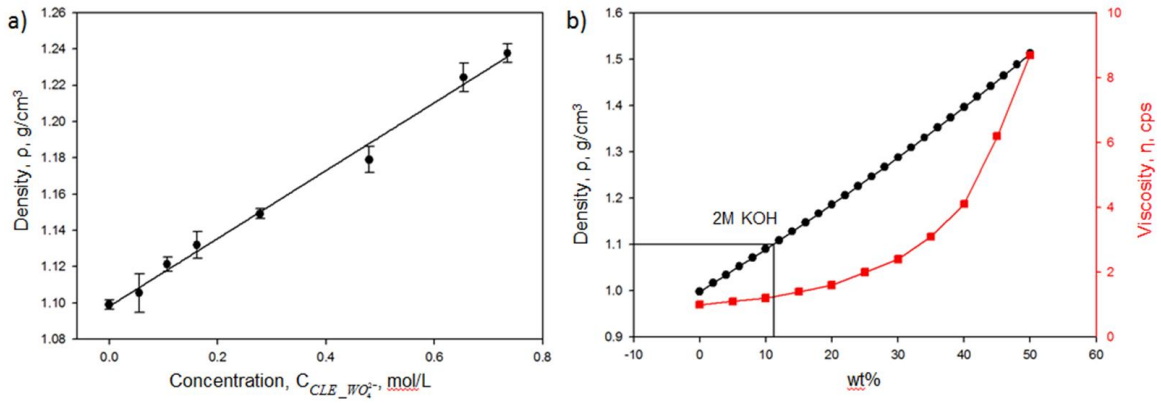

Figure 3.7. (a) Dependence of the density of tungstate solutions (CLE technique, applied potential of 10V) on concentration of tungstate ions in the 2M KOH electrolyte. (b) Density [64] and viscosity [65] of aqueous KOH solution as a function of mass fraction obtained from the literature.

The surface tension measurements were performed using Kruss DSA10 instrument with 1.25mm needle diameter for all solutions. Once glass syringe was filled with the solution a pendant drop was produced and images were recorded using Kruss DSA software for further analysis. All measurements were carried out at the room temperature. Five measurements were taken for each solution to get a standard deviation.

The surface tension of water measured with this technique was equal to $\sigma_w = 71.82 \pm 0.38 mN/m$. The surface tension of the 2M KOH was equal to $\sigma_{2MKOH} = 75.17 \pm 0.1 mN/m$ and of the 1M KOH, $\sigma_{1MKOH} = 73.35 \pm 0.17 mN/m$. The value of surface tensions of the KOH solutions agreed fairly well with the values reported in earlier studies (Figure 3.8) [10-12, 17, 21].

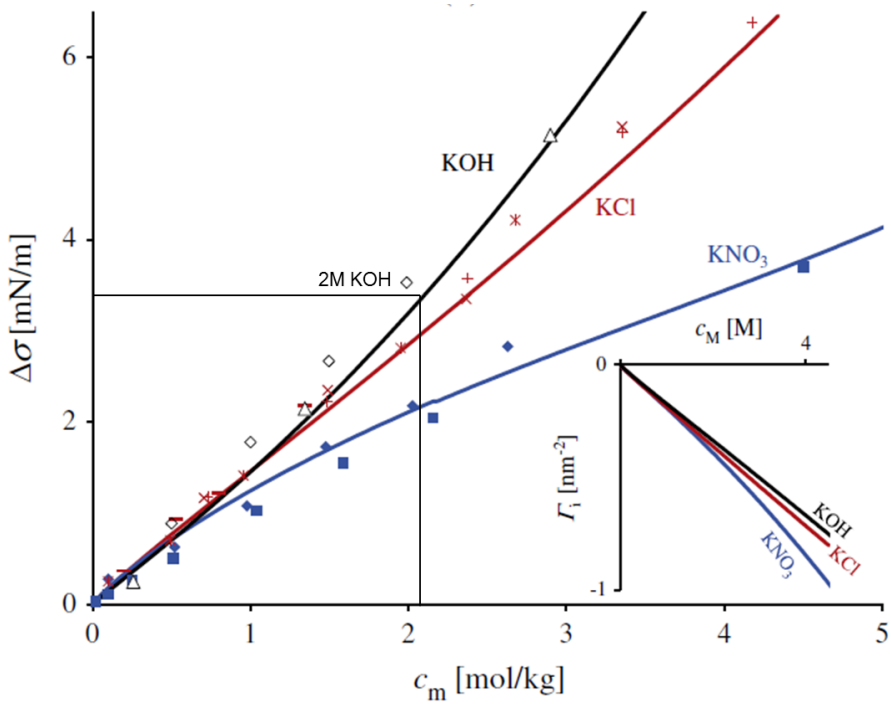

Figure 3.8. Surface tensions change as a function of the concentration for potassium salts. The insert shows the adsorption isotherm as a function of concentration [12].

The potassium hydroxide aqueous solutions with tungstate ions were studied under the microscope. The inserts in Figure 3.9 shows a sequence of images of the solutions prepared by electropolishing of tungsten in 2M KOH electrolyte for different periods of time. It can be seen that the solution stays clear up to the 0.12 mole fraction of the K_2WO_4 compound that corresponds to 0.2M concentration of the tungstate ions in the

mixture. Also, the surface tension decreases during this time. After that, the precipitates start to appear in the solution that correlates with the stabilization of the surface tension.

pH analysis of tungstate solutions

The pH was measured using pH meter from Denver Instruments UltraBASIC US-10 and double checked with the pH strips. Remarkably the pH of the potassium hydroxide with tungstate ions solutions decreased reaching pH9 at the 0.65M concentration of the tungstate ions. From Chapter 2 we found that the tungstate ions start to precipitate at the pH bellow 8 forming $WO_3 \cdot H_2O$.

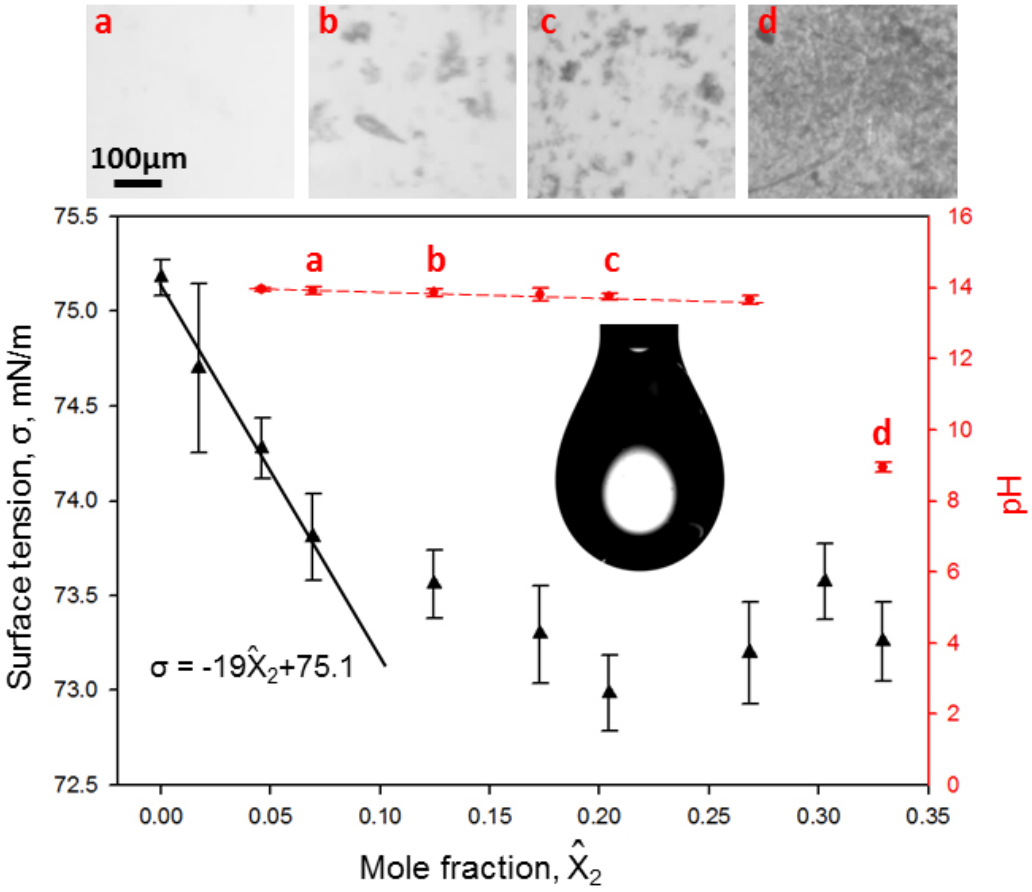

Figure 3.9. Surface tension (black dots) and pH (red rhombs) as a function of the K_2WO_4 mole fraction. The inserts are optical images of the mixtures.

Now, using eq. (3.51) and knowing the $d\sigma/d\hat{X}_2 = -0.019$ from Figure 3.9, the Gibbs adsorption can be estimated as $\hat{\Gamma}^H = 1.2 \cdot 10^{-5} mol/m^2$. Thus, it can be concluded that when the tungstate ions were added to the mixture, the Gibbs adsorption appears positive. In contrast, the initial Gibbs adsorption of the KOH solution is negative. This means that the tungstate ions were adsorbed at the surface decreasing the surface tension of the entire mixture.

Average area occupied by a single ion at the air-liquid interface

Knowing the value of the total Gibbs adsorption at the initial point when $\hat{X}_2 = 0$, area A at the surface occupied by a single ion can be found using the following equation:

$$A = \frac{1}{N_A \cdot \hat{\Gamma}^H} = 0.14 nm^2, \tag{3.55}$$

where N_A is the Avogadro's number $N_A = 6.02 \cdot 10^{23}\ mol^{-1}$.

Average area of the tungstate ion

The tungstate ion is a polyatomic ion that consists of four oxygen atoms that surround one tungsten atom that is positioned in the center of the ion. When ions are formed the atoms arrange themselves in the way to lower the internal energy of the system[66]. To achieve that, they form three dimensional units, arranging atoms using covalent bonding with the shortest length. In the case of tungstate ion we have four atoms of oxygen and the optimal configuration for this ion is a tetrahedral arrangement of atoms that is shown in Figure 3.10.

The ionic radii of oxygen and tungsten ions can be found in literature and presented in table in Figure 3.10. The tungstate ion radii then can be approximated as $r_{WO_4^{2-}} = r_{W^{6+}} + 2r_{O^{2-}}$ and was found to be 0.302 nm.

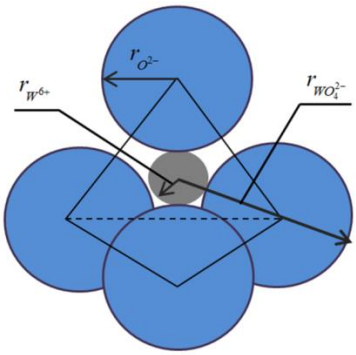

Atom	Ionic radius r, nm	Ref.
O^{2-}	0.130	[67]
W^{6+}	0.042	[66]
WO_4^{2-}	0.302	Calculated

Figure 3.10. Tetrahedral coordination of oxygen around tungsten ion W^{6+} and the values of their radiuses.

Assume that one tungstate ion positioned at the air-liquid interface with one oxygen atom pointing out towards the air with the rest of the oxygen atoms pointing inwards and the next tungstate ion sitting at the air-liquid interface with three oxygen atoms pointing towards the air and one oxygen atom pointing into the liquid. In this case, the area occupied by two tungstate ions at the interface can be approximated by the cross section of the four oxygen atoms. The cross section of a single oxygen atom found as $A_{O^{2-}} = \pi r_{O^{2-}}^2 = 0.053 nm^2$. Now, two tungsten ions situated at the air-liquid interface would occupy the area $A_{2ions} = 4A_{O^{2-}} = 0.212 nm^2$, or average area occupied by a single tungstate ion is then $A_{ion} = 0.106 nm^2$. Comparing the average area occupied by a single ion at the air-liquid interface estimated from the Gibbs adsorption isotherm eq. (3.55) and the average area of tungstate ion situated at the air-liquid interface, it can be concluded that the ions are closely packed at the surface of the liquid.

3.3.2. Composition and thermal analysis

SEM-EDS analysis

The precipitates in solutions were filtered out and washed 5 times with DI water. After that they were left to dry in the air at room temperature for 24h. The precipitates appeared to have white dull color. They were analyzed using the FESEM-Hitachi S4800 scanning electron microscope equipped with the Oxford INCA Energy 200 Energy Dispersive Spectroscopy (EDS). The precipitates were mounted on aluminum stubs with carbon-graphite tape for fixation.

Elemental maps of the W, O and K of the samples of white precipitates are shown in Figure 3.11. This map shows that the rod-like structure consists mostly of tungsten and oxygen elements. The potassium is mostly distributed around the rods and most likely represents the residue of the KOH electrolyte.

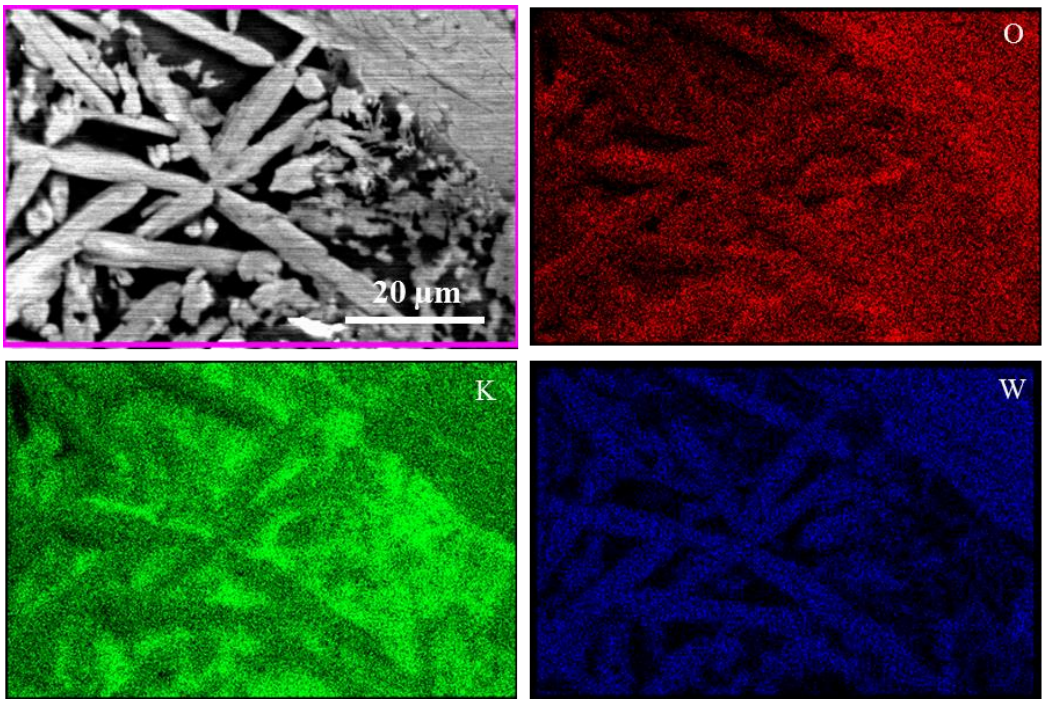

Figure 3.11. SEM-EDS elemental maps for precipitates collected from the solutions prepared with the CLE method. Gray is the SEM image of the structures, “O” is a map of oxygen presence, “K” is a map of potassium presence, “W” is a map of tungsten presence on the sample.

Figure 3.12 shows the EDS data collected from the white precipitates. From the data shown in the inserted table it can be concluded that the precipitates consist of some oxides or hydrates of tungsten where the potassium is possibly bonded to the tungsten compound or present as a residue in the sample.

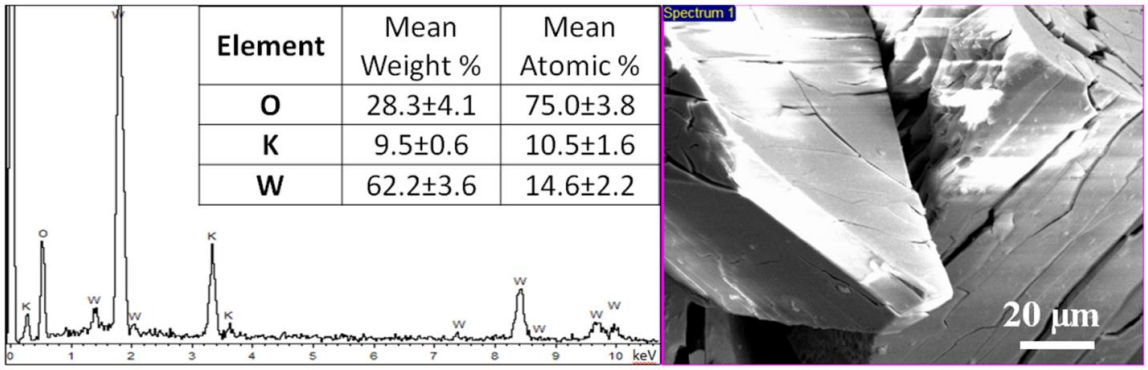

Figure 3.12. SEM-EDS analysis of the precipitates.

XRD analysis

The X-ray diffraction (XRD) patterns were acquired using a Rigaku Ultima IV powder diffractometer equipped with Cu *Kα* radiation (λ=1.5418 Å) in the angular range from 10˚ to 80˚ *2θ*. The XRD measurements were carried out at the room temperature. The data was analyzed using PDXL software version 1.4.0.0. Figure 3.13 shows the XRD patterns collected from (a) commercial crystalline H_2WO_4 powder that was purchased from Alfa Aeser, A Johnson Matthey Company, CAS number 7783-03-1, (b) from the commercial H_2WO_4 powder after the DSC run that was identified as a WO_3 compound, (c) from the white precipitates collected from solution. From Figure 3.13 (c) it can be seen that the precipitates have an amorphous structure that does not allow determining the composition of the compound using this technique.

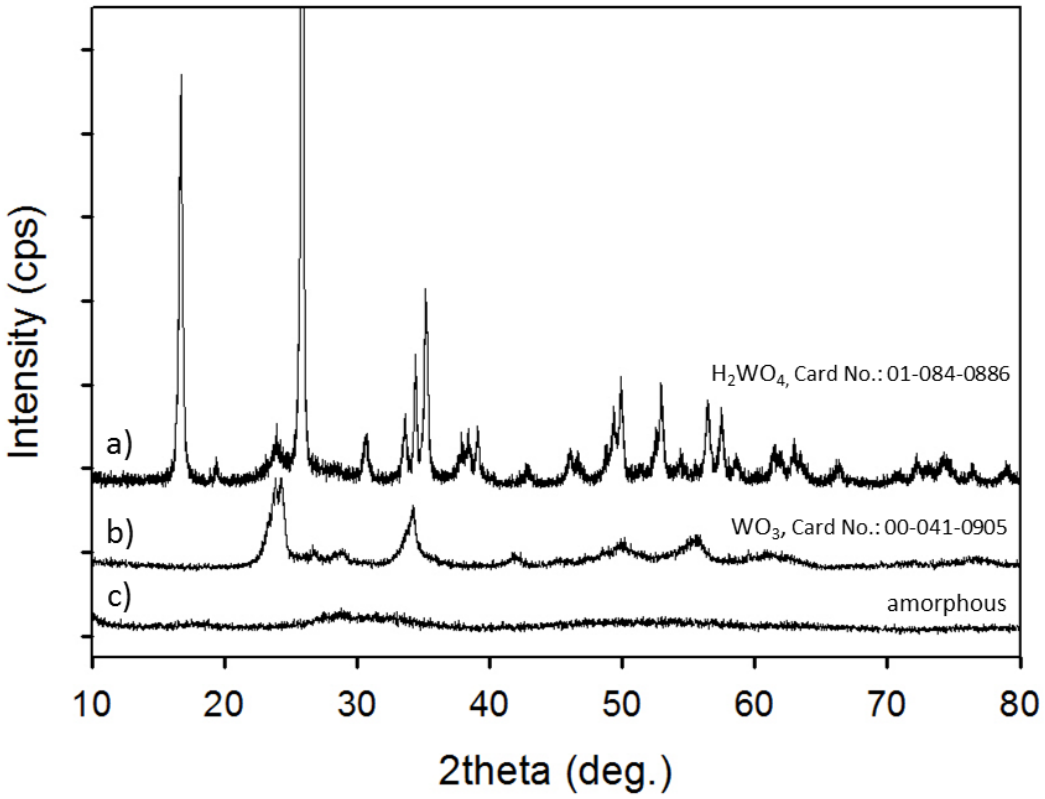

Figure 3.13. XRD pattern of the (a) commercial H_2WO_4 powder (b) commercial H_2WO_4 powder after DSC run and (c) precipitates from solution (electrolyte after electropolishing the tungsten plate with the CLE technique).

Thermal analysis

The Thermal Gravimetric Analysis (TGA) was performed on TA Instruments TGA Q5000 V3.13 Build 261 with a ramp 10°C/min from 25°C to 400°C in nitrogen gas. First the sample was equilibrated at room temperature under nitrogen purge for 10 min prior to heating. The Differential Scanning Calorimetry (DSC) was performed on TA Instruments DSC Q1000 V9.9 Build 303. First the sample was equilibrated at 25°C followed by the temperature increase with the 10°C/min ramp to 400°C in helium gas. To

analyze the data TA Instruments Universal Analysis 2000 V3.9A and 4.7A software was used.

The DSC and TGA curves are shown in Figure 3.14. From the DSC curve, in our experiment on amorphous samples, it can be seen that there is one endothermic peak at 138˚C which is accompanied by the noticeable mass loss of 4.9wt.%. The total mass loss during the heating from the room temperature to 400˚C was 7.5wt.%.

The endothermic peaks in the range of 100-300C temperatures are commonly reported for tungsten and other compounds [68-80]. Figure 3.14 (b) presents the DSC/TGA curves from the commercial crystalline H_2WO_4 powder. It can be seen that the endothermic peak for the commercial sample occurs at a higher temperature, T=241˚C. The total mass loss during the heating from the room temperature to 400˚C was 6.8wt.% that correlates with the values from the literature [78]. In Figure 3.13 (a) and (b) we show the XRD patterns of the commercial sample before and after the DSC run which show that H_2WO_4 loses its hydrogen and oxygen during the heating process and transforms to WO_3. A thorough analysis of the crystalline samples of tungsten oxides and hydrates reveals that these compounds undergo phase transitions with the change of the lattice symmetry and release of the volatile oxygen and hydrogen [68-80]. This suggests that the local microstructure of oxides and hydrates undergo a similar change, but the energy required to reorder the lattice constituents can be different because of the lack of crystal order. Therefore, the peak temperature is lover on the amorphous samples.

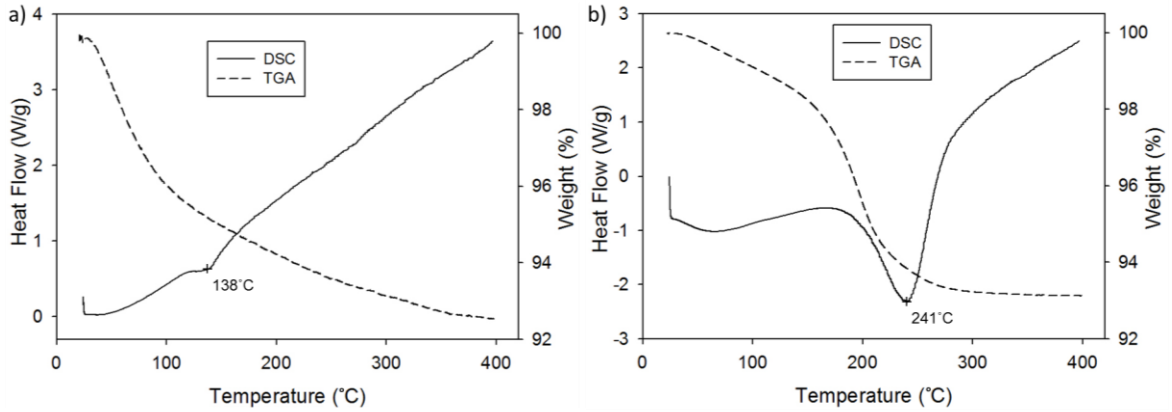

Figure 3.14. DSC and TGA curves: (a) on the white amorphous precipitates from the electrolyte, and (b) on the commercial crystalline H_2WO_4 sample.

In summary, the results from EDS analysis point to the presence of the tungsten oxides/hydrates in the precipitates, as well as thermal analysis revealed the presence of the structurally bound or hydrated water. This indicates that the precipitates are most likely consisting of tungsten hydrates that are present in the amorphous form.

3.4. Flow kinetics of the reaction products

When tungsten wire is electropolished using the CLE technique by applying the 3V potential, it oxidizes to form tungstate ions that are negative and miscible with the electrolyte. These ions are attracted to the tungsten surface that is positively charged. Some properties of this film produced in the 2M KOH solution were studied previously [81-83]. It was found that the ions form a viscous film flowing over the immersed part of the tungsten wire. This film is heavier, hence denser than the electrolyte and tend to flow in a downwards motion. As it can be seen from Figure 3.15 and Figure 3.16 the jet has a sharp interface with the electrolyte and as the distance from the wire increases, it

contracts. This suggests that the film and electrolyte are weakly miscible and have some interfacial tension between each other that prevents the jet from fast diffusion into the electrolyte. The jet remained stable at least for 20 seconds during the electropolishing suggesting that the radial diffusion is not significant. Due to the jet stability and its interfacial tension it can be assumed that the reaction products situated mostly inside the jet. Hence, by tracing the jet motion some physical parameters of the jet can be estimated.

3.4.1. Peclet number

The electrochemical etching of tungsten wire was performed using the two-electrode system consisting of cathode and anode. The stainless still rode with 1.5 cm diameter and 5 cm length served as a cathode. The tungsten wire (99.95% Advent Research Materials Ltd.) with 0.5 mm diameter and 4 cm length served as an anode. Both electrodes were immersed into the beaker with 1M KOH electrolyte and connected to a potentiostat CHI600D (CH Instruments, Inc.). The immersion length for tungsten wire was 1.5 mm and for stainless still 3.5 cm. The hollow glass non-porous microspheres SPHERICEL® 60P18 from Potters Industries LLC were added to the electrolyte to visualize the flow. The mean diameter of the microspheres was around 33 μm and density of 600±50kg/m^3. A constant potential of 3V was applied to the system. The current was recorded along with the video focusing on the immersed part of the tungsten wire. To record a video the Flea®3 USB 3.0 Digital Camera (Point Grey Research, Inc.) with attached Short UNIMAC MacroZoom Lens, MS-50D (Meiji Techno America) was used.

The videos were recorded at 60fps. Analysis of the captured videos was performed using VirtualDub and ImageJ (NIH) software.

First, to distinguish what governs the flow it is important to estimate the Peclet number. The Peclet number is a ratio of the advection rate to the rate of diffusion of the particle in the fluid flow. In the case of electropolishing it can be used to define whether the advection or diffusion of the corrosion products (tungstate ions) is predominant. The Peclet number can be found using the following relations:

$$Pe = \frac{h_f v_f}{D}, \tag{3.56}$$

where Pe is the Peclet number, h_f is the thickness of the film on the side of the tungsten wire before the detachment from the wire, v_f is the velocity of the film on the side of the wire, D is the diffusion coefficient of the tungstate ions in KOH electrolyte [84].

Figure 3.15 shows a glass particle travelling on the side of the tungsten wire downwards. Using these images, the velocity of that particle can be estimated. The thickness h_f was estimated using five particles as $h_f = 1.16 \cdot 10^{-4} \pm 6.4 \cdot 10^{-6} m$ and velocity as $v_f = 4.19 \cdot 10^{-4} \pm 1.7 \cdot 10^{-5} m/s$. Thus, using eq. (3.56) the Peclet number can be estimates as $Pe = 48.4 \pm 2$.

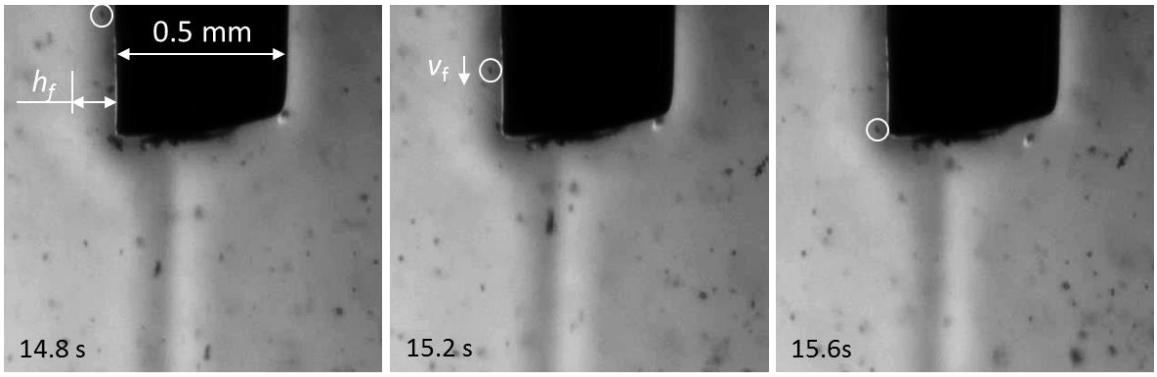

Figure 3.15. The flow of the reaction products around tungsten wire. The glass beads are shown in the circles. Electropolishing was performed with 3V applied potential in 1M KOH electrolyte with 0.5 mm tungsten wire with the immersion depth of 1.5 mm.

The value of the Peclet number shows that the advection overcomes the diffusion, meaning that the reaction products do not have time to diffuse from the tungsten surface or from the jet and are situated inside the film or jet. Knowing this, the density of the jet can be found disregarding the diffusion processes.

3.4.2. Density estimations

The maximum difference in density $\Delta\rho_{\max} = \rho_{rp} - \rho_{el}$ between the electrolyte with density ρ_{el} and the reaction products ρ_{rp} flowing downwards from the wire can be estimated thought the relation of the dissolution rate G of the tungsten and the volumetric flow rate Q of the jet after detachment from the end of the wire as follows [81]:

$$\Delta\rho_{\max} = \frac{G}{Q} \tag{3.57}$$

The dissolution rate of the tungsten G can be calculated using the Faraday's law [81, 85] as follows:

$$G = \frac{IM}{zF}, \tag{3.58}$$

where $I = 6.1 \pm 0.01 mA$ is a current, M=183g/mol is the tungsten molar mass, z=6 is the tungsten valence number, and F=96485C/mol is Faraday's constant.

The volumetric flow rate can be found using the jet velocity and the jet radius R_j at each point as follows:

$$Q = v_j \pi R_j^{\,2} \tag{3.59}$$

Figure 3.16 show the sequence of images extracted from the videos recorded during the electropolishing of the tungsten wire in 1M KOH solution saturated with glass particles.

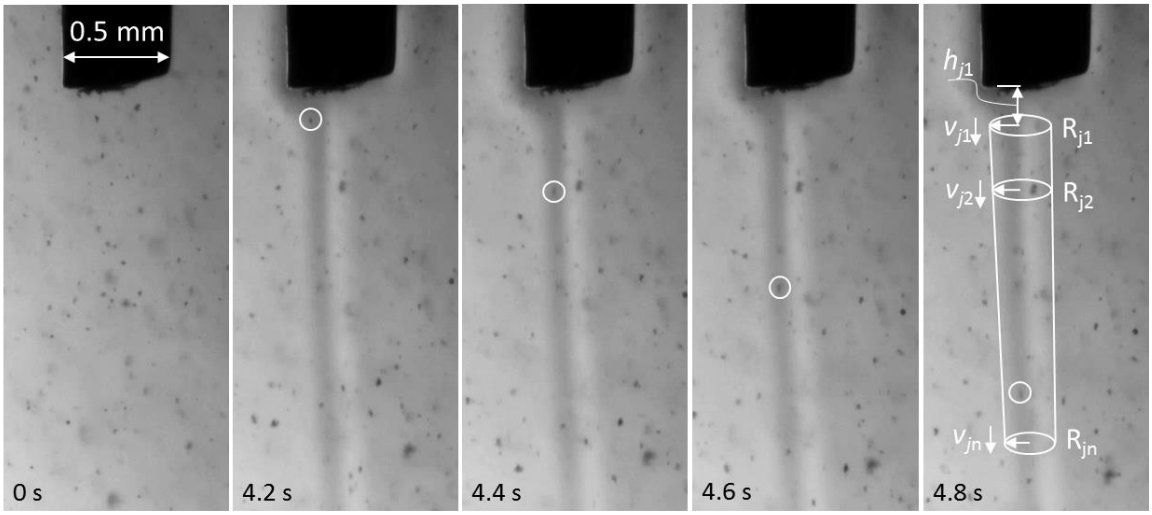

Figure 3.16. The flow kinetics of the reaction products tracked using glass beads (circled). The 0.5 mm in diameter wire was immersed into 1M KOH electrolyte for 1.5 mm length and the potential of 3V was applied to the cell.

By tracing the position of the glass particles from frame to frame (Figure 3.16) the jet velocity v_j was determined. Each particle was traced starting from the end of the wire

with a step of ~0.04 s intervals making around n=20 measurements per particle. Along with the position of the particle along the jet, the measurements of the jet radius R_j were made as well. Figure 3.17 (a) shows the plot of the velocity of the jet, after detachment from the wire, as a function of the jet radius. The fit of the data suggests that the jet radius is inversely proportional to the square root of the jet velocity. The same conclusion was drawn earlier [81] and our data is in agreement with it. Therefore, using eq.(3.59), we conclude that $R_j = Q/\sqrt{v_j \pi}$, and the flow rate is constant and equal to $Q = 0.062 \pm 0.007 mm^3/s$.

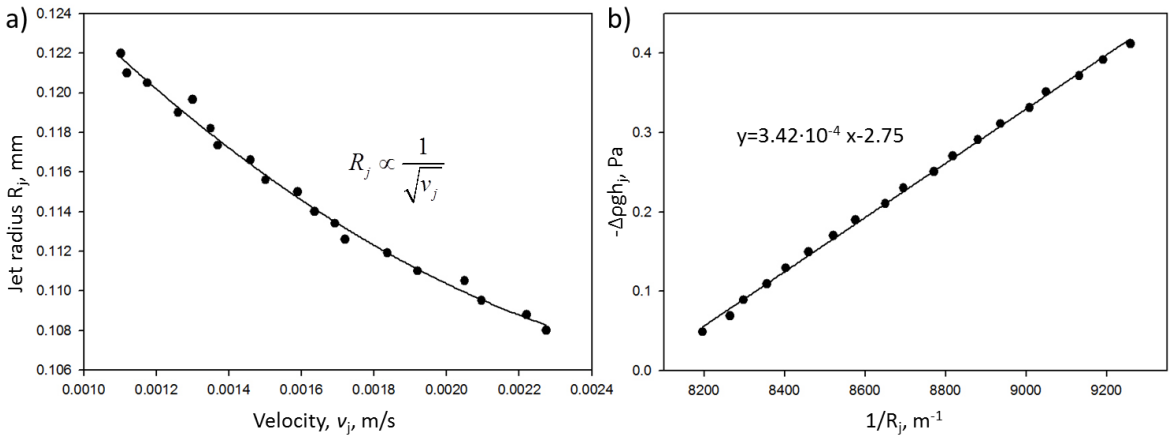

Figure 3.17. (a) Velocity of the jet versus the jet radius. (b) Hydrostatic pressure dependence on the jet curvature. Dots represent the experimental values and the lines represent the fitting.

Using the data from Figure 3.16 and solving eq. (3.57) the maximum density difference between the flow and surrounding electrolyte was found to be $\Delta\rho_{max} = 28.59 \pm 3.6 kg/m^3$.

3.4.3. Interfacial tension estimation

As it was discussed earlier, the film around the wire and the jet that consists of the reaction products of tungsten dissolution, have distinct edges separating them from the electrolyte. This signifies the existence of the interfacial tension between these two liquids. Using the model employing the pressure balance for a static liquid column[81], the interfacial tension can be found as:

$$-\Delta\rho g h_j + \frac{\sigma}{R_j} = const \tag{3.60}$$

where the σ is the interfacial tension, h_j is the jet height from the end of the wire, g is gravitational acceleration, R_j is a jet a jet radius, and $\Delta\rho$ is the density difference between the jet and the electrolyte.

Using eq. (3.60) and data from Figure 3.16 and Figure 3.17 (a) the relation between the hydrostatic pressure and $1/R_j$ was plotted in Figure 3.17 (b). From the slop of the fitted data the interfacial tension was estimated as $\sigma \approx 0.34 mN/m$.

3.4.4. Viscosity estimation

The spherical glass particle travelling downwards in the jet has several forces imposed on it. The buoyancy and drag forces act on the sphere upwards and the gravitational force pulls on it downwards. The force balance reads:

$$F_{buoyancy} - mg + F_{drag} = 0 \tag{3.61}$$

Since the flow rate is constant and the Peclet number is high, it can be assumed that the flow in the jet is laminar. In this case the Stokes' law can be used to determine the drag force. Now, eq. (3.61) can be rewritten in the following form:

$$\frac{4}{3}\pi r^3 g(\rho_s - \rho_f) - 6\pi\eta r v_t = 0 \tag{3.62}$$

The velocity v_t is the relative viscosity that is found as difference between the sphere velocity v_s ($v_s = v_j$) and the fluid velocity in the jet v_f:

$$v_t = v_s - v_f = v_j - \frac{Q}{\pi R_j^2} \tag{3.63}$$

To determine the viscosity, the position of the glass sphere was tracked for 0.5mm from the end of the wire, where the velocity of the jet was constant $v_j = 0.0012 m/s$.

$$\eta = \frac{2r^2 g\left(\rho_s - \rho_f\right)}{9\left(v_j - \frac{Q}{\pi R_j^2}\right)} \approx 0.0018 Pa \cdot s, \tag{3.64}$$

where the sphere radius is $r = 16.5 \cdot 10^{-6} m$, the density of the sphere is $\rho_s = 600 kg/m^3$, and the density of the fluid is $\rho_f \approx 1084 kg/m^3$. The standard deviation was estimates as $0.0003 Pa \cdot s$.

3.4.5. Elastic modulus estimation

The tomography with the transmission X-ray microscope was performed in Brookhaven National Laboratory (see Chapter 6 for more details) on samples prepared with the CLE technique. The tomography run with X-ray energy of 8960 eV was performed resulting in collection of 1441 projections with the field of view 40 μm^2 by 40

μm^2. After the measurement the background was subtracted and an automatic alignment using the run-out correction system was applied. A standard filtered back-projection reconstruction algorithm was used to construct the 3D images [86]. Threshholding was applied to the reconstructed image stacks using Avizo® program, VSG, version 8.0.

The tungsten wire was electropolished using the CLE technique until the lower (immersed into electrolyte) part of the wire was dropped off and the meniscus that was originally created on the wire was snapped off the wire. After that the wire was left undisturbed in the cell for 1 h to stabilize after which the tomography was performed. The tomography of the needle prepared with the CLE technique shows a smooth surface of the tungsten tip (Figure 3.18) without any porous shell. However, the presence of the micrometer thin viscous bridge was observed. This bridge connected the tungsten tip with the top part of the wire. Most likely, this bridge connected the tungsten tip with the dropped piece. The visible part of the bridge connected the tungsten tip with the surface of the liquid. The distance between the tip of the wire and the electrolyte surface was approximately 70 μm. The bridge appeared to have some nuclei trapped inside that remained intact during the tomography scan. It should be noted that during the stabilization period before the tomography was performed the bridge was left in the air. Therefore, water evaporated leading to gradual increase of the viscosity inside the bridge. Also, according to our solubility analysis, evaporation of water lead to precipitation of tungsten compounds.

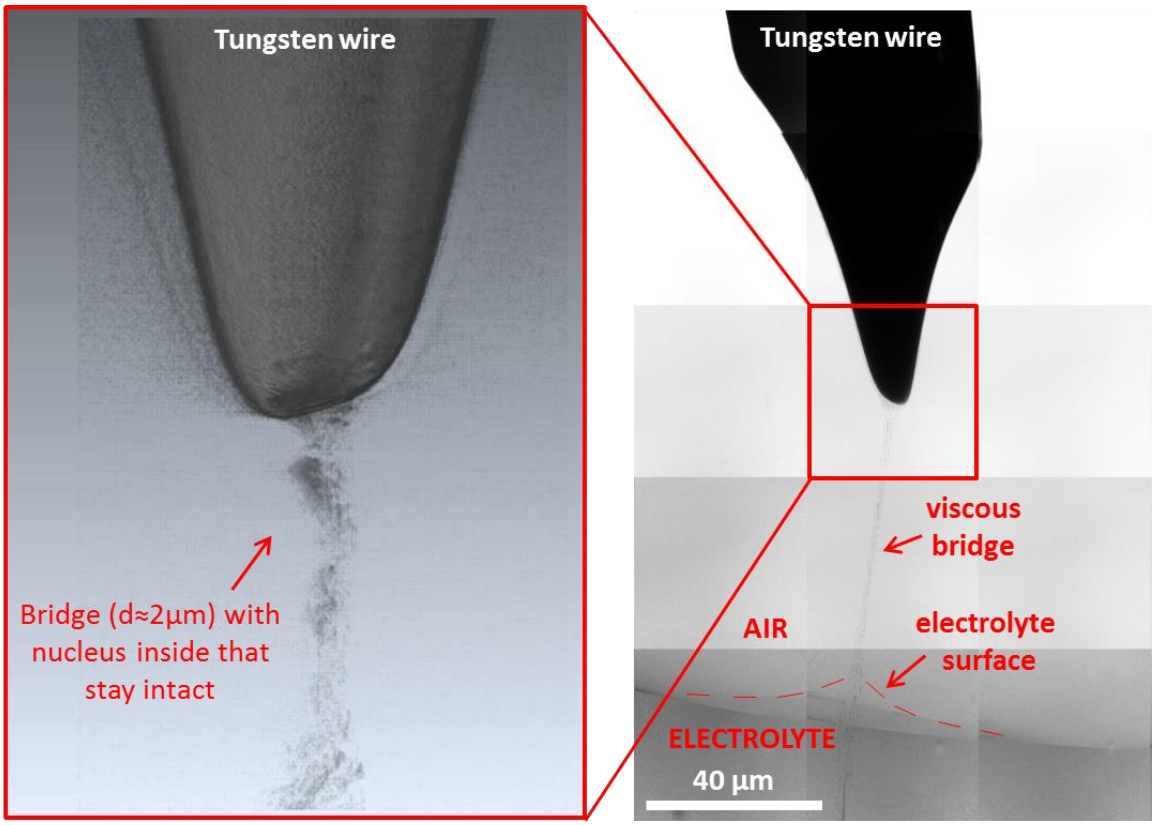

Figure 3.18. The image in the red box is a tomography of the CLE prepared needle with a bridge connecting the tip of the needle with the electrolyte surface. The X-ray image on the right depicts the region where the tomography was performed.

If we assume that the bridge has the same surface tension as that of the electrolyte, then using Figure 3.18 one can estimate the Young's modulus E of the liquid bridge balancing the capillary pressure with the radial stress σ_{rr}. Assuming that the bridge is made of a gel, one can estimate the radial stress through the Young's modulus of the gel $\sigma_{rr} \approx E$. Therefore, the order of magnitude estimate gives:

$$E = \frac{2\sigma}{d} = \frac{2 \cdot 73 mN/m}{2\mu m} = 73 kN/m^2 \tag{3.65}$$

Indeed, such value of the Young's modulus corresponds to a strong gel structure, for example alginate hydrogels have the same order of magnitude values [87, 88]. However, if the bridge was made of tungsten oxides or hydrates the Young's modulus would be greater.

3.5. Conclusions

The complex multicompound ionic mixture consisting of KOH dissociated in water and tungstate ions added to the mixture through electrochemical etching of tungsten showed an unusual behavior of the surface tension with concentration of tungstate ions. With increase of the tungstate ions the surface tension first decreased slightly meanwhile remaining optically clear until it began to precipitate. When the precipitation occurred, the surface tension stabilized. In order to understand the nature of the surface tension decrease we constructed the Gibbs adsorption isotherm that shows whether the ions are adsorbed at the air-liquid interface or repelled from the surface.

The Gibbs adsorption for the mixture of the KOH dissolved in water was found to be negative, that implies that the ions are repelled from the surface, thus increasing the surface tension with the increase of the KOH concentration. Yet, when the tungsten ions using electropolishing were added to the electrolyte consisting of the KOH dissolved in water, the Gibbs adsorption of the mixture was found to be positive. This leads to the conclusion that the tungstate ions are attracted to the air-liquid interface and are adsorbed at the surface, hence decreasing the surface tension of the mixture. We also found that the ions are densely packed at the surface in the multicomponent mixture. When the

concentration of tungstate ions reaches the 0.2M, the ions start to precipitate thereby leaving the air-liquid interface and accumulating in the bulk. This restores the initial composition of the air-liquid interface.

Characterization of the precipitates revealed that the precipitates are possibly consisting of amorphous tungsten hydrates. X-ray diffraction revealed the amorphous nature of the precipitates and energy dispersive X-ray spectroscopy showed the presence of the oxygen in the sample. Finally, thermal analysis revealed the presence of the structurally bounded water that lead to the conclusion that the precipitates consist of some type of tungsten hydrate.

Furthermore, the flow kinetics of the reaction products in the form of viscous fluid flowing downwards along the tungsten wire was studied to define their properties. It was found that the difference in density of the fluid consisting of reaction products and the surrounding electrolyte is $\Delta\rho_{\max} = 28.59 \pm 3.6 kg/m^3$ with interfacial tension of $\sigma \approx 0.34 mN/m$. We also found the viscosity of the jet as $\eta = 0.0018 \pm 0.0003 Pa \cdot s$ which is almost twice higher than the viscosity of water and 1M potassium hydroxide solution. Also, using the transmission X-ray microscope tomography it was discovered that after the tungsten wire broke off during the CLE procedure and the meniscus dropped from the wire, the viscous jet was connecting the top part and the bottom, broken off parts of the wire. It showed a remarkable stability; around 2h after the reaction was stopped. The X-ray images revealed the nuclei trapped inside the jet that was estimated to have an elastic modulus equal to $73 kN/m^2$ that is similar to the elastic modulus of gel-like structures, such as alginate gels.

3.6. References

[1] Kalantarian A, Saad S M I and Neumann A W 2013 Accuracy of surface tension measurement from drop shapes: The role of image analysis *Advances in Colloid and Interface Science* **199** 15-22

[2] Chang Y Y and Lin S Y 2011 Surface tension measurement of glass melts using sessile or pendant drop methods *J. Taiwan Inst. Chem. Eng.* **42** 922-8

[3] Lee J Y and Hildemann L M 2014 Surface tensions of solutions containing dicarboxylic acid mixtures *Atmos. Environ.* **89** 260-7

[4] Lorand R, Miklos M, Judit T, Zsofia K and Lajos N 2014 A comparison of contact angle measurement results obtained on bare, treated, and coated alloy samples by both dynamic sessile drop and Wilhelmy method *Period. Polytech.-Chem. Eng.* **58** 53-9

[5] Ghatee M H and Ghazipour H 2014 Highly accurate liquid-liquid interfacial tension measurement by a convenient capillary apparatus *Fluid Phase Equilib.* **377** 76-81

[6] Adamson A W 1990 *Physical chemistry of surfaces* (New York: A Wiley-Interscience publication)

[7] Ali K, Anwar ul H, Bilal S and Siddiqi S 2006 Concentration and temperature dependence of surface parameters of some aqueous salt solutions *Colloid Surf. A-Physicochem. Eng. Asp.* **272** 105-10

[8] Wang P M, Anderko A and Young R D 2011 Modeling surface tension of concentrated and mixed-solvent electrolyte systems *Ind. Eng. Chem. Res.* **50** 4086-98

[9] Markin V S and Volkov A G 2002 Quantitative theory of surface tension and surface potential of aqueous solutions of electrolytes *J. Phys. Chem. B* **106** 11810-7

[10] Marcus Y 2010 Surface tension and aqueous electrolytes and ions *J. Chem. Eng. Data* **55** 3641-4

[11] Li Z, Lu B C-Y 2001 Surface tension of aqueous eletrolyte solutions at high concentrations-representation and prediction *Chemical Engineering Science* **56** 2879-88

[12] Slavchov R I and Novev J K 2012 Surface tension of concentrated electrolyte solutions *J Colloid Interf Sci* **387** 234-43

[13] Mysels K J 1986 Surface-tension of solutions of pure sodium dodecyl-sulfate *Langmuir* **2** 423-8

[14] Shah A U A, Ali K and Bilal S 2013 Surface tension, surface excess concentration, enthalpy and entropy of surface formation of aqueous salt solutions *Colloid Surf. A-Physicochem. Eng. Asp.* **417** 183-90

[15] Ali K, Shah A, Bilal S and Azhar ul H 2008 Thermodynamic parameters of surface formation of some aqueous salt solutions *Colloid Surf. A-Physicochem. Eng. Asp.* **330** 28-34

[16] Ali K, Shah A and Bilal S 2009 Surface tensions and thermodynamic parameters of surface formation of aqueous salt solutions: III. Aqueous solution of KCl, KBr and KI *Colloid Surf. A-Physicochem. Eng. Asp.* **337** 194-9

[17] Drzymala J and Lyklema J 2012 Surface tension of aqueous electrolyte solutions. Thermodynamics *J Phys Chem A* **116** 6465-72

[18] Matubayasi N 2014 *Surface tension and related thermodynamic quantities of aqueous electrolyte solutions* vol 157 (CRC Press Taylor&Francis Group)

[19] Weissenborn P K and Pugh R J 1995 Surface-tension and bubble coalescence phenomena of aqueous-solutions of electrolytes *Langmuir* **11** 1422-6

[20] Mucha M, Frigato T, Levering L M, Allen H C, Tobias D J, Dang L X and Jungwirth P 2005 Unified molecular picture of the surfaces of aqueous acid, base, and salt solutions *J. Phys. Chem. B* **109** 7617-23

[21] Jungwirth P and Tobias D J 2006 Specific ion effects at the air/water interface *Chem. Rev.* **106** 1259-81

[22] Liu M Y, Beattie J K and Gray-Weale A 2012 The surface relaxation of water *J. Phys. Chem. B* **116** 8981-8

[23] Manciu M and Ruckenstein E 2003 Specific ion effects via ion hydration: I. Surface tension *Advances in Colloid and Interface Science* **105** 63-101

[24] Frumkin A N I, Z.A.; Gerovich M A 1956 K voprosu o raznosti potentsialov na granitse voda gas *Zhurnal fizicheskoi khimii* **30** 1455-68

[25] Randles J E B 1977 Structure at the free surface of water and aqueous electrolyte solutions *Physics and Chemistry of Liquids* **7** 107-79

[26] Randles J E B and Schiffri D J 1965 Temperature-dependence of surface potential of aqueous electrolytes *J. Electroanal. Chem.* **10** 480-&

[27] Trasatti S 1974 Relative and absolute electrochemical quantities-components of potential difference across electrode-solution interface *Journal of the Chemical Society-Faraday Transactions I* **70** 1752-68

[28] Borazio A, Farrell J R and McTigue P 1985 Charge-distribution at the gas water interface- the surface-potential of water *J. Electroanal. Chem.* **193** 103-12

[29] Nihonyanagi S, Ishiyama T, Lee T, Yamaguchi S, Bonn M, Morita A and Tahara T 2011 Unified molecular view of the air/water interface based on experimental and theoretical chi((2)) spectra of an isotopically diluted water surface *Journal of the American Chemical Society* **133** 16875-80

[30] Chaplin M 2009 Theory vs experiment: what is the surface charge of water? *Water Journal* **1** 1-28

[31] Horinek D, Herz A, Vrbka L, Sedlmeier F, Mamatkulov S I and Netz R R 2009 Specific ion adsorption at the air/water interface: The role of hydrophobic solvation *Chem. Phys. Lett.* **479** 173-83

[32] dos Santos A P, Diehl A and Levin Y 2010 Surface tensions, surface potentials, and the hofmeister series of electrolyte solutions *Langmuir* **26** 10778-83

[33] Petersen P B, Johnson J C, Knutsen K P and Saykally R J 2004 Direct experimental validation of the Jones-Ray effect *Chem. Phys. Lett.* **397** 46-50

[34] Langmuir I 1938 Repalsive forces between charged surfaces in water, and the cause of the Jones-Ray effect *Science (New York, N.Y.)* **88** 430-2

[35] Petersen P B and Saykally R J 2005 Adsorption of ions to the surface of dilute electroyte solutions: The Jones-Ray effect revisited *Journal of the American Chemical Society* **127** 15446-52

[36] Dole M 1938 A theory of surface tension of aquous solutions **60**

[37] Jones G R, Ray W A 1935 The surface thension of solutions *J. Am. Chem. Soc.* **57** 957-8

[38] Jones G R, Ray W A 1937 The surface tension of solutions of electrolytes as a function of the concentration. I. A differential method for measuring relative surface tension *J. Am. Chem. Soc.* **59** 187-98

[39] Jones G R, Ray W A 1941 The surface tension of solutions of electrolytes as a function of the concentration. II* **63** 288-94

[40] Jones G R, Ray W A 1941 The surface tension of solutions of electrolytes as a function of the concentration. III. Sodium Chloride *J. Am. Chem. Soc.* **63** 3262-3

[41] Jones G R, Ray W A 1942 The surface tension of solutions of electrolytes as a function of the concentration. IV. Magnesium Sulfate *J. Am. Chem. Soc.* **64** 2744-5

[42] Karraker K A and Radke C J 2002 Disjoining pressures zeta potentials and surface tensions of aqueous non-ionic surfactant/electrolyte solutions: theory and comparison to experiment *Advances in Colloid and Interface Science* **96** 231-64

[43] Malik W U, Jain A K, Siddiqui M J 1976 Interaction of cationic surfactants with polytungstate *Indian J. Chem.* **15A** 346-7

[44] Langmuir D 1997 *Aqueous Environmental Geochemistry* (Prentice-Hall, Inc.)

[45] Keizo Ogino M A 1992 *Mixed Surfactant Systems* (New York: Marcel Dekker, Inc.)

[46] Ralston J and Healy T W 1973 Specific cation effects on water structure at air-water and air-octadecanol, monolayer-water interfaces *J Colloid Interf Sci* **42** 629-44

[47] Motomura K, Ando N, Matsuki H and Aratono M 1990 Thermodynamic studies on adsorption at interfaces. 7. Adsorption and micelle formation of binary surfactant mixtures *J Colloid Interf Sci* **139** 188-97

[48] Motomura K, Iyota H, Ikeda N and Aratono M 1988 Thermodynamic studies on adsorption at interfaces. 6. Interface between cyclohexane benzene mixture and water *J Colloid Interf Sci* **126** 26-36

[49] Motomura K, Iwanaga S I, Yamanaka M, Aratono M and Matuura R 1982 Thermodynamic studies on adsorption at interfaces. 5. Adsorption from micellar solution *J Colloid Interf Sci* **86** 151-7

[50] Motomura K, Iwanaga S I, Hayami Y, Uryu S and Matuura R 1981 Thermodynamic studies on adsorption at interfaces. 4. Dodecylammonium chloride at water-air interface *J Colloid Interf Sci* **80** 32-8

[51] Motomura K, Aratono M, Matubayasi N and Matuura R 1978 Thermodynamic studies on adsorption at interfaces. 3. Sodium dodecyl-sulfate at water-hexane interface *J Colloid Interf Sci* **67** 247-54

[52] Motomura K 1978 Thermodynamic studies on adsorption at interfaces. 1. General formulation *J Colloid Interf Sci* **64** 348-55

[53] Motomura K, Matubayasi N, Aratono M and Matuura R 1978 Thermodynamic studies on adsorption at interfaces. 2. One surface-active component system-tetradecanol at hexane-water interface *J Colloid Interf Sci* **64** 356-61

[54] Matsuki H, Ando N, Aratono M and Motomura K 1989 Adsorption at water air interface and micelle formation of decylammonium bromide and decylammonium chloride mixture *Bull. Chem. Soc. Jpn.* **62** 2507-11

[55] Matubayashi N, Yamaguchi S, Yamamoto K and Matsuo H 1999 Thermodynamic quantities of surface formation of aqueous electrolyte solutions - II. Mixed aqueous solutions of NaCl and MgCl2 *J Colloid Interf Sci* **209** 403-7

[56] Matubayasi N, Takayama K, Ito R and Takata R 2011 Thermodynamic quantities of surface formation of aqueous electrolyte solutions X. Aqueous solution of 2:1 valence-type salts *J Colloid Interf Sci* **356** 713-7

[57] Matubayasi N, Takayama K and Ohata T 2010 Thermodynamic quantities of surface formation of aqueous electrolyte solutions IX. Aqueous solutions of ammonium salts *J Colloid Interf Sci* **344** 209-13

[58] Matubayasi N, Tsuchihashi S and Yoshikawa R 2009 Thermodynamic quantities of surface formation of aqueous electrolyte solutions VIII. Aqueous solutions of sulfates salts *J Colloid Interf Sci* **329** 357-60

[59] Matubayasi N and Yoshikawa R 2007 Thermodynamic quantities of surface formation of aqueous electrolyte solutions - VII. Aqueous solution of alkali metal nitrates LiNO3, NaNO3, and KNO3 *J Colloid Interf Sci* **315** 597-600

[60] Matubayasi N, Yamamoto K, Yamaguchi S I, Matsuo H and Ikeda N 1999 Thermodynamic quantities of surface formation of aqueous electrolyte solutions - III. Aqueous solutions of alkali metal chloride *J Colloid Interf Sci* **214** 101-5

[61] Matubayashi N, Matsuo H, Yamamoto K, Yamaguchi S and Matuzawa A 1999 Thermodynamic quantities of surface formation of aqueous electrolyte solutions - I. Aqueous solutions of NaCl, MgCl2, and LaCl3 *J Colloid Interf Sci* **209** 398-402

[62] Karov Z G, Khochuev I Y, Lepeshkov I N, Karaeva L I 1989 Solubility and certain properties of the saturated solutions in the K2WO4-KOH-H2O system at 25C *Russian Journal of Inorganic Chemistry* **34** 1681-4

[63] Korotchenko N A, T A D, Bogdanov G A and Zakharkina L I 1975 The K2WO4-H2O system *Russian Journal of Inorganic Chemistry* **20** 1241-3

[64] Costa Akerlof P B 1941 The density of aqueous solutions of potassium hydroxide *J. Am. Chem. Soc.* **63** 1085-8

[65] Corporation O Viscosity (cps) of cqueous KOH (wt%) solutions https://koh.olinchloralkali.com/TechnicalInformation/default.aspx

[66] Database of Ionic Radii. Hosted by the Atomistic Simulation Group in the Materials Department of Imperial College http://abulafia.mt.ic.ac.uk/shannon/ptable.php

[67] Walther J V 2005 *Essentials of Geochemistry* (Sudbury, Massachusetts: Jones and Bartlett Publishers)

[68] Zhang L, Tang X C, Lu Z G, Wang Z M, Li L X and Xiao Y H 2011 Facile synthesis and photocatalytic activity of hierarchical WO3 core-shell microspheres *Appl Surf Sci* **258** 1719-24

[69] Nithya V D, Selvan R K, Vasylechko L and Sanjeeviraja C 2014 Surfactant assisted sonochemical synthesis of Bi2WO6 nanoparticles and their improved electrochemical properties for use in pseudocapacitors *RSC Adv.* **4** 4343-52

[70] Yan A H, Xie C S, Zeng D W, Cai S Z and Hu M L 2010 Synthesis, formation mechanism and sensing properties of WO3 hydrate nanowire netted-spheres *Materials Research Bulletin* **45** 1541-7

[71] Cao J, Luo B D, Lin H L, Xu B Y and Chen S F 2012 Thermodecomposition synthesis of WO3/H2WO4 heterostructures with enhanced visible light photocatalytic properties *Appl. Catal. B-Environ.* **111** 288-96

[72] Gotic M, Ivanda M, Popovic S and Music S 2000 Synthesis of tungsten trioxide hydrates and their structural properties *Mater. Sci. Eng. B-Solid State Mater. Adv. Technol.* **77** 193-201

[73] Mokrejs P, Langmaier F, Janacova D, Mladek M, Kolomaznik K and Vasek V 2009 Thermal study and solubility tests of films based on amaranth flour starch-protein hydrolysate *Journal of Thermal Analysis and Calorimetry* **98** 299-307

[74] Shveikin G P and Kedin N A 2014 Products of carbothermal reduction of tungsten oxides in argon flow *Russian Journal of Inorganic Chemistry* **59** 153-8

[75] Gialanella S, Girardi F, Ischia G, Lonardelli I, Mattarelli M and Montagna M 2010 On the goethite to hematite phase transformation *Journal of Thermal Analysis and Calorimetry* **102** 867-73

[76] Stoilova D and Koleva V 1995 Thermal dehydration of magnesium selenate hydrates *Thermochimica Acta* **255** 33-8

[77] Stoilova D and Koleva V 1997 TG, DTA, DSC and X-ray powder diffraction studies on some nickel selenate hydrates *Thermochimica Acta* **290** 85-91

[78] Ahmadi M, Sahoo S, Younesi R, Gaur A P S, Katiyar R S and Guinel M J F 2014 WO3 nano-ribbons: their phase transformation from tungstite (WO3 center dot H2O) to tungsten oxide (WO3) *Journal of Materials Science* **49** 5899-909

[79] Marashi M S, Khaki J V and Zebarjad S M 2012 Comparing thermal and mechanochemical decomposition of ammonium paratungstate (APT) *International Journal of Refractory Metals & Hard Materials* **30** 177-9

[80] Yang Liu Q L, Shian Gao and Jian Ku Shang 2014 Template-free solvothermal synthesis of WO3/WO3·H2O hollow spheres and their enhanced photocatalytic activity from the mixture phase effect *CrystEngComm* **16** 7493-501

[81] Kulakov M, Luzinov I and Kornev K G 2009 Capillary and surface effects in the formation of nanosharp tungsten tips by electropolishing *Langmuir* **25** 4462-8

[82] Ibe J P, Bey P P, Brandow S L, Brizzolara R A, Burnham N A, Dilella D P, Lee K P, Marrian C R K and Colton R J 1990 On the electrochemical etching of tips for scanning tunneling microscopy *J Vac Sci Technol A* **8** 3570-5

[83] Melmed A J 1991 The art and science and other aspects of making sharp tips *J Vac Sci Technol B* **9** 601-8

[84] Davydov A D, Grigin A P, Shaldaev V S and Malofeeva A N 2002 Limiting current of tungsten electrochemical dissolution under conditions of natural convection - Vertical plane electrode *J Electrochem Soc* **149** E6-E11

[85] Nave M, Rubin B, Maximov V, Creager S and Kornev K G 2013 Transport-limited electrochemical formation of long nanosharp probes from tungsten *Nanotechnology* **24** 355702

[86] Natterer F 2001 *The Mathematics of Computerized Tomography* (New York: Wiley)

[87] Papajova E, Bujdos M, Chorvat D, Stach M and Lacik I 2012 Method for preparation of planar alginate hydrogels by external gelling using an aerosol of gelling solution *Carbohydr. Polym.* **90** 472-82

[88] Darnell M C, Sun J Y, Mehta M, Johnson C, Arany P R, Suo Z G and Mooney D J 2013 Performance and biocompatibility of extremely tough alginate/polyacrylamide hydrogels *Biomaterials* **34** 8042-8

4. ELECTROCHEMICAL DISSOLUTION OF TUNGSTEN IN AQUEOUS SOLUTIONS

4.1. Introduction

In Chapter 2 we reviewed thermodynamic stability of tungsten compounds in aqueous solutions. Now it is important to show how tungsten and its compounds, immersed in an aqueous solution, behave upon application of an external electric field.

Electrochemical behavior of metals in aqueous solutions can be described by the Nernst equation that ties together the Gibbs free energy or chemical potential with the electrode potential, pH, concentration, pressure and temperature[1-5]. It allows determine which species are thermodynamically stable at specific electrochemical conditions.

It is important to note that the pH value considered in thermodynamics corresponds to the pH value of the solution belonging to a boundary layer sitting in direct contact with the metal surface. It is also called local or surface pH. The local pH of the solution at the surface of the metal may be different from the pH in the bulk, especially during a localized corrosion. The local pH usually increases at the reducing electrode and decreases at the oxidizing electrode, where oxides and hydroxides are formed [6].

The first studies and plots showing the relationship between pH and electrode potential were published during 1920s by W.M. Clark. In 1930s Marcel Pourbaix began to work on potential-pH diagrams, writing a doctoral dissertation on this topic followed

by the release of a book in 1963, “Atlas of electrochemical equilibria in aqueous solutions”[6]. In this book, a theory of electrochemical thermodynamics along with the development of methods used to establish the potential-pH diagrams were reviewed and diagrams of 90 chemical elements were presented. After that the potential-pH diagrams were also called the Pourbaix diagrams. In 2010 G. K. Schweitzer and L.L. Pesterfield published a book “The Aqueous Chemistry of the Elements” [7] with updated explanation of how to construct and read the Pourbaix diagrams along with the details of employment of the precipitation and complexion agents. They revised the Pourbaix diagrams for different elements. Previously omitted compounds were added. A number of different studies that employ the Pourbaix diagrams were published, but the majority of the Pourbaix diagrams are plotted in 2D [1-4, 8, 9] in terms of potential Eh versus pH dependence. The 3D diagrams are much less common in the literature [10, 11].

First 3D diagram was presented by W.M. Clark in 1928 where he plotted potential versus pH versus percent oxidation. In 1965 R.M. Garrels and C.L. Christ[12] presented the plots of potential-pH versus pressure in their book called “Solutions, Minerals, and Equilibria”. In 1980, K.R. Bullock published a paper plotting potential-pH versus anion activity [11]. Finally, in 2012 G.K. Schweitzer and his associates published a highly informative paper describing in details the methods to calculate and plot potential-pH versus concentration of soluble species [10]. They recognized the importance and convenience of the 3D diagrams and presented rotatable diagrams for Mg, Al, Fe.

There are several numerical methods [13-17] and software available to construct these plots in 2D such as: FactSage^{TM} (available for online construction of potential-pH

diagram), The Geochemist's Workbench®10 from Aqueous Solutions LLC and ect. Also, an online tutorial was built by DoITPoMS of University of Cambridge representing some theoretical material and information on building of 3D diagrams [18].

In this Chapter, thermodynamics of an electrochemical reaction and method of constructing the Pourbaix diagram is reviewed and the 3D Pourbaix diagrams for tungsten in aqueous solutions are presented. The 3D diagrams were built in Wolfram Mahtematica® program. L.L. Pesterfield and J.B. Maddox provided the original code and we modified it for the tungsten case.

4.2. Thermodynamics of an electrochemical cell and the Nernst equation

An electrochemical cell consists of two half-cells. A half-cell consists of a conductive electrode immersed into an electrolyte. The electrolyte can be either solid or liquid where ions can migrate. When the electric potentials are applied to the metal electrodes as shown in Figure 4.1, the metal surfaces are charged. As a result, an electrochemical reaction is initiated at the metal surfaces. This reaction facilitates a charge-transfer from electrons in the metals to ions in the electrolyte. As a result, the charge continues to flow from one electrode to the other through the electrolyte. Therefore, the circuit consisting of a sequence of electrode-electrolyte-electrode-battery is closed. In the course of these reactions one electrode, where the oxidation reaction occurs, loses electrons. Oxidation reaction is called the anodic reaction and proceeds giving up electrons and increasing the oxidation state of the metal (see the right hand side

in Figure 4.1). Another electrode where the reduction reaction occurs, acquires these electrons. The reduction reaction is also called the cathodic reaction and it proceeds by accepting the electrons and decreasing the oxidation state of hydrogen. This is shown in Figure 4.1. The **red**uction/**ox**idation reaction is called the redox reaction.

Figure 4.1 shows an example of electrochemical cell with two half-cells where two half reactions, reduction and oxidation reactions, respectively, occur. In order to support these reactions and current, the metals have to be held at the potential which is different from that of the surrounding electrolyte. The potential of the cathode relative to that of the electrolyte is called a reduction (cathodic) potential E_c and the potential of the anode relative to the that of the electrolyte is called an oxidation (anodic) potential E_a. The summation of these two potentials will give an overall cell potential $E_{cell} = E_c + E_a$.

While an overall cell potential E_{cell} can be measured with a voltmeter, the individual potentials of the electrodes cannot be measured directly. Therefore, in order to determine the individual potential of electrodes, a non-reactive electrode with a well-defined reference potential has to be applied. The electrode with a stable and defined potential is called the reference electrode.

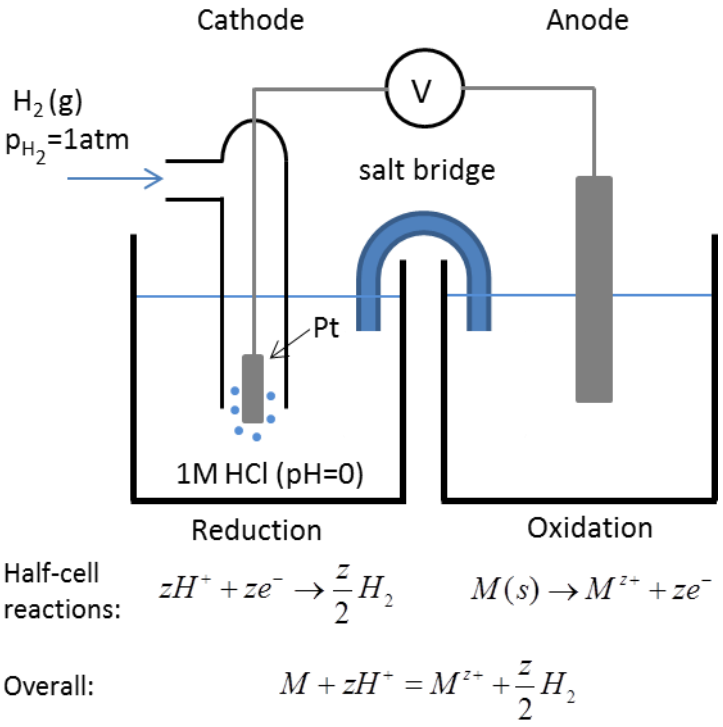

Figure 4.1. The equilibrium reaction between a metal M and hydrogen, where z is the stoichiometric coefficient of hydrogen ions participating in the reaction. Here on a left hand side the SHE electrode is presented and on the right hand side the electrode with unknown potential. The HCl is chosen as an example of an electrolyte with 1M molar concentration and pH0.

One example of a reference electrode is the standard hydrogen electrode (SHE) that is used to determine standard equilibrium potentials and it consists of a platinum wire immersed in an acidic electrolyte with H^+ activity of 1mol/L (pH0) and hydrogen gas bubbling around it at 1 atm. pressure and its potential is set to be 0V (Figure 4.1). Electrodes with more oxidizing properties with respect to the hydrogen electrode were assigned to have a "+" sign, while electrodes with more reducing properties have a "-" sign. This means that the electrodes with a higher value of the standard reduction potential accept electrons easier.

A standard reduction potential is introduced as follows. The standard reduction potential E^0 is a potential of the electrode under the standard conditions, when the reacting metal is assumed "pure" without any dopants and a pressure for each fluid involved in the reaction is p = 1 atm., the temperature T=25°C and activity of all dissolved species is equal to 1. It can be also called the standard equilibrium potential and the standard electrode potential. The standard equilibrium potential can be determined by two ways: experimentally and theoretically. In order to determine E^0 experimentally, the electrode of interest should be coupled with a reference electrode (half-cell) with a known potential.

When an electrochemical cell consists of two electrodes that are not the reference electrodes, the potential of a half cell electrode $E_{half-cell}$ that is different from the standard cannot be measured: both potentials change during chemical reactions. For this reason a third electrode reference electrode is introduced in the system and coupled with the electrode of interest. In Figure 4.2 a schematic of a three electrode system is shown. The working electrode (WE) is an electrode of interest where the reactions occur. The counter electrode (CE) supports the current flowing between the CE and WE; it is made of non-reactant material, for example Pt wire. The reference electrode (RE) is the electrode with a known and stable potential that is coupled with the WE, but does not support current through it. Its purpose is to measure and control the potential of the WE. The potential of the electrode measured relative to a SHE as the reference electrode is denoted Eh. The potential measured against any other reference electrode can be recalculated to the SHE electrode. There are many reference electrodes with different parameters, but the most

popular are the silver chloride electrode, Ag/AgCl ($Eh = +\ 0.197V$ saturated), the saturated calomel electrode SCE ($Eh = +0.241V$) and the copper-copper (II) sulfate electrode CSE ($Eh = +0.314V$).

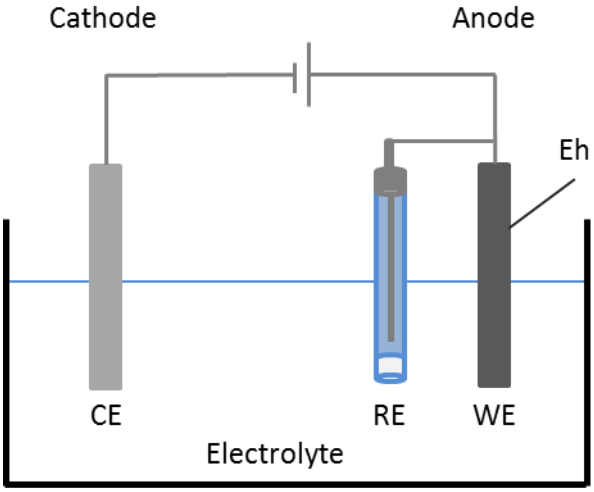

Figure 4.2. Three-electrodes system, where CE is a counter electrode, RE – reference electrode, WE – working electrode, Eh is a potential of the WE against SHE.

In order to obtain a relation between the physico-chemical parameters of the reaction and its potential, we employ the Nernst equation.

Consider the following equilibrium half-cell reaction:

$$aA + mH^{+} + ne^{-} = bB + cH_2O, \tag{4.1}$$

where A represents a metallic ion (oxidized species), B represents a corresponding metal (reduced species), e^- is an electron, H_2O - water, and H^+ - hydrogen ion; a,m,n,b,c are the stoichiometric coefficients. A and B also can represent the dissolved species, oxides or hydroxides.

The equilibrium potential E_e is a potential at which reactants and products of the reaction are in equilibrium between each other. In equilibrium, the potential E_e can be associated with the Gibbs free energy ΔG through the fundamental equation:

$$\Delta G = -nFE_e, \tag{4.2}$$

where n is the amount of electrons involved in the reaction and F=96485 C/mol is Faraday's constant. Equation (4.2) assumes that the energy consumed in the reaction comes from the energy of electrode charging.

Energy change is correlated with the temperature, pressure and activities of reacting species. To compare the energy change it is required to compare them under the same conditions. In thermodynamics this reference state is defined as a standard state.

Therefore, the relationship between the standard equilibrium potential and standard Gibbs free energy will be as follows:

$$\Delta G^0 = -nFE^0 \tag{4.3}$$

As we know from Chapter 2 the Gibbs free energy can be expressed in the following form:

$$\Delta G = \Delta G^0 + RT \ln \frac{[B]^b [H_2O]^c}{[A]^a [H^+]^m}, \tag{4.4}$$

where square brackets [ ], as defined in Chapter 2, represent the molar concentration of the species in the brackets over standard molar concentration, $[i]=C_i/1M$.

Now using equations (4.2) and (4.3)we can rewrite eq. (4.4) as:

$$-nFE_e = -nFE^0 + RT \ln \frac{[B]^b [H_2O]^c}{[A]^a [H^+]^m}, \tag{4.5}$$

or

$$E_e = E^0 - \frac{RT}{nF} \ln \frac{[B]^b [H_2O]^c}{[A]^a [H^+]^m} \tag{4.6}$$

Since $\ln X = 2.303 \log_{10} X$ we can rewrite eq. (4.6) in the form:

$$E_e = E^0 - \frac{2.303RT}{nF} \log \frac{[B]^b [H_2O]^c}{[A]^a [H^+]^m} \tag{4.7}$$

Also, introducing the acidity metric as:

$$pH = -\log[H^+] \tag{4.8}$$

Equation (4.7) is rewritten as:

$$E_e = E^0 - \frac{2.303RT}{nF} \log \frac{[B]^b}{[A]^a} - \frac{2.303RTm}{nF} pH \tag{4.9}$$

At room temperature T=298.15°K, equation (4.9) can be simplified to:

$$E_e = E^0 - \frac{0.059V}{n} \log \frac{[B]^b}{[A]^a} - \frac{(0.059V) \cdot m}{n} pH, \tag{4.10}$$

where V is the unit of the potential (volt) and E^0 is written as follows:

$$E^0 = -\frac{\Delta G^0}{nF} = -\frac{(b\bar{G}_B^0 + c\bar{G}_{H_2O}^0) - (a\bar{G}_A^0 + m\bar{G}_{H^+}^0)}{nF} \tag{4.11}$$

For the reactions that do not require application of a potential, the Nernst equation can be rewritten as:

$$\log \frac{[B]^b}{[A]^a} = \log K + mpH, \tag{4.12}$$

where logK is expressed as follows:

$$\log K = \frac{\Delta G^0}{-2.303RT} \tag{4.13}$$

At temperature T=298.15°K, equation (4.13) can be simplified to:

$$\log K = \frac{\Delta G^0}{-5.71kJ / mol} \tag{4.14}$$

4.3. Pourbaix diagrams

4.3.1. Basic rules for constructing Pourbaix diagrams

In order to build the Pourbaix diagram one needs to consider the following steps [6, 7, 18, 19]:

a) List possible species of the element of interest (tungsten W) containing one or more of its compounds: the element itself (W), oxygen-containing compound (WO_2) and hydrogen containing compound (H_2WO_4).

b) Plot the dependence of the potential Eh versus pH and arrange all species according to the following rule. In the vertical direction of the increasing potential, write the species starting from the lower end ending up at the higher oxidation number. If there are more than one species that have the same oxidation number, list them in the horizontal direction of increasing pH with the increasing hydroxylation level or decreasing protonation level of the species.

c) Write the corresponding transformation reactions involving A and B species, as a reactant and product respectively, and water, hydrogen ion and electrons. The reactions should be balanced in the following order: first balance the metal atoms

by adding stoichiometric numbers, and then balance the oxygen atoms with water (H_2O) at the appropriate side, hydrogen atoms with hydrogen ions (H^+) and charge with electrons.

d) Write the Nernst equation for each reaction and solve for Eh as a function of electrolyte pH and concentration of the soluble species. For reaction that does not involve electrons the Nernst equation should be solved for electrolyte pH as a function of concentration of the soluble species.

e) Plot the final Nernst equations in 2D[1-4, 8, 9, 20, 21] (x,y) or 3D[10, 11] (x,y,z) plot, where the potential *Eh* is plotted on the y-axis, electrolyte pH on the x-axis and concentration M of soluble species, activity, temperature or other parameters on z-axis.

4.3.2. Worked example of the Pourbaix diagram: electrolysis of water

In order to evaluate the behavior of the chemical species in aqueous solutions, one needs to take into account and define the behavior of water upon application of external potential. This example serves as an illustration of the construction of the Pourbaix diagram.

When two electrodes are immersed in water and an external potential is applied to them, an electric current starts to flow from one electrode to another. The passage of the current through the water splits the water molecule in oxygen and hydrogen gas with oxygen bubbling around a positively charged electrode and hydrogen around a negatively charged electrode. This process is called electrolysis or decomposition of water.

There are two cathodic reactions possible in water:

$$2H_2O + 2e^- = H_2 + 2OH^- \quad \text{or} \quad 2H^+ + 2e^- = H_2 \tag{4.15}$$

$$O_2 + 2H_2O + 4e^- = 4OH^- \quad \text{or} \quad O_2 + 4H^+ + 4e^- = 2H_2O \tag{4.16}$$

Using eq. (4.11) and values of the Gibbs free energies (Table 4.1) of the species one can solve the Nernst equations for these reactions. For the first reaction, the Gibbs free energies are equal to zero and therefore, the standard equilibrium potential is as follows:

$$E^0 = -\frac{\Delta G^0}{nF} = -\frac{(0 - 2 \cdot 0)\,J/mol}{2 \cdot 96485 C/mol} = 0V \tag{4.17}$$

Using eq. (4.10) the equilibrium potential can be calculated as:

$$E_e = E^0 - \frac{(0.059V) \cdot m}{n} pH = 0 - \frac{(0.059V) \cdot 2}{2} pH = -(0.059V)\,pH, \tag{4.18}$$

or

$$E_e = -(0.059V)\,pH \tag{4.19}$$

This equation can be plotted as a linear dependence of E_e on pH. Along this line, the water is in equilibrium with the dissolved hydrogen gas. Bellow this line, hydrogen gas will be the predominant species and will be thermodynamically stable relative to water. This means that hydrogen gas will evolve in the form of bubbles on the electrode, until all water evaporates.

The Nernst equation for the second reaction can be written as follows:

$$E^0 = -\frac{\Delta G^0}{nF} = -\frac{(2 \cdot (-237200) - 4 \cdot 0)\,J/mol}{4 \cdot 96485 C/mol} = 1.23V \tag{4.20}$$

The equilibrium potential is as follows:

$$E_e = E^0 - \frac{(0.059V)\cdot m}{n}\, pH = 1.23V - \frac{(0.059V)\cdot 4}{4}\, pH = \\ = 1.23V - (0.059V)\, pH, \tag{4.21}$$

or

$$E_e = 1.23V - (0.059V)\, pH \tag{4.22}$$

Equation (4.22) shows that water is in equilibrium with oxygen gas along this line, meaning that oxygen bubbles will be produced around the electrode. Above this line, the oxygen gas will be the predominant species and will be stable relative to water. In between of these two lines, water is the most thermodynamically stable compound and if dissolved hydrogen or oxygen is present they will be reduced to water.

The plotted Nernst equations (4.19) and (4.22), for the reactions (4.15) and (4.16) respectively, are shown in Figure 4.3, where we added the third z-axis for a general Nernst equation:

$$E_e = E^o - (0.059V)\, pH - \log[C] \tag{4.23}$$

This equation describes equilibrium of water in an electrochemical cell in the presence of another dissolved species of the relative concentration C.

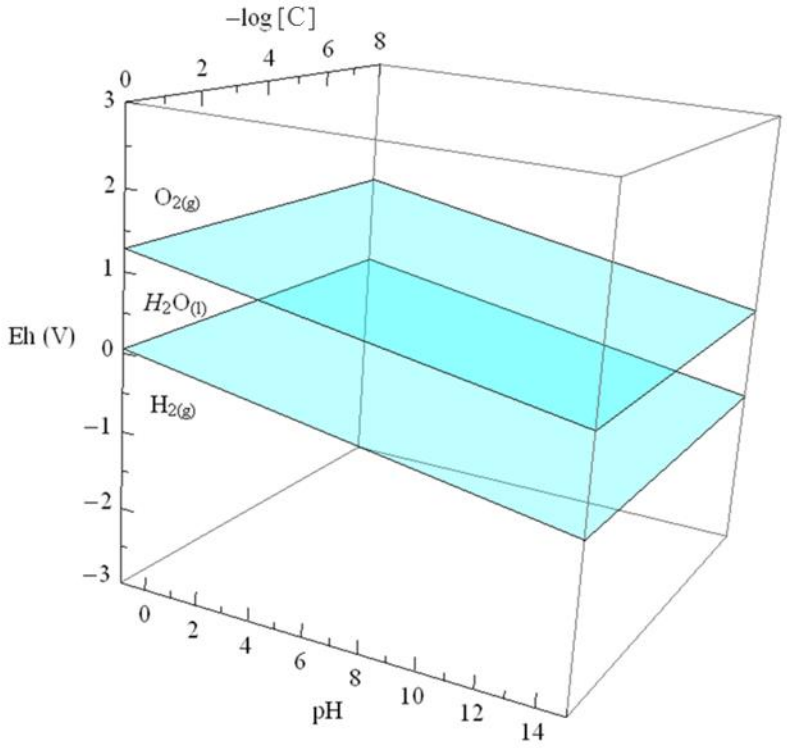

Figure 4.3. Pourbaix Eh-pH-C diagram for water, where Eh is the electrode potential measured relative to a SHE, [M] is the concentration of the dissolved species over standard concentration, pH is the negative log 10 concentration of the hydrogen ion.

In summary, the Pourbaix diagram for water, Figure 4.3, is divided in three sections. The bottom section shows that water will be cathodically electrolyzed to hydrogen gas. In the middle section, water will be the only thermodynamically stable compound. The top section shows that water can be decomposed to produce oxygen gas.

This example of the Pourbaix diagram provides the main idea of classification of different compounds with respect to their electrochemical stability. We proceed with this idea to the case of tungsten which is known to form much richer library of compounds and react with water to form oxides and hydroxides[22].

4.3.3. Pourbaix diagram (Eh-pH-C) for tungsten in aqueous solution

Tungsten is a transition metal and it exhibits various oxidations states from -2 to +8, but the most common and stable oxidation state is +6. There are several stable and unstable compounds that are usually described in the literature. The unstable compounds were not well identified and studied due to their unstable nature. The examples of these compounds are: $WO, W_4O_3, W_2O_3, W_5O_{14}$ and ect.[22]. Other oxides such as: WO_2, WO_3 are stable oxides and are well defined in the literature [23]. Tungsten dissolves to tungstate ions $WO_4^{2-}(aq)$ if submersed into an aqueous alkaline solution. Tungstate ions under neutral and acidic conditions transform into a variety of different polytungstate ions and finally precipitates as a white trioxide trihydrate $WO_3 \cdot 3H_2O(s)$. Tungsten trioxide trihydrate converts to a light pale yellow trioxide dihydrate $WO_3 \cdot 2H_2O(s)$ when loses a hydrated water molecule and finally to a yellow trioxide hydrate $WO_3 \cdot H_2O(s)$ [6]. There are also many isopolyanions transiting from one to another depending on pH of the solution. Examples of isopolyanions are [7, 22, 24]: $HW_6O_{21}^{5-}(aq)$, $H_2W_{12}O_{42}^{10-}(aq)$, $W_6O_{21}^{6-}(aq)$, $W_7O_{24}^{6-}(aq)$, $W_{12}O_{41}^{10-}(aq)$, $H_2W_{12}O_{40}^{6-}(aq)$, $W_{12}O_{39}^{6-}(aq)$, $W_{10}O_{32}^{4-}(aq)$. Thus, due to a variety of compounds that tungsten is able to form with oxygen and hydrogen, their determination, selection and classification is a very challenging task [22, 23].

Several examples of the published Eh-pH diagrams of tungsten in aqueous solution can be found in the literature [6, 8, 9, 25-29] and some of them are shown in Figure 4.4. These diagrams illustrate the lack of agreement on what diagram is the most

stable and correlates with the experimental data. For instance, Emil A. Kneer and colleagues [9] presented a diagram, shown in Figure 4.4 (c), where they consider WO_3 oxide as a more stable than its hydrated forms and introduce polytungstate ions in the diagram that were not considered before. Mustafa Anik [28] presented two diagrams (Figure 4.4 (a), (b)) in 2010 year, stating that the (a) - diagram represents a stable diagram and (b) - diagram is metastable. Anik's version of the (b) - diagram represents a version of the diagram published by M.Pourbaix [6]. In 1966 when Pourbaix published his diagram, neither the Gibbs free energy nor chemical potential of the hydrated forms of tungsten trioxide and polytungstate ions were known. The (b) - diagram was presented by several scientists [8, 25] thought the years after M. Pourbaix published his book. Yet, G.K. Schweitzer and L.L. Pesterfield [7] were the first to consider and present the diagram with $WO_3 \cdot 2H_2O$ shown in Figure 4.4 (d). The 3D diagram for tungsten was never presented in the literature due to the complexity of its construction. Therefore, we took this challenge and constructed this diagram.

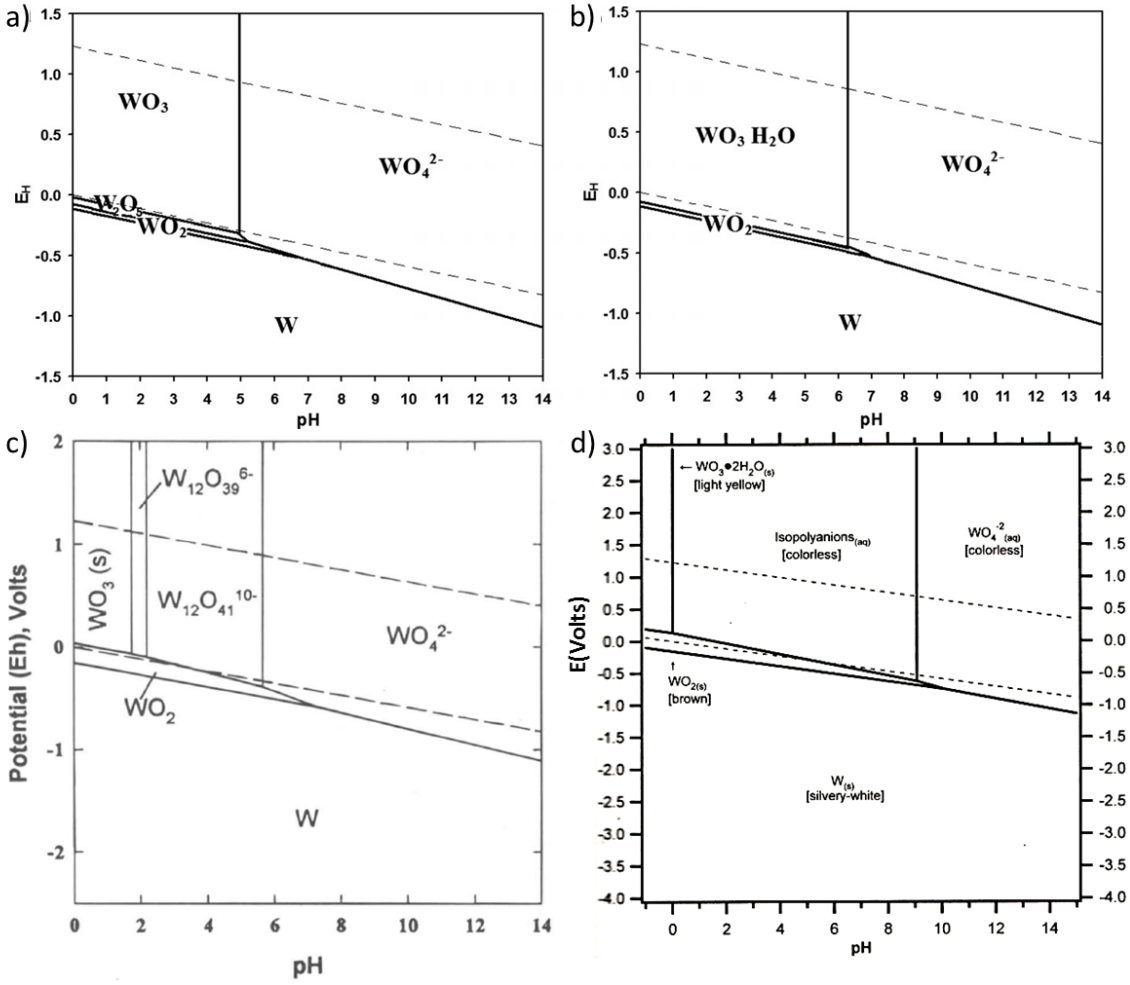

Figure 4.4. Pourbaix Eh-pH diagram for tungsten in aqueous solutions (W-H_2O) at 25°C with concentration of soluble species: (a), (b) $[WO_4^{2-}]=10^{-4}M$ [28] published in 2010, (c) $[WO_4^{2-}]=10^{-4}M$ [9] published in 1996, (d) $[WO_4^{2-}]=10^{-1}M$ [7] published in 2010.

To construct the Pourbaix diagram for tungsten, the steps listed in Section 3.2 of this Chapter were followed:

a) First, a list of possible compounds for tungsten were obtained from inorganic chemistry books and publications and listed in Table 4.1 along with the values of the Gibbs standard free energy $\bar{G}^0$.

Table 4.1. List of known tungsten compounds and water with their Gibbs free energies. (z- oxidation number, (s) - solid, (l) - liquid, (aq) - aqueous).

z	Name	Species (state)	Color	$\bar{G}^0$, (kJ/mol)	References
Solid tungsten compounds					
0	Tungsten	$W(s)$	Silvery-white	0.0	[7]
+4	Tungsten (IV) dioxide	$WO_2(s)$	Brown	-534.1	[7]
+5	Tungsten (V) "pentoxide"	$W_2O_5(s)$	Blue	-1284.1	[6]
+6	Tungsten (VI) trioxide	$WO_3(s)$	Yellow	-763.9	[7, 30]
	Tungsten (VI) trioxide monohydrate or tungstic acid	$WO_3 \cdot H_2O(s)$ or $H_2WO_4(s)$	Yellow	-1020.9	[8]
	Tungsten (VI) trioxide dihydrate	$WO_3 \cdot 2H_2O(s)$	Light/pale yellow	-1220.0	[7]
	Tungsten (VI) trioxide trihydrate or acid	$WO_3 \cdot 3H_2O(s)$ or $H_6WO_6(s)$	White	-	[6]
+8	Pertungstic acid	$H_2WO_5 \cdot H_2O(s)$ or $WO_3 \cdot H_2O_2 \cdot H_2O(s)$	-	-	[6, 22]
Dissolved tungsten compounds					
+3	Tungsten (III) ion	$WO^{3+}(aq)$	Green-yellow	-	[7]
+6	Dioxotungsten (VI)	$WO_2^{2+}(aq)$	Colorless	-502.1	[7]
	Tungstate (VI) ion	$WO_4^{2-}(aq)$	Colorless	-916.7	[7]
	Hydrogentungstate	$HWO_4^{-}(aq)$	Colorless	-938.1	[7]
	Polytungstate ion	$HW_6O_{21}^{5-}(aq)$	Colorless	-5175.6	[7]
+8	"Pertungstic" ion	$WO_5^{2-}(aq)$	Colorless	-	[6, 22]
Solution					
	Water	$H_2O(l)$		-237.2	[7]
	Hydrogen ion	$H^{+}(aq)$		0.0	[7]
	Hydroxide	$OH^{-}(aq)$		-157.3	[7]

b) Second, all species listed in Table 4.1are placed on the potential-pH diagram. First, compounds in the order of increasing oxidation number from 0 to +8 are

placed from the bottom of the diagram to the top. Then, compounds with the same oxidation numbers (+6) are arranged horizontally in the direction of increasing pH, in order of decreasing protonation or increasing hydroxylation. Note, that for the construction of our diagram, due to the volume of the isopolyanions compounds, the $HW_6O_{21}^{5-}(aq)$ compound has the lowest Gibbs free energy and will be used as an example representing the general region of isopolyanions formation. The constructed approximate diagram is presented in Figure 4.5.

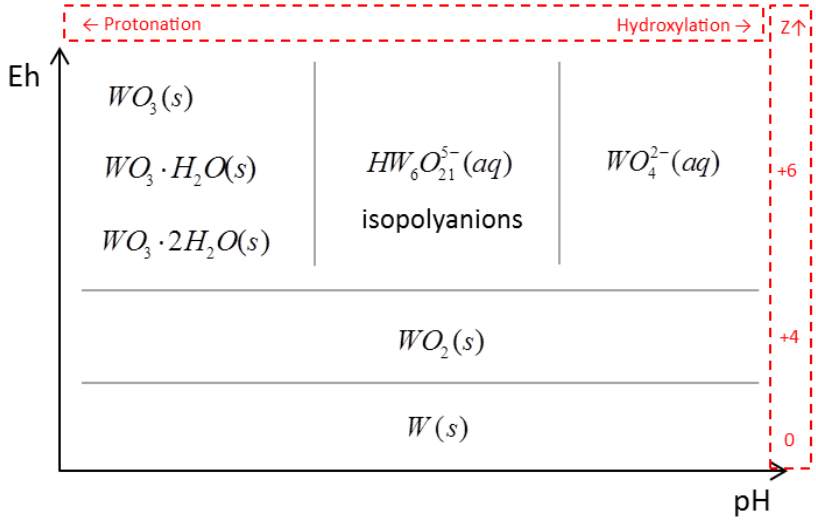

Figure 4.5. An approximate Eh-pH diagram showing potential location of the compounds on the 2D potential-pH diagram.

c) Now, electrochemical reactions for each species from Table 4.1are written according to the balance rule.

For example, for the electrochemical reaction involving tungsten oxidizing to tungsten dioxide $WO_2(s)/W(s)$ the reaction balance steps are shown below:

-Write formulas for the two substances with “equal” sign between them:

$$WO_2 ... = W ...$$

-Balance the oxygen with H_2O at the appropriate side:

$$WO_2 ... = W + 2H_2O ...$$

-Balance the hydrogen with H^+:

$$WO_2 + 4H^+ ... = W + 2H_2O ...$$

-Balance electric charges with e^-:

$$WO_2 + 4H^+ + 4e^- = W + 2H_2O$$

The rest of the balanced chemical reactions that are considered for construction of the Pourbaix diagram are presented in Table 4.2.

Table 4.2. List of species, reactions and the Nernst equations used to build the 3D Pourbaix diagram for tungsten [6-8].

№	Couple	Chemical Reaction	Nernst Equation	ΔG, (kJ/mol)
1	$WO_2(s)/W(s)$	$WO_2 + 4H^+ + 4e^- = W + 2H_2O$	$E_e = -0.15 - 0.059\,pH$	59.7
2	$WO_3(s)/WO_2(s)$	$WO_3 + 2H^+ + 2e^- = WO_2 + H_2O$	$E_e = 0.038 - 0.059\,pH$	-7.4
3	$WO_3(s)/HW_6O_{21}^{5-}(aq)$	$6WO_3 + 3H_2O = HW_6O_{21}^{5-} + 5H^+$	$5\,pH = \log[HW_6O_{21}^{5-}] + 20.92$	119.4
4	$HW_6O_{21}^{5-}(aq)/WO_4^{2-}(aq)$	$HW_6O_{21}^{5-} + 3H_2O = 6WO_4^{2-} + 7H^+$	$7\,pH = 6\log[WO_4^{2-}] - \log[HW_6O_{21}^{5-}] + 67.82$	387.0
5	$WO_3(s)/WO_4^{2-}(aq)$	$WO_3 + H_2O = WO_4^{2-} + 2H^+$	$2\,pH = \log[WO_4^{2-}] + 14.79$	84.4
6	$WO_4^{2-}(aq)/W(s)$	$WO_4^{2-} + 8H^+ + 6e^- = W + 4H_2O$	$E_e = 0.06 + 0.01\log[WO_4^{2-}] - 0.079\,pH$	-32.1
7	$WO_4^{2-}(aq)/WO_2(s)$	$WO_4^{2-} + 4H^+ + 2e^- = WO_2 + 2H_2O$	$E_e = 0.48 + 0.03\log[WO_4^{2-}] - 0.118\,pH$	-91.8
8	$HW_6O_{21}^{5-}(aq)/WO_2(s)$	$HW_6O_{21}^{5-} + 17H^+ + 12e^- = 6WO_2 + 9H_2O$	$E_e = 0.14 + 0.005\log[HW_6O_{21}^{5-}] - 0.084\,pH$	-163.8
9	$WO_3 \cdot H_2O(s)/WO_2(s)$	$WO_3 \cdot H_2O + 2H^+ + 2e^- = WO_2 + 2H_2O$	$E_e = -0.06 - 0.059\,pH$	12.4
10	$WO_3 \cdot H_2O(s)/HW_6O_{21}^{5-}(aq)$	$6(WO_3 \cdot H_2O) = HW_6O_{21}^{5-} + 3H_2O + 5H^+$	$5\,pH = \log[HW_6O_{21}^{5-}] + 41.74$	238.2
11	$WO_3 \cdot H_2O(s)/WO_4^{2-}(aq)$	$WO_3 \cdot H_2O(s) = WO_4^{2-} + 2H^+$	$2\,pH = \log[WO_4^{2-}] + 18.28$	104.2
12	$WO_3 \cdot 2H_2O(s)/WO_4^{2-}(aq)$	$WO_3 \cdot 2H_2O = WO_4^{2-} + 2H^+ + H_2O$	$2\,pH = \log[WO_4^{2-}] + 11.58$	66.1

13	$WO_3 \cdot 2H_2O(s) / WO_2(s)$	$WO_3 \cdot 2H_2O + 2H^+ + 2e^- = WO_2 + 3H_2O$	$E_e = 0.13 - 0.059\,pH$	-25.7
14	$WO_3 \cdot 2H_2O(s) / HW_6O_{21}^{5-}(aq)$	$6(WO_3 \cdot 2H_2O) = HW_6O_{21}^{5-} + 9H_2O + 5H^+$	$5\,pH = \log[HW_6O_{21}^{5-}] + 1.68$	9.6

d) Using chemical reactions from Table 4.2, the Nernst equations were solved for each reaction for the potential E_0 with respect to pH and concentration M of the dissolved species:

For example, according to the previous step, the electrochemical reaction for the reaction couple $WO_2(s) / W(s)$ is written as follows:

$$WO_2 + 4H^+ + 4e^- = W + 2H_2O \tag{4.24}$$

The standard equilibrium potential is calculated using equation (4.11) and Table 4.1 with $a = 1, b = 1, c = 2, m = 4, n = 4$ as follows:

$$E^0 = -\frac{\Delta G^0}{nF} = -\frac{(b\bar{G}_W^0 + c\bar{G}_{H_2O}^0) - (a\bar{G}_{WO_2}^0 + m\bar{G}_{H^+}^0)}{nF} = -\frac{((1\cdot 0 + 2\cdot(-237200)) - (1\cdot(-534100) + 4\cdot 0))\,J/mol}{4\cdot 96485\,C/mol} = -0.15V \tag{4.25}$$

Then using equation (4.10) an equilibrium potential is calculated as:

$$E_e = E^0 - \frac{0.059V}{n}\log\frac{[B]^b}{[A]^a} - \frac{(0.059V)\cdot m}{n}\,pH = -0.15V - \frac{0.059V}{n}\log\frac{[W]}{[WO_2]} - \frac{(0.059V)\cdot 4}{4}\,pH = -0.15V - (0.059V)\,pH \tag{4.26}$$

Therefore, the final form of Nernst equation for the pair $W(s) / WO_2(s)$ is:

$$E_e = -0.15V - (0.059V)\,pH \tag{4.27}$$

The final Nernst equations for all considered reactions are presented in Table 4.2. The more detailed derivations can be found in Appendix 4.5.

c) Finally, all Nernst equations from Table 4.2 can be plotted on a 2D or 3D graph erasing the top parts of the lines at their intersections with each other.

Figure 4.6 (a) shows the plot of the equations, taken from Table 4.2, $E_e = -0.15V - (0.059V)\,pH$ and $E_e = 0.06V + (0.01V)\log(WO_4^{2-}) - (0.079V)\,pH$ for transition pairs $WO_2(s)/W(s)$ and $WO_4^{2-}(aq)/W(s)$ respectively. The two equations intersect at a point on the diagram and the upper parts of the lines are erased for the constructing purposes. The summary of the species and corresponding conversion reactions with the derived Nernst equations are shown in Table 4.2. Using this approach all Nernst equations are plotted on the Eh-pH-M graph erasing the parts of the planes at their intersections. The resulting graph is shown in Figure 4.7.

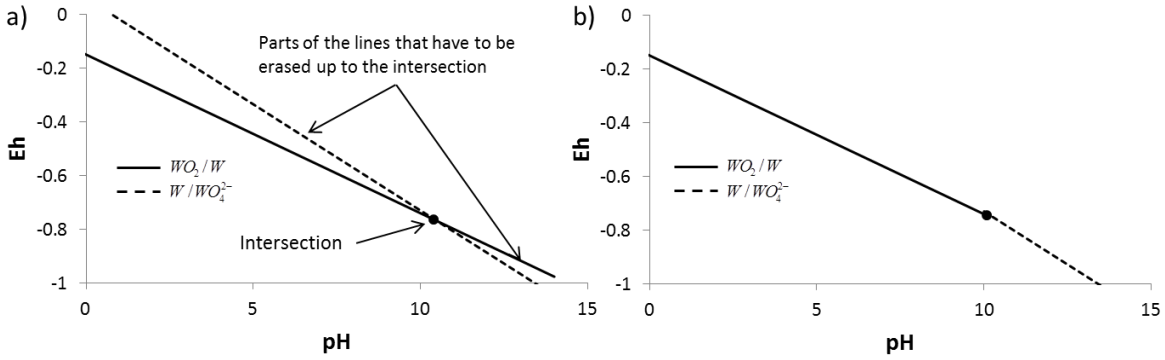

Figure 4.6. Eh-pH plot of the Nernst equations for $WO_2(s)/W(s)$ and $WO_4^{2-}(aq)/W(s)$ reaction pairs: (a) plot of the Nernst equations and (b) the graph after the line erase that is used for further construction of the Pourbaix diagram.

Three Pourbaix diagrams shown in Figure 4.7, Figure 4.8 and Figure 4.9 are constructed for tungsten, separately considering thermodynamically stable species: WO_3, $WO_3 \cdot H_2O$ and $WO_3 \cdot 2H_2O$ respectively. In these figures electrochemical potential Eh related to electrolyte characteristics represented through pH and concentration C of the dissolved species $WO_4^{2-}, HW_6O_{21}^{5-}$ in an aqueous electrolyte.

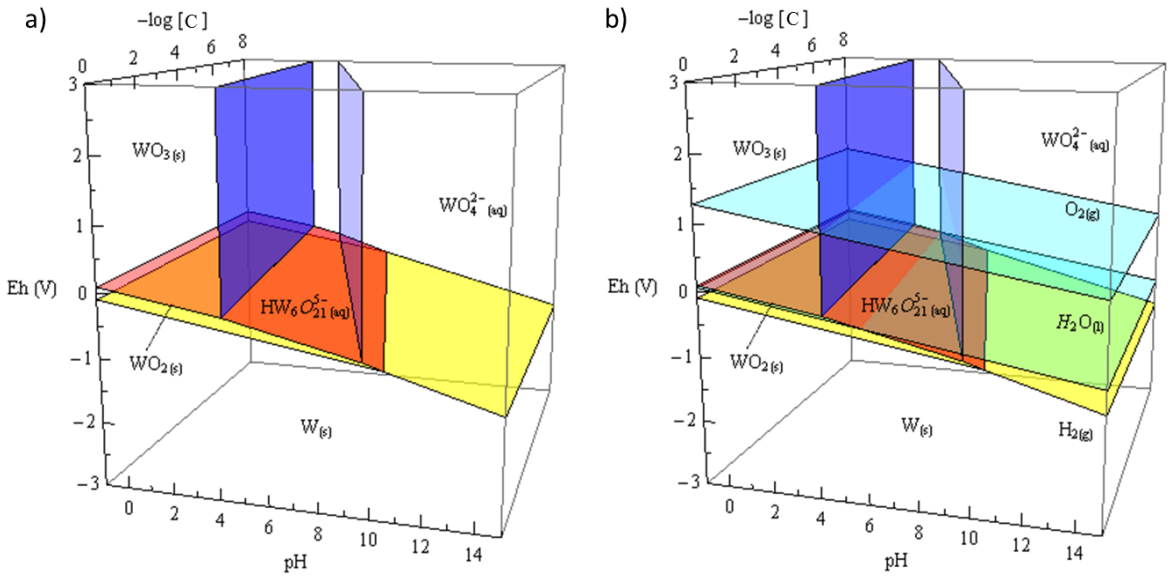

Figure 4.7. Pourbaix Eh-pH-C diagram for tungsten in aqueous solution at temperature T=298.15°K considering stability of WO_3: (a) without water stability planes, (b) with water stability planes.

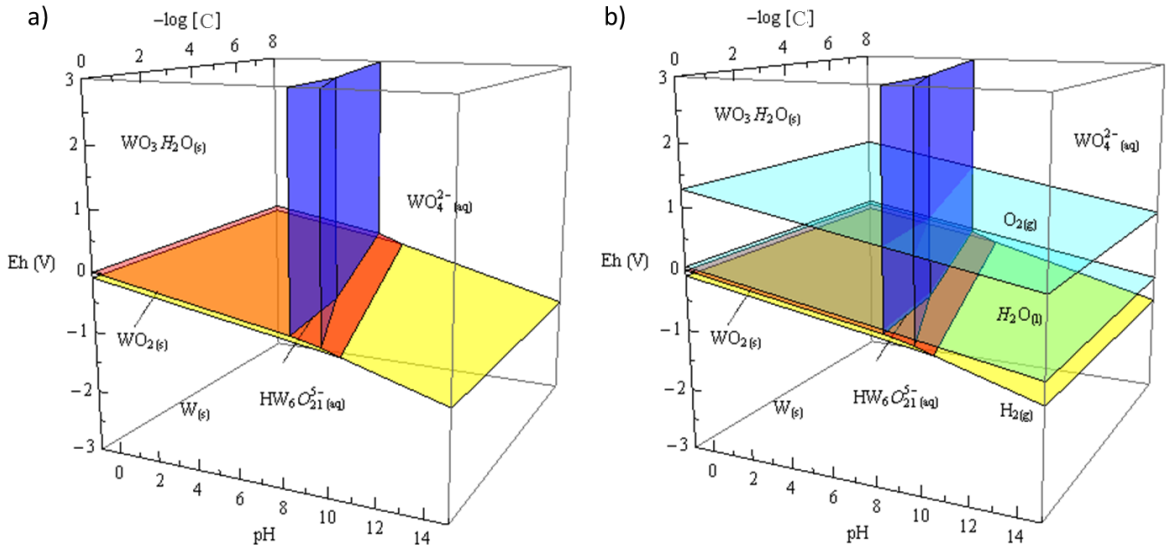

Figure 4.8. Pourbaix Eh-pH-C diagram for tungsten in aqueous solution at temperature T=298.15°K considering stability of $WO_3 \cdot H_2O$: (a) without water stability planes, (b) with water stability planes.

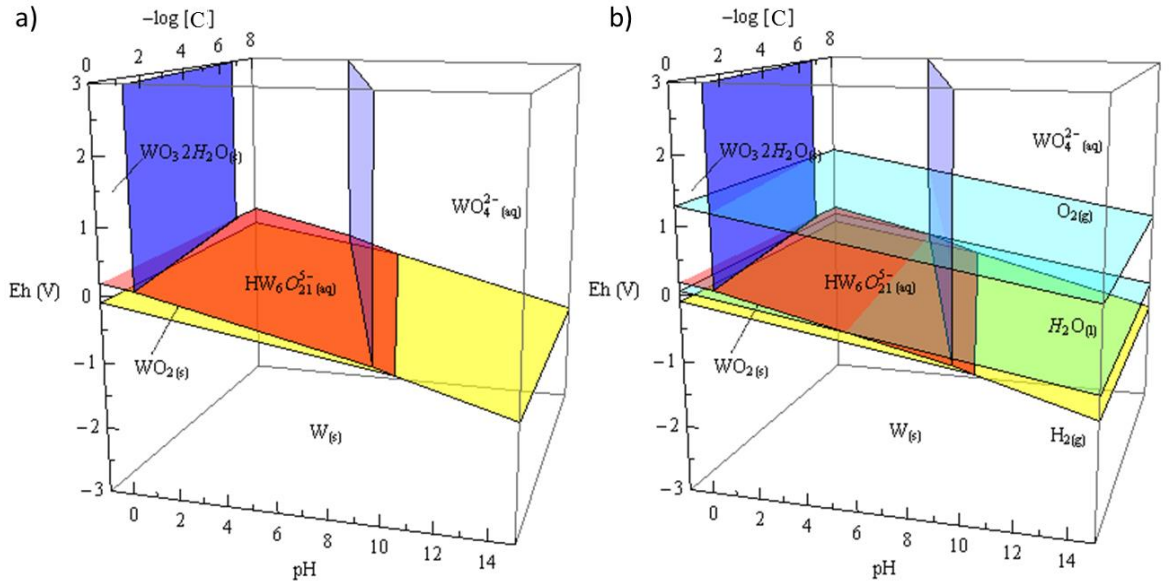

Figure 4.9. Pourbaix Eh-pH-C diagram for tungsten in aqueous solution at temperature T=298.15°K considering stability of $WO_3 \cdot 2H_2O$: (a) without water stability planes, (b) with water stability planes.

Each line in Figure 4.7, Figure 4.8 and Figure 4.9 represents an equilibrium reaction presented in Table 4.2 and plotted using the Nernst equation. Along these lines the species involved in the reaction are in equilibrium with each other and the deviation from these lines shows what type of species become more stable relative to others. For example, the region where tungsten is the only stable species at corresponding Eh, pH and C values is marked with W. This means that if tungsten is immersed in an electrolyte and a potential is applied, it will not react producing reaction products (oxides, ions and ect.), but will be stable, in other words it will be immune. In the region marked with WO_2 the only stable species are tungsten dioxides meaning that if tungsten is immersed in the electrolyte and a potential is applied, it will react with it producing tungsten dioxide that is in solid state and will be covering the surface of the tungsten protecting it from corroding. Along the line separating these two regions tungsten and tungsten dioxide are in equilibrium with each other, thus both species can exist at this specific conditions along the line. In the region marked as WO_3, $WO_3 \cdot H_2O$ and $WO_3 \cdot 2H_2O$ the stable species are tungsten trioxide or its hydrated forms. The same for the $WO_4^{2-}(aq)$ region, where tungsten, immersed into electrolyte with specific applied voltage, will react with electrolyte producing tungstate ions that are soluble in electrolyte and will promote corrosion reaction until all tungsten is converted to tungstate ions.

4.3.4. Comparison of the Pourbaix diagrams

In order to compare our Pourbaix diagrams with the diagrams available in the literature and presented in Figure 4.4 we made the 2D cuts from the 3D diagrams

presented in Figure 4.7 - Figure 4.9 choosing the ions concentrations specified in the literature. The resulting graphs are presented in Figure 4.10.

From Figure 4.10 it can be seen that the diagram with stable species WO_3 has a resemblance with the diagram provided in ref. [9] and Figure 4.4 (c). However, the authors considered two different polytungstate species without mentioning the source of the data used to construct the diagram. The diagram presented by Anik in ref. [28] (Figure 4.4 (a)) do not take into consideration any polytungstate ions. We believe that polytungstates have to be included in the diagram because they have very lowest Gibbs energy and hence the most stable species present in the aqueous solutions with tungsten. The diagram with WO_3 presented in Figure 4.10 (a) takes into consideration the $HW_6O_{21}^{5-}$ species and hence different from the previously published 2D Pourbaix diagrams.

The diagram in Figure 4.10 (b) with stable species $WO_3 \cdot H_2O$ correlates with the diagram constructed by Anik in ref. [28] (Figure 4.4 (b)). Even though Anik did not consider polytungstate species, the diagrams are similar because these species are unstable in that range of ion concentrations.

The diagram in Figure 4.10 (c) with stable species $WO_3 \cdot 2H_2O$ corresponds to the diagram presented in Figure 4.4 (d).

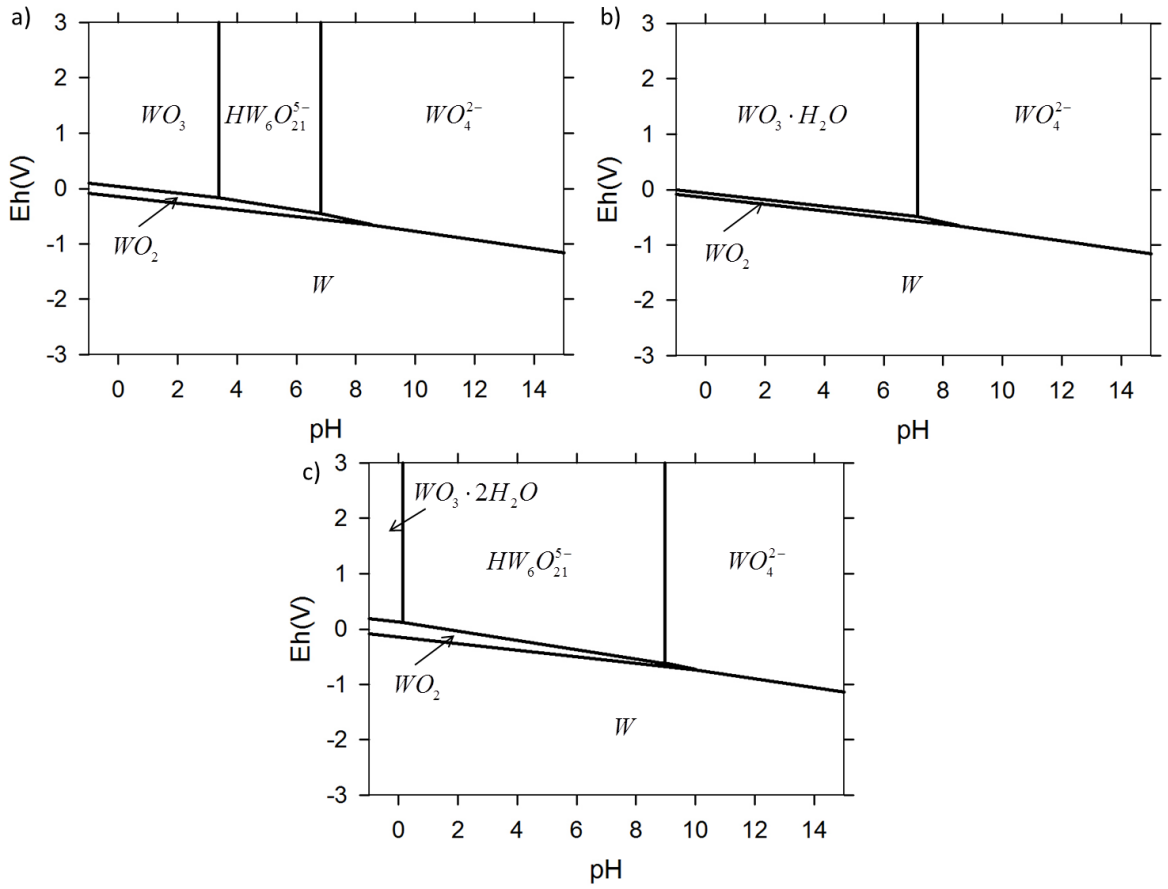

Figure 4.10 The 2D Eh-pH Pourbaix diagrams for tungsten in aqueous solutions at 25˚C: (a) considering the stability of WO_3 with concentration of soluble species $[WO_4^{2-}]=[HW_6O_{21}^{5-}]=10^{-4}M$, (b) considering the stability of $WO_3 \cdot H_2O$ with concentration of soluble species $[WO_4^{2-}]=10^{-4}M$, (c) considering the stability of $WO_3 \cdot 2H_2O$ with concentration of soluble species $[WO_4^{2-}]=[HW_6O_{21}^{5-}]=10^{-1}M$.

4.4. Conclusions

The 3D Eh-pH-C diagrams for tungsten in aqueous solution at the room temperature were successfully constructed (Figure 4.7, Figure 4.8 and Figure 4.9). It can be seen that in the electrolyte with pH14 tungsten remains immune to corrosion when potential is set bellow Eh < -1.2V. Above this critical potential, tungsten would corrode producing the $WO_4^{2-}(aq)$ ions soluble in water. This means that all tungsten will eventually convert to the tungstate ions at some rate. No other species will be stable at these conditions. However, if pH of the electrolyte is lowered bellow pH10, then once the tungstate ions concentration reaches 1M, it will start to precipitate as $WO_3 \cdot H_2O$ that is insoluble in electrolyte. If the pH of electrolyte drops below pH4, then WO_3 will precipitate out. Finally, when pH drops below pH1, then the compound with precipitates out as $WO_3 \cdot 2H_2O$. Unfortunately, due to the unavailability of the Gibbs free energy data for the $WO_3 \cdot 3H_2O$ compound, it is not possible to determine its thermodynamic stability in aqueous solution.

4.5. Appendix

4.5.1. Derivation of the Nernst equations for construction of the Pourbaix diagram

Nernst equations presented in Table 4.2 are derived bellow following numerical order in which they appear in the table:

1) The electrochemical reaction involving tungsten oxidizing to tungsten dioxide $WO_2(s)/W(s)$:

$$WO_2 + 4H^+ + 4e^- = W + 2H_2O \tag{4.28}$$

$$E^0 = -\frac{((0+2\cdot(-237200))-(-534100+4\cdot 0))\,J/mol}{4\cdot 96485C/mol} = -0.15V \tag{4.29}$$

$$E_e = -0.15V - \frac{0.059V}{n}\log\frac{[W]}{[WO_2]} - \frac{(0.059V)\cdot 4}{4}\,pH = -0.15V - (0.059V)\,pH \tag{4.30}$$

$$E_e = -0.15V - (0.059V)\,pH \tag{4.31}$$

2) The electrochemical reaction for the pair $WO_3(s)/WO_2(s)$ is written as follows:

$$WO_3 + 2H^+ + 2e^- = WO_2 + H_2O \tag{4.32}$$

$$E^0 = -\frac{\left[(-534100-237200)-(-763900+2\cdot 0)\right]J/mol}{2\cdot 96485C/mol} = 0.038V \tag{4.33}$$

$$E_e = 0.038V - 0 - \frac{(0.059V)\cdot 2}{2}\,pH = 0.038V - (0.059V)\,pH \tag{4.34}$$

3) The chemical reaction for the pair $WO_3(s)/HW_6O_{21}^{5-}(aq)$ is written as follows:

$$6WO_3 + 3H_2O = HW_6O_{21}^{5-} + 5H^+ \tag{4.35}$$

$$\log K_{eq} = \frac{\left[(-5175.6) - (6 \cdot (-763.9) + 3 \cdot (-237.2))\right] kJ / mol}{-5.71 kJ / mol} = -20.92 \tag{4.36}$$

$$5\,pH = \log[HW_6O_{21}^{5-}] + 20.92 \tag{4.37}$$

4) The chemical reaction for the pair $HW_6O_{21}^{5-}(aq) / WO_4^{2-}(aq)$ is written as follows:

$$HW_6O_{21}^{5-} + 3H_2O = 6WO_4^{2-} + 7H^+ \tag{4.38}$$

$$\log K_{eq} = \frac{\left[(6 \cdot (-916.7) + 7 \cdot 0) - (-5175.6 + 3 \cdot (-237.2))\right] kJ / mol}{-5.71 kJ / mol} = -67.82 \tag{4.39}$$

$$7\,pH = 6\log[WO_4^{2-}] - \log[HW_6O_{21}^{5-}] + 67.82 \tag{4.40}$$

5) The chemical reaction for the pair $WO_3(s) / WO_4^{2-}(aq)$ is written as follows:

$$WO_3 + H_2O = WO_4^{2-} + 2H^+ \tag{4.41}$$

$$\log K_{eq} = \frac{\left[(-916.7 + 2 \cdot 0) - (-763.9 - 237.2)\right] kJ / mol}{-5.71 kJ / mol} = -14.79 \tag{4.42}$$

$$2\,pH = \log[WO_4^{2-}] + 14.79 \tag{4.43}$$

6) The electrochemical reaction for the pair $WO_4^{2-}(aq) / W(s)$ is written as follows:

$$WO_4^{2-} + 8H^+ + 6e^- = W + 4H_2O \tag{4.44}$$

$$E^0 = -\frac{\left[(0 + 4 \cdot (-237200)) - (-916700 + 8 \cdot 0)\right] J / mol}{6 \cdot 96485 C / mol} = 0.06V \tag{4.45}$$

$$E_e = 0.06V - \frac{0.059V}{6} \log \frac{[W]}{[WO_4^{2-}]} - \frac{(0.059V) \cdot 2}{2} = 0.06V + (0.01V) \log[WO_4^{2-}] - (0.079V)\,pH \tag{4.46}$$

7) The electrochemical reaction for the pair $WO_4^{2-}(aq)/WO_2(s)$ is written as follows:

$$WO_4^{2-} + 4H^+ + 2e^- = WO_2 + 2H_2O \tag{4.47}$$

$$E^0 = -\frac{\left[(-534100 + 2\cdot(-237200)) - (-916700 + 4\cdot 0)\right] J/mol}{2\cdot 96485 C/mol} = 0.48V \tag{4.48}$$

$$E_e = 0.48V - \frac{0.059V}{2}\log\frac{[WO_2]}{[WO_4^{2-}]} - \frac{(0.059V)\cdot 4}{2} = 0.48V + (0.03V)\log[WO_4^{2-}] - (0.118V)\,pH \tag{4.49}$$

8) The electrochemical reaction for the pair $HW_6O_{21}^{5-}(aq)/WO_2(s)$ is written as follows:

$$HW_6O_{21}^{5-} + 17H^+ + 12e^- = 6WO_2 + 9H_2O \tag{4.50}$$

$$E^0 = -\frac{\left[(6\cdot(-534100) + 9\cdot(-237200)) - (-5175600 + 17\cdot 0)\right] J/mol}{12\cdot 96485 C/mol} = 0.14V \tag{4.51}$$

$$E_e = 0.14V - \frac{0.059V}{12}\log\frac{[WO_2]^6}{[HW_6O_{21}^{5-}]} - \frac{(0.059V)\cdot 17}{12} = 0.14V + (0.005V)\log[HW_6O_{21}^{5-}] - (0.084V)\,pH \tag{4.52}$$

9) The electrochemical reaction for the pair $WO_3\cdot H_2O(s)/WO_2(s)$ is written as follows:

$$WO_3\cdot H_2O + 2H^+ + 2e^- = WO_2 + 2H_2O \tag{4.53}$$

$$E^0 = -\frac{\left[(-534100 + 2\cdot(-237200)) - (-1020900 + 2\cdot 0)\right] J/mol}{2\cdot 96485 C/mol} = -0.06V \tag{4.54}$$

$$E_e = -0.06V - 0 - \frac{(0.059V)\cdot 2}{2} = -0.06V - (0.059V)\,pH \tag{4.55}$$

10) The chemical reaction for the pair $WO_3 \cdot H_2O(s) / HW_6O_{21}^{5-}(aq)$ is written as follows:

$$6(WO_3 \cdot H_2O) = HW_6O_{21}^{5-} + 3H_2O + 5H^+ \tag{4.56}$$

$$\log K_{eq} = \frac{\left[(-5175.6 + 3\cdot(-237.2) + 5\cdot 0) - (6\cdot(-1020.9))\right] kJ / mol}{-5.71 kJ / mol} = -41.74 \tag{4.57}$$

$$5\,pH = \log[HW_6O_{21}^{5-}] + 41.74 \tag{4.58}$$

11) The chemical reaction for the pair $WO_3 \cdot H_2O(s) / WO_4^{2-}(aq)$ is written as follows:

$$WO_3 \cdot H_2O(s) = WO_4^{2-} + 2H^+ \tag{4.59}$$

$$\log K = \frac{\left[(-916.7 + 2\cdot 0) - (-1020.9)\right] kJ / mol}{-5.71 kJ / mol} = -18.28 \tag{4.60}$$

$$2\,pH = \log[WO_4^{2-}] + 18.28 \tag{4.61}$$

12) The chemical reaction for the pair $WO_3 \cdot 2H_2O(s) / WO_4^{2-}(aq)$ is written as follows:

$$WO_3 \cdot 2H_2O = WO_4^{2-} + 2H^+ + H_2O \tag{4.62}$$

$$\log K = \frac{\left[(-916.7 + 2\cdot 0) - (-1220.0)\right] kJ / mol}{-5.71 kJ / mol} = -11.58 \tag{4.63}$$

$$2\,pH = \log[WO_4^{2-}] + 11.58 \tag{4.64}$$

13) The electrochemical reaction for the pair $WO_3 \cdot 2H_2O(s) / WO_2(s)$ is written as follows:

$$WO_3 \cdot 2H_2O + 2H^+ + 2e^- = WO_2 + 3H_2O \tag{4.65}$$

$$E^0 = -\frac{\left[(-534100 + 3\cdot(-237200)) - (-1220000 + 2\cdot 0)\right] J/mol}{2\cdot 96485 C/mol} = 0.13V \qquad (4.66)$$

$$E_e = 0.13V - 0 - \frac{(0.059V)\cdot 2}{2} = 0.13V - (0.059V)\,pH \qquad (4.67)$$

14) The chemical reaction for the pair $WO_3\cdot 2H_2O(s)/HW_6O_{21}^{5-}(aq)$ is written as follows:

$$6(WO_3\cdot 2H_2O) = HW_6O_{21}^{5-} + 9H_2O + 5H^+ \qquad (4.68)$$

$$\log K = \frac{\left[(-5175.6 + 9\cdot 237.2 + 5\cdot 0) - (6\cdot(-1220.0))\right] kJ/mol}{-5.71 kJ/mol} = -1.68 \qquad (4.69)$$

$$5\,pH = \log[HW_6O_{21}^{5-}] + 1.68 \qquad (4.70)$$

4.5.2. Construction of the Pourbaix diagram using Mathematica® program

In order to construct a 3D diagram in Wolfram Mahtematica® program, Graphics3D function was used, where the Nernst equations were plotted as polygons in the (x, y, z) diagram with $x = pH$, $y = -\log[C]$ and $z = E_e$. As an example, construction of the diagram shown in Figure 4.9 is presented below.

Steps taken in order to construct 3D diagram in Wolfram Mahtematica®:

1) First step is to plot the Nernst equations for the reactions and determine the intersection points. Figure 4.6 (a) shows the plot of the equations for pairs WO_2/W and WO_4^{2-}/W. The two equations intersect with each other and intersection points between them and with the axes can be determined.

2) To determine intersections between the Nernst equations for different reactions, the equations for the two reactions was equaled and solved for pH .

For the pairs WO_2 / W and WO_4^{2-} / W the pH will be as follows:

$$-0.15V - (0.059V)\,pH = 0.06V + (0.01V)\log[WO_4^{2-}] - (0.079V)\,pH \tag{4.71}$$

$$pH = \frac{0.21V + (0.01V)\log[WO_4^{2-}]}{0.02V} \tag{4.72}$$

Using the obtained equation for pH its value can be found by using the defined $-\log[C]$ value at the borders of the diagram:

For $(x, 0, z)$ border $-\log[C] = 0$ then:

$$pH = \frac{0.21V}{0.02V} = 10.5 \tag{4.73}$$

For $(x, 8, z)$ border $-\log[C] = 8$ then:

$$pH = \frac{0.21V - (0.01V)\cdot 8}{0.02V} = 6.5 \tag{4.74}$$

Now, the calculated pH values can be used to find E_e at the intersection:

$$E_e = -0.15V - (0.059V)\cdot pH = -0.15V - 0.059V \cdot 10.5 = -0.77V \tag{4.75}$$

And

$$E_e = -0.15V - (0.059V)\cdot pH = -0.15V - 0.059V \cdot 6.5 = -0.53V \tag{4.76}$$

The coordinates of the intersections between the two planes representing the transitions between the stability regions of the compounds are $(10.5, 0, -0.77)$ and $(6.5, 8, -0.53)$.

3) Intersections between the Nernst equations and the borders of the diagram were found. This was done by setting the limiting values on $-\log[C]$, pH and E_e where the plane representing the transition reaction intersects the borders of the diagram.

Since the intersection for pairs WO_2/W and WO_4^{2-}/W was found earlier, an intersection with the edges for both of the transition equations have to be found.

The plane represented by the equation $E_e = -0.15V - (0.059V)\,pH$ of $WO_2(s)/W(s)$ extends towards the edges of the diagram with coordinates: $(-1, 0, z)$ and $(-1, 8, z)$. The intersection was found by solving the Nernst equation for E_e. The Nernst equation for this pair does not depend on C, therefore it will have the same value of E_e for both intersections:

$$E_e = -0.15V - (0.059V)\,pH = -0.15V - (0.059V)\cdot(-1) = -0.091V \qquad (4.77)$$

The coordinates of the intersections of WO_2/W with the edges of the diagram: $(0, 0, -0.091)$ and $(0, 8, -0.091)$.

The plane represented by the equation $E_e = 0.06V + (0.01V)\log[WO_4^{2-}] - (0.079V)\,pH$ of the pair WO_4^{2-}/W intercepts the edges of the diagram in two places: edges $(15, 0, z)$ and $(15, 8, z)$.

The Nernst equation was solved for E_e, or coordinates $(15, 0, z)$:

$$E_e = 0.06V + (0.01V)\cdot 0 - (0.079V)\cdot 15 = -1.125V \qquad (4.78)$$

And for coordinates $(15, 8, z)$:

$$E_e = 0.06V - (0.01V)\cdot 8 - (0.079V)\cdot 15 = -1.205V \tag{4.79}$$

The coordinates of the intersections of $WO_4^{2-}(aq)/W(s)$ with the edges of the diagram: $(15, 0, -1.125)$ and $(15, 8, -1.205)$.

The resulting plot of the two planes is shown in Figure 4.11 (a). The coordinates for the plane representing the transition between the two compounds WO_2/W are $(-1, 0, z)$, $(-1, 8, z)$, $(6.5, 8, -0.53)$, $(10.5, 0, -0.77)$. The coordinates for the $WO_4^{2-}(aq)/W(s)$ are $(10.5, 0, -0.77)$, $(6.5, 8, -0.53)$, $(15, 8, -1.205)$, $(15, 0, -1.125)$. Then the transition planes for the pairs $WO_3 \cdot 2H_2O/WO_2$, $HW_6O_{21}^{5-}/WO_2$, WO_4^{2-}/WO_2 are calculated using the presented steps and plotted on the diagram (Figure 4.11 (b)). Next, planes for the $WO_3 \cdot 2H_2O/HW_6O_{21}^{5-}$, $HW_6O_{21}^{5-}/WO_4^{2-}$ compounds are calculated and plotted on the graph (Figure 4.11 (c)).

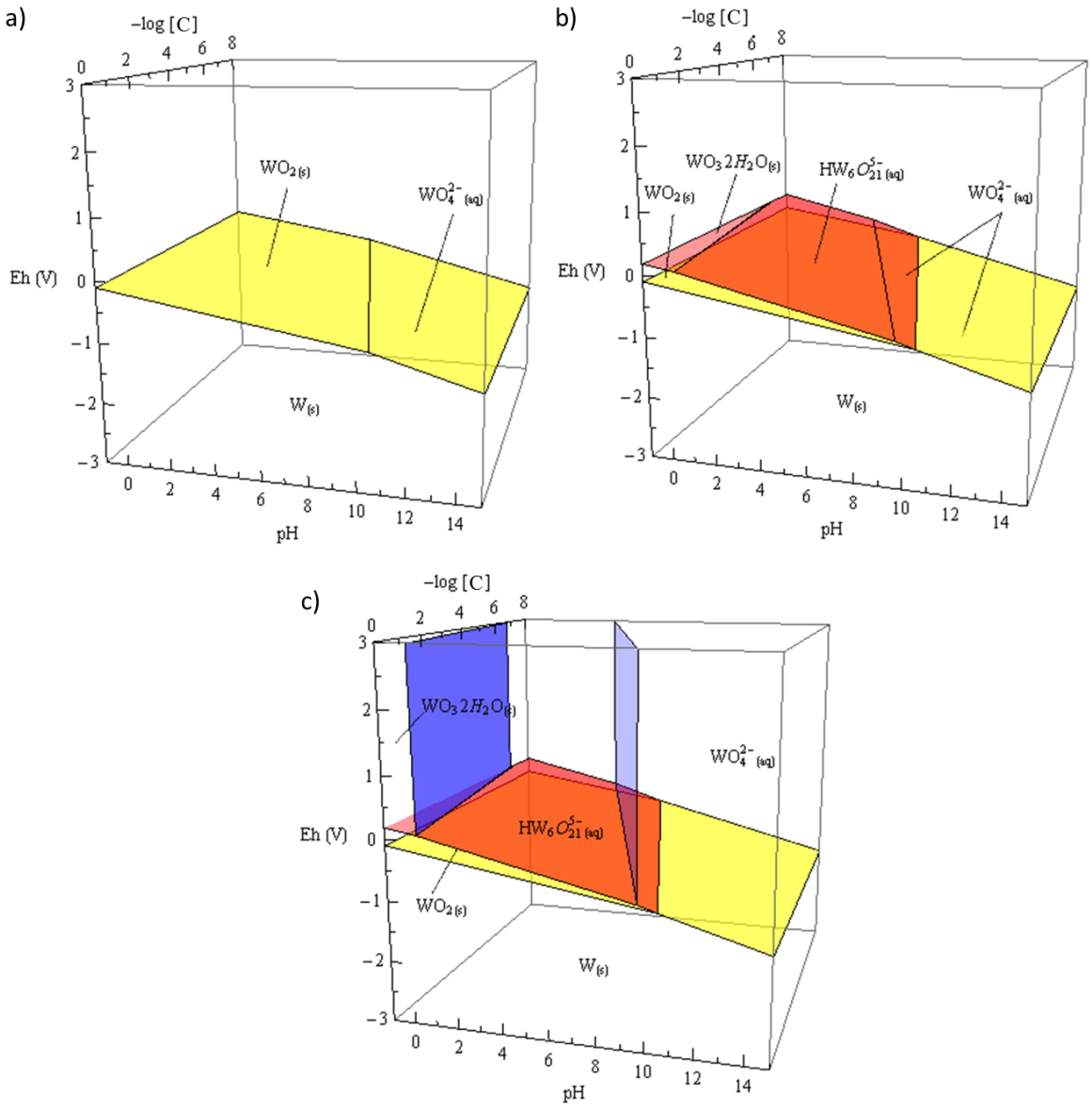

Figure 4.11. Steps of construction of the Pourbaix diagram: (a) planes for tungsten transition to tungsten dioxide and to tungstate ion, (b) addition of planes for transition of tungsten dioxide to tungsten trioxide dihydrate, polytungstate and tungstate ions, (c) addition of transition planes from tungsten trioxide dehydrate to polytungstate ion and from polytungstate ion to polytungstate ion.

4.6. References

[1] Cook W G and Olive R P 2012 Pourbaix diagrams for the iron-water system extended to high-subcritical and low-supercritical conditions *Corrosion Science* **55** 326-31

[2] Beverskog B and Puigdomenech I 1996 Revised Pourbaix diagrams for iron at 25-300 degrees C *Corros Sci* **38** 2121-35

[3] Beverskog B and Puigdomenech I 1997 Revised pourbaix diagrams for copper at 25 to 300 degrees C *J Electrochem Soc* **144** 3476-83

[4] Beverskog B and Puigdomenech I 1997 Revised Pourbaix diagrams for nickel at 25-300 degrees C *Corros Sci* **39** 969-80

[5] Nickchi T and Alfantazi A 2013 Potential-temperature (E-T) diagrams for iron, nickel, and chromium in sulfate solutions up to 473 K *Electrochim. Acta* **104** 69-77

[6] Pourbaix M 1966 *Atlas of electrochemical equilibria in aqueous solutions* (Oxford, New York,: Pergamon Press)

[7] Schweitzer G K and Pesterfield L L 2010 *The Aqueous Chemistry of the Elements* (Oxford; New York: Oxford University Press)

[8] Osseo-Asare K 1982 Solution chemistry of tungsten leaching systems *Metallurgical Transactions B* **13B** 555-64

[9] Kneer E A, Raghunath C, Raghavan S and Jeon J S 1996 Electrochemistry of chemical vapor deposited tungsten films with relevance to chemical mechanical polishing *J Electrochem Soc* **143** 4095-100

[10] Pesterfield L L, Maddox J B, Crocker M S and Schweitzer G K 2012 Pourbaix (E-pH-M) diagrams in three dimensions *Journal of Chemical Education* **89** 891-9

[11] Bullock K R 1980 Effect of anion activity on electrochemical equilibria - 3-dimentional potential-pH diagram for PB-H2SO4-H2O system *J Electrochem Soc* **127** 662-4

[12] Garrels R M, Christ C L 1965 *Solutions, Minerals, and Equilibria* (New York, NY: Harper & Row. Publishers)

[13] Brook P A 1971 Computer method of calculating potential-pH diagrams *Corros Sci* **11** 389-&

[14] Williams B G and Patrick W H 1977 Computer method for construction of Eh-pH diagrams *Journal of Chemical Education* **54** 107

[15] Salhi R 2005 A rigorous calculation method for determining potential-pH diagrams part I: Copper in aqueous solutions of various complexing agents *Iran J. Chem. Chem. Eng.-Int. Engl. Ed.* **24** 29-39

[16] Salhi R and Bouhidel K E 2005 A rigorous calculation method for determining potential-pH diagrams in metal-ammonia-water systems *Asian J. Chem.* **17** 245-58

[17] Angus J C and Angus C T 1985 Computation of Pourbaix diagrams using virtual species - implementation on personal computers *J Electrochem Soc* **132** 1014-9

[18] Burstein G T 2013 University of Cambridge http://www.doitpoms.ac.uk/tlplib/pourbaix/index.php

[19] Jones D A 1991 *Principles and Prevention of Corrosion* (New York, Toronto: Macmillan Pub. Co.; Collier Macmillan Canada; Maxwell Macmillan International Pub. Group)

[20] Munoz-Portero M J, Garcia-Anton J, Guinon J L and Perez-Herranz V 2009 Pourbaix diagrams for chromium in concentrated aqueous lithium bromide solutions at 25 degrees C *Corros Sci* **51** 807-19

[21] Munoz-Portero M J, Garcia-Anton J, Guinon J L and Perez-Herranz V 2007 Pourbaix Diagrams for nickel in concentrated aqueous lithium bromide solutions at 25 degrees C *Corrosion* **63** 625-34

[22] Wang C Y, Li K C 1955 *Tungsten. Its History, Geology, Ore-Dressing, Metallurgy, Chemistry, Analysis, Applications and Economics* (New York: Reinhold Publishing Corporation)

[23] Lassner E and Schubert W-D 1999 *Tungsten: properties, chemistry, technology of the element, alloys, and chemical compounds* (New York: Kluwer Academic/Plenum Publishers)

[24] Pope M T 1983 *Heteropoly and Isopoly Oxometalates* (Springer-Verlag)

[25] Anik M and Osseo-Asare K 2002 Effect of pH on the anodic behavior of tungsten *J Electrochem Soc* **149** B224-B33

[26] Anik M 2009 pH-dependent anodic reaction behavior of tungsten in acidic phosphate solutions *Electrochim. Acta* **54** 3943-51

[27] Anik M and Cansizoglu T 2006 Dissolution kinetics of WO3 in acidic solutions *J. Appl. Electrochem.* **36** 603-8

[28] Anik M 2010 Anodic reaction characteristics of tungsten in basic phosphate solutions *Corros Sci* **52** 3109-17

[29] Patrick E, Orazem M E, Sanchez J C and Nishida T 2011 Corrosion of tungsten microelectrodes used in neural recording applications *J. Neurosci. Methods* **198** 158-71

[30] Pradyot P 2002 *Handbook of Inorganic Chemicals* (McGraw-Hill Professional)

5. MORPHOLOGY OF THE SHELL FORMED DURING THE PLE REGIME

5.1. Introduction

In Chapter 1 we discussed two regimes used to prepare nano-sharp needles. These regimes showed significant differences due to the magnitude of the applied potential. In one regime, at the potentials higher than 3V the tungsten polishing proceeded with formation of the highly viscous film that surrounded the needle and was flowing down. When the potential was lowered bellow 3V that prompted the formation of the solid porous shell around the tungsten as a result of the complex oxidation reaction on tungsten surface. In Chapter 4 we presented the Pourbaix diagrams and discussed the possible stability of some tungsten compounds that can explain the formation of the shell on tungsten surface. In this Chapter, the shell structure and its composition were studied using variety of experimental techniques to support the conclusions drawn from the Pourbaix diagrams.

5.2. Experimental techniques

5.2.1. Transmission X-ray microscope (TXM) tomography

The tomography experiments were performed on samples prepared with the PLE technique [1]. Tungsten wires with diameter of 75 μm and 125 μm (99.95% purity,

purchased from Advent Research Materials Ltd.) were electropolished in KOH solution. Each tomography run was performed with X-ray energy 8960 eV, 1441 projections with the field of view 40 μm^2 by 40 μm^2. After the measurements the background was subtracted and an automatic alignment using the run-out correction system was applied. A standard filtered back-projection reconstruction algorithm was used to construct the 3D images [2]. Threshholding was applied to the reconstructed image stacks using Avizo® program, VSG, version 8.0.

5.2.2. Optical imaging

To visualize the shell structure Olympus BX51 optical microscope with an attached Spot Boost camera (Diagnostic Instruments, Inc.) was used. The tungsten wire (99.95%, Advent Research Materials Ltd) with 0.125 mm diameter was placed horizontally in the Petri dish filled with 2M KOH electrolyte. The stainless steel wire was used as a cathode. The electrodes were connected to a potentiostat CHI 660D (CH Instruments, Inc.) and a constant potential of 1.6V was applied to the system.

5.2.3. Composition characterization

The produced tungsten probes were analyzed using the FESEM-Hitachi S4800 scanning electron microscope equipped with the Oxford INCA Energy 200 Energy Dispersive Spectroscopy (EDS). The tungsten probes were rinsed with the DI water and mounted on aluminum stubs with carbon-graphite tape for fixation. The following settings were used for imaging: accelerating voltage 10 kV, emission current 10.6 μA,

working distance 4.4 mm. The images were analyzed with Matlab® and ImageJ software. Prior to the EDS measurements, the electropolished samples were placed in the Petri-dish for drying at the room temperature. The following settings were used for the EDS analysis: accelerating voltage 20 kV, emission current 10.2μA, and working distance 14.8 mm. Calibration was performed with the pure copper tape.

The X-ray diffraction (XRD) patterns were acquired using a Rigaku Ultima IV powder diffractometer equipped with Cu *Kα* radiation (λ=1.5418 Å) in the angular range from 5˚ to 70 ˚ or 110˚ *2θ*. The XRD measurements were carried out at the room temperature. The data was analyzed using PDXL software version 1.4.0.0. The XRD measurements were carried out at the room temperature. Tungsten sheet with thickness of 1.5 mm (Midwest Tungsten Service, Inc.) was cut in square 17.5x17.5 mm pieces using diamond saw. The samples were polished with send paper and cleaned with ethanol followed by sonication in acetone for 20 min. After that the samples were dried and electropolished in 2M KOH electrolyte using two-electrode system with constant applied voltage of 2V (see Chapter 1. for details on experimental procedure). After etching for 1 h tungsten plates with the shell were carefully removed from electrolyte and left to dry in the air for 24 h.

The infrared IR spectrum was recorded over the spectral range 525 – 4000 cm^{-1} using a Thermo-Nicolet Magna 550 FTIR spectrometer equipped with a Diamond ATR accessory.

5.2.4. Thermal analysis

For thermal analysis the tungsten plate was electropolished in 2M KOH solution for 1 h. Then the shell was removed from the plate and rinsed with DI water before drying in the air for 24 h.

The Thermal Gravimetric Analysis (TGA) was performed on TA Instruments TGA Q5000 V3.13 Build 261 with a ramp 10°C/min from 25°C to 400°C in nitrogen gas. First the sample was equilibrated at room temperature under nitrogen purge for 10 min prior to heating.

The Differential Scanning Calorimetry (DSC) was performed on TA Instruments DSC Q1000 V9.9 Build 303. First the sample was equilibrated at 25°C followed by the temperature increase with the 10°C/min ramp to 400°C in helium gas. To analyze the data TA Instruments Universal Analysis 2000 V3.9A and 4.7A software was used.

5.3. Shell structure and composition

5.3.1. Structure analysis

First, *ex situ* tomography scan was performed on the tungsten wire with initial diameter of 75 μm electropolished with 1.55V applied potential in 1M KOH solution on TXM stage using the single tube setup described in Chapter 6. After the electropolishing procedure was finished, the electrolyte was withdrawn from the cell using the 1ml syringe with a needle gage 27 and the needle covered with the shell was left undisturbed in the cell for 1 h to stabilize after which the tomography was performed. Figure 5.1

shows the results of the tomography scan. The shell appears to have a rough porous surface completely covering the tungsten needle inside.

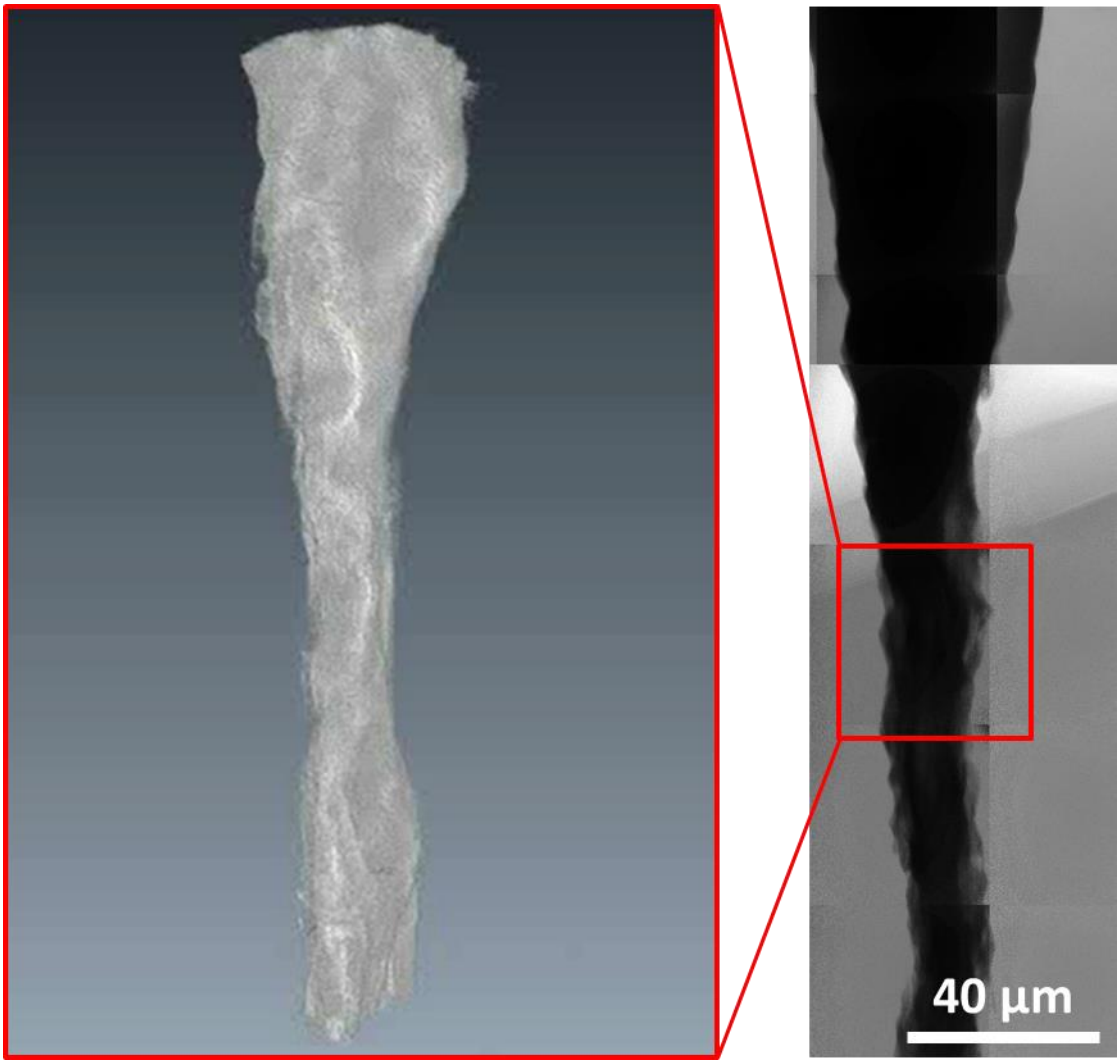

Figure 5.1. The image in the red box is a tomography of the PLE prepared needle covered by the solid shell after the reaction was stopped. The X-ray image on the right depicts the region where the tomography was performed.

To accompany the findings of X-ray tomography images we employed an optical microscopy to look more closely at the structure of the shell prepared by applying 1.55V. Figure 5.2 revealed the presence of a thick shell consisting of the darker colored grains

trapped in the lighter colored material. This indicates that the shell has a complex structure and most likely is porous.

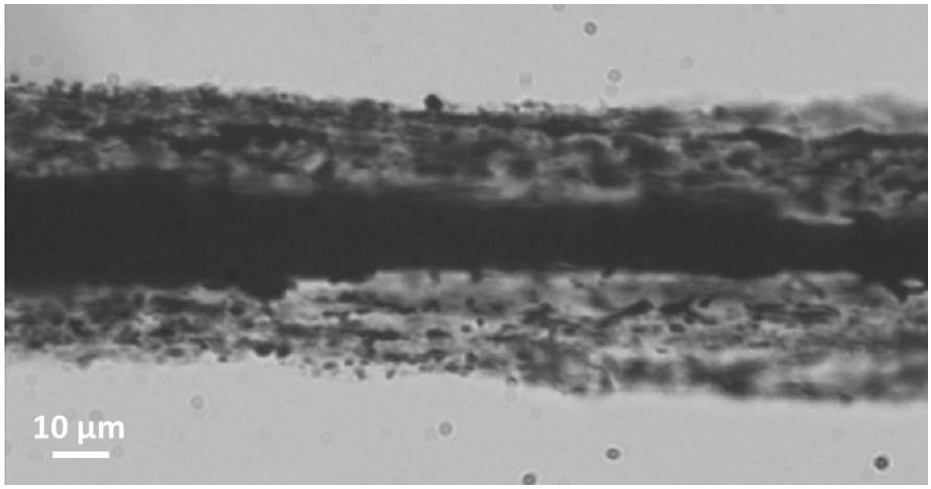

Figure 5.2. Tungsten wire covered with the shell.

Second, *ex situ* tomography on the tungsten needle with diameter of 125 µm electropolished with 2V applied potential in 2M KOH solution using the setup described in Chapter 1for the PLE technique. After the electropolishing procedure was finished, the sample was carefully withdrawn from the solution in order to keep the shell intact. The sample was dried in the air and stored in the Petri dish for approximately one month before the tomography was performed. Figure 5.3 shows the results of the tomography scan. The shell was covering only portion of the tungsten tip, because the shell is very loosely bonded to the needle and during the withdrawal procedure the majority of the shell is removed by the liquid. The shell appears to have an irregular porous structure (Figure 5.3 (c), (d)).

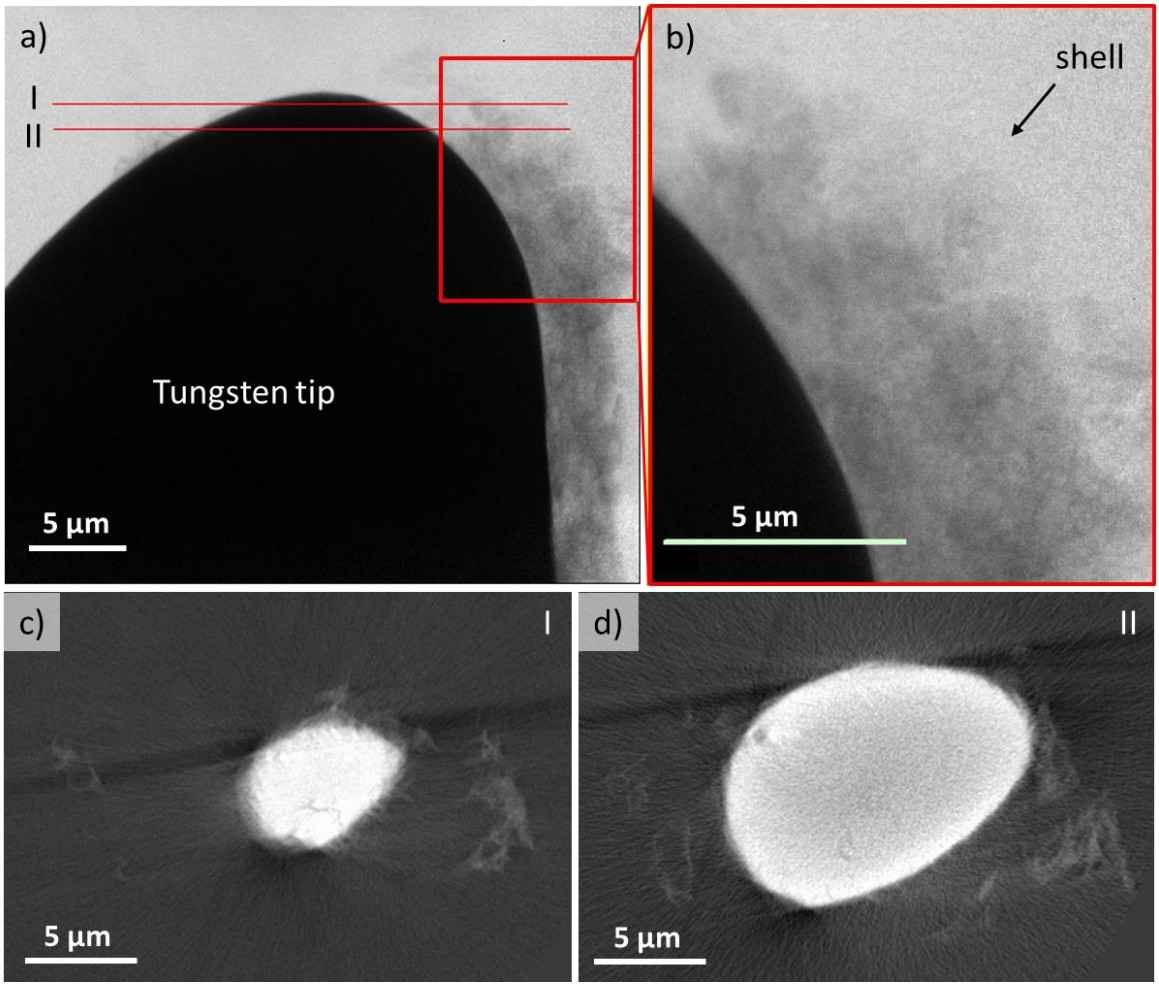

Figure 5.3. TXM tomography: (a) 2D image of the tungsten tip with the shell, (b) enlarged section from the image (a) of the shell, (c), (d) cross-sections from 3D reconstruction of images collected during tomography: I and II red lines depicted in the image (a) indicate the cross-section location.

5.3.2. Composition analysis

The Pourbaix diagrams from Chapter 4 suggest that for the given experimental conditions, 0.57V < Eh < 1.37V at $\approx pH14$, the only stable products of tungsten are the WO_4^{2-} ions dissolved in water. To confirm/disregard this hypothesis, we conducted the energy-dispersive X-ray spectroscopy (EDS) of the porous shells (n=9 samples total) shown in Figure 1.3 (c), (d). The porous shells were collected from the electropolished tungsten wires of 1 mm diameter; these wires were electropolished at ΔE=2V for 1h in 2M KOH. Then, we performed a similar analysis of the surface of tungsten tips shown in Figure 1.4 (regime II). Electropolishing of the tungsten wires with the diameter of 0.125mm was conducted at ΔE=1.5V for 300sec in 2M KOH. Next, the wires were rinsed with the DI water. These EDS analyses revealed the presence of tungsten oxides, Figure 5.4 (a), (b), (c). Potassium hydroxide was left in the shells because the shells were not rinsed with the DI water, Figure 5.4 (a). Otherwise, the shells could be destroyed. Spectrum in Figure 5.4 (b) was taken from a spot situated 30μm from the tip and located in the middle of the wire. Spectrum in Figure 5.4 (c) was taken from the same sample but the spot was chosen closer to the side positioned 30μm from the tip. Thus, these two spectra provide an idea about a circumferential distribution of chemical elements at the level of 30μm from the tip. A Monte Carlo simulation program CASINO® suggests that the depth of beam penetration during EDS scan for tungsten is about ~0.33μm. Therefore, the EDS mostly probe tungsten. Other elements located at the wire surface provide a weak, yet important contribution to the signal.

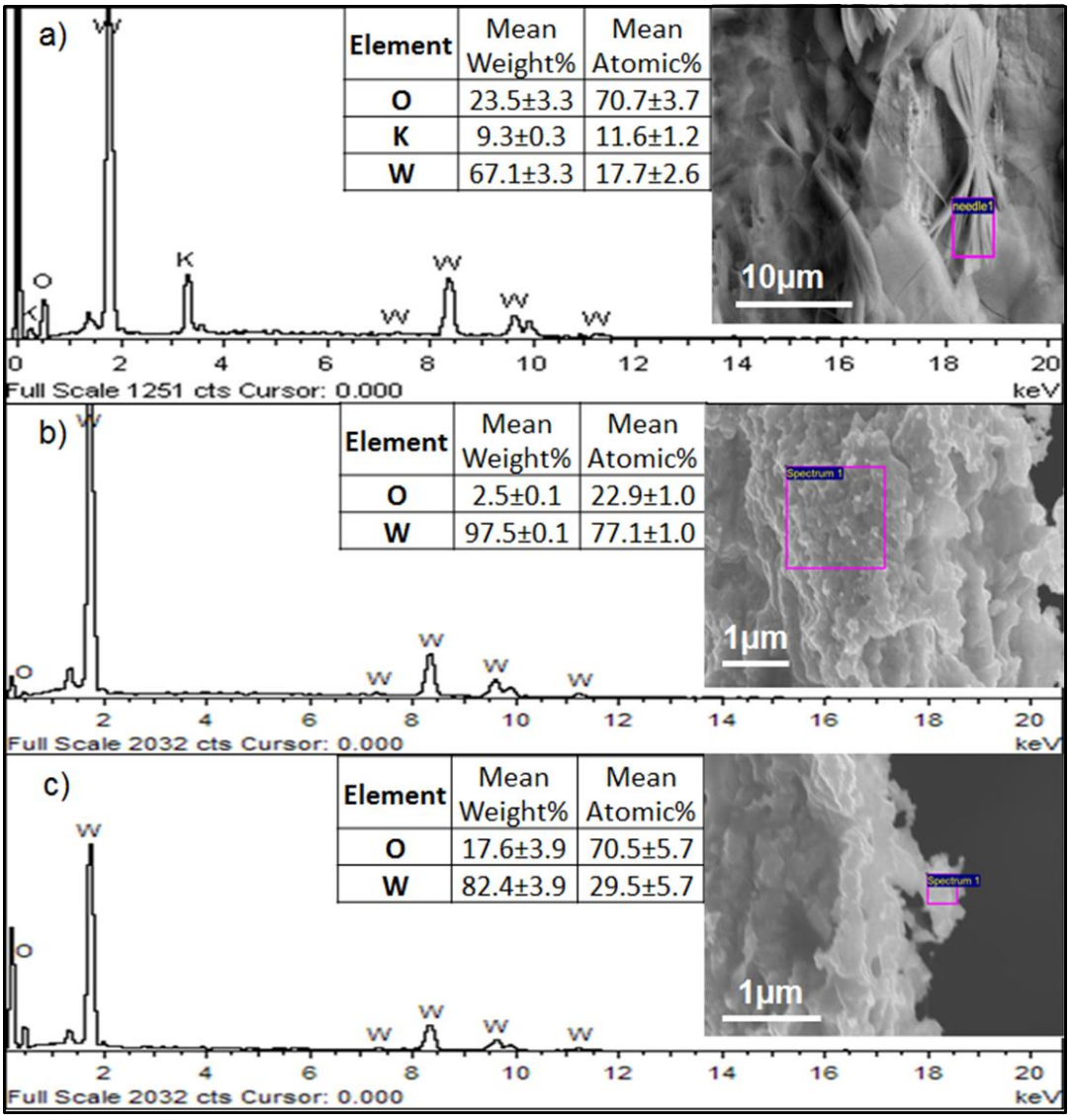

Figure 5.4. Results of the EDS analysis of the chemical composition of: (a) the porous shells and (b), (c) the tip surfaces.

These observations contradict the predictions of the equilibrium Pourbaix diagram. The constancy of pH of the reaction products during the eletropolishing becomes questionable. It is therefore instructive to investigate the diagrams for lower pH levels. According to the Pourbaix diagram, as the pH level changes to the more acidic side, one

expects to see the WO_2 and H_2WO_4 crystals coexisting with the electrolyte [3-6]. A remarkable stability of the solid porous shell encourages us to think that the surface pH of the tungsten tends to decrease during the reaction across the film. This hypothesis can explain a gradual change of pH from the bulk values to those required by the Pourbaix diagram. In Chapter 3 we found that after electropolishing of tungsten in the KOH electrolyte with pH level around pH14 the electrolyte pH was lowered down to pH9 above the 0.27 mole fraction of the tungstate ions concentration in the solution or 0.5M of tungstate ions. Similar results were shown in the Anik's paper [3] where he measured the surface pH of the tungsten during electropolishing in an electrolyte solution with pH10 (Figure 5.5). He found that the local pH near the surface of the anode changed from pH10 to pH3.1 during electropolishing.

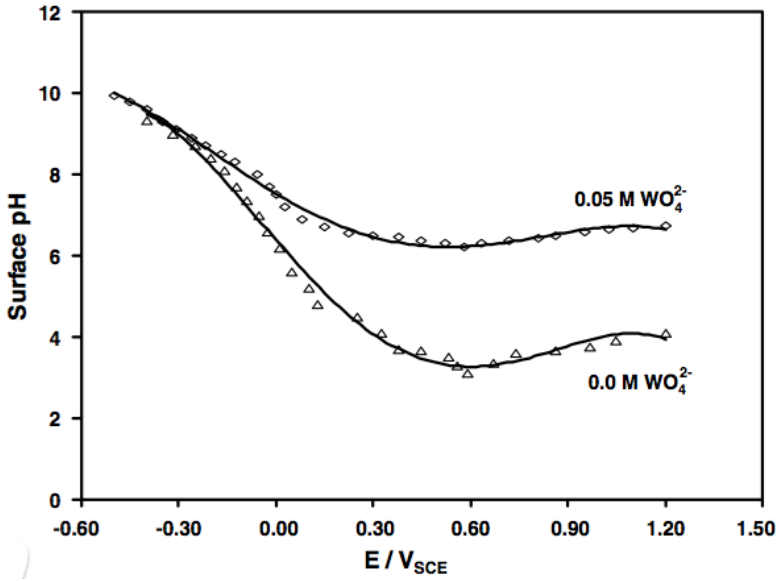

Figure 5.5. Surface pH dependence on applied potential [3].

Figure 5.6 shows the X-ray diffraction pattern of the tungsten plate covered with the shell. The pattern from the tungsten (W) plate corresponds to pure tungsten. The pattern from the W plate with shell revealed the broad peak between 20 and 40 degrees that corresponds to the amorphous structure, while sharp peaks correspond to the substrate which is the tungsten plate.

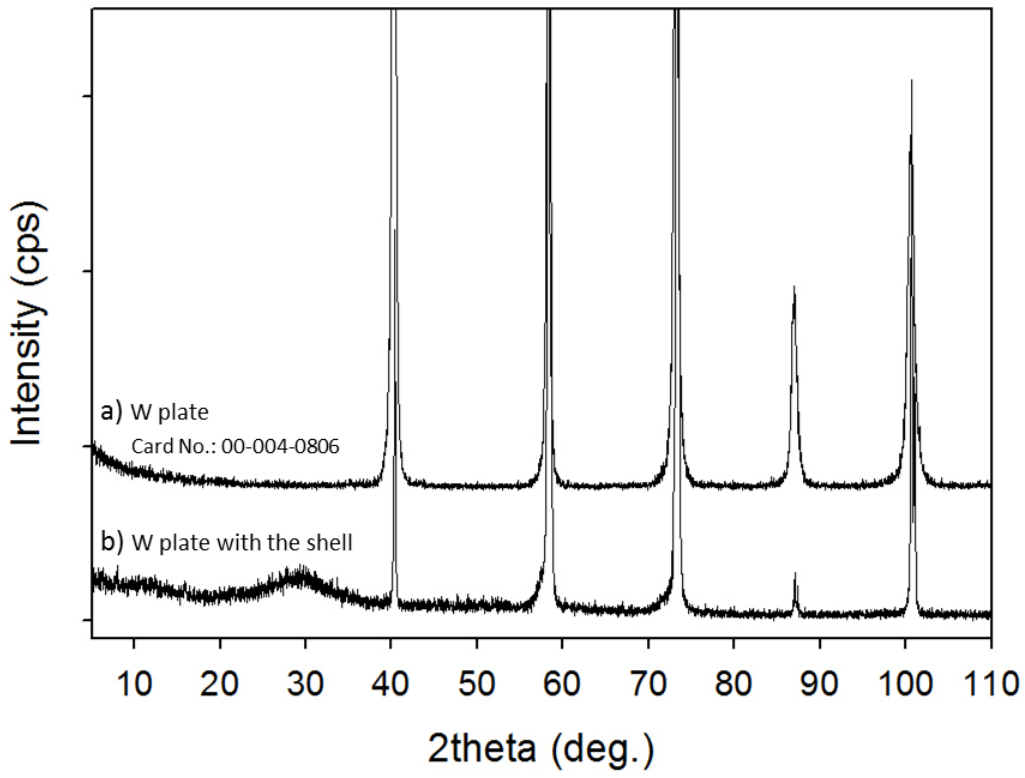

Figure 5.6. XRD patterns of the: (a) tungsten plate and (b) tungsten plate with the shell prepared by electropolishing the tungsten plate in 2M KOH electrolyte with 2V applied potential.

The IR spectrum of the shell is shown in Figure 5.7. The broad adsorption peaks in the 3200-3550 cm^{-1} range and strong peaks in the 1000-1200 cm^{-1} range are associated with O-H stretching vibrations of H-bonded water [7-9]. The peaks around 1595-1625 cm^{-1} range are associated with O-H coordinated water bending vibrations [7, 9-11]. The

adsorption around 500-900 cm^{-1} corresponds to O-W-O stretching [7, 10]. The peaks around 948-1007 $cm^{-1}$are related to the W=O valence vibrations [7, 9, 11]. This indicates that there is a presence of the tungsten trioxide hydrate in the shell; however the hydration level cannot be firmly determined.

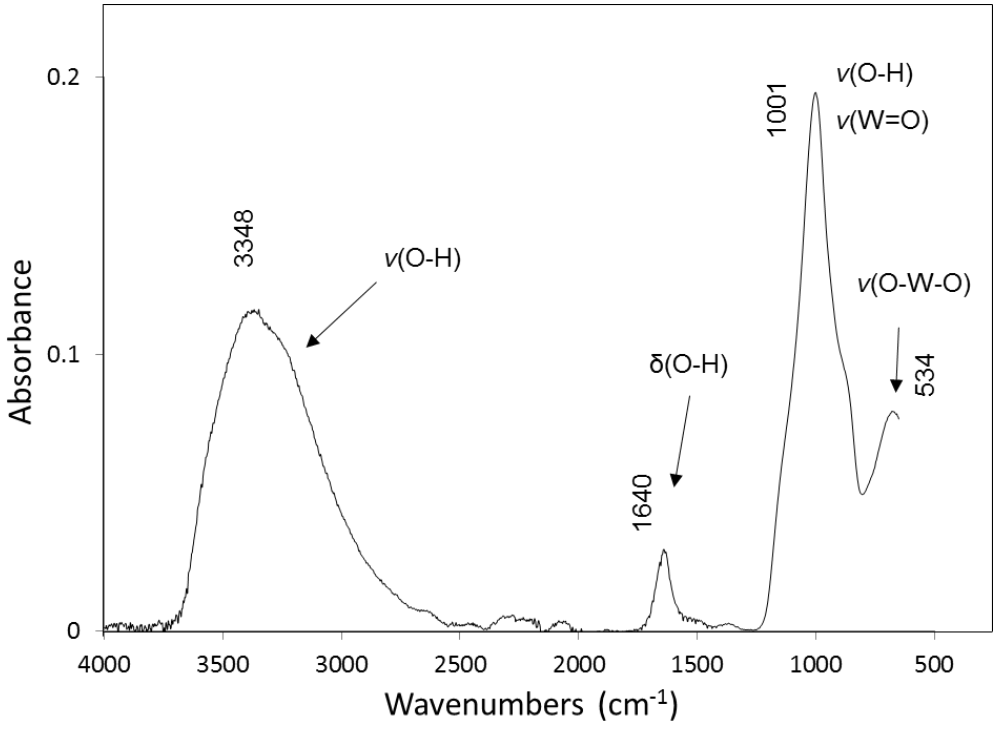

Figure 5.7. IR spectra of the shell prepared by electropolishing the tungsten plate in 2M KOH electrolyte with 2V applied potential.

Figure 5.8 shows the TGA and DSC scan on the shell. From DSC curve it can be seen that there is one endothermic peak at 130.3˚C. The mass loss during this period was equal to 2.7wt.%. As we already discussed in Chapter 3 section 3.3.2, the endothermic peaks are associated with the phase transitions and change of the lattice symmetry in tungsten oxides and hydrates [7, 12-16]. The total mass loss during the heating from the room temperature to 400˚C was 4.5wt.%.

By looking at the XRD spectra, it is not possible to determine the chemical composition of the compound that was formed during the electropolishing procedure, but based on the IR and DSC/TGA graphs we can suggest that it is likely to be a hydrate.

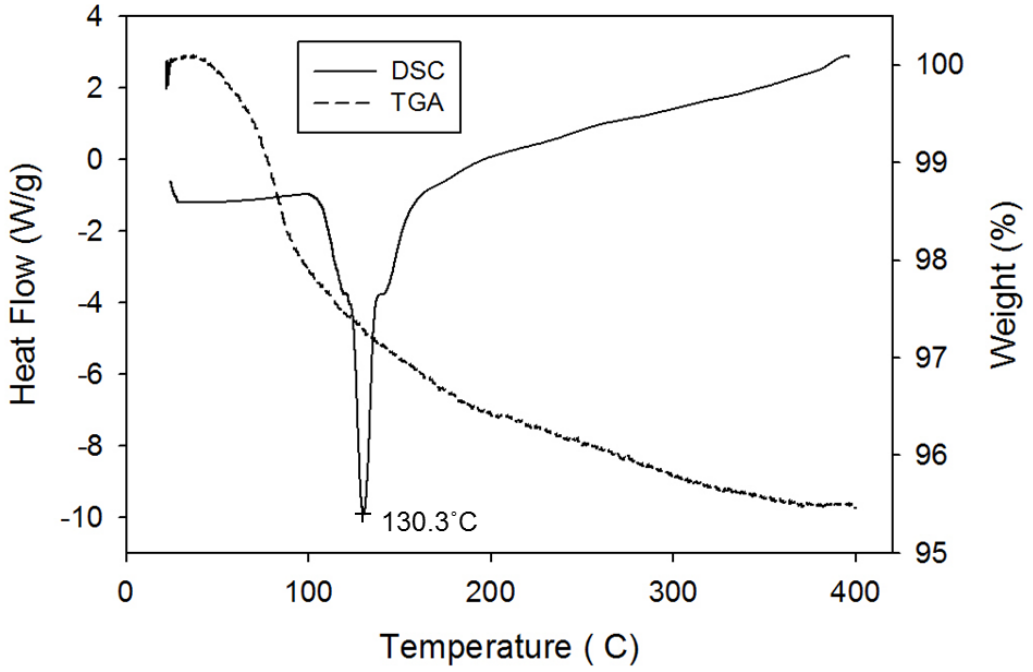

Figure 5.8. DSC and TGA on the shell collected from the plate electropolished in 2M KOH with applied potential of 2V.

We hypothesize that during the CLE regime when high voltages (10V) are applied to the electrodes, the rate of electrochemical etching of the tungsten is high and the anodic polarization occurs with the hydroxide ions used up as soon as they arrive to the tungsten surface producing WO_4^{2-} ions. The flowing film immediately removes these heavy ions so that every time the newly developed tungsten surface is exposed to new hydroxide ions. During the PLE regime, when the applied voltage is decreased down to 2V. The liquid film enriched with the ions increases its viscosity and hence the time of residence of the ions in the vicinity of tungsten surface increases. The

$WO_2, WO_3, H_2O \cdot WO_3$ molecules are produced in the pathway of electrochemical reactions and as their concentration increases, they precipitate out to form the amorphous structure. This structure is attracted to the tungsten surface by the van der Waals and dipole image forces. The amorphous structure build up a solid skeleton and some other oxides can be formed inside this skeleton. Therefore, we believe that the semisolid film is a porous film consisting of different stable insoluble oxides, $WO_2, WO_3, WO_3 \cdot H_2O$ [6].

These oxides and the corresponding film separate the metal surface from the electrolyte; hence the diffusion of ions toward the tungstate surface is hindered. The shielding porous layer significantly reduces the downward and upward flows of the reaction products making the distribution of ions along the wire almost uniform. This, in turn, reduces a chance to form a neck. We assume that the tungsten wire is wrapped by a porous film which is permeable by the hydroxide ions. According to the Pourbaix diagram presented in Chapter 4, the boundary of the porous film is specified by the pH level equal to pH9. The external surface of the porous film dissolves into the ions WO_4^{2-}, which are diffused into the film forming a flow streaming downwards. The hydroxide ions move toward the tungsten surface where they consume the tungsten and form new oxides. In this simplified model, we have two moving boundaries, the internal and external surfaces of the porous film.

5.4. Gasochromic properties of the precipitates

It is well known, that tungsten oxides change the color upon the passage of the gas through them [17-29]. This phenomenon is called gasochromism. We performed a set

of experiments where the hydrogen gas was passing through the shell formed on the tungsten. The setup consisted of the tungsten plate 17.5x17.5 mm (anode) and a stainless steel rod (cathode) that were immersed into 1.5mL of the 2M KOH electrolyte (Figure 5.9 (a)). The electrodes were placed 3 mm apart from each other and connected to a potentiostat. The distance between the cathode and the anode ensured the access of the hydrogen gas to the shell. The constant potential of 2V was applied to the system for 1h. During this procedure the shell was growing on the anode (tungsten plate). On the cathode, there was evolution of the hydrogen gas. As a result of the hydrogen gas bubbling through the shell, the electrolyte changed its color from clear to deep blue. It was also noticed, that some precipitates accumulated at the bottom of the beaker (Figure 5.9 (a)). After the electropolishing was stopped, the electrolyte with precipitates from the bottom of the beaker was collected in the vial (Figure 5.9 (b)). During the following ~10 minutes, the color of the electrolyte gradually changed from deep blue to clear (Figure 5.9 (c)). The pH measurements of the electrolyte showed that the pH changed from pH level around pH14 to pH9. The precipitated were filtered out and washed with DI water 5 times and left to dry in the air at room temperature for 24h. The precipitate had shiny white color.

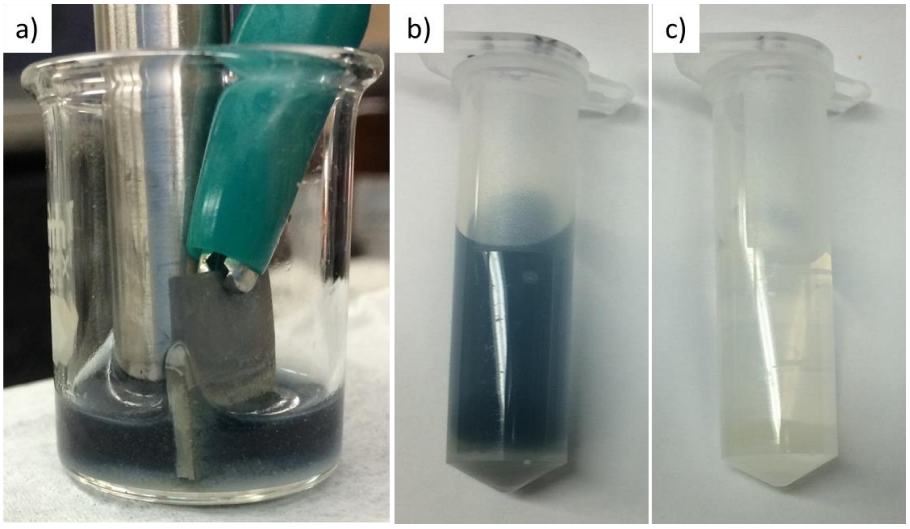

Figure 5.9. (a) Electrochemical cell setup, (b) electrolyte with precipitates collected after 1h of electropolishing, (c) electrolyte with precipitates from the image (b) after 10 minutes.

The EDS analyses on the precipitates are shown in Figure 5.10. It can be seen that there is some oxygen present in the sample and the amount of oxygen, tungsten and potassium is very similar to the amounts found in the shell (Figure 5.4 (a)).

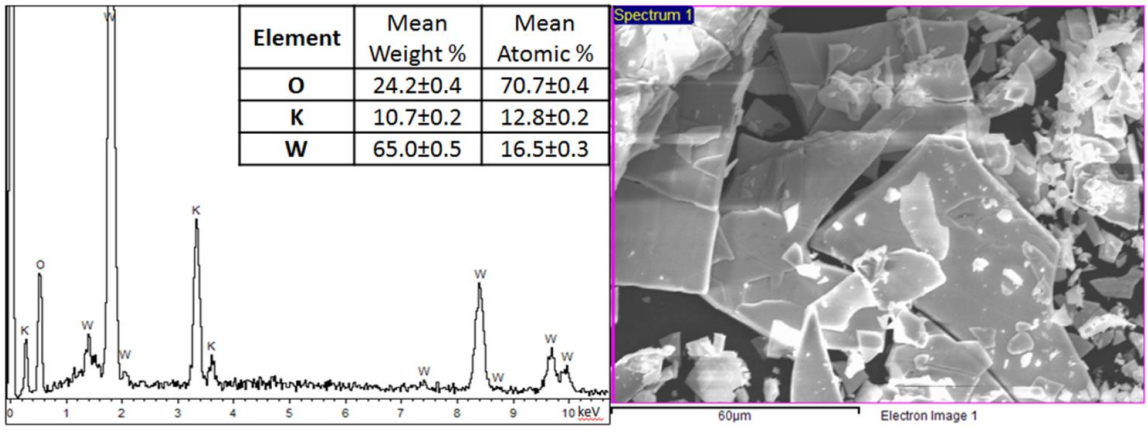

Figure 5.10. SEM-EDS on the precipitates.

The X-ray diffraction patterns on the precipitates before and after DSC run are shown in Figure 5.11. The analysis of the X-ray pattern on the sample as prepared, before

the DSC run, revealed the presence of decapotassium dihydrogendodecatungstate deca-hydrate $K_{10}(H_2W_{12}O_{42})\cdot 10(H_2O)$ card number 01-086-0917. After the DSC run was performed on the precipitates, the X-ray pattern showed that the sample become amorphous. This can be due to decomposition of the sample during the DSC run which showed three distinct decomposition endothermic peaks (Figure 5.13).

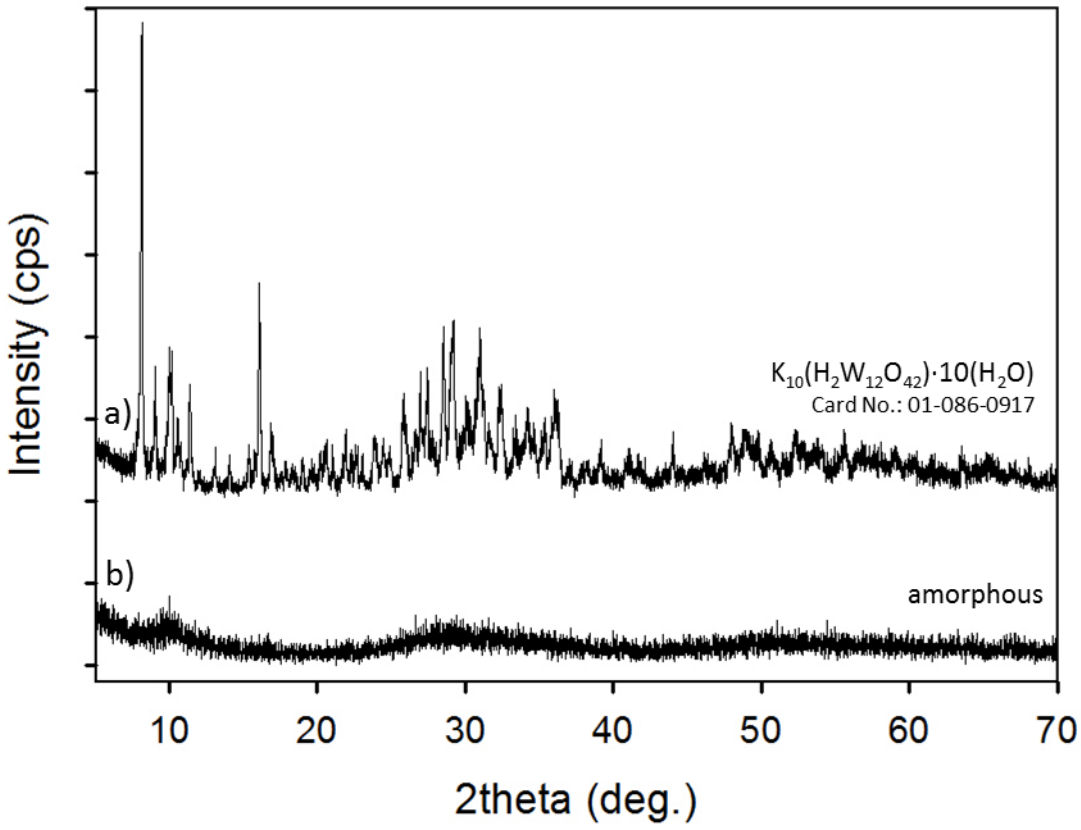

Figure 5.11. XRD patterns of the precipitates (a) before and (b) after the DSC run.

The $K_{10}(H_2W_{12}O_{42})\cdot 10(H_2O)$ structure was reported earlier [30] to form when K_2WO_4 and $WO_3\cdot H_2O$ are stirred together in water. This supports the hypothesis and findings that the shell most likely consists of tungsten trioxide hydrate $WO_3\cdot H_2O$.

The IR spectrum of the precipitates is shown in Figure 5.12 and indicates the presence of the tungsten trioxide hydrate in the sample. The peak at 3358 and 1627 cm^{-1} represent the stretching and bending vibrations of the O-H groups of coordinated water. The peak at 951 cm^{-1} is result of the valence W=O vibrations and the variety of peaks from 500-900 cm^{-1} corresponds to O-W-O stretching [7, 10].

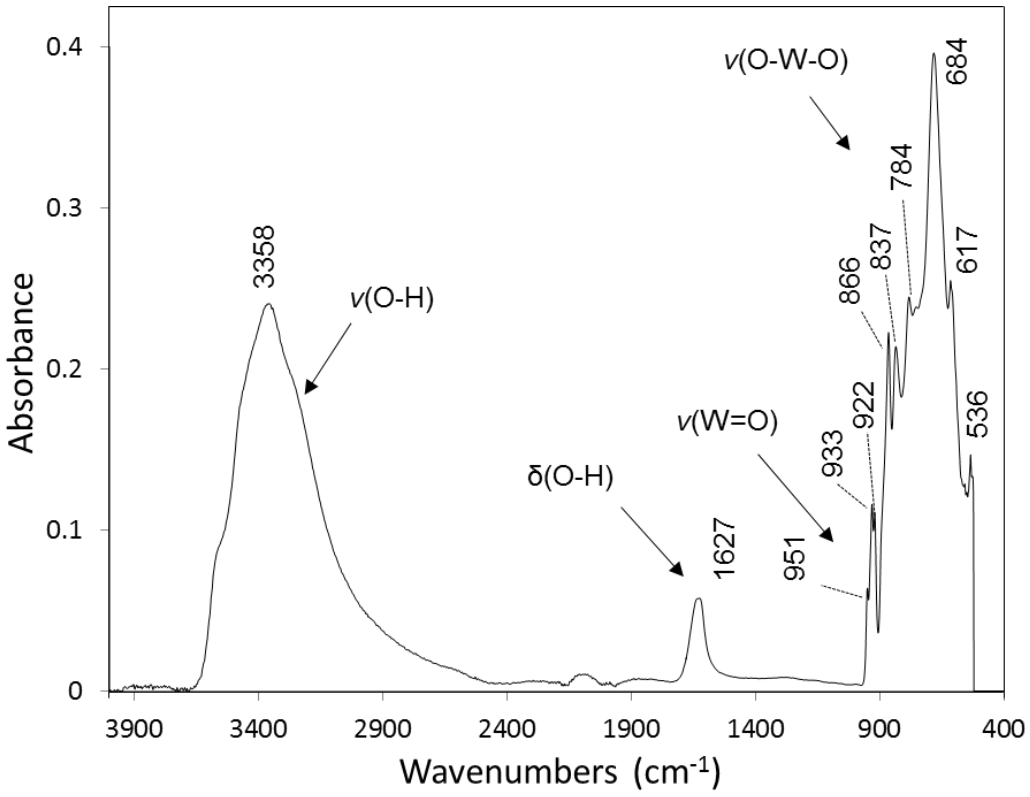

Figure 5.12. IR spectrum of the precipitate formed after electropolishing the tungsten plate in 1.5ml of 2M KOH solution with 2V applied potential for 1h. The distance between the cathode and anode was 3mm.

Figure 5.13 shows the DSC and TGA curves from precipitates. The first endothermic peak on DSC curve at 153˚C can be associated with the first step of the compound decomposition from $K_{10}(H_2W_{12}O_{42})\cdot 10(H_2O)$ to $K_{10}(H_2W_{12}O_{42})$ [7, 12-16].

From the TGA curve the estimated weight loss associated with this peak is equal to 3.46wt.%. The next endothermic peak on the DSC curve at 283.4˚C is accompanied with 0.83wt.% mass loss and can be attributed to the second step of the decomposition of the $K_{10}(H_2W_{12}O_{42})$ with the loss of oxygen, hydrogen and potassium from the structure. The last DSC peak at 377.7˚C with 0.25wt.% weight loss can be associated with decomposition of the remaining compound which resulted in the formation of the amorphous structure (Figure 5.11).

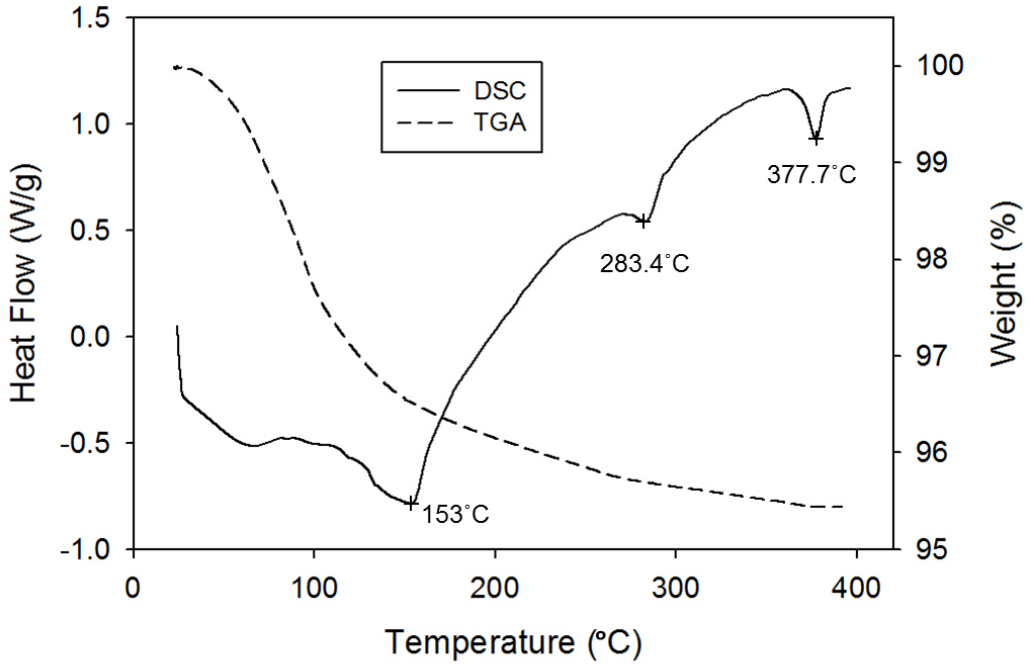

Figure 5.13. DSC and TGA curves of precipitates.

5.5. Conclusions

In summary, using different characterization techniques it was concluded that the shell surrounding the needle during the PLE regime possibly consists of amorphous tungsten trioxide hydrate. The amorphous nature of the shell was discovered using X-ray diffraction analysis and the presence of oxygen was detected using EDS. Also, DSC, TGA and IR techniques revealed the presence of the structurally bonded water. The structure of the shell appeared to be rough and porous with some grains trapped in it.

5.6. References

[1] Nave M, Rubin B, Maximov V, Creager S and Kornev K G 2013 Transport-limited electrochemical formation of long nanosharp probes from tungsten *Nanotechnology* **24** 355702

[2] Natterer F *The Mathematics of Computerized Tomography* (New York: Wiley)

[3] Anik M 2006 Effect of concentration gradient on the anodic behavior of tungsten *Corros Sci* **48** 4158-73

[4] Anik M 2010 Anodic reaction characteristics of tungsten in basic phosphate solutions *Corros Sci* **52** 3109-17

[5] Lassner E and Schubert W-D 1999 *Tungsten: properties, chemistry, technology of the element, alloys, and chemical compounds* (New York: Kluwer Academic/Plenum Publishers)

[6] Kelsey G S 1977 Anodic-oxidation of tungsten in aqueous base *J Electrochem Soc* **124** 814-9

[7] Cao J, Luo B D, Lin H L, Xu B Y and Chen S F 2012 Thermodecomposition synthesis of WO3/H2WO4 heterostructures with enhanced visible light photocatalytic properties *Appl. Catal. B-Environ.* **111** 288-96

[8] Silverstein R M, Webster F X, Keimle D J 2005 *Spectrometric identification of organic compounds* (John Willey & Sons, Inc.)

[9] Daniel M F, Desbat B, Lassegues J C, Gerand B and Figlarz M 1987 Infrared and Raman-study of WO3 tungsten trioxides and WO3, xH2O tungsten trioxides hydrates *J. Solid State Chem.* **67** 235-47

[10] Nogueira H I S, Cavaleiro A M V, Rocha J, Trindade T and de Jesus J D P 2004 Synthesis and characterization of tungsten trioxide powders prepared from tungstic acids *Materials Research Bulletin* **39** 683-93

[11] Salmaoui S, Sediri F, Gharbi N, Perruchot C and Jouini M 2013 Hexagonal hydrated tungsten oxide nanomaterials: Hydrothermal synthesis and electrochemical properties *Electrochim. Acta* **108** 634-43

[12] Zhang L, Tang X C, Lu Z G, Wang Z M, Li L X and Xiao Y H 2011 Facile synthesis and photocatalytic activity of hierarchical WO3 core-shell microspheres *Appl Surf Sci* **258** 1719-24

[13] Nithya V D, Selvan R K, Vasylechko L and Sanjeeviraja C 2014 Surfactant assisted sonochemical synthesis of Bi2WO6 nanoparticles and their improved electrochemical properties for use in pseudocapacitors *RSC Adv.* **4** 4343-52

[14] Yan A H, Xie C S, Zeng D W, Cai S Z and Hu M L 2010 Synthesis, formation mechanism and sensing properties of WO3 hydrate nanowire netted-spheres *Materials Research Bulletin* **45** 1541-7

[15] Gotic M, Ivanda M, Popovic S and Music S 2000 Synthesis of tungsten trioxide hydrates and their structural properties *Mater. Sci. Eng. B-Solid State Mater. Adv. Technol.* **77** 193-201

[16] Mokrejs P, Langmaier F, Janacova D, Mladek M, Kolomaznik K and Vasek V 2009 Thermal study and solubility tests of films based on amaranth flour starch-protein hydrolysate *Journal of Thermal Analysis and Calorimetry* **98** 299-307

[17] Opara-Krasovec U, Jese R, Orel B, Grdadolnik J and Drazic G 2002 Structural, vibrational and gasochromic properties of porous WO3 films templated with a sol-gel organic-inorganic hybrid *Mon. Chem.* **133** 1115-33

[18] Georg A, Graf W, Neumann R and Wittwer V 2000 Stability of gasochromic WO3 films *Sol. Energy Mater. Sol. Cells* **63** 165-76

[19] Georg A, Graf W, Neumann R and Wittwer V 2001 The role of water in gasochromic WO3 films *Thin Solid Films* **384** 269-75

[20] Baetens R, Jelle B P and Gustavsen A 2010 Properties, requirements and possibilities of smart windows for dynamic daylight and solar energy control in buildings: A state-of-the-art review *Sol. Energy Mater. Sol. Cells* **94** 87-105

[21] Lu C H, Hon M H, Kuan C Y and Leu I C 2014 Preparation of WO3 nanorods by a hydrothermal method for electrochromic device *Jpn. J. Appl. Phys.* **53**

[22] Hernandez H E L, Perez C S and Valenzuela A 2008 *Riao/Optilas 2007,* ed N U Wetter and J Frejlich (Melville: Amer Inst Physics) pp 583-8

[23] Hernandez H E L, Perez C S, Valenzuela A G, Garcia A E and Lopez M A C 2007 *Sixth Symposium: Optics in Industry,* ed J C GutierrezVega, *et al.* (Bellingham: Spie-Int Soc Optical Engineering)

[24] Georg A, Graf W, Neumann R and Wittwer V 2000 Mechanism of the gasochromic coloration of porous WO3 films *Solid State Ionics* **127** 319-28

[25] Zhang Z H, Wu G M, Gao G H, Wu J D and Feng W 2011 Influence of MoO3 addition on the gasochromism of WO3 thin films *Seventh International Conference on Thin Film Physics and Applications* **7995**

[26] Hung C J, Huang Y H, Chen C H, Lin P and Tseng T Y 2014 Hydrothermal formation of tungsten trioxide nanowire networks on seed-free substrates and their properties in electrochromic device *IEEE Trans. Compon. Pack. Manuf. Technol.* **4** 831-9

[27] Chen H J, Xu N S, Deng S Z, Lu D Y, Li Z L, Zhou J and Chen J 2007 Gasochromic effect and relative mechanism of WO3 nanowire films *Nanotechnology* **18**

[28] Georg A, Graf W and Wittwer V 2001 The gasochromic colouration of sputtered WO3 films with a low water content *Electrochim. Acta* **46** 2001-5

[29] Zheng F, Lu H, Guo M and Zhang M 2013 Effect of substrate pre-treatment on controllable synthesis of hexagonal WO3 nanorod arrays and their electrochromic properties *Crystengcomm* **15** 5828-37

[30] Fuchs J, Palm R and Hartl H 1996 K7HW5O19 center dot 10H(2)O - A novel isopolyoxotungstate(VI) *Angew. Chem.-Int. Edit. Engl.* **35** 2651-3

6. *In situ* VISUALIZATION OF ELECTROCHEMICAL REACTIONS WITH TRANSMISSION X-RAY MICROSCOPY

6.1. Introduction

In this Chapter, we study kinetics of growth and the structure formation of the porous surface films formed around tungsten wire during electropolishing. These films were introduced in Chapter 1, but the physico-chemical mechanisms of their formation remained unknown. In this chapter, we sketch a scenario of the electrochemical reactions occurring at the tungsten surface and suggest a mechanism of formation of different oxide films based on the *in situ* X-ray imaging and analysis of surface phenomena associated with the electro-chemical polishing.

A tour de force was undertaken to develop a technique for the nanoscale *in situ* visualization of electrochemical processes accompanying electropolishing of tungsten wires. Imaging of electrochemical processes is a very challenging task, especially at the nanoscale level. In this respect, the X-ray phase contrast imaging is advantageous because it allows one to penetrate through the optically dense media and in real time distinguish the morphological features of growing solid films with a high resolution.

As described in Chapter 3, the surface tension of the electrolyte changes upon release of the reaction products at the surface of tungsten. Using X-ray imaging we investigated the change of the meniscus shape during electropolishing. Both techniques, PLE and CLE, were investigated to demonstrate the associated changes of the meniscus profile during electropolishing. We used the nodoid model [1-4] to describe the shape of meniscus confined between the tungsten wire and the capillary wall. This model was employed to fit the meniscus profile with the experimental one and to explain the associated changes of the meniscus profile through the changes in electrolyte concentration caused by the electrochemical reaction. Thus, a transition from CLE to PLE regimes depends on the thermodynamic pathway of electrochemical dissolution of tungsten and can be traced back to the pH changes at the tungsten surface and adsorption/desorption phenomena occurring at this surface.

6.2. Experimental procedure

6.2.1. Transmission X-ray microscopy

We employed the transmission X-ray microscopy (TXM) with the beam line X8C of the National Synchrotron Light Source in Brookhaven National Laboratory [5]. This beam line was used to record the *in situ* electrochemical polishing of tungsten wires with diameter of 50 μm, 75 μm and 125 μm at room temperature.

The schematic of the TXM microscope is shown in Figure 6.1, where the X-ray beam with the 8960 eV energy is focused by the capillary condenser on the sample, tungsten wire. A Fresnel zone plate is used as an objective lens to form an image onto the

CCD detector (2048 x 2048 pixels) with the camera binning 2 x 2 pixels or 4 x 4 pixels with pixel size of 38.9 nm or 77.9 nm respectively. The images were continuously collected with the 1 s exposure time. The field of view was 40 x 40 μm^2.

This technique offers a resolution at a sub-30 nm level in 2D and sub-50 nm in 3D [5]. It also allows continuously collecting images from the stationary sample to form *in situ* 2D movies, or collecting images at the multiple angles while the sample is rotated around its axis using a rotation stage for tomography.

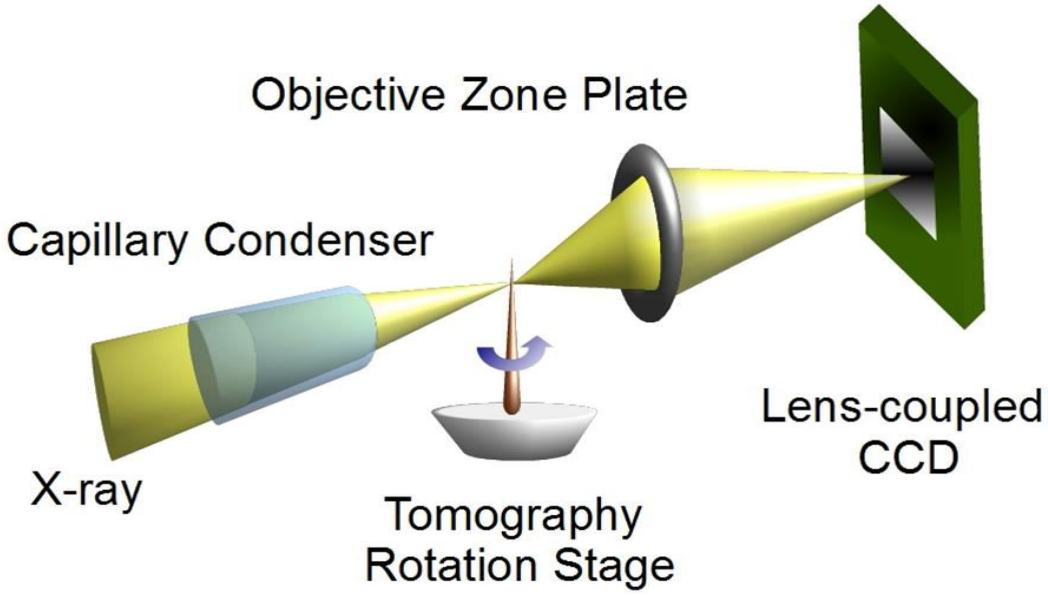

Figure 6.1. Schematic of the TXM instrument [6]

6.2.2. Materials

A 85% potassium hydroxide (KOH) was purchased from AlfaAser® Company. Potassium hydroxide aqueous solution with concentration of 1M was prepared by dissolving KOH flakes in deionized water. The solution was stirred and left to settle for one hour before the experiment. The pH was measured with the pH meter from Denver Instruments UltraBASIC US-10 and for the 1M KOH solution was around pH14. Using Kruss DSA10 instrument with the 1.25mm needle diameter, we measured the surface tension of this solution $\sigma_{1MKOH} = 73.35 \pm 0.17 mN/m$.

The stainless steel wires with 100 μm or 500 μm diameter and 10 mm length were used as cathodes. The tungsten wires of two diameters 125 μm and 75 μm with 99.95% purity were purchased from Advent Research Materials Ltd and served as anodes.

6.3. *In situ* imaging of the tungsten wire during electrochemical polishing when the wire is completely submersed into the electrolyte

6.3.1. A single-tube-electrochemical-cell

For the X-ray visualization, an electrochemical cell composed of a single tube was specially constructed. This cell allowed one to monitor the morphological changes occurring at the tungsten surface along the submersed part of the wire. Figure 6.2 shows a schematic of the setup, where a kapton capillary tube with the inside diameter of 2.05 mm and the length of 20 mm was imbedded from both sides into the thermally cured

Polydimethylsiloxane (PDMS) disks. A tungsten wire was threaded through the needle gage 34, from the bottom side through the PDMS disk into the kapton capillary. Using epoxy, the other side of the tungsten wire was attached to the positive side of the battery. This method allowed one to have about 3mm long piece of the tungsten wire with the diameter of 125 μm inside the tube. The X-ray beam was focused at the 40 μm by 40 μm spot situated 300 μm bellow the free end of the wire. A stainless steel wire with diameter of 500 μm was placed through the PDMS disk from the top side of the capillary tube and was attached to the negative side of the battery with an insulated copper wire.

To start and finish the electrochemical reaction on demand, the copper wire was connected/disconnected with the cathode. In this setup, the cathode and anode were interchangeable. Next, the battery with the tube was glued with epoxy to the kinematic base and placed into the Petri dish to prevent any spills on the TXM stage. The electrolyte was injected into the tube from the top through the pierced hole of the PDMS disk using the 1ml syringe with a gage 27 needle. As shown in Figure 6.2, the tungsten wire was completely submersed into the electrolyte and the meniscus separating the electrolyte from the air was located above the free end of the wire. This setup was designed to study the morphological changes of the tungsten/electrolyte interface and separate these changes from those associated with the free surface of meniscus [7, 8].

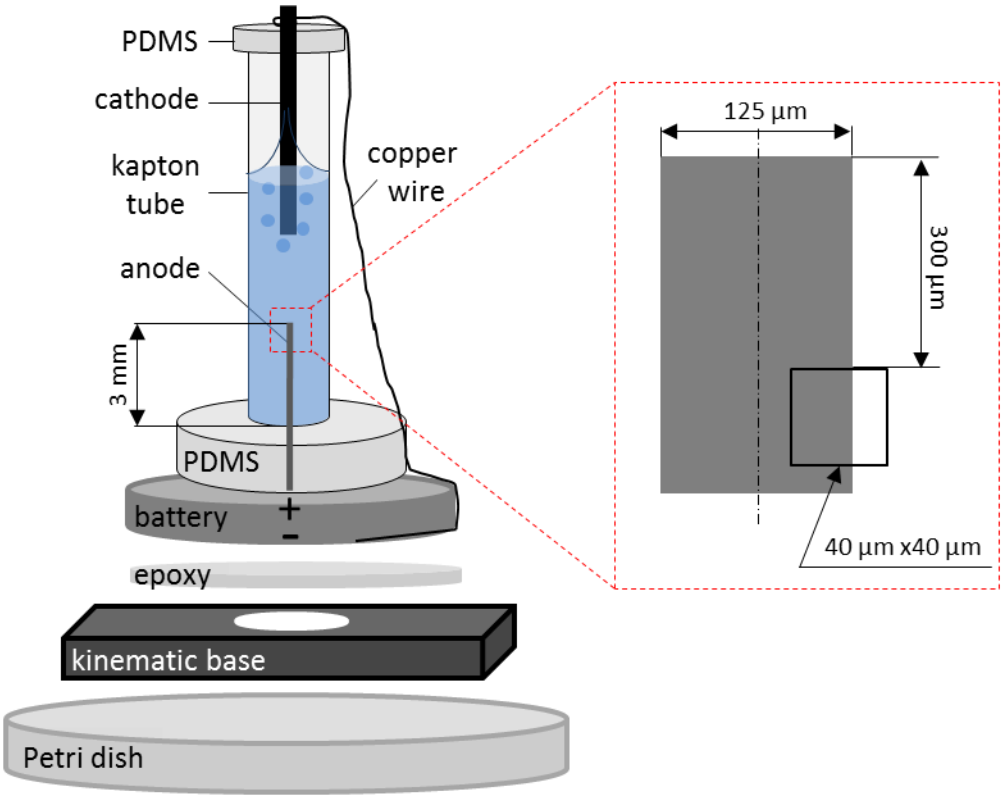

Figure 6.2. The setup of the single-tube-electrochemical-cell.

6.3.2. Morphological changes of the tungsten surface during electropolishing

PLE regime

A sequence of the X-ray images in Figure 6.3 demonstrates the morphological changes of the tungsten surface during electropolishing. The tungsten wire appears black. At the electrochemical reaction progresses, the black region becomes separated from the electrolyte (shown gray) by two distinguishable layers. The first layer that is sitting on top of the tungsten appears darker, hence it is denser. The second layer which is directly exposed to the electrolyte is much brighter, hence it is less dense. The image borders are

fixed in space as shown in the insert of Figure 6.2, therefore, one can follow the electropolishing kinetics by tracing the position of the dark boundary and the boundaries of associated layers. From the sequence in Figure 6.3 (a), one infers that the thickness of the darker layer does not change significantly as compared to that of the brighter layer. Once formed, the first layer remains almost unchanged while the second layer increases in thickness. The level of darkness of the 75 s image in Figure 6.3 (a) is very low suggesting that at the end of electropolishing, the second layer becomes very porous.

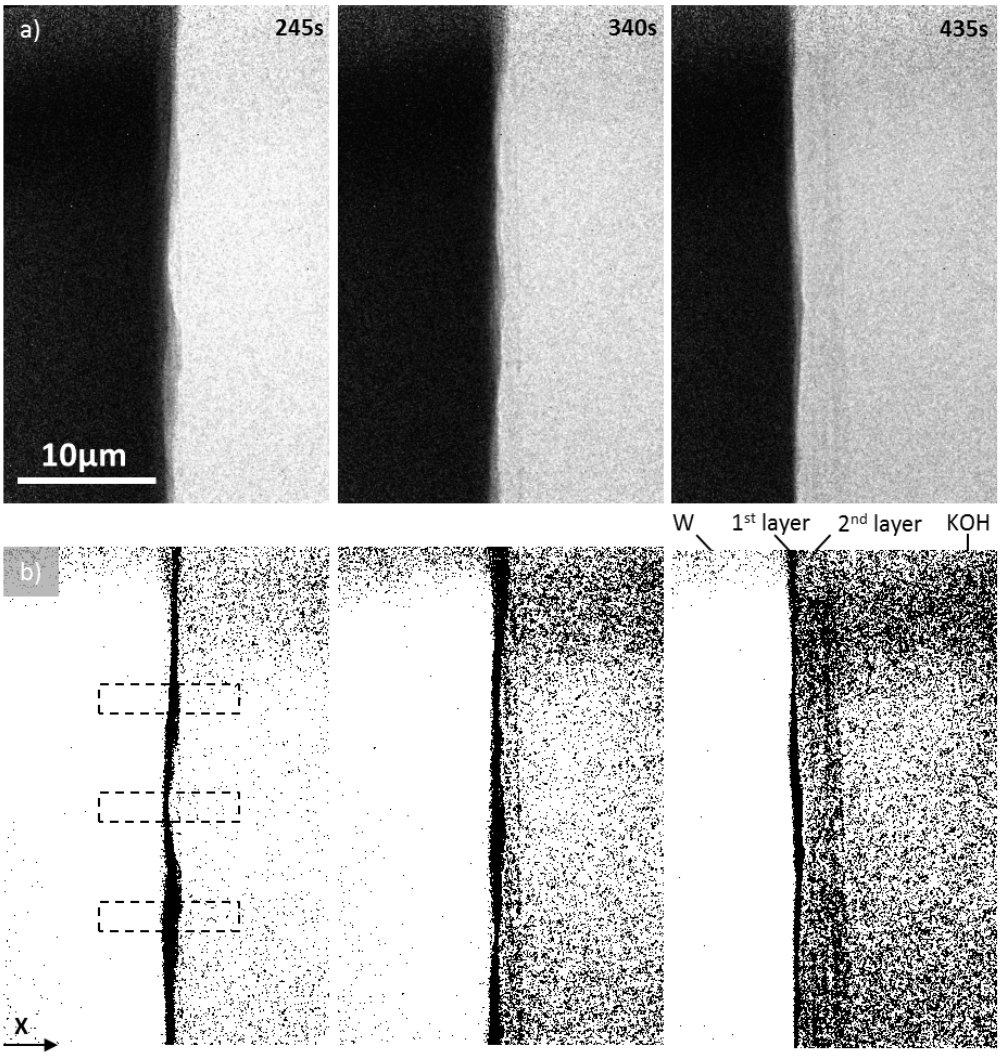

Figure 6.3. The morphological changes of the wire surface during the PLE regime conducted at the voltage difference E=1.55V: (a) a sequence of the *in situ* images showing the layered structure of the tungsten surface and the change of the layer thickness as the reaction progresses, (b) the same sequence of images processed with the ImageJ (NIH) to track the change of the layer thicknesses with time. The layer thicknesses from three dashed boxes were chosen for quantitate analysis.

The images were processed with the ImageJ software (NIH). The original RGB images (Figure 6.3 (a)) were first converted into the 8-bit images, and then into the binary black and white images using thresholding (Figure 6.3b). To determine the rate of change

of the layer thicknesses, three 10 µm × 2 µm dashed boxes shown in Figure 6.3 b were analyzed using Plot Profile function. The thicknesses of the layers as a function of time were extracted and plotted in Figure 6.4. The errors are estimated based on the variation in the thickness layer between the three measured dashed boxes. From the plot is can be seen that the thickness of the first layer remains the same through the reaction, but the thickness of the second layer increases linearly with time.

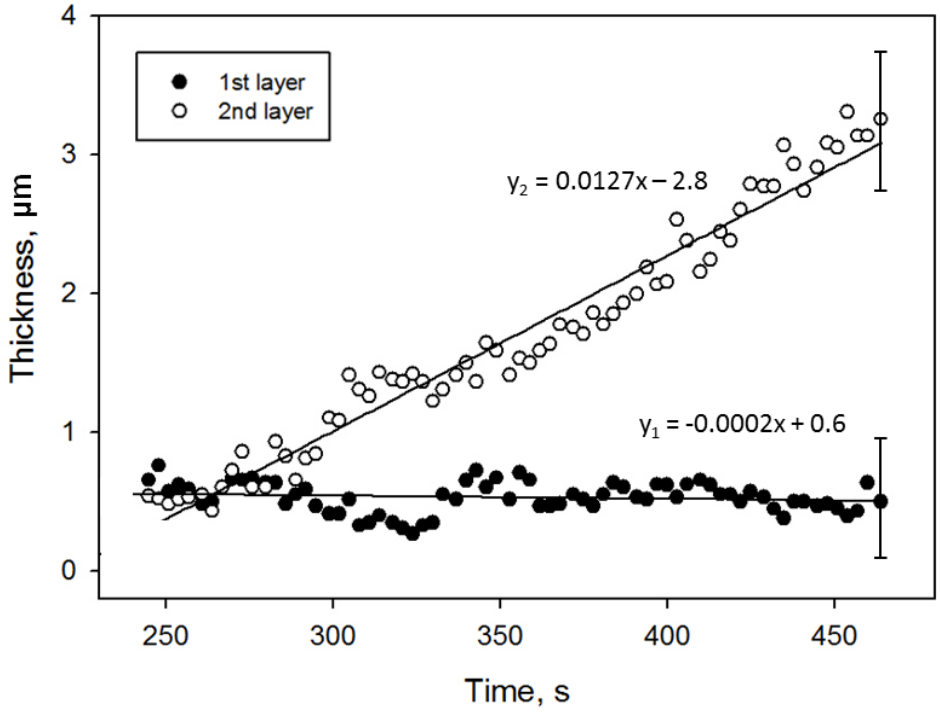

Figure 6.4. The thickness of the layers as a function of time during PLE regime. The error bars corresponds to the highest standard deviation in the experiments.

In Chapter 4 (Figure 6.5 (c)) we concluded that the only stable species that can coexist with the aqueous electrolyte at the positive potentials Eh are the tungstate ions and tungsten trioxide hydrate. The tungstate ions are soluble in the electrolyte and may be present at the pH greater than pH8. One can think that in the bulk of the electrolyte far

away from the tungsten surface where the different products of electrochemical reaction would not contribute to the pH value, tungstate can be present only in the form of these ions. Bellow pH8, the Pourbaix diagram does not allow these ions to occur and the tungsten ions cannot be free either. They would immediately form trioxide hydrate coexisting in equilibrium with the electrolyte.

According to these theoretical results, we can propose a scenario in which the pH value decreases from the bulk toward the tungsten surface. In the bulk of electrolyte where the pH value is large, e.g. pH14 in our experiments, tungsten would be present only as a constituent of the tungstate ions. When we move closer to the wire surface, the pH value should decrease. Indeed, closer to the wire surface the negative tungstate ions get attracted to the wire. Therefore, the hydroxyl groups and protons should also decrease since the tungstate ions displace them. The closer the tungstate ions to the wire, the greater the chance for the electrolyte solution to be oversaturated with them. As shown in Ref. [7], the solution undergoes a phase transition where a viscous film leaning to the wire surface has distinct properties from that of the bulk. Most important is the immiscibility of this viscous film. We therefore proposed that the viscous film was composed of an oversaturated solution of tungstate ions.

If the pH value decreases below some critical value, the solution of tungstate ions cannot exist anymore: these ions react with the hydroxyl groups to form tungsten trioxide hydrate. According to the Pourbaix diagram, tungsten trioxide hydrate can coexist with the electrolyte only as a solid phase (Figure 6.5 (b)). Therefore, if one assumes that tungsten trioxide hydrate nucleates first as a submicron amorphous features [9], it would

be attracted to the wire surface by the van der Waals forces. A similar assumption has been used for explanation of the pore formation in alumina membranes where boehmite AlO2H nanocrystals were hypothesized to play a significant role in building up the barrier layer [10-12]. In the favorable conditions, tungsten trioxide hydrate nuclei would build up a layer. Therefore, we hypothesize that the porous film observed at the wire surface is made of tungsten trioxide hydrate amorphous features sintered together to form a porous solid film. This scenario satisfies the conditions of thermodynamic equilibrium of different species on the Pourbaix diagram. However, the proposed scenario does not follow a scenario of anodic electropolishing of metals [11, 13-23] which does not take into account thermodynamic constrains. These constrains are set on by the Pourbaix diagrams. To the best of our knowledge, while the two-layer model has been sugested for almost half a century ago, the current literature dealing with electropolishing does not address the thermodynamic limitations associated with incorporation of electrolyte anions such as OH groups into the oxide structure [11, 13-23].

The Pourbaix diagram constructed for the aqueous electrolytes is unable to predict the chemical composition of the first layer separating tungsten from the tungsten trioxide hydrate layer. In the X-ray phase contrast images, the first layer appears much denser than the second and we hypothesize that it is likely to be made of a solid tungsten oxide. This hypothesis is supported by multiple observations on tungsten surface [8, 24-26]. However, we cannot predict what type of oxide can be stable in these conditions.

The proposed scenario provides a sufficient flexibility for observation of different regimes of electropolishing. The local concentration of tungstate ions and the pH values

are interconnected through the Pourbaix diagram hence cannot be arbitrary changed. As we mentioned, the oversaturated solution of the tungstate ions cannot exist below some critical pH value. This value depends on the concentration of tungstate ions in solution. Figure 6.5 (c) and (d) demonstrate that at the beginning of the electrochemical etching, when concentration of the tungstate ions is very small, for example, $[WO_4^{2-}] = 10^{-8} M$, the hydrate can be stable in the acidic environment, at the pH level lower than pH5.14 (Figure 6.5 (d)). However, once the concentration of the tungstate ions increases, for instance, up to $[WO_4^{2-}] = 10^{-2.64} M$, the hydrate becomes stable in more basic environment with the pH value lower than pH7.82 (Figure 6.5 (e)).

Therefore, during the PLE regime, electrochemical oxidation of tungsten in a potassium hydroxide solution proceeds with the formation of the following reaction products: tungsten oxide forming a layer on the tungsten surface, then tungsten trioxide hydrate layer which is sitting in contact with the tungsten oxide layer and separate it from the electrolyte. The layer of tungsten trioxide hydrate is porous and can contain aqueous solution of tungstate and potassium ions. In the bulk of electrolyte, we expect to observe only tungstate and potassium ions.

As follows from the EDS analysis showed in Chapter 5 for the shell from PLE regime, the stoichiometric ratio of oxygen to tungsten at the surface of tungsten is about 2.4 suggesting that the WO_2 oxide is a best candidate to be the constituent of the oxide layer formed in the PLE regime. The Pourbaix diagrams support this hypothesis. Indeed, for the positive potentials *Eh*, if we move from the bulk where only tungstate ions can be found toward the porous shell formed by the insoluble $WO_3 \cdot H_2O$ compound, we see that

the only oxide which is able to coexist with this compound is the WO_2 oxide. However, one has to assume that the applied potential has to drop at the oxide surface to make this phase coexistence possible. This potential drop is most likely related to a complex band bending at the surface of tungsten dioxide and a complex zone structure which place the tungsten dioxide between metals and semiconductors [27-35]. We do not consider this problem in dissertation.

This partitioning explains the X-ray images in Figure 6.3 (a), where the dark part is tungsten; next to it is a thin gray layer representing the tungsten oxide and then a thick light gray layer represents the tungsten trioxide hydrate amorphous features fused together. Optical imaging was used to complement this scenario. Figure 6.5 (a) shows the kinetics of the layers formation. Before application of voltage, there were no any flows of electrolyte around the tungsten wire. Once the voltage is applied, the tungsten surface appears surrounded by a denser fluid that flows downwards (Figure 6.5 (a)), the 100s image, arrows point a layer of a denser fluid). This electropolishing regime with a flowing film was analyzed in details in Ref. [7] and proved to represents a highly concentrated solution of tungstate ions that are formed as a result of the tungsten oxidation process. The 255s image in Figure 6.5 (a) illustrates the formation of a solid porous layer completely wrapping the tungsten wire. The analysis of movies suggests that a thin viscous film is always flowing down over the surface of this porous layer. Therefore, the layer of highly concentrated solution of tungstate ions fills the pores and spreads beyond the boundary of the porous tungsten trioxide hydrate film.

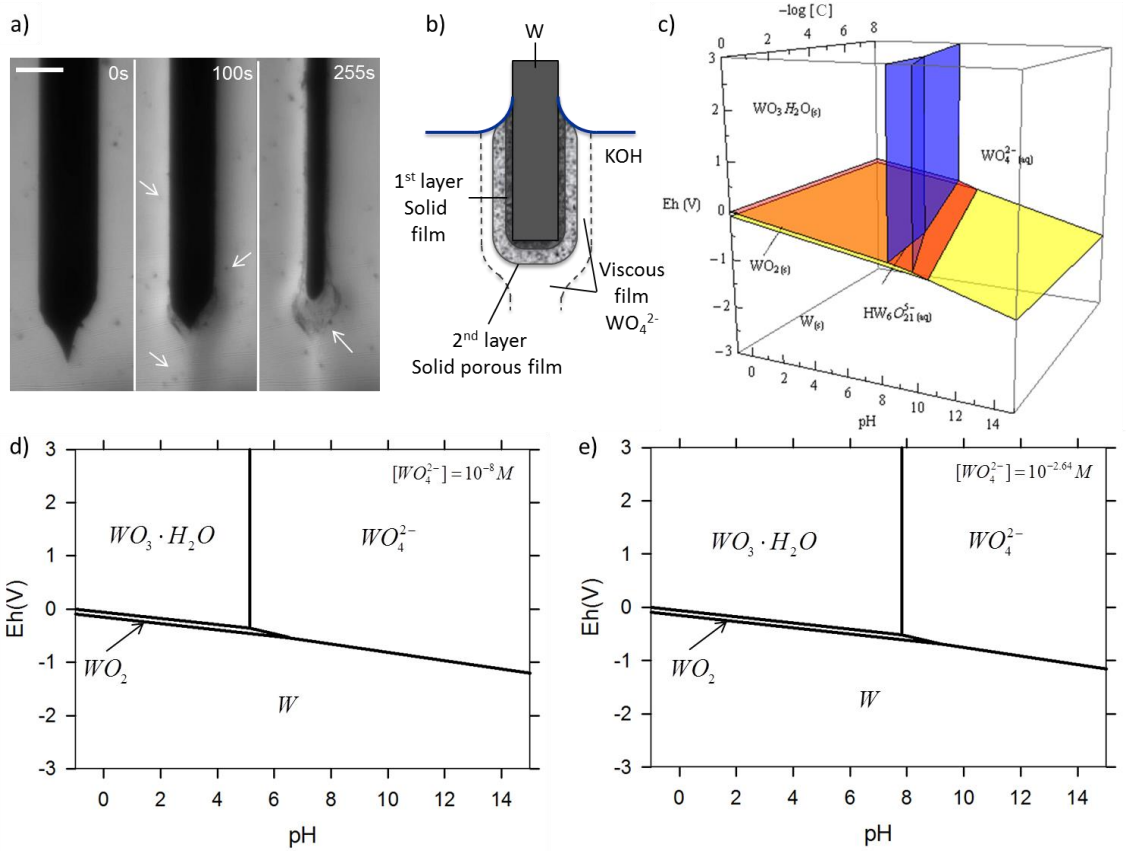

Figure 6.5. (a) Kinetics of the PLE regime where the arrows on the 100s frame point the viscous film and the arrows on the 255s frame the mark a solid porous film; (b) the schematic of the layer hierarchi: electrolyte - highly viscous immiscible film - porous layer – dense layer of s tungsten compaund – tungsten wire; (c) the 3D Pourbaix diagram for tungsten in aqueous solution; (d), (e) the 2D cross-sections of the 3D Pourbaix diagram taken at the concentration of soluble species $\left[WO_4^{2-}\right]=10^{-8}M$, $\left[WO_4^{2-}\right]=10^{-2.64}M$ respectively.

The existing models of formation of oxide layers and incorporation of polyelectrolyte anions into it with creation of the second layer assume that the thickness of oxide film increases linearly with time at a constant current [15]. Our experimental conditions provided almost constant current, Figure 1.3 (a), but we did not observe any dependence of the thickness of oxide layer on time. This suggests that the amount of

metal ions consumed in the oxidation reaction is exactly equal to the amount of oxide molecules removed from the oxide surface either in the form of dissociated ions or as new chemical complexes.

CLE regime

During the CLE regime, we did not observe the second layer, Figure 6.6. To distinguish the oxide layer growing on top of the tungsten surface, we used the same image tracking algorithm in the ImageJ program. During the time of observation, the layer appeared very stable and its thickness $h = 0.52 \pm 0.13$ μm did not change appreciably throughout the experiment. The thickness h was approximately the same as that we observed in the PLE regime for the first layer. We therefore hypothesize that this layer is formed by some tungsten oxide.

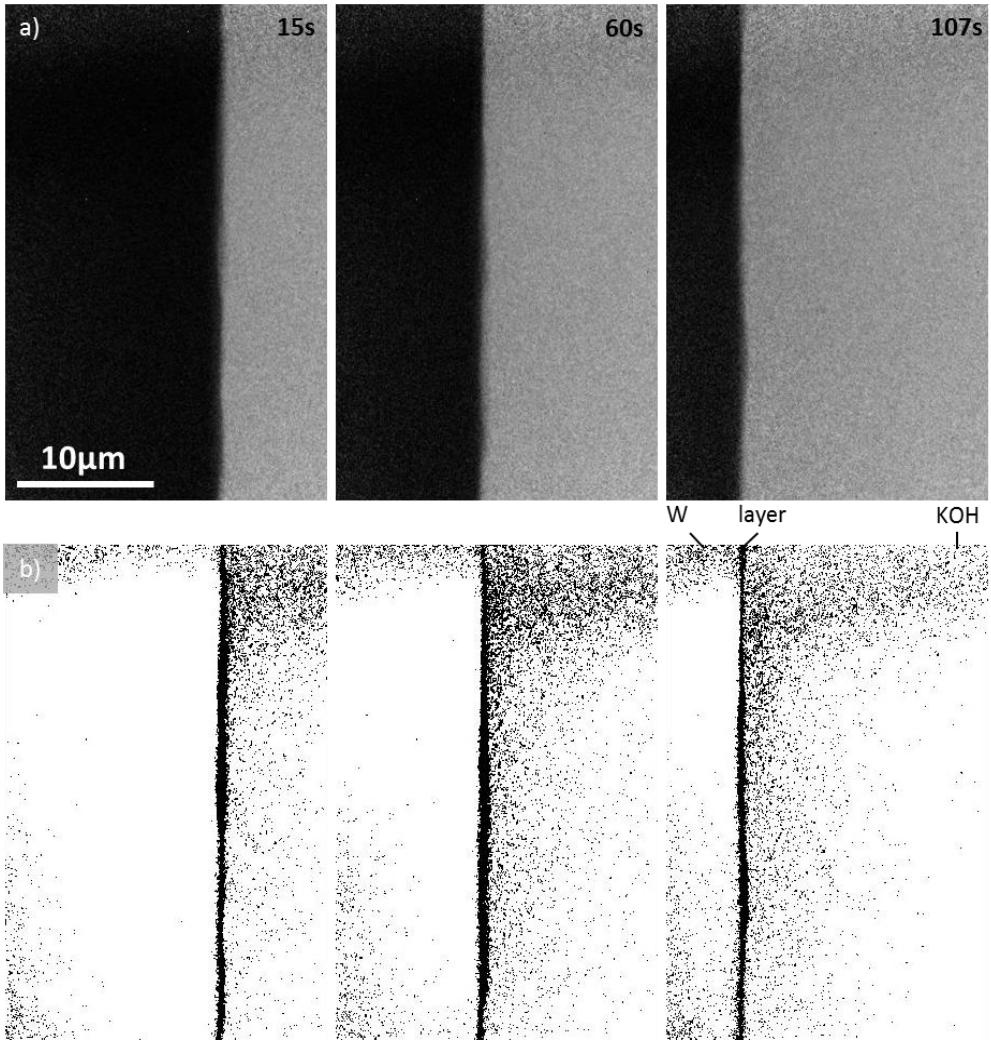

Figure 6.6. CLE oxidation kinetics of tungsten; experiments were conducted at the voltage difference of E=3V: (a) segments of the *in situ* images showing the growth of the single layer on top of the tungsten surface, (b) ImageJ processed pictures demonstrate the evolution of the layer formation.

In order to prove these hypotheses we will examine the wetting properties of the tungsten wires electropolished in different regimes. It is well known that the surface tension and contact angles of electrolyte solutions are very sensitive to the concentration of dissolved salts and adsorption ions on the electrolyte/substrate interfaces [36-40]. However, usually contact angle measurements are not accompanied by the surface

tension measurements and vice versa. For this reason we designed a new electrochemical cell, presented in the following Section, which can measure all parameters simultaneously. In Chapter 3 we confirmed a strong dependence of surface tension of tungstate solutions on the concentration of dissolved ions and we will use these data to investigate the feasibility of the proposed scenario of formation of the porous film.

6.4. *In situ* imaging of the tungsten wire electrochemical etching in the meniscus region

6.4.1. U-shaped electrochemical cell

The single tube microfluidic cell with tungsten wire did not suit the experimental procedure of imaging the menisci when the tungsten wire is partially submersed in the electrolyte: the hydrogen bubbles formed at the cathode disturb the meniscus surface. In order to make the *in situ* visualization of the morphological changes of the wire surface and meniscus development, a special microfluidic electrochemical cell was designed and constructed.

The cell consisted of two kapton tubes of different diameters inserted into the four way flow cell to make up a U-shaped electrochemical device. The double elbow connector of the four way flow cell has the inside diameter of 1.19 mm, the height of 10.5 mm and the width of 22.9 mm. This double elbow connector was made of polypropylene and purchased from Value Plastics, Inc (Figure 6.7 (a), (b)). In the experiments, two extra ports of the four way flow cell were closed (Figure 6.7 (c)) by melting the plastic and

sealing the openings of this vessel. In general, these extra ports can be used to pump electrolytes into the cell or for using additional electrodes.

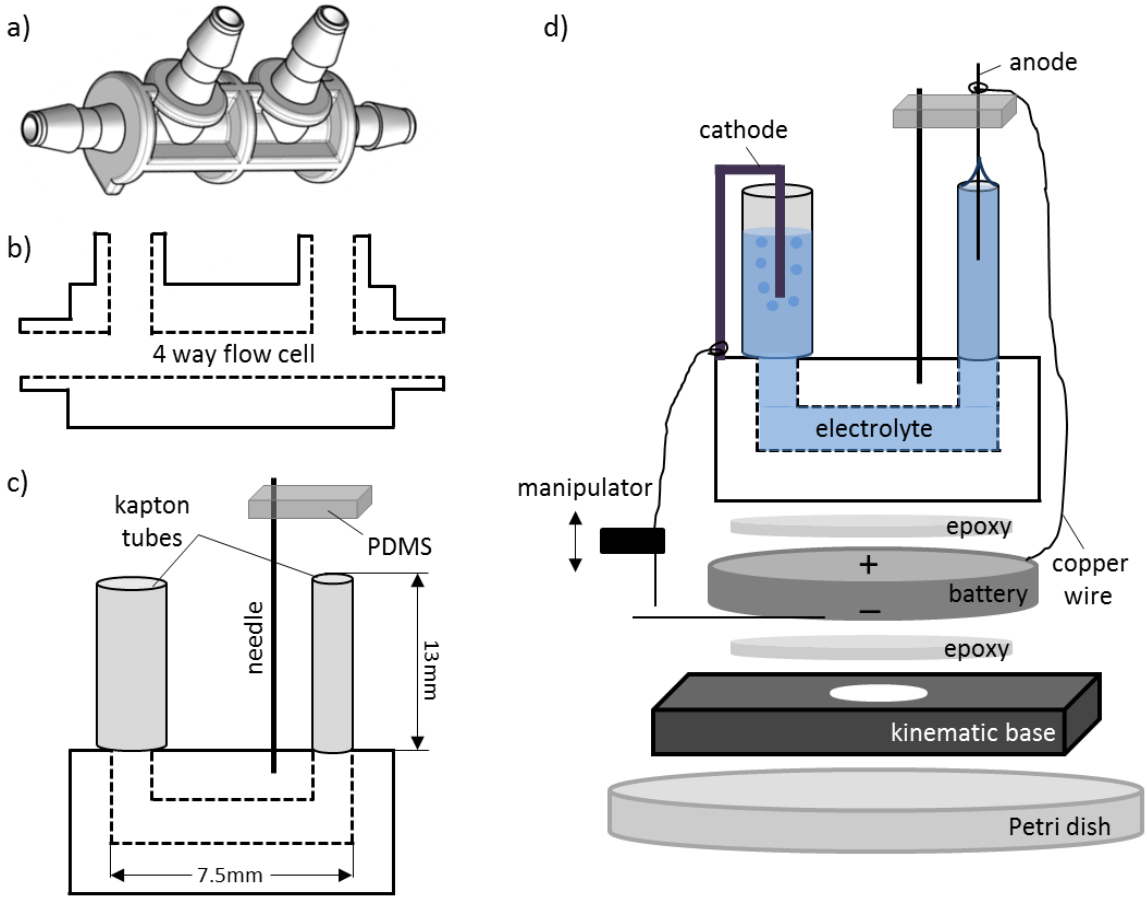

Figure 6.7. The setup of the microfluidic electrochemical cell: (a) a schematic of the four way flow cell [41], (b) the cross section of the flow cell, (c) kapton tubes are inserted vertically into two ports of the four way flow cell; two extra ends are being sealed. To hold the anode, a needle with the PDMS mold was vertically inserted into the wall of the four way flow cell. (d) The U-shaped flow cell filled with the electrolyte. The electrodes are inserted in the tubes, both connected to a battery underneath the cell. Using epoxy, the battery was glued from one side to the kinematic base and from another side to the flow cell.

The inside diameters of kapton tubes were 1.02 mm and 2.05 mm and the walls of these tubes have 76 μm thicknesses. The flow cell with the kapton tubes was glued with epoxy to the disk-like battery and then to the kinematic base (Figure 6.7 (d)) purchased from THORLABS, Inc.

Two types of batteries from NUON® were used in the experiments: the 1.55V silver oxide and 3V lithium batteries. The copper wire was used to connect the battery to the electrodes. Also, a 2D manipulator was used to control the initiation/completion of the electrochemical reaction by mechanically connecting/disconnecting the copper wires.

The potassium hydroxide electrolyte was injected into the U-shaped capillary from the top of the wider tube using a 1ml syringe with a needle gage 27. A thinner tube was filled to the top providing the h'_1=13mm height liquid column. The liquid column of the height of h_2=6mm was simultaneously formed with the other arm of the U-shaped tube, Figure 6.7 (d).

Both electrodes, cathode and anode, were immersed into different legs of the U-shaped microfluidic cell pre-filled with the aqueous solution of potassium hydroxide. The anode with diameter of 75 μm was placed into the thinner leg of the U-shaped tube and connected with a copper wire to a plus side of the disk-like battery located under the cell. The cathode with diameter of 100 μm was placed in the wider capillary and connected through the copper wire to the minus side of the same battery.

6.4.2. Pressure difference in the U-shaped microfluidic cell

When the capillary is brought in contact with the liquid, it spontaneously flows inside the tube, rising up to a certain height. The schematic in Figure 6.8 demonstrates the liquid rise in the capillary, where R is the capillary radius, h is the height of the liquid column, θ is the contact angle that the liquid makes with the wall of the capillary and R' is the radius of the meniscus.

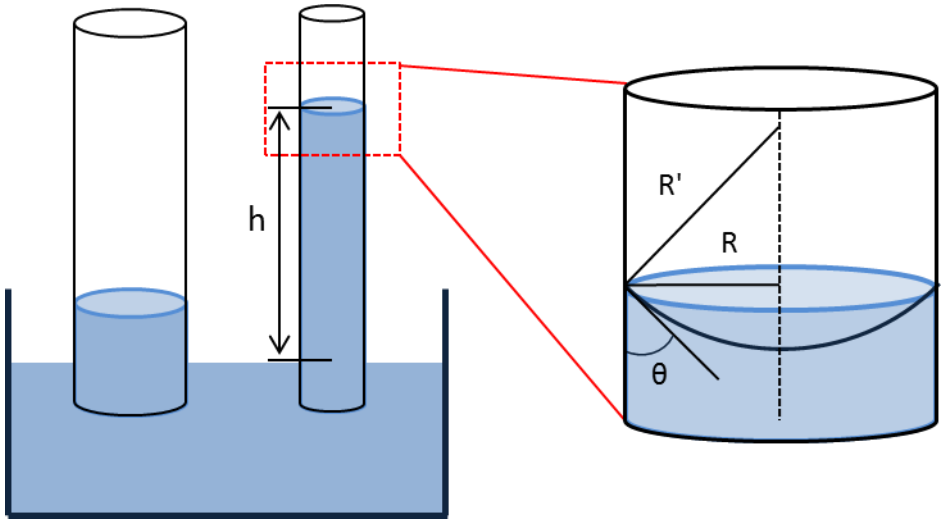

Figure 6.8. The schematic of the liquid rise in the capillaries immersed into the beaker with water; an enlarged view of the meniscus inside the capillary show the tube radius, meniscus radius and the contact angle.

The Young-Laplace law states that the pressure difference ΔP across the liquid interface relates to the surface tension of the liquid and the radius of the capillary in the following form:

$$\Delta P = P_{atm} - P_l = \frac{2\sigma \cos\theta}{R}, \tag{6.1}$$

where P_{atm} is an atmospheric pressure, P_l is a pressure under the meniscus.

According to hydrostatics, when the liquid column reaches its equilibrium, the pressure in the liquid at height h reads:

$$\Delta P = P_0 - P_l = \rho g h, \tag{6.2}$$

where $g = 9.8 m/s^2$ is the gravitational acceleration and ρ is the liquid density. The reference pressure P_0 is unknown in advance and must be found from the analysis of the pressure distribution in the U-shaped tube.

Rearranging and combining two eq. (6.1) and eq. (6.2) we can write:

$$P_{atm} - \frac{2\sigma \cos\theta}{R_c} = P_o - \rho g h \tag{6.3}$$

In the case of the U-shaped tube that is shown in Figure 6.9 (a) we can write eq. (6.3) for each capillary separately. Thus, for the capillary number 1, having the liquid column of height h_1 one can rewrite:

$$P_{atm} - \frac{2\sigma \cos\theta_1}{R_1} = P_o - \rho g h_1 \tag{6.4}$$

And for the capillary number 2 with the liquid column of height h_2 we have:

$$P_{atm} - \frac{2\sigma \cos\theta_2}{R_2} = P_o - \rho g h_2 \tag{6.5}$$

Subtracting eq. (6.4) from eq. (6.5) the following relation is obtained:

$$2\sigma\left(\frac{\cos\theta_1}{R_1} - \frac{\cos\theta_2}{R_2}\right) = \rho g\left(h_1 - h_2\right) \tag{6.6}$$

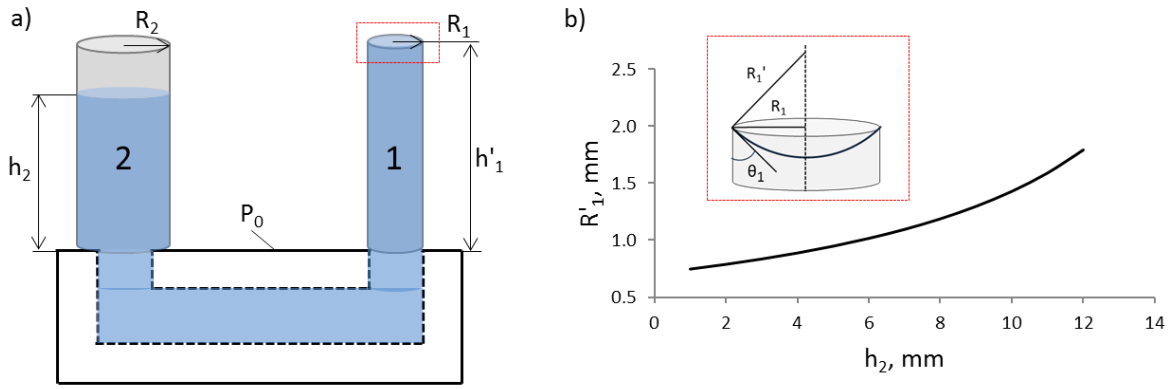

Figure 6.9. (a) A schematic of the U-shaped tube with capillaries, (b) meniscus radius in the capillary number 1 as a function of the liquid height in the capillary number 2. The insert shows illustration of the menisci in the capillary number 1.

In our experiments, we filled the thinner tube up to the brim. Therefore, the height of the liquid column h_1' stays constant in capillary 1 (Figure 6.9 (b) insert). However, the radius of meniscus R_1' in this capillary changes with the change of the liquid elevation in tube 2. We rewrite eq. (6.6) in the following form:

$$\frac{2\sigma}{R_1'} - \frac{2\sigma\cos\theta_2}{R_2} = \rho g\left(h_1' - h_2\right) \tag{6.7}$$

For convenience, eq. (6.7) can be rewritten as:

$$R_1' = \frac{R_2}{\cos\theta_2}\cdot\frac{1}{\left(\dfrac{\rho g\left(h_1' - h_2\right)R_2}{2\sigma\cos\theta_2} + 1\right)}, \tag{6.8}$$

where the height of the liquid column in the thinner capillary is equal to $h_1' = 13mm$, the contact angle $\theta_2 = 60°$ was found experimentally, the liquid density of 1M

KOH electrolyte is $\rho_{1MKOH} = 1058 kg/m^3$ [42] and surface tension $\sigma_{1MKOH} = 73.32 mN/m$ [43].

The correlation between the meniscus radii in capillary 1 with the height of the liquid column in capillary 2 is presented in Figure 6.9 (b). During the *in situ* X-ray experiment, the liquid in capillary 2 does not changes significantly. It stayed almost constant at the $h_2 = 6 \pm 0.5 mm$ height bending the meniscus in capillary 1 to $R_1' = 1.015 \pm 0.05 mm$.

These estimates helped to find the optimal height of the liquid in capillary number 2 in order for the meniscus in the capillary number 1 to be the most stable in this configuration. When the height of the meniscus resting on the wall of the capillary 2 was around 6mm, the meniscus in the capillary 1 was filled to its rim. When the height of the meniscus in the capillary 2 was lowered by 100 μm down, the meniscus in the capillary 1 stayed at the rim but meniscus sagging R_1' was changed by 10 μm. This change in the meniscus sagging was considered negligible. Therefore, the setup for the *in situ* visualization of electrochemical reaction with transmission x-ray microscopy was designed taking into account these approximations.

6.4.3. Meniscus evolution during electrochemical etching

During electrochemical etching, the metal continuously oxidizes with release of the reaction products into the electrolyte. Therefore, the latter changes its chemical composition and, consequently, its surface tension. The meniscus is quasi-stationary in all

experiments; hence it is safe to assume that the concentration of adsorbed ions is uniform over the meniscus surface. Changes in the surface tension during the electrochemical reaction has been previously noticed in the literature [38-40, 44, 45], but this effect has never been thoroughly studied. To confirm that the surface tension does change during the reaction, we examined the behavior of meniscus formed at the tungsten wire and supported by the capillary tube, Figure 6.10.

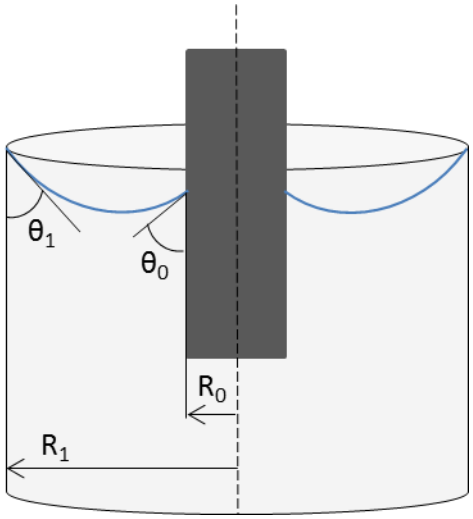

Figure 6.10. A schematic of the wire immersed in the liquid in the thin capillary depicting the meniscus formed on the wall of the capillary and on the wire.

We assume that the wire is positioned along the axis of the thinner tube (Figure 6.10). If the capillary pressure under meniscus formed between the wire and capillary wall is ΔP, the force balance reads [2]:

$$\pi\left(R_1^2 - R_0^2\right)\Delta P = -\sigma\left(2\pi R_1 \cos\theta_1 + 2\pi R_0 \cos\theta_0\right), \tag{6.9}$$

where R_1 is the radius of capillary 1, R_0 is the radius of the wire immersed into the liquid, θ_1 is the contact angles that the meniscus makes with the brim of the capillary and

θ_0 is the contact angle that the meniscus makes with the wire (Figure 6.10). Solving eq. (6.9) for the capillary pressure, one obtains:

$$\Delta P = -\frac{2\sigma\left(R_1\cos\theta_1 + R_0\cos\theta_0\right)}{\left(R_1^2 - R_0^2\right)} \tag{6.10}$$

This pressure difference is comparable with the pressure difference in eq. (6.8). Therefore, the effect of the meniscus deformation caused by the wire has to be taken into account when we analyze the behavior of menisci in the U-shaped tube.

As follows from eq.(6.10), when the cathode is inserted in the second tube, the capillary pressure does not change significantly. Indeed, considering the limit as R'_0/R_2 goes to zero, the leading term of the asymptotic expansion of eq. (6.10) takes on the form:

$$\begin{aligned}\Delta P &= -\frac{2\sigma\left(R_2\cos\theta_2 + R_0'\cos\theta_0'\right)}{\left(R_2^2 - R_0'^2\right)} = \\ &= -\frac{2\sigma\left(\cos\theta + (R_0'/R_2)\cos\theta_0'\right)}{R_2\left(1 - R_0'^2/R_2^2\right)} \approx -\frac{2\sigma\left(\cos\theta_2\right)}{R_2},\end{aligned} \tag{6.11}$$

where R'_0 is the radius of the cathode.

In other words, the capillary pressure in the second tube is still controlled by the semi-spherical part of the meniscus and the perturbation of the meniscus by the wire is not significant for this tube. Hence, eq. (6.5) still holds true. However, we have to change eq. (6.4) replacing the capillary pressure with eq. (6.10) as:

$$P_{atm} - \frac{2\sigma\left(R_1\cos\theta_1 + R_0\cos\theta_0\right)}{\left(R_1^2 - R_0^2\right)} = P_o - \rho g h_1' \tag{6.12}$$

Subtracting eq. (6.12) from eq. (6.5) the following relation is obtained:

$$2\sigma\left(\frac{\left(R_1\cos\theta_1+R_0\cos\theta_0\right)}{\left(R_1^2-R_0^2\right)}-\frac{\cos\theta_2}{R_2}\right)=\rho g\left(h_1'-h_2\right) \tag{6.13}$$

This relation connects the height of the meniscus in capillary 1, h_1', angle θ_1 and other parameters of the U-shaped tube and anode. Thus, if the contact angles θ_1 and θ_0 are known, measuring the height of the meniscus in the capillary 2, one completely specifies the position of meniscus in the capillary 1. We suggest using the experimental meniscus profile to determine contact angle θ_1 by fitting it with the model prediction.

Determination of the meniscus shape

The curved surface of the meniscus that is formed when the wire is immersed into the liquid inside the thin capillary can be fitted with the nodoid. The nodoid is one of axisymmetric solutions of the capillary equation, when the gravity is absent. The equation for the nodoid relates the pressure and surface tension of the liquid, thus enabling us to use this model to find the surface tension of the electrolyte under meniscus by fitting the nodoid to the shape of the meniscus.

To define the shape of the meniscus created by immersing the wire into the liquid in the thin capillary (Figure 6.10) one needs to solve the Laplace law of capillarity:

$$\Delta P=\sigma\left(\frac{1}{r_1}-\frac{1}{r_2}\right)=2H\sigma \tag{6.14}$$

If we put forward an assumption that locally each surface described as a portion of an egg or a saddle, then introducing an orthogonal system of curvilinear coordinates,

we can say that each curve can be a circle of either radius r_1 or r_2. Consider that each curve can be described by the function y=y(x) (Figure 6.11 (a)).

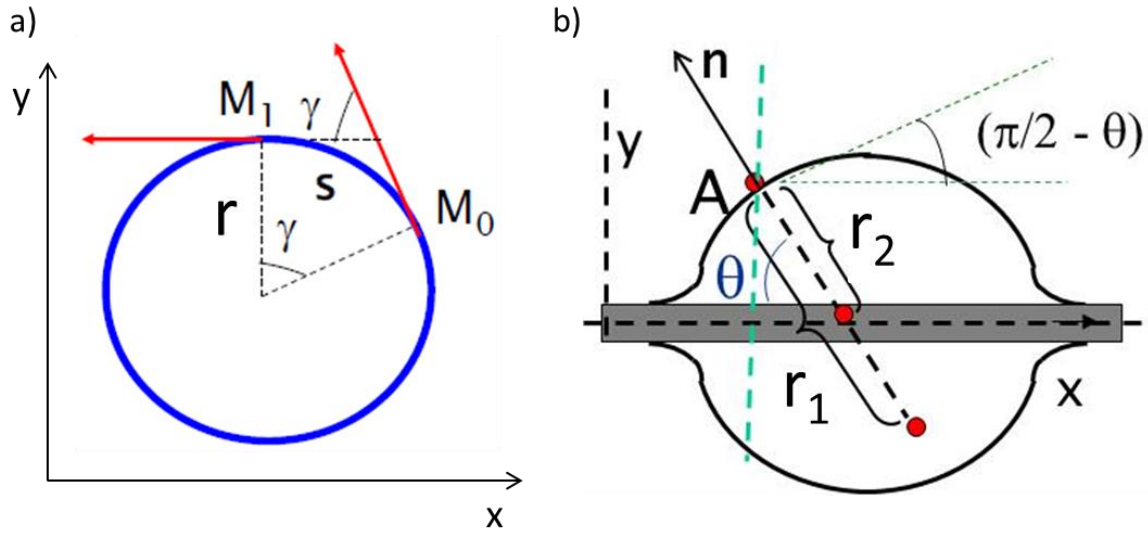

Figure 6.11. (a) Definition of the curvature through the rate of change of the direction of the tangent vector. (b) Schematic of a drop on a wire. It helps define the curvatures in the derivation of the nodoid.

From Figure 6.11 (a) we can see that if we move from the point M_0 to the point M_1 the tangent line rotates and the angle γ changes accompanied by the distance s that the initial point travels when it rotates. Therefore, as s→0 the curvature K can be expressed as:

$$K = \frac{\lim \gamma}{s} = \frac{d\gamma}{ds} \tag{6.15}$$

From a simple geometry the angle γ is written as:

$$\gamma = \arctan \frac{dy}{dx} \tag{6.16}$$

Using eq. (6.16) we can define dγ/ds as:

$$\frac{d\gamma}{ds} = d\left(\frac{dy}{dx}\right) \Big/ ds\left[1+\left(\frac{dy}{dx}\right)^2\right] \tag{6.17}$$

Accounting for the equation for the distance that the point travels we get:

$$ds = \sqrt{(dx)^2 + (dy)^2} = dx\sqrt{\left[1+\left(\frac{dy}{dx}\right)^2\right]} \tag{6.18}$$

Finally, the curvature K is expressed as:

$$K = \frac{d^2y}{dx^2}\left[1+\left(\frac{dy}{dx}\right)^2\right]^{-3/2} \tag{6.19}$$

Now, using the schematic in Figure 6.11 (b) and taking into account the definition of curvature, 2H, the Laplace's law, is written as:

$$2H = -\frac{d^2y/dx^2}{\left[1+(dy/dx)^2\right]^{3/2}} + \frac{1}{r_2} \tag{6.20}$$

Using the geometry from Figure 6.11 (b) the radius r_2 can be expressed as:

$$r_2 = \frac{y}{\sin\theta} = y\sqrt{1+\cot^2\theta} \tag{6.21}$$

where $\cot\theta = dy/dx$, then eq. (6.21) can be rewritten as:

$$r_2 = x\sqrt{1+\left(\frac{dy}{dx}\right)^2} \tag{6.22}$$

If we combine eq. (6.14) with eq. (6.20) and rearranging it we can write the Laplace law as a system of two equations:

$$dy/dx = u \tag{6.23}$$

$$\frac{du}{dx} = \frac{1+u^2}{y} - \frac{\Delta P\left(1+u^2\right)^{3/2}}{\sigma} \tag{6.24}$$

These two equations must be solved together to describe the meniscus profile.

Meniscus as a Nodoid. Determination of the meniscus height

One can suggest the following algorithm to fit the experimental meniscus profile:

1. First define the constant parameters obtained from the experiment:

$R_0 = 37.5\mu m, R_1 = 510\mu m, R_2 = 1025\mu m, \theta_2 = 60°$

2. Define the contact angle θ_0 from the images using the pixels nearest to the wire surface.

3. Substituting ΔP from eq. (6.10) into eq. (6.24) the following equation is obtained:

$$\begin{cases} \dfrac{dy}{dx} = u \\ \dfrac{du}{dx} = \dfrac{1+u^2}{y} - \dfrac{2\left(R_1\cos\theta_1 + R_0\cos\theta_0\right)\left(1+u^2\right)^{3/2}}{\left(R_1^2 - R_0^2\right)} \end{cases} \tag{6.25}$$

Fitting the solution of eqs. (6.25) to the meniscus image one can find the contact angle θ_1. These equations describe the shape of the liquid/air interface between the tungsten wire and the capillary walls. Figure 6.12 shows the fit where the meniscus profile from the tungsten wire surface was fitted and extended showing the sag point and the meniscus on the wall of the capillary.

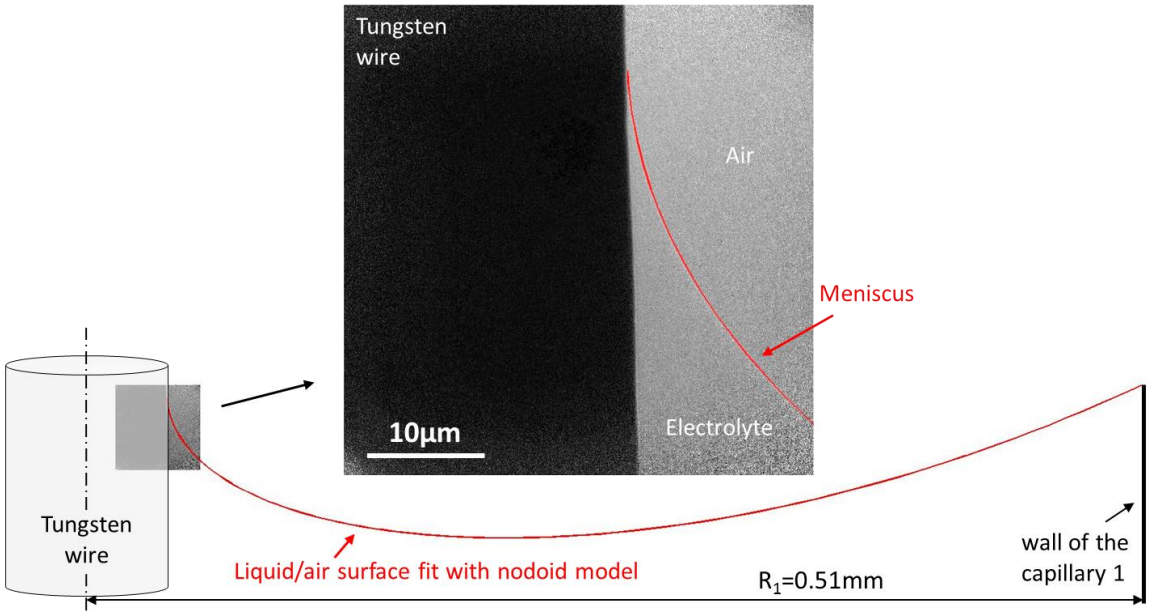

Figure 6.12. Meniscus on a tungsten wire and its nodoid model.

Figure 6.13 represent results of the fit with the nodoid model for meniscus on tungsten wire for the CLE and PLE techniques.

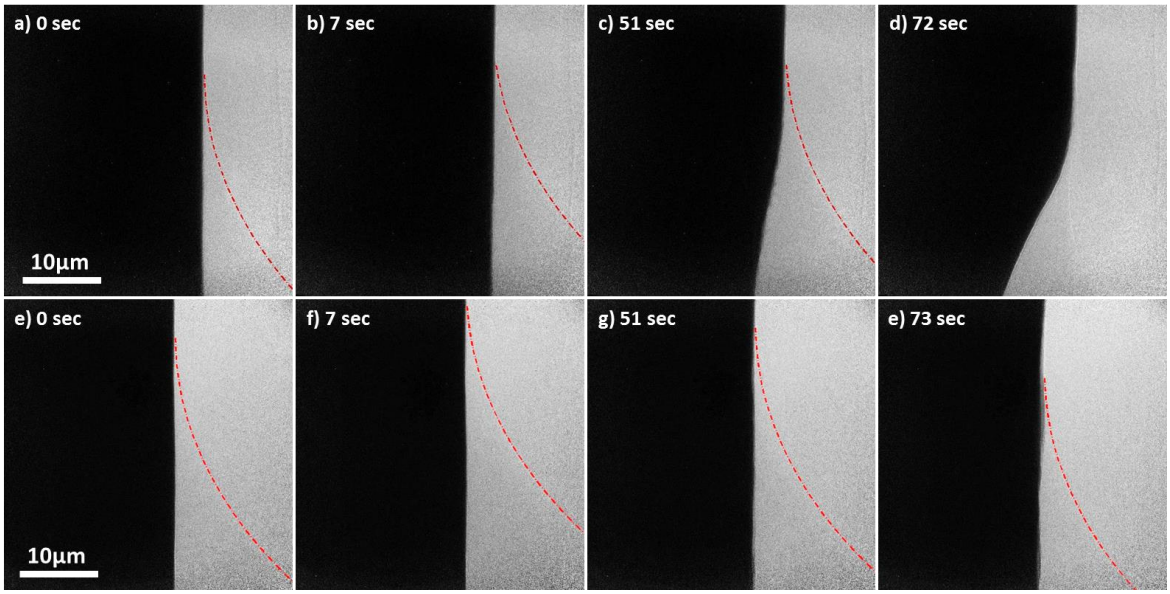

Figure 6.13. The meniscus on tungsten wire: (a), (b), (c), (d) menisci formed during the CLE and (e), (f), (g), (e) PLE

technique. The red dashed line is the nodoid equation describing the meniscus shape.

4. Using eq.(6.13) and knowing the height of meniscus h_1' and corresponding h_2 from the experiment the surface tension of the liquid under the meniscus can be found as follows:

$$\sigma = \frac{\left[\rho g\left(h_1' - h_2\right)\right]/2}{\left(\frac{\left(R_1\cos\theta_1 + R_0\cos\theta_0\right)}{\left(R_1^2 - R_0^2\right)} - \frac{\cos\theta_2}{R_2}\right)} \tag{6.26}$$

Utilizing the proposed algorithm the surface tension of the liquid under the meniscus prior to electropolishing was found to be $\sigma_{1MKOH} = 73.26 \pm 0.01 mN/m$. The shape of the original meniscus and its continuation beyond the field of view using the nodoid model is shown in Figure 6.13 (a). Figure 6.14 confirms that the nodoid model does describe the meniscus shape during the electrochemical reactions. Thus, any flow effects are not significant and we can interpret the surface tension and contact angle data using thermodynamics.

The surface tension and the contact angle that the meniscus makes with the tungsten wire were tracked for both CLE and PLE regimes during the first 60 seconds. The results of the image analysis are shown in Figure 6.14, where the error bars represent the fitting deviation of experimental data. In both cases, the surface tension first drops and then gradually increases; however, in the CLE regime, the decrease of the surface tension is much steeper. The contact angle demonstrates a more complex dependence on time. An initial steep increase of the contact angle with the same slope suggests that the

surface of the tungsten wire gets covered with the same compound which has a smaller surface energy relative to that of the original wire. Remarkably, the contact angles in both cases cannot grow indefinitely; they reach some maxima and then decrease. In the CLE regime, the maximum achievable contact angle is greater, i.e. the surface energy decreases even further compared to the PLE case. Decrease of the contact angle implies that the surface is getting more polar. In the CLE case this decrease is much stronger suggesting that the surface gets covered either with ions or dipoles.

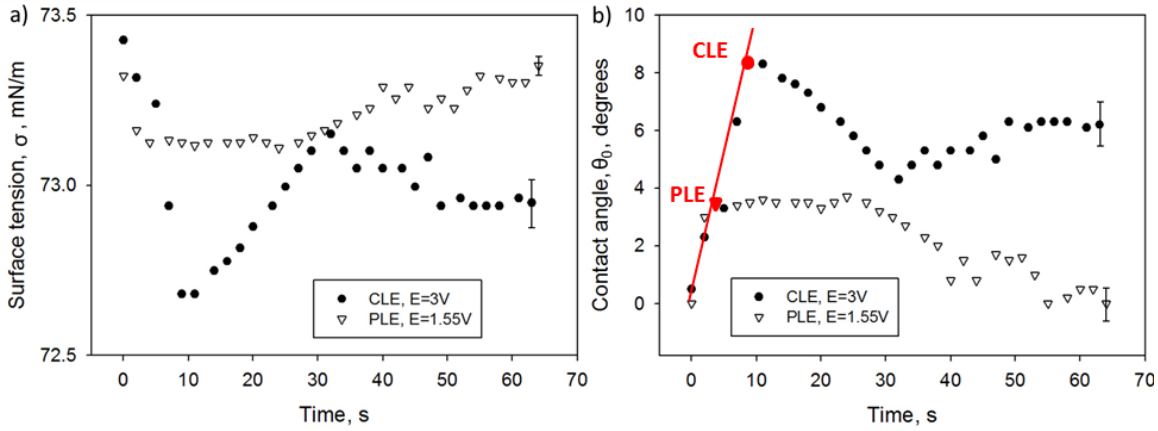

Figure 6.14. (a) Surface tension and (b) contact angle θ_0 dependence on time during electropolishing of tungsten in 1M KOH electrolyte using the CLE and PLE techniques.

In Chapter 3 we calculated the Gibbs adsorption isotherm based on the surface tension experiments with solutions of different concentrations of the tungstate ions in 2M KOH electrolyte. Employing these results the behavior of the surface tension for the 1M KOH solution with tungstate ions was estimated and is presented in Figure 6.15. By correlating the data shown in Figure 6.15 with the surface tension obtained using the nodoid model presented in Figure 6.14 (a) it can be stated that the concentration of the tungstate ions during the CLE technique increases to approximately 0.03M under the

meniscus region and then decreases to 0.015M. Since the oxide film does not change its thickness, this decrease of concentration of tungstate ions implies that these ions do not get adsorbed on the meniscus surfaces but most likely form some complexes inside the flowing viscous film. As a result, the film viscosity increases.

For the PLE regime, the concentration of the tungstate ions increases to approximately 0.01M followed by the decrease back to almost zero at the end. Thus, the tungstate ions get absorbed inside the porous film which keeps growing in expense of these ions.

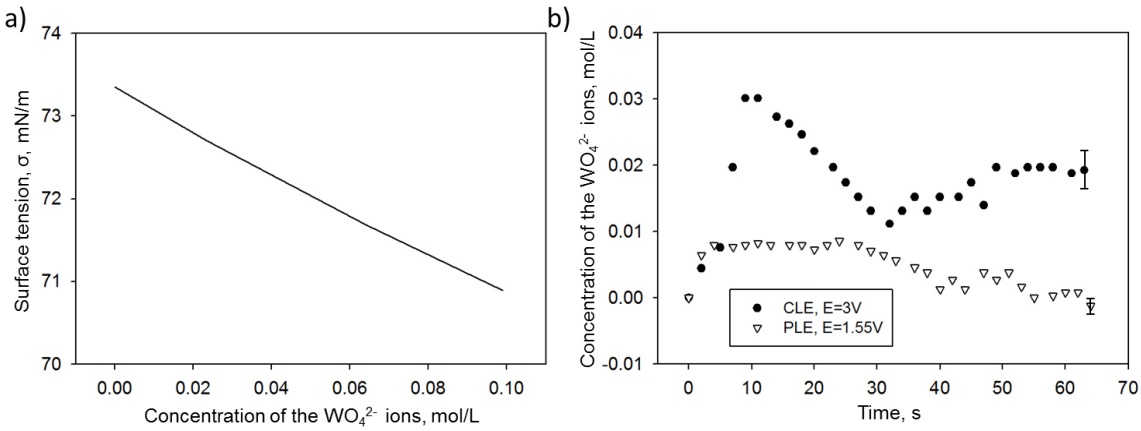

Figure 6.15. (a) The surface tension dependence on the tungstate ion concentration, (b) concentration of the tungstate ions change during the electropolishing in the CLE and PLE regimes.

The data presented in Figure 6.14 and Figure 6.15 can be interpreted employing the Gibbs adsorption isotherm. We employ the Young equation:

$$-\sigma_{sl} = \sigma_{\mathrm{lg}} \cos\theta_0 - \sigma_{sg}, \tag{6.27}$$

where subscript sl marks the solid electrode - liquid interfacial tension, lg marks the liquid - gas interfacial tension, and sg marks the solid electrode - gas interfacial tension.

Since the interfacial tension at the solid electrode - gas interface does not change during the electrochemical reaction; equation (6.27) can be rewritten in its differential form as:

$$-d\sigma_{sl} = d(\sigma_{\mathrm{lg}} \cos\theta_0) \tag{6.28}$$

Evaluating the incremental change of the right side of eq. (6.28), the change of the solid-liquid interfacial energy can be found as:

$$-d\sigma_{sl} = d\sigma_{\mathrm{lg}} \cos\theta_0 + \sigma_{\mathrm{lg}} d\cos\theta_0 \tag{6.29}$$

On the other hand, the Gibbs adsorption equation from Chapter 3 for dilute solutions is written as:

$$\Gamma = \frac{-d\sigma_{sl}}{dC} \cdot \frac{C}{RT} = \left[\frac{d\sigma_{\mathrm{lg}}}{dC} \cos\theta_0 + \frac{d\cos\theta_0}{dC} \sigma_{\mathrm{lg}} \right] \cdot \frac{C}{RT}, \tag{6.30}$$

where R is the gas constant, T is the temperature and C is the concentration of the tungstate ions. Equation (6.30) relates adsorption Γ on the electrode - electrolyte interface to the measured contact angle (Figure 6.14 (b)) and the surface tension of the electrolyte as a function of the tungstate ions concentration.

Calculating the adsorption isotherms, it was assumed that during the initial 10 seconds from the beginning of the electrochemical reaction only ions are present at the surface of the tungsten wire. During this time, the surface tension drops significantly and then stabilizes or begins to increase (Figure 6.14 (a)). After that, due to the formation of

the oxide/hydrate layers, the adsorption model cannot be applied. Figure 6.16 shows the resulting plot of the Gibbs adsorption isotherm for the CLE and PLE regimes.

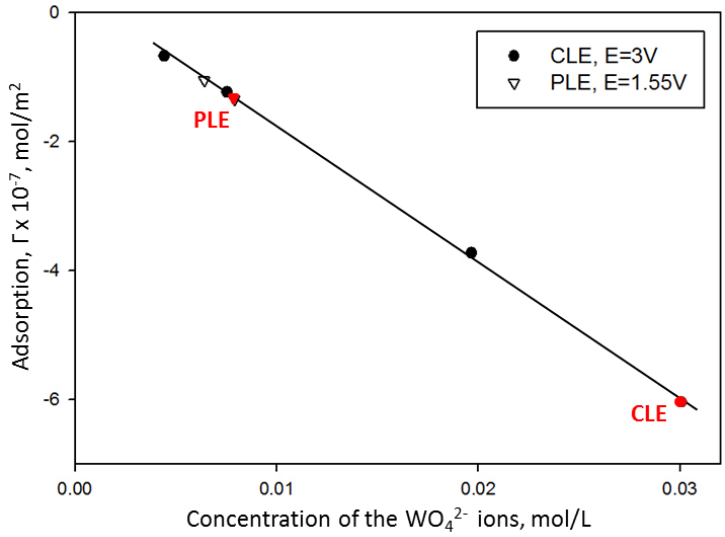

Figure 6.16. The adsorption isotherm for ion adsorption on the electrode surface for the CLE and PLE regimes.

Using the Gibbs adsorption data from Figure 6.11 and eq.(3.55) one can estimate the area occupied by a single adsorbed specie on the surface of the electrode. The Gibbs adsorption for the PLE regime is $\Gamma = -1.3\times10^{-7} mol/m^2$, then using eq.(3.55) we obtain the area occupied by adsorbate as $A = 12.4 nm^2$; in the CLE regime, the Gibbs adsorption was found to be $\Gamma = -6\times10^{-7} mol/m^2$, hence the corresponding area per adsorbate is $A = 2.7 nm^2$.

Since the metal oxide films have the lower surface energies relative to mother metals, the oxide surfaces are less wettable by the electrolyte and hence the contact angles increase [36]. It is evident that the adsorption isotherm for the CLE and PLE regimes are distinct and hence different compounds are formed. In the CLE regime, the area occupied by an adsorbate is about four times smaller than that for the PLE regime.

This suggests that a more complex compound is formed at the tungsten surface during the PLE regime. Therefore, our scenario of the hydrate formation on the tungsten surface is quite probable.

6.5. Conclusions

In this Chapter an X-ray imaging technique was used to study the electrochemical etching of the tungsten wires. We focused on the etching kinetics along the immersed part of the wire and in the meniscus region. The imaging of the tungsten surface submersed into the electrolyte using both CLE and PLE regimes showed a remarkable difference in the oxidation kinetics and the structure of the reaction products. We were able to observe and distinguish several layers with different densities that were growing on top of the tungsten during the PLE regime. Employing the finding made in Chapter 4 we identified the layers as tungsten dioxide and tungsten trioxide monohydrate.

To study the reaction under the meniscus we employed the nodoid model to describe the behavior of the meniscus formed between the tungsten wire and the wall of the capillary. Using this model we were able to fit the meniscus and find the surface tension of the liquid below it. By correlating previous findings described in Chapter 3 and the results of the fit made with the nodoid model we found the concentration of the reaction products under the meniscus. Also, using the Gibbs adsorption isotherm, we confirmed that the tungsten surface was covered by different compounds during the CLE and PLE regimes.

6.6. References

[1] Niven R K 2006 Force stability of pore-scale fluid bridges and ganglia in axisymmetric and non-axisymmetric configurations *Journal of Petroleum Science and Engineering* **52** 1-18

[2] Langbein D 2002 *Capillary Surfaces* (Springer)

[3] Chen B G and Kamien R D 2009 Nematic films and radially anisotropic Delaunay surfaces *European Physical Journal E* **28** 315-29

[4] Mayer R P and Stowe R A 2005 Nodoids and toroids: comparison of two geometries for the meniscus profile of a wetting liquid between two touching isolated spheres and extensions to the model of a collection of packed spheres *J Colloid Interf Sci* **285** 781-8

[5] Wang J, Chen Y C K, Yuan Q X, Tkachuk A, Erdonmez C, Hornberger B and Feser M 2012 Automated markerless full field hard x-ray microscopic tomography at sub-50 nm 3-dimension spatial resolution *Appl. Phys. Lett.* **100**

[6] Chen Y-c K 2011 *X-ray Imaging of Nanoporous Gold: Evolution of Morphology and Internal Strain during Dealloying and Coarsening* (Ann Arbor: Northwestern University) p 157

[7] Kulakov M, Luzinov I and Kornev K G 2009 Capillary and Surface Effects in the Formation of Nanosharp Tungsten Tips by Electropolishing *Langmuir* **25** 4462-8

[8] Nave M, Rubin B, Maximov V, Creager S and Kornev K G 2013 Transport-limited electrochemical formation of long nanosharp probes from tungsten *Nanotechnology* **24**

[9] Nielsen M H, Aloni S and De Yoreo J J 2014 In situ TEM imaging of CaCO3 nucleation reveals coexistence of direct and indirect pathways *Science* **345** 1158-62

[10] Pashchanka M and Schneider J J 2011 Origin of self-organisation in porous anodic alumina films derived from analogy with Rayleigh-Benard convection cells *Journal of Materials Chemistry* **21** 18761-7

[11] Michalska-Domanska M, Norek M, Stepniowski W J and Budner B 2013 Fabrication of high quality anodic aluminum oxide (AAO) on low purity aluminum-A comparative study with the AAO produced on high purity aluminum *Electrochimica Acta* **105** 424-32

[12] Stepniowski W J, Forbot D, Norek M, Michalska-Domanska M and Krol A 2014 The impact of viscosity of the electrolyte on the formation of nanoporous anodic aluminum oxide *Electrochimica Acta* **133** 57-64

[13] Davies J A, Domeij B, Pringle J P S and Brown F 1965 Migration of metal and oxygen during anodic film formation Journal of the Electroch*emical Society* **112** 675-&

[14] Garcia-Vergara S J, Skeldon P, Thompson G E and Habazaki H 2007 Stress generated porosity in anodic alumina formed in sulphuric acid electrolyte *Corrosion Science* **49** 3772-82

[15] Mirzoev R A, Davydov A D and Stepanova N I 2011 The effect of electrolyte anions incorporated into anodic oxide films on the experimental transport numbers of ions *Electrochimica Acta* **56** 4414-9

[16] Pringle J P S 1973 Transport numbers of metal and oxygen during anodic-oxidation of tantalum Jo*urnal of the Electrochemical Society* **120** 398-407

[17] Pringle J P S 1973 Migration of oxygen during anodic-oxidation of tantalum Journal of the Electrochemical *Society* **120** 1391-400

[18] Amsel G, Cherki C, Feuillad G and Nadai J P 1969 Influence of electrolyte on composition of anodic oxide films on tantalum *Journal of Physics and Chemistry of Solids* **30** 2117-&

[19] Chen C T and Hutchins G A 1985 Crystalline anodic oxide-growth on aluminum foil in an aqueous ammonium dihydrogen phosphate anodization electrolyte Journal of the Electrochemical Society 132 1567-74

[20] Lu Q, Mato S, Skeldon P, Thompson G E, Masheder D, Habazaki H and Shimizu K 2002 Anodic film growth on tantalum in dilute phosphoric acid solution at 20 and 85 degrees C *Electrochimica Acta* **47** 2761-7

[21] Ono S, Kuramochi K and Asoh H 2009 Effects of electrolyte pH and temperature on dielectric properties of anodic oxide films formed on niobium *Corrosion Science* **51** 1513-8

[22] Shimizu K, Brown G M, Habazaki H, Kobayashi K, Skeldon P, Thompson G E and Wood G C 1999 Impurity distributions in barrier anodic films on aluminium: a GDOES depth profiling study *Electrochimica Acta* **44** 2297-306

[23] Wood G C, Skeldon P, Thompson G E and Shimizu K 1996 A model for the incorporation of electrolyte species into anodic alumina *Journal of the Electrochemical Society* **143** 74-83

[24] Lassner E and Schubert W-D 1999 *Tungsten: properties, chemistry, technology of the element, alloys, and chemical compounds* (New York: Kluwer Academic/Plenum Publishers)

[25] Lillard R S, Kanner G S and Butt D P 1998 The nature of oxide films on tungsten in acidic and alkaline solutions *Journal of the Electrochemical Society* **145** 2718-25

[26] Kelsey G S 1977 Anodic-oxidation of tungsten in aqueous base *J Electrochem Soc* **124** 814-9

[27] Gerische H 1969 Charge transfer processes at semiconductor-electrolyte interfaces in connection with problems of catalysis *Surface Science* **18** 97-&

[28] Odenweller T 1990 On the theory of the semiconductor electrolyte-interface (I) *Journal of the Electrochemical Society* **137** 2457-61

[29] Zhang Z and Yates J T 2012 Band Bending in Semiconductors: Chemical and Physical Consequences at Surfaces and Interfaces *Chemical Reviews* **112** 5520-51

[30] Aoki T, Tatsuhiko M, Suzuki A, Kenji T and Okuda M 2006 Write-once optical recording using WO2 films prepared by pulsed laser deposition *Thin Solid Films* **509** 107-12

[31] Coskun S and Koziol K K K 2014 A facile water-assisted route for synthesis of tungsten dioxide (WO2) nanopowders *Powder Technology* **256** 1-4

[32] Davico G E, Schwartz R L, Ramond T M and Lineberger W C 1999 An experimental study of the low-lying electronic states of WO2 *Journal of Physical Chemistry A* **103** 6167-72

[33] Gong Y, Zhou M F and Andrews L 2009 Spectroscopic and Theoretical Studies of Transition Metal Oxides and Dioxygen Complexes *Chemical Reviews* **109** 6765-808

[34] Katrib A, Hemming F, Wehrer P, Hilaire L and Maire G 1995 The multi-surface structure and catalytic properties of partially reduced WO3, WO2 and WC+O-2 or W+O-2 as characterized by XPS *Journal of Electron Spectroscopy and Related Phenomena* **76** 195-200

[35] Shaposhnikov V L, Migas D B, Rodin V N and Borisenko V E 2011 Ab initio investigation of structural and electronic properties of tungsten dioxide *Physica Status Solidi B-Basic Solid State Physics* **248** 1471-6

[36] Adamson A W and Gast A P 1997 *Physical chemistry of surfaces* (New York: Wiley)

[37] Chang S C, Wang Y L, Hung C C, Lee W H and Hwang G J 2007 Role of surface tension in copper electroplating *J. Vac. Sci. Technol. A* **25** 566-9

[38] Tenan M A, Teschke O, Kleinke M U and Galembeck F 1990 Surface-tension effects on cell pattern-formation during anodic metal dissolution *Langmuir* **6** 1640-6

[39] Teschke O, Tenan M A and Galembeck F 1989 Wetting effect on the hydrodynamics of thin-film formation *J Colloid Interf Sci* **127** 88-96

[40] Brockmeier A, Santos Rodriguez F J, Harrison M and Hilleringmann U 2012 Surface tension and its role for vertical wet etching of silicon *J. Micromech. Microeng.* **22**

[41] Four-port thru flow double elbow, part number: 4PLL210-6005 (Value Plastics, Inc.)

[42] Costa Akerlof P B 1941 The density of aqueous solutions of potassium hydroxide *J. Am. Chem. Soc.* **63** 1085-8

[43] Drzymala J and Lyklema J 2012 Surface tension of aqueous electrolyte solutions. Thermodynamics *J Phys Chem A* **116** 6465-72

[44] Markin V S and Volkov A G 2002 Quantitative theory of surface tension and surface potential of aqueous solutions of electrolytes *J. Phys. Chem. B* **106** 11810-7

[45] Teschke O, Kleinke M U and Tenan M A 1992 Surface tension-induced convection as a particle aggregation mechanism *J Colloid Interf Sci* **151** 477-89

7. CELL PIERCING USING TUNGSTEN NANOSHARP NEEDLES

7.1. Introduction

Tungsten long probes prepared using PLE regime appear attractive for different biomedical applications such as histological microdissection [1], in vitro cutting of living tissues and cells [2], capillary electrophoresis [3-5] and cell piercing [6-8]. One particular challenging application is related to the piercing of single cells and microorganisms. Available probes of atomic force microscopes are not suitable to perform this task: the cantilever would either break or the force would not be sufficient for membrane poking. Recently, carbon nanotubes where proposed for cell piercing. The 200nm thick nanotubes can penetrate the cell membranes [7]. Some nanowires attached to the optical fiber are also able to withstand the stress and penetrate the cell membrane [9]. We examined the nanosharp tungsten wires with respect to their ability to withstand the compression stresses caused by the cell membrane during piercing.

7.2. Experimental setup

Vascular smooth muscle cells (VSMC) were used to prove the piercing efficiency. First, primary culture of VSMC was harvested from adult female Sprague-Dawley rats using the protocol described earlier [10]. Cells were cultures in Dulbecco's Modified Eagle Medium with 4.5g/L glucose, L-glutamine and sodium pyruvate, supplemented

with 10% Fetal Bovine Serum and 1% Antibiotic/Antimycotic solution and fresh medium was exchanged every 48 hours. Cells were grown till passage number 7 in T-75 polystyrene flasks and prior piercing experiments were passaged on 15 mm round glass coverslips, coated with type I collagen (Figure 7.1 (a)). For the piercing experiment, glass coverslips were placed in a Petri dish (Figure 7.1 (b)), then filled with 5 ml of warm growth medium and placed under the microscope (Figure 7.1 (c)). Additionally, the Live-Dead® Viability/Cytotoxicity assay kit (Life Technologies, Inc.) was used to validate piercing of the cell. The kit consists of two components: a) Calcein AM, 4 mM in anhydrous dimethylsulfoxide (DMSO) and b) Ethidium homodimer III (EthD-III), 2 mM in DMSO/H2O 1:4 (v/v), which were added to the medium during piercing experiments in concentrations that were specified in the manufacturer's protocol. Once added to cells, Calcein AM penetrates membranes of living cells and converted into cell membrane-impermeable Calcein dye which was retained in live cells producing green fluorescence (ex/em ~495 nm/~515 nm). After the cell was probed, the membrane impermeable EthD-III entered inside the cell and bonded to the nucleic acids, producing red fluorescence (ex/em ~530 nm/~635 nm).

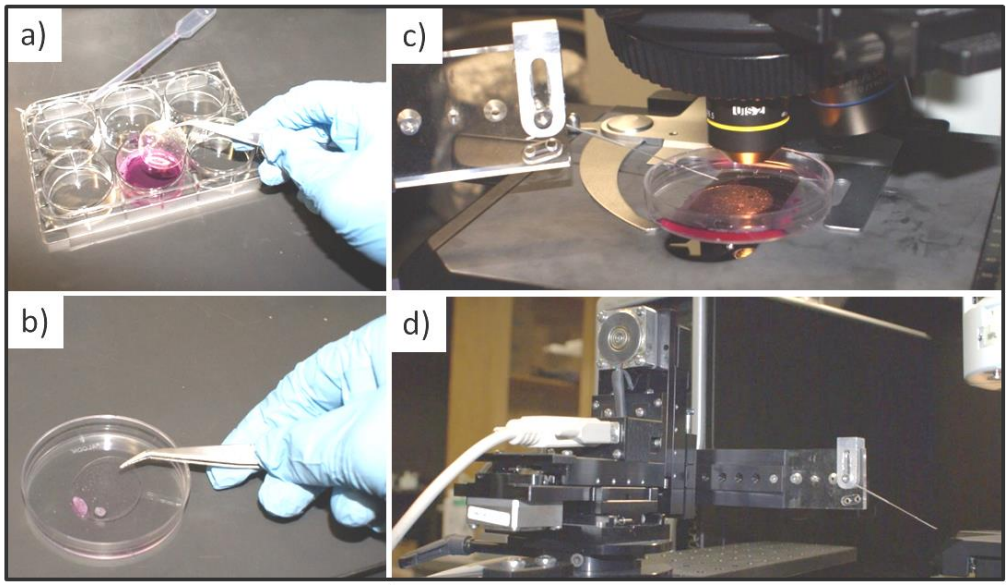

Figure 7.1. Preparation for cell piercing procedure: (a) plate with cells on the slide covered with the medium, (b) Slide placed in a dish, (c) manipulator with the needle attached to its holder, (d) dish with the cells on a stage and needle pointed at it.

The set up for the cell piercing consisted of PLE tungsten probe inserted into the hypodermic needle that afterwards was attached to the nanomanipulator MP-285 (Sutter Instrument Co.) (Figure 7.1 (d)). The probes where guided with nanomanipulator in order to provide precise control of the piercing procedure. The manipulator was operated though the knob (Figure 7.2) that allowed moving the probe in three dimensions.

For visualization of the piercing process Olympus BX51 optical microscope with an attached Spot Boost camera (Diagnostic Instruments, Inc.) and a computer was used (Figure 7.2).

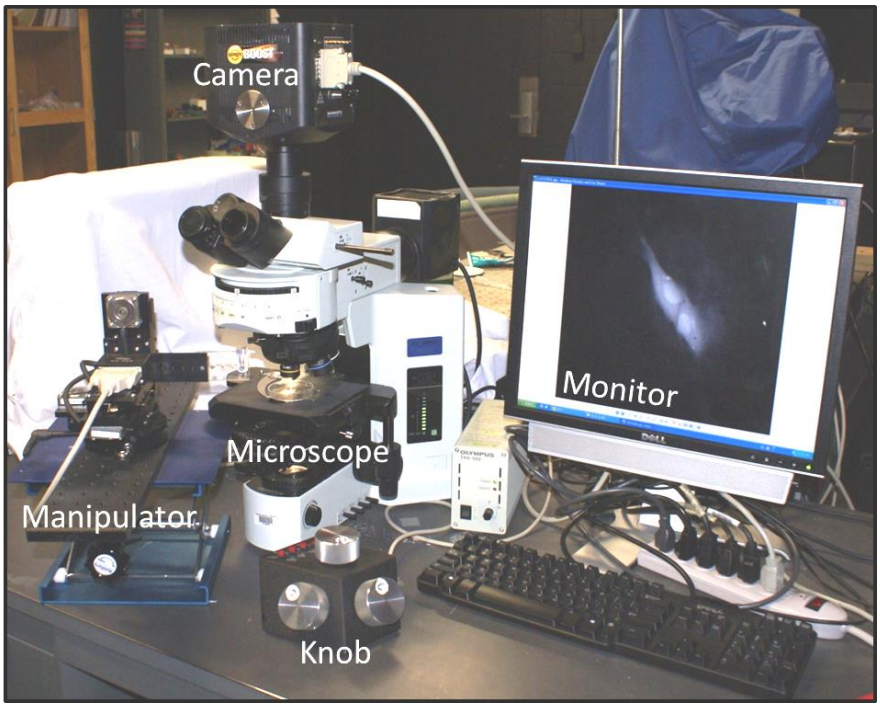

Figure 7.2. Setup for cell piercing.

Next, focusing on cells was performed in bright field with 10x (Figure 7.3) or 50 x (Figure 7.4) objectives. Then, using TRITC filter fluorescent imaging of the cells membranes was obtained.

7.3. Results and discussion

Figure 7.3 and Figure 7.4 represents a series of pictures taken before, during, and after the cell piercing. Figure 7.3 (a) shows the image where green corresponds to Calcein AM that penetrated membranes of living cells producing green fluorescence (ex/em ~495 nm/~515 nm). There is no red fluorescence present, meaning all cells are alive. Figure 7.3 (b), (c) shows the piercing procedure with tungsten tip. Figure 7.3 (c) shows image of the cells after they were probed. The membrane impermeable EthD-III entered inside the cell

and bonded to the nucleic acids, producing red fluorescence (ex/em ~530 nm/~635 nm). The Adobe Photoshop was used to process fluorescent images of cell piercing experiment in order to show the green and red fluorescence from black and white pictures.

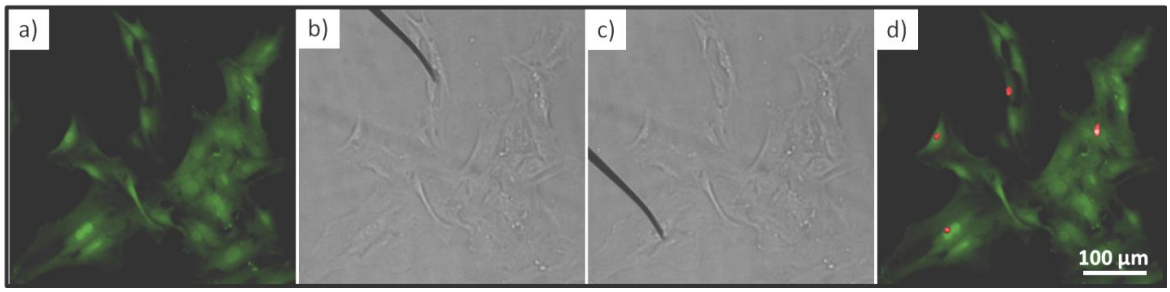

Figure 7.3. Fluorescent microscope images of the vascular smooth muscle cell (10^x magnification) : (a) cells before probing (green color displays membranes of the live cells), (b), (c) cell probing with tungsten needle in bright field, (c) cells after probing (red color shows nuclei of the probed cells).

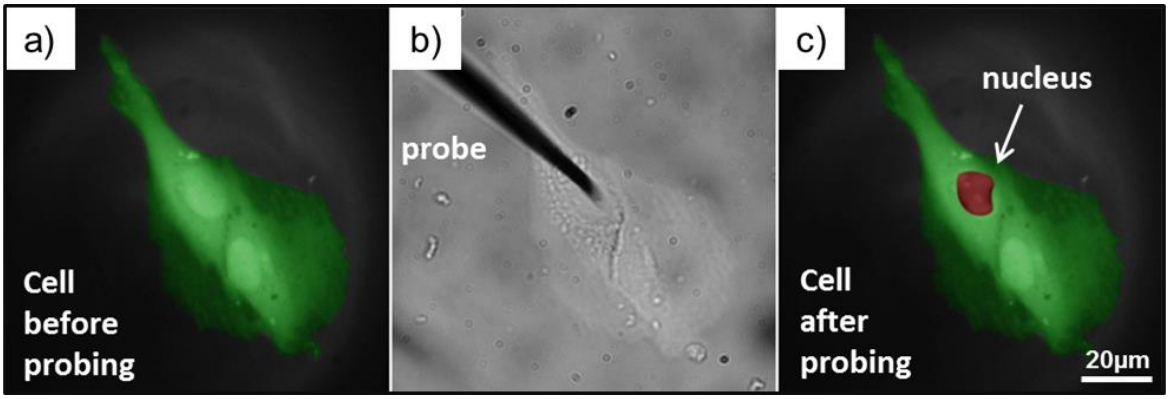

Figure 7.4. Fluorescent microscope images of the vascular smooth muscle cell (50^x magnification). The live-dead-assay cell kit was applied (a) before, (b) during and (c) after piercing of the single cell. The green color corresponds to Calcein AM dye and the red color to EthD-III.

Using vascular smooth muscle cells with Live-Dead® Viability/Cytotoxicity assay kit (Life Technologies, Inc.) [11] it was confirmed that the tungsten probe did not break and the cell membrane was successfully pierced using the designed probes.

7.4. Conclusions

Analyzing the fluorescent response of the cells, we concluded that the cell membrane could be successfully pierced without damaging the probe. Even when hitting the substrate, the probe stayed intact without any breakup. Conventional probes produced by the CLE methods were also tested for cell piercing. Due to the short length of the needle, it was not possible to manipulate the probe and simultaneously observe the targeted cell. In these experiments, the cells were smashed over the glass cover slips and were completely destroyed.

7.5. References

[1] Going J J and Lamb R F 1996 Practical histological microdissection for PCR analysis *Journal of Pathology* **179** 121-4

[2] Hirvonen J, Ronkanen P, Ylikomi T, Blauer M, Suuronen R, Skottman H and Kallio P 2008 Microcutting of living tissue slices and stem cell colonies by using mechanical tool and liquid jet *2008 2nd Ieee Ras & Embs International Conference on Biomedical Robotics and Biomechatronics (Biorob 2008), Vols 1 and 2* 700-5

[3] Ewing A G, Wallingford R A and Curry P D 1988 Chemical-analysis of single cells with capillary zone electrophoresis *Abstracts of Papers of the American Chemical Society* **196** 177-ANYL

[4] Sloss S and Ewing A G 1993 Improved method for end-column amperometric detection for capillary electrophoresis *Analytical Chemistry* **65** 577-81

[5] Wallingford R A and Ewing A G 1988 Amperometric detection of catechols in capillary zone electrophoresis with normal and micellar solutions *Analytical Chemistry* **60** 258-63

[6] Yum K, Wang N and Yu M F 2010 Nanoneedle: A multifunctional tool for biological studies in living cells *Nanoscale* **2** 363-72

[7] Singhal R, Orynbayeva Z, Sundaram R V K, Niu J J, Bhattacharyya S, Vitol E A, Schrlau M G, Papazoglou E S, Friedman G and Gogotsi Y 2011 Multifunctional carbon-nanotube cellular endoscopes *Nat Nanotechnol* **6** 57-64

[8] Schrlau M G and Bau H H 2010 Carbon nanopipettes for cell surgery *Jala-J Assoc Lab Aut* **15** 145-51

[9] Yan R, Park J-H, Choi Y, Heo C-J, Yang S-M, Lee L P and Yang P 2011 Nanowire-based single-cell endoscopy *Nature Nanomaterials* advance online publication

[10] Xu S, Fu J, Chen J, Xiao P, Lan T, Le K, Cheng F, He L, Shen X, Huang H and Liu P 2009 Development of an optimized protocol for primary culture of smooth muscle cells from rat thoracic aortas *Cytotechnology* **61** 65-72

[11] Zhou S D, Cui Z F and Urban J 2011 Dead cell counts during serum cultivation are underestimated by the fluorescent live/dead assay *Biotechnol J* **6** 513-8